

**Development of a compact wireless SAW Pirani
vacuum microsensors with extended range and sensitivity**

Zur Erlangung des akademischen Grades einer
DOKTORIN DER INGENIEURWISSENSCHAFTEN (Dr.-Ing.)
von der KIT-Fakultät für Maschinenbau des
Karlsruher Instituts für Technologie (KIT)

genehmigte
DISSERTATION
von

M.Sc. M.Sc. CSCA Sofia Toto

Tag der mündlichen Prüfung: 08. März 2023
Referent: Prof. Dr. Jan G. Korvink
Korreferent: PD Dr. Ulrich Gengenbach

Abstract

Vacuum sensors still have restricted sensing ranges and require bulky wiring as well as complex integration into vacuum chambers. A compact sensor able to extend the sensing range between high vacuum and atmospheric pressure while operating wirelessly is highly desirable. The focus of this work lies in the design, simulation, manufacturing and experimental validation of a wireless compact vacuum microsensor with extended range and sensitivity. First a new sensor was designed using available and newly designed components. Second the sensor components were simulated to optimise their parameters. Third, a prototype was manufactured and assembled using the available micromachining and semiconductor technologies. Fourth the prototype was characterised at ambient and vacuum conditions to validate its performances.

Two techniques have been combined to form the transducing principle, namely Pirani sensing and Surface Acoustic Waves. The design of the sensor components boiled down to four units: sensing unit, heating unit, interrogation unit and the packaging. All units were inserted inside a compact cube. Some components were newly designed while other components were bought, modified and then coupled together. The sensing unit consists of a new chip with improved sensing performances thanks to an optimised surface to volume ratio. The heating unit was assembled using two inductively coupled coils and their conditioning electronics. The interrogation unit was made with a micro patch antenna. A polymer cubic shaped packaging was designed to enclose all the components inside a vacuum chamber.

Second, the simulation of the sensors components behaviour was dealt with. The sensing chip heat transfer responsible for the pressure measurement was evaluated from high vacuum to atmospheric pressure in order to optimise its dimensions. The use of a suspended Y-Z-cut Lithium Niobate chip, with a TCF of 94 ppm/K revealed an improved performance achieving a sensing range between 10^{-4} Pa and 10^5 Pa. The heating unit coils electronic coupling was simulated as well to optimise the power transfer and coupling distance.

The third part concerns the manufacturing and assembly steps of the prototype using the available semiconductor technologies and equipment. A SAW chip was sputtered with a 100 nm gold layer at its bottom to form the heating resistance and wirebonding was used to connect it electrically to the rest of the sensor. A PCB containing the heating and sensing unit was prepared. A PTFE cubic package was manufactured. Fourth, the sensor components were first characterised separately to verify their performances, then together at ambient conditions. Later on, the sensor was integrated inside vacuum and a pressure dependent behaviour of the sensing chip was observed.

The relevance of a wireless transmission method was confronted with conventional wired methods. The results of the experimental work outside vacuum and inside vacuum revealed the feasibility and relevance of the new concept.

Zusammenfassung

Vakuumsensoren haben nach wie vor einen begrenzten Messbereich und erfordern eine aufwendige Verkabelung sowie eine komplexe Integration in Vakuumkammern. Ein kompakter Sensor, der in der Lage ist, den Erfassungsbereich zwischen Hochvakuum und Atmosphärendruck zu erweitern und dabei drahtlos zu arbeiten, ist äußerst wünschenswert. Der Schwerpunkt dieser Arbeit liegt auf dem Entwurf, der Simulation, der Herstellung und der experimentellen Validierung eines drahtlosen kompakten Vakuum-Mikrosensors mit erweiterter Reichweite und Empfindlichkeit. Zunächst wurde ein neuer Sensor unter Verwendung vorhandener und neu entwickelter Komponenten entworfen. Zweitens wurden die Sensorkomponenten simuliert, um ihre Parameter zu optimieren. Drittens wurde ein Prototyp unter Verwendung der verfügbaren Mikrobearbeitungs- und Halbleitertechnologien hergestellt und montiert. Viertens wurde der Prototyp unter Umgebungs- und Vakuumbedingungen charakterisiert, um seine Leistungen zu validieren.

Für das Wandlerprinzip wurden zwei Techniken kombiniert, nämlich Pirani-Sensorik und akustische Oberflächenwellen. Das Design der Sensorkomponenten bestand aus vier Einheiten: Sensoreinheit, Heizeinheit, Abfrageeinheit und Gehäuse. Alle Einheiten wurden in einen kompakten Würfel eingebaut. Einige Komponenten wurden neu entwickelt, während andere gekauft, modifiziert und dann miteinander verbunden wurden. Die Sensoreinheit besteht aus einem neuen Chip mit verbesserter Sensorleistung dank eines optimierten Verhältnisses von Oberfläche zu Volumen. Die Heizeinheit wurde aus zwei induktiv gekoppelten Spulen und der zugehörigen Konditionierungselektronik zusammengesetzt. Die Abfrageeinheit wurde mit einer Mikro-Patch-Antenne hergestellt. Ein würfelförmiges Polymergehäuse wurde entwickelt, um alle Komponenten in einer Vakuumkammer unterzubringen.

Zweitens wurde die Simulation des Verhaltens der Sensorkomponenten behandelt. Die für die Druckmessung verantwortliche Wärmeübertragung des Sensorchips wurde vom Hochvakuum bis zum Atmosphärendruck untersucht, um seine Abmessungen zu optimieren. Die Verwendung eines hängenden Lithium-Niobat-Chips mit Y-Z-Schnitt und einem TCF von 94 ppm/K führte zu einer verbesserten Leistung in einem Messbereich zwischen 10^{-4} Pa und 10^5 Pa. Die elektronische Kopplung der Heizspulen wurde ebenfalls simuliert, um die Leistungsübertragung und den Kopplungsabstand zu optimieren.

Der dritte Teil betrifft die Herstellungs- und Montageschritte des Prototyps unter Verwendung der verfügbaren Halbleitertechnologien und -ausrüstung. Ein SAW Chip wurde mit einer 100 nm dicken Goldschicht an der Unterseite gesputtert, um den Heizwiderstand zu bilden, und mit Hilfe von Drahtbonding elektrisch mit dem Rest des Sensors verbunden. Es wurde eine Leiterplatte vorbereitet, die die Heiz- und Sensoreinheit enthält. Ein kubisches Gehäuse wurde aus PTFE hergestellt.

Viertens wurden die Sensorkomponenten zunächst separat charakterisiert, um ihre Leistungen zu überprüfen, und dann zusammen unter Umgebungsbedingungen. Später wurde der Sensor im Vakuum integriert, und es wurde ein druckabhängiges Verhalten des Sensorchips beobachtet.

Die Relevanz eines drahtlosen Übertragungsverfahrens wurde den herkömmlichen drahtgebundenen Methoden gegenübergestellt. Die Ergebnisse der experimentellen Arbeiten außerhalb und innerhalb des Vakuums zeigten die Machbarkeit und Relevanz des neuen Konzepts.

Contents

Abstract	i
Zusammenfassung	iii
Symbols and Abbreviations	vii
1 Introduction	1
1.1 Preamble	1
1.2 Motivation	1
1.3 Thesis outline	3
1.4 Thesis contributions to the state of the art	4
1.5 Publications	5
2 Theoretical background	9
2.1 Sensors	9
2.2 Gas kinetic theory	23
2.3 Pressure sensors	29
2.4 Pirani sensors	37
2.4.1 Pirani operating principle	37
2.4.2 Pirani sensor modelling	38
2.4.3 Pirani sensors state of the art	43
2.5 Wireless power transfer and wireless sensing	44
2.5.1 Coils coupling for wireless power transfer circuit design	44
2.5.2 State of the art of wireless power transfer	52
2.5.3 Wireless sensors	54
2.6 Surface Acoustic Waves	56
2.6.1 SAW sensors structure	58
2.6.2 SAW sensors applications	60
2.7 SAW Pirani sensors	62
2.7.1 SAW signal processing	63
2.8 Microfabrication technologies	66
2.9 Vacuum considerations	71

3	Modelling and Simulation	73
3.1	Matlab simulation of the Pirani principle	73
3.1.1	Response time	73
3.1.2	Initial temperature	74
3.1.3	Gas gap	74
3.1.4	Gaseous heat transfer over total heat transfer ratio	75
3.1.5	Sensor area	76
3.1.6	Summary	77
3.2	Simulation of the thermal behaviour of a Surface Acoustic Wave sensor	78
3.3	Simulation of the packaged sensor in COMSOL	90
3.3.1	Preliminaries	91
3.3.2	Materials and methods	93
3.3.3	Results and discussion	103
3.4	MOSFET circuit	113
4	Design of the sensor	117
4.1	Heating unit	119
4.2	Interrogation unit	124
4.3	Sensing chip	128
4.4	Packaging	132
4.5	PCB	134
5	Experiments	137
5.1	Manufacturing	137
5.1.1	Experimental procedure	137
5.1.2	Results	143
5.1.3	Discussion	144
5.2	Measurements outside vacuum	152
5.2.1	Experimental procedure	153
5.2.2	Results	163
5.2.3	Discussion	164
5.3	Measurements in vacuum	166
5.3.1	Experimental setup	167
5.3.2	Results	172
5.3.3	Discussion	177
6	Discussion of results	185
6.1	Working design	185

6.2 Simulation	187
6.3 Manufacturing	188
6.4 Vacuum integration	188
7 Conclusion and outlook	191
Bibliography	195
8 Acknowledgements	203
List of Figures	205
List of Tables	211
9 Appendices	213
9.1 Pirani curves obtained with Matlab	213

Symbols and Abbreviations

Formulas

A	Surface	m^2
c	Specific Heat Capacity	$J/(kgK)$
f	Frequency	Hz
h	Height	m
L	Inductance	H
l	Length	m
R	Resistance	Ω
T	Temperature	$^{\circ}C$
t	Time	s
v	Velocity	m/s
ε	Permittivity	F/m
μ	Permeability	H/m
μ_r	relative Permeability	–

Constants

σ	Stefan-Boltzmann constant $5,67 \cdot 10^{-8}$	$W/(m^2K^4)$
----------	--	--------------

Abbreviations

AC	Alternating current
CAN	Controller Area Network
CDG	Capacitive Diaphragm Gauge
DC	Direct current
EHV	Extreme high vacuum
FPGA	Field Programmable Grid Array
FSO	Full Scale Operating range
GPIB	General Purpose Interface Bus
IDT	Interdigital Transducer
MEMS	Micro Electro Mechanical Sensors

PCB	Printed Circuit Board
ppm	Parts per million
PROM	Programmable Read Only Memory
PTFE	Polytetrafluoroethylene
PXI	PCI Extensions for Instrumentation
RS232	Recommended Standard 232
Rx	Receiving part
SAW	Surface Acoustic Waves
SMD	Surface Mounted Device
SRAM	Static Random Access Memory
TCF	Temperature Coefficient of Frequency
TFT	Thin Film Transistor
Tx	Transmitting part
UHV	Ultra High Vacuum
VNA	Vector Network Analyzer

1 Introduction

1.1 Preamble

After the introduction of the transistor in 1956 by Intel, microelectronics have found their way to a wide variety of applications. Since then, they are present in products ranging from smartphones to aeroplanes crossing many applications and disciplines. Micro Electro Mechanical Systems (MEMS) refer to micromachined structures with mechanical, thermal and fluid functions for sensors, actuators, and micromachines.

Along with sinking of fabrication cost of Complementary Metal Oxide Semiconductor (CMOS) digital circuit technology, research and industry witnessed the proliferation of CMOS compatible microsensor structures and measurement circuits within their setups [1].

Miniaturization is intimately linked to process intensification in addition to material and space saving. As a result, there has always been a non stopping demand for developments and enhancements in all relevant aspects including theory, methodology, hardware, and manufacturing.

By processing the signals from all sensors, considerable advances in process performance can be achieved. Such advances include an increased Signal to Noise Ratio (SNR) and resolution, a larger measurement range, or a decreased response time. These advantages of MEMS sensors made them a fundamental concept applied in almost all commercial electronic devices. Indeed, each cell phone or tablet or graphic card contains many MEMS that enables it to process incoming information and display information output.

Besides, utilizing several sensors requires more connections to carry the signals, more power and space to address these signals. This leads to increased cost, size, and complexity of the system, which scale with the number of sensors in the system [2].

1.2 Motivation

Sensors are the connecting elements between the digital and the real world which makes them one of the key elements for implementing the Internet of Things. Without suitable sensors, no process information allowing to anticipate and plan the behaviour of processes and products is available [3]. Wireless sensor networks are key components of the Internet of Things [4]. A sensing system is built up from a number of major parts that include:

- a transducer converting a physical signal into an electrical one.
- an electronics circuit sending output values
- a packaging
- a software that controls the sensing and processes the resulting signals.

Pressure is an essential process parameter in many industrial and experimental setups. Many industries and research setups involve vacuum processes [5]. The development of quantum computers for instance requires reliable vacuum control[6]. Agro-processing industry needs vacuum clean environment and controlled atmospheres for conservation and hygienic purposes. Those are examples among many industrial and research applications of involving vacuum.

Heat conductivity vacuum gauges and more specifically Pirani gauges are based on the pressure dependence of thermal conductivity of gases at subatmospheric pressures. A heated element inserted in a vacuum environment exchanges heat with the surrounding gas molecules. The steady state temperature of the element is used to deduce the value of the pressure. Thus, Pirani sensors are used for sensing rough vacuum where they have an unsurpassed accuracy. Device miniaturization and MEMS development have also impacted heat conductivity gauges to which Pirani sensors belong. Micro pressure sensors are considered as efficient devices with improved sensing performances compared to macroscopic pressure sensors. This can be explained by shorter heat transfer distances and increased surface-to-volume ratios. In the case of Pirani based pressure sensing, miniaturization of the sensing element increases the sensitivity of measurement by reducing the ratio of parasitic heat transfer in the total balance. However, all the MEMS Pirani available off-the-shelf or presented in literature require wiring to their conditioning electronics. In a vacuum environment, this implies the use of bulky wiring and feedthroughs that increase the energy and maintenance cost to operate a vacuum chamber properly as well as the leakage risk. Integration of a measurement device inside a tight installation introduces constraints and requirements. The opportunity of a wireless operation of a Pirani sensor would provide many conveniences to make their daily use easier and more efficient although it raises some challenges within a vacuum environment mostly made of metal. A wireless sensor is portable and can be used for different installations. Besides, wireless sensing avoids leakages due to wires in vacuum.

Surface Acoustic Waves (SAW) belong to the technologies used for micro pressure sensors. SAW sensors are considered as accurate temperature, pressure, humidity and chemical species sensors. They also offer the opportunity of wireless operation and RFID [7]. They are passive, low cost and low power sensors [8].

Surface Acoustic Waves Radio Frequency Identification (SAW RFID) is among the most interesting RFID systems in terms of energy consumption and power efficiency. In fact, SAW RFID readers use low power RF pulses as interrogation signals, while other RFID technology, such as integrated circuit based RFID and Substrate Integrated Waveguide (SIW) cavity resonator-based RFID, require higher power and continuous request signals [9]. Besides, the development of wireless telecommunications enables

the development of portable and flexible devices easier to operate and integrate all along eliminating the bulky wiring.

Therefore, in the present thesis the topic of vacuum pressure sensors and wireless compact sensing has been considered using the Pirani principle and Surface Acoustic Waves. Having this in mind, the following work aims to develop a new wireless compact vacuum sensor combining Surface Acoustic Waves and the Pirani principle. It shows research results to verify if such a concept is feasible and of interest for all its stakeholders.

1.3 Thesis outline

This thesis consists of five chapters structured in three main parts, accompanied by one introductory chapter and the conclusion. The thesis is organised as follows:

- Chapter 1 provides a quick introduction with the motivation of the topic and the objectives.
- Chapter 2 presents an overview of the theoretical sensor technology concepts referred to by the rest of the thesis as well as the state of the art for the various technical aspects addressed in this thesis. In the beginning, the fundamentals of metrology are explained. Then, pressure transducing principles are presented followed by Surface Acoustic Waves. The gas kinetic concepts and physical variables used in the scope of this thesis are described, followed by the thermal and electrical modelling of conventional Pirani sensors. Later on the theory of wireless induction coupling is presented. To conclude the chapter, glimpses on the state of art solutions are given for Pirani sensors, wireless sensors, SAW signal processing, semiconductor technologies, vacuum considerations and SAW-Pirani sensors.
- Chapter 3 assesses the simulations performed in order to dimension and select the parameters of the sensor components resulting in a first comprehensive design.
- Chapter 4 introduces a wireless compact SAW Pirani sensor as a novel solution to the size, cost, and complexity issues related to vacuum sensing. The design of the sensor system and its different units is explained.
- Chapter 5 starts with an overview of the manufacturing steps leading to a prototype using micro-fabrication techniques and semiconductor technologies. The second part of the chapter presents a prototype and characterisation experiments for this device. It shows the measurements results of various parts of the prototype. Moreover, investigation results for the influence of environmental parameters on the performance of the chip are displayed. Finally, the chapter exhibits results of using the chip in vacuum, and compares them with corresponding results obtained from commercial systems.

- In the following Chapter 6, all the results of the thesis are discussed, and advantages and drawbacks of these are highlighted.
- Finally Chapter 7 concludes the entire thesis and gives an outlook for future work.

1.4 Thesis contributions to the state of the art

The analysis of the state of the art prior to the research work presented here highlights several technical issues and challenges:

- Vacuum sensors still have very restricted sensing ranges, hence the necessity for several transducers combined to sense high vacuum to atmospheric pressure.
- The sensors have bulky wiring, housing and a rather high power consumption [10, 11].
- Wireless interrogation and heating for pressure and vacuum sensing still requires coils and antennas with sizes bigger than 10 cm diameter [11].
- No thermal analysis of SAW sensors in vacuum using gas kinetic theory is available.

This research work suggests several solutions to these preliminary issues, which are:

- A compact sensing system with extended range and sensitivity compared to existing devices was developed.
- Miniaturised wireless technologies were implemented. Small conditioning electronics for wireless transmission were validated.
- Limits of some semiconductor processes were pushed:
 - Processing the chip on two sides, top and bottom
 - soldering of small surfaces
 - wirebonding with suspended wires
- A smaller chip was designed.
- RFID was introduced on the sensor as well.
- A system integration in a tiny space compatible with 2 distinct waves propagations was achieved.
- After varying several dimensional parameters of the sensor chip, simulation showed that pressures between 10^{-4} Pa and 10^5 Pa can be sensed via the gas thermal conductivity variation.

Modelling and simulation were used to design a new optimised chip. The equations were obtained using gas kinetic theory. A parameter sensitivity analysis was conducted to improve the vacuum sensing performance via dimensioning. The surface to volume ratio, the gas gap and the emissivity of the interacting surfaces influence the heat transfer. Therefore, they have been chosen in a way to improve the pressure sensing performance.

Further extensions of the sensor's operating range were achieved with heat transfer enhancement techniques, more precisely with optimisation of the dimensions of the sensing chip. The radiative heat transfer has been addressed by modifying the chip surface emissivity as well as the emissivity values of the surrounding surfaces. After working on extracting the maximum of 'useful signal' from the gas, effort was invested on amplifying this useful signal at the chip level. In order to reduce the thermal losses due to solid conduction, the chip was suspended via wires inside a microchannel.

The investigation of different heating methods, different interrogation methods, different chip materials and different packaging materials lead to interesting conclusions in order to improve vacuum sensor performances:

- the use of a piezoelectric substrate with the highest Temperature Coefficient of Frequency increases the sensitivity
- the implementation of a wireless transmission method compatible with vacuum chambers made of stainless steel removes the bulky wiring. This can be achieved by using a glass window or even using the metallic material as an intermediate antenna
- the energy range necessary for the sensor operation is compatible with the possible coupling distance in a vacuum environment.

1.5 Publications

Journal publications

The main contributions of this thesis to the field lead to three published journal papers with contribution as main author:

- **Toto, S.**, Nicolay, P., Morini, G. L., Rapp, M., Korvink, J. G. and Brandner, J. J. 2019. Design and Simulation of a Wireless SAW-Pirani Sensor with Extended Range and Sensitivity. *Sensors (Basel, Switzerland)*, 19(10), 2421. <https://doi.org/10.3390/s19102421>
- **Toto, S.**, Pascal Nicolay, Gian Luca Morini, Achim Voigt, Jan G. Korvink and Juergen J. Brandner 2021. Toward a Compact Wireless Surface Acoustic Wave Pirani Microsensor with Extended Range and Sensitivity, *Heat Transfer Engineering*, 42:6, 565-578. <https://doi.org/10.1080/01457632.2019.1707409>

- **Toto, S.,** Jouda, M., Korvink, J.G., Sundarayanan, S., Voigt, A., Davoodi, H. and Brandner, J.J. Characterization of a Wireless Vacuum Sensor Prototype Based on the SAW-Pirani Principle. *Processes* 2020, 8, 1685. <https://doi.org/10.3390/pr8121685>

Conference contributions

The results obtained within this thesis were presented during several conferences:

- **Toto, Sofia.** Design, development and validation of a Micro-Pirani pressure sensor for micro and macro scale applications. *Proceedings of the 1st MIGRATE Workshop, June 26-30, 2016 – Strasbourg, France.* (talk and poster)
- **Toto, Sofia,** Morini, Gian-Luca and Haas-Santo, Katja. Thermal behaviour of a SAW transducer for pressure measurements. *Proceedings of the 2nd MIGRATE Workshop, June 29 - 30, 2017 - Sofia, Bulgaria.* (talk and poster)
- **Toto, Sofia,** Korvink, Jan, Voigt, Achim, Wuest, Martin and Brandner, Juergen. Characterization of a SAW chip and wireless application of the Pirani principle in vacuum. *Proceedings of the 3rd MIGRATE Workshop, June 27-29, 2018 – Bastia, France.* (talk and poster)
- **Toto, Sofia,** Wuest, Martin, Nicolay, Pascal, Morini, Gian Luca and Brandner, Juergen. Design and manufacturing of a wireless SAW-Pirani sensor with extended range. *15th European Vacuum Conference, Geneva, Switzerland, 17-22 June 2018.* (talk) Elsevier Student Award.
- **Toto, Sofia,** Nicolay, Pascal, Morini, Gian Luca, Rapp, Michael, Korvink, Jan and Brandner, Juergen. SAW-Pirani vacuum sensor with extended range and sensitivity. *6th Micro and Nano Flows Conference, Atlanta, USA, 9-12 September 2018.* (talk)
- **Toto, Sofia,** Nicolay, Pascal, Morini, Gian-Luca and Brandner, Juergen. Design of a SAW Pirani sensor with extended range and sensitivity. *Proceedings of the 5th European Conference on Microfluidics – μ Flu18 and 3rd European Conference on Non-Equilibrium Gas Flows – NEGF18, February 28-March 2, 2018 – Strasbourg, France.* (talk)
- **Toto, Sofia** and Brandner, Juergen. Design and manufacturing of a wireless SAW-Pirani sensor with extended range and sensitivity. *German Physics Society Spring Meeting, March 31- April 5, 2019 - Regensburg, Germany.* (invited talk)
- **Toto, Sofia ,** Sundarayanan, Suparna, Voigt, Achim, Korvink, Jan and Brandner, Juergen. Characterization of a wireless vacuum sensor prototype based on the SAW Pirani principle. *Proceedings of the International Symposium on Thermal Effects in Gas flows In Microscale October 24-25, 2019 – Ettlingen, Germany.* (talk and poster)

Patent

A patent for the sensor developed within this thesis has been filed under the German Patent Office DPMA with the number 102019126837 and the title "SAW-Pirani-Druckmesssensor und -system".

2 Theoretical background

2.1 Sensors

Measurement definition

In any human activity, the idea of measuring corresponds to the establishment of a relationship between a natural or artificial phenomenon and some symbols, usually numbers, in order to build a representation as accurate as possible. This representation is classified inside an ordered scale of values. From a technological point of view, the job of a measurement is to guarantee the quality of a product or a process according to a legal reference. It enables the control and development of a production process or to carry out experiments to improve, consolidate or create knowledge [12].

The measurement itself is the operation aiming to determine the value of a physical quantity. A measurement is an act of assigning a specific value to a physical variable. That physical variable is the measured parameter. A measurement system is a tool used for quantifying the measured value. A measurement is used to extend the abilities of the human senses that, while they can detect and recognise different degrees of roughness, length, sound, colour and smell, are limited and relative ; they are not suitable for assigning specific values to sensed parameters very precisely [13].

Sensors definition

The word instrumentation is assigned to all systems allowing measurement acquisition on an investigation object, artefact or the feedback control of a process. In this way, instruments are the measurement and control tools. Such an operation requires the implementation of a measurement device in which every element plays a defined role inside a chain. At the beginning of the measurement chain there is the sensor in charge of the sampling of the information from the process and transforming it into an electrical signal. This transformation is called transduction and is performed via the smart use of a physical law. The transduction principles used in sensors design are very diverse. Besides, the physical quantities that need to be measured are multiple. The ambient conditions and operating conditions depend on the application. The combination of these factors in order to adapt the measurement system to each specific need results in an extreme diversification of the sensors available in the market [12].

A system is made of components that work together to accomplish a specific objective while a transducer converts the sensed information into a detectable signal. The term transducer often recursively refers to a packaged device, which may contain a sensor, transducer, and even some signal conditioning elements.

Figure 2.1 shows the general template for a measurement system. The signal might be mechanical, electrical, optical, or of any other form that can be meaningfully recorded. Sensor selection, placement, and installation are important to ensure that the sensor output accurately reflects the measurement objective. The interpretation of all information passed through and indicated by the sensor system depends on what is actually detected by the sensor. The goal of a measurement system is to convert the sensed information into a form that can be easily quantified. The output stage indicates or records the value measured. This might be a simple readout display, a marked scale, or even a recording device [13].

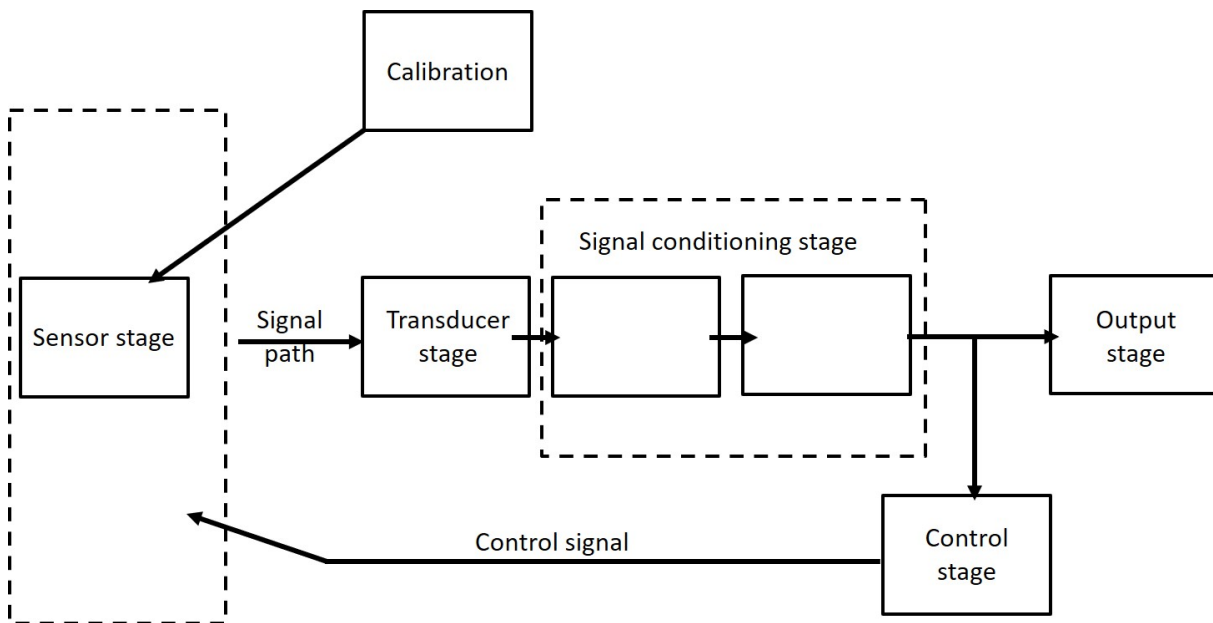


Figure 2.1 – Components of a general measurement system. From [12].

The components of a sensing device are [12]:

1. test sample is an element that selectively reacts to the measurand. It transforms the quantity to measure into another measurable quantity. This quantity is the output of the test sample.
2. transducing element is a sensitive element that translates the test sample's reaction into an electric quantity.
3. protective housing is a mechanical protection of the sensor. It ensures the independence of the output of the sensor from influencing variables.
4. signal conditioning stage has many roles such as:
 - electric power supply of the sensor when needed
 - shaping and the amplification of the output signal
 - filtering, correcting and analog signal processing
 - signal conversion (analog/digital, voltage/frequency)

5. output stage that transmits the sensor value to the user via human machine interface or communication protocol such as the digital buses I2C or SPI

These stages form the bridge between the input to the measurement system and the system output, a quantity that is used to infer the value of the physical variable measured. The signal-conditioning stage takes the transducer signal and modifies it to a predefined scale. This optional intermediate stage might be used to perform tasks such as increasing the magnitude of the signal by amplification, removing portions of the signal through some filtering or providing mechanical or optical linkage between the transducer and the output stage.

The quantity to be measured is called measurand. The measurand is usually not directly usable and is the input signal of the sensor. The job of the sensor is to transform an interest quantity into an electrical quantity directly measurable. This quantity needs to be independent as much as possible from other quantities that can influence the behaviour of the sensor. Those quantities are called influence quantities or noise. The measuring signal is a usable electrical quantity that can be an electrical impedance, an electric load, a current or a voltage[14]. The transduction relationship between the measurement and the measurand is often nonlinear. It depends on:

- the physical law controlling the sensor
- the practical setup of the sensor
- the sensor environment

The measurement chain gathers all the devices playing a specific role arranged in multistage between the input device, the sensor and the output element. It includes visualisation or data storage tools of the measurement tool. The measurement chains are more or less complex: open chain, looped, parallel channels with common components. The measurement chain accomplishes five different tasks: the transduction, the conversion, the transmission, the signal processing and the display of the information. Sensors are able to measure very diverse physical quantities of interest. These quantities can be static or dynamic. In static measurements, the measurand has a stable value or changes slowly (compared to the measurement time). It is the continuous phenomena field. The static domain or quasi static concerns phenomena changing from 0 to 10 Hz. In dynamic mode, the measurand changes with time with a high frequency. The dynamic domain is divided into various ranges [15]:

- Very low frequencies from 10 to 250 Hz
- Low frequencies from 250 Hz to 2 kHz
- Medium frequencies from 2 kHz to 10 kHz
- High frequencies (HF) beyond 10 kHz.

If the sensor's response depends on a physical quantity different from the measurand, this quantity is called influencing variable. Although the influencing variables cannot be discussed independently of the measurement principle, some of them are [14]:

- temperature, which is the most common and the most disrupting
- humidity
- acoustic vibrations, mechanical vibrations and impacts
- electromagnetic disturbance
- electric power supply of the sensor

Active sensors

Sensors are divided into two categories according to the output signal origin. Active sensors operate as generators and passive sensors operate as impedances. Active sensors are designed from physical effects that convert the energy of the measurand into an electrical energy in the form of a voltage, a current or electrical load (generator). The self energy of the measurand can be mechanical, thermal or radiative. It is the case for thermocouples and piezoelectrical sensors. The usually delivered signals have low power and need to be amplified to be interpreted or to be remotely transmitted. Table 2.1 lists the physical phenomena used by active sensors.

Table 2.1 – Physical phenomena used by active sensors.

Measurand	Physical principle	Quantity measured
Temperature	Thermoelectricity	Voltage
Luminous flux	Photoemission, Pyroelectricity and Photovoltaic	Current, Electric charge and Voltage
Force, Pressure and Acceleration	Piezoelectricity	Charge
Position	Hall effect	Voltage
Velocity	Electromagnetic induction	Voltage

Passive sensors

For passive sensors, the impedance of the sensors (resistance, capacitance or inductance see Table 2.2) is sensitive to the values of the measurand that acts upon the dimensions (thickness, length) or upon the electrical properties of the sensor (permeability, dielectric or resistivity). Those impedance variations are measurable only via a conditioning circuit. Passive sensors are passive electrical elements that dissipate energy via the Joule effect:

$$E_r = RI^2 \quad (2.1)$$

where E is the energy, R the resistance and I the current, which store electrostatic energy

$$E_c = \frac{1}{2}CV^2 \quad (2.2)$$

where C is the capacitance and V the voltage, or electromagnetic energy.

$$E_l = \frac{1}{2}LI^2 \quad (2.3)$$

where L is the inductance and I the current. They act as modulators on the energy supplied by an exterior source. The output signal is often a direct current (DC) voltage or frequency modulated voltage [12]. Passive sensors conditioning aims to translate impedance variations of the transducing element into an electrical signal. The conditioner consists of a source of voltage or current and generally other impedances. There are two main types of conditioners: oscillators and potentiometric mounts.

Table 2.2 – Sensitive electric properties in passive sensors.

Measurand	Sensitive electric property	Material type
Temperature	Resistivity	Platinum, Nickel, Semi-conductor
Very low temperature	Dielectric constant	Glass
Luminous flow	Resistivity	Semiconductors
Strain	Resistivity	Resistive alloys NiCr
Strain	Magnetic permeability	Ferromagnetic alloys
Position	Resistivity	Resistive polymers
Humidity	Resistivity	Lithium chloride
Humidity	Dielectric constant	Alumina, polymer
Liquid level	Dielectric constant	Insulating liquids

Physical transducing principles

Several transducing principles have been discovered being able to detect several physical quantities. This section presents electromagnetic induction and the piezoelectric effect, which are both used in the scope of this thesis. Table 2.3 summarizes the sensing principles mentioned in this section.

Table 2.3 – Sensing principles and variables presented

Transducing principle	Variable measured
Electromagnetic Induction	Magnetic Field, Position
Piezoelectric Effect	Stress, Strain, Temperature, Force, Pressure, Acceleration, Distance, Level, Vibration

Electromagnetic induction is the production of a voltage across an electrical conductor in a changing magnetic field. It is notably used for velocity measurement [14]. Electromagnetic induction sensors

are widely used to detect magnetic and/or conductive objects that are concealed in some manner. The sensors generate a time-varying magnetic field that is used to excite a dipole moment on the object which generates a secondary magnetic field that is used to detect the object. A coil driven by a time-varying current is used to generate a magnetic excitation. The transmit coil is driven by a generator that drives a current through the coil creating the magnetic field. Many types of time signals can be used, from pulsed to multi-frequency sinusoidal. However, most of the power from the generator is dissipated as heat in the coil or the generator. Still, a small amount of power is transferred to the target or surrounding media as eddy currents.

In the 1880s, the Curie brothers showed that some anisotropic materials can generate an electric polarization under an external mechanical strain (piezoelectric effect) or a mechanical strain under an external electric field (reverse effect). The efficiency of this electromechanical conversion in a material is measured by its electromechanical coupling coefficient:

$$K^2 = e^2 / c\epsilon \quad (2.4)$$

where e , c , and ϵ are the piezoelectric coupling, stiffness, and the dielectric coefficient, respectively of the material for a given propagation direction [16].

In a homogeneous piezoelectric material, the stress components T_{ij} at each point are dependent on the electric field E in addition to the stress components S_{ij} . Assuming the quantities are small enough, the following relationship is considered linear:

$$T_{ij} = \sum_k \sum_l c_{ijkl}^E S_{kl} - \sum_k e_{kij} E_k. \quad (2.5)$$

The superscript on c_{ijkl}^E identifies it as the stiffness tensor for constant electric field, this tensor relates changes in T_{ij} to changes in S_{kl} when E is held constant [17]. For example, lead zirconate titanate crystals will generate measurable piezoelectricity when their static structure is deformed by about 0.1% of the original dimension. Those same crystals will change about 0.1% of their static dimension when an external electric field is applied to the material.

Piezoelectric materials are pyroelectric, which makes them sensitive to temperature changes. A temperature change may induce crystal deformation and hence an electrical output. The Curie temperature of a piezoelectric material is the temperature above which the material loses its piezoelectric properties. The Curie temperature of Lithium Niobate, which is a material used in this thesis, is 1210°C for instance. Below this temperature, it is ferroelectric, above the Curie temperature it is paraelectric and nonpolar.

The inverse piezoelectric effect is used in the production of ultrasonic sound waves and SAW. The piezoelectric effect is used for force, pressure and acceleration measurement in many devices [18].

In a piezoelectric force sensor, the force to be measured is directly transferred to the piezoelectric crystal. Force piezoelectric sensors measure dynamic force along a single axis. Dynamic force can include compression, tensile, shear, and torque force. When a dynamic force is applied, the piezoelectric crystals

deform under this force and produce an electrical signal. This electrical output can then be used to measure the force applied.

In a piezoelectric pressure sensor the measured pressure is applied to a thin metal membrane. The total force on the membrane – that is the pressure times the active area of the membrane – is mechanically transferred to the crystal. Piezoelectric pressure sensors are used to measure dynamic changes in pressure, typically liquid or gaseous pressure changes. Pressure piezo sensors are commonly used in measuring explosions, blasts, turbulence, and engine combustion. Those pressure sensors are able to detect variations in pressure very rapidly, generating an electrical signal that can be used to react to these variations. Piezoelectric pressure sensors are also sensitive to acceleration, because the mass of the housing produces an inertial force on the crystal when accelerated. For applications where pressure has to be measured in a vibrating or otherwise moving environment, special pressure sensors are designed with a compensating crystal, to minimize the acceleration sensitivity.

An accelerometer consists of one or more piezoelectric crystals and a proof mass (or seismic mass). One electrode is connected to the common surface of the crystals, the other to the housing. A piezoelectric accelerometer converts changes in mechanical acceleration, vibration, or shock into a measurable electrical output. When the accelerometer piezo sensor is subjected to an accelerative force, it produces an electrical signal proportional to the amount of force applied. A slab of piezoelectric material is held perpendicular to the expected movement, and a block of material is loaded onto the slab. When the object accelerates, the block presses onto the piezoelectric slab creating a charge, which is then passed on to an amplifier or computer.

Ultrasonic piezoelectric sensors are often used to measure distance, liquid levels and flow. They can also be used in cleaning and medical equipment. Ultrasonic piezo sensors are placed outside the medium being measured to receive relevant information. Often, two ultrasonic piezoelectric elements are utilised with one acting as the transmitter and one acting as the receiver (sensor). The piezo transmitter emits ultrasonic pulses that are reflected back to the piezoelectric sensor and converted into a readable measurement. These sensors perform best when operated at the resonant frequency, which is determined by the material and dimensions of the piezo component. The closer the piezo component is to its resonant frequency, the higher the signal and amplitude of vibration.

Piezo sensors take on two forms to accomplish their measurements: active and passive. Active piezoelectric sensors use a transmitter-receiver system releasing intermittent ultrasonic pulses to gauge the environment. The transmitter operates at its resonant frequency to optimise efficiency. The receiver, upon obtaining a signal, generates an electric impulse. The delay is analysed to determine distance or depth. Examples of this can be seen in level sensors or ultrasonic sensors.

Passive piezoelectric sensors wait for a signal, like a microphone, and convert that into output. These specifically shaped piezo ceramics generate electricity after receiving a signal and are inactive when no signal is present. Passive piezo sensors often operate below their resonance frequency to optimise their sensing range. Common applications include touch switches and accelerometers.

Piezoelectric sensors are mostly used for measuring vibrations, acceleration, strain, force, and movement. They are suitable for a broad range of industries due to their ability to both operate in confined spaces and high temperatures, and yield high frequency response, transient response, and output. The absence of moving parts allows a piezoelectric sensor to be mounted in a robust package and hermetically sealed. All piezo sensors can be custom made into different shapes depending on their use, including piezo tubes, piezo strips, piezo discs, and piezo plates, which grants them manufacturing flexibility.

Sensors mounting

Since sensor transducers need to be integrated inside an electrical circuit, several circuit configurations can be implemented among which potentiometers, bridge mounts and oscillators. A potentiometer is a three-terminal resistor with a sliding or rotating contact that forms an adjustable voltage divider. Potentiometric mounts are the easiest to implement. However, they are sensitive to the electric source fluctuations and to parasitics. In this type of setup, the sensor's impedance is in series with a known impedance. When the sensor is purely resistive, continuous current or voltage sources are used. For capacitive or inductive impedances, a sinusoidal source is used [19].

Bridge mount is derived from the potentiometric mount. It consists of a double potentiometer with a differential voltage measurement. The measurement is less sensitive to the power source deviations and therefore to noise. For the resistive sensors, Wheatstone bridges are used. Figure 2.2 shows a Wheatstone bridge sensor configuration. For capacitive sensors, Nernst bridge or Sauty bridge are used, whereas Hay bridge or Maxwell bridge are used for inductive sensors [12].

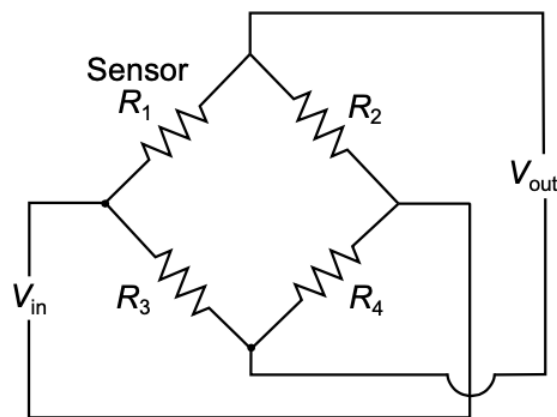


Figure 2.2 – Wheatstone bridge circuit configuration for a sensor.

Oscillators deliver a signal whose frequency is modulated by the measurand, which grants a good protection from noise. Moreover, it is easier to convert into numerical signal since only period counting is required. There are two types of oscillators [14]:

- in a sinusoidal oscillator the oscillator frequency is set by the resonance frequency of a circuit made of an inductance and a capacitance in series or in parallel. The variation of the measurand around its original value modulates the oscillator frequency.
- a relaxation oscillator generates rectangular signals whose frequency is linked to the components of the circuit. This frequency is modulated by the measurand impedance variations.

Sensors output

The final output of a sensor can take several forms. The most common output is an electrical signal. Sensors with electrical signal output can be divided into three categories[20]:

1. analog sensors: the signal supplied by the sensor is analog and often of low power. They are qualified as low level sensors. When conditioning electronics are inserted in the sensor box, the output signal will have higher power (0-10 V or 4-20 mA) and the sensor is called sensor-transmitter.
2. digital sensors: the sensor output signal is directly encoded in a digital way within the sensor. The signal can be absolute in the case of a parallel transmission mode (the signal is coded on many bits that are transmitted in parallel via many wires) or incremental in the case of a series transmission (the signal coded on several bits will be transmitted via one wire, the bits of the code being sequentially transmitted). In the last case, the signal consists of a succession of electric impulses that need to be counted to obtain the measured value. Numerical sensors are often called coders and counters.
3. logical sensors: the signal has two states or possible values. The transition corresponds to crossing the threshold by the measurand.

The signal transmission method depends on the sensor type (analog, digital or logic). In the case of an analog signal, there is direct transmission mode for a short distance and transmission mode by modulation of a carrier wave (modification of the high frequency wave properties by the measurement signal). The carrier wave is a transmission medium for a long distance and a sinusoidal wave is usually chosen whose amplitude phase or frequency are modulated. In the case of digital sensors, parallel links RJ25 or serial link RS 232 as well as different instrument buses (GPIB, USB, PXI, CAN, SPI, I2C etc.) are used. Digital transmission is more robust against noise likely to appear in the transmission line.

A smart sensor is a measurement system for a physical quantity made of a measurement chain monitored by a microprocessor and a bidirectional communication interface. It offers many advantages such as remote configuration, accuracy, self maintaining and task management.

The measurement chain encloses [14]:

- the main sensor specific to the targeted measurand and recognisable by a code stored in a PROM (Programmable Read Only Memory)
- secondary sensors specific to the influencing quantities and affecting the response of the main sensor

- signal digitising systems for each sensor
- a microprocessor responsible for acquisition management, influencing quantities correction, linearisation and sensor health monitoring

Metrologic properties of a sensor

Several parameters are used to characterize the performances of a sensor, which are:

- resolution
- response time
- operating range

The resolution of a sensor is the minimum detectable change of the measurand in the measurement system's readout. Resolution of measurement is often mixed up with accuracy: the accuracy is the fidelity of the system's readout to the actual measurand while resolution is the smallest variation that can be detected. The response time of a sensor reflects the speed of a sensor. It expresses the ability of the sensor to follow in the time the variations of the quantity being measured. The response time is the time between any detectable change of the measured quantity and the reaction of the sensor. The faster the sensor, the smaller the response time. The response time is also a key parameter for choosing a sensor for quantities that vary fast with time. The span is the difference between the maximum and minimum values of operating range of an instrument. The range is the lower to upper limits of an instrument or test.

A calibration is operated when known inputs ranging from the minimum to the maximum values for which the measurement system is to be used are applied [14]. These limits define the operating range of the system. The input operating range is defined as extending from the minimum value x_{\min} to the maximum value x_{\max} . The input operating range may be expressed in terms of the difference of the limits as:

$$r_i = x_{\max} - x_{\min} \quad (2.6)$$

This is equivalent to specifying the output operating range from y_{\min} to y_{\max} . The output span or full-scale operating range (FSO) is expressed as:

$$r_o = y_{\max} - y_{\min} \quad (2.7)$$

It is important to avoid extrapolation beyond the range of known calibration during measurement since the behaviour of the measurement system is uncharted in these regions. As such, the range of calibration

should be carefully selected. In practice the measurement range is a major criterion for the choice of a sensor.

Calibration

The expression $signal = f(measurand)$ is established by means of an operation called calibration: a standard gives different values of the measurand, the electrical signal values given by the sensor are measured and the calibration curve $s = f(m)$ is calculated. This curve is then used to deduce the measurand value for any value of s . Many instruments are designed to achieve a linear relationship between the applied static input and indicated output values[13]. Such a linear static calibration curve has the general form:

$$y_L(x) = a_0 + a_1x \quad (2.8)$$

where the curve fit $y_L(x)$ provides a predicted output value based on a linear relation between x and y . However, in real systems, truly linear behavior is only approximately achieved [12]. Figure 2.3 shows common instrument errors.

Measurement device specifications usually provide a statement as to the expected linearity of the static calibration curve for the device. The relationship between $y_L(x)$ and measured value $y(x)$ is a measure of the nonlinear behaviour of a system:

$$u_L(x) = y(x) - y_L(x) \quad (2.9)$$

where $u_L(x)$ is a measure of the linearity error that arises in describing the actual system behaviour by equation 2.8. For a measurement system that is essentially linear in behaviour, the extent of possible non-linearity in a measurement device is often specified in terms of the maximum expected linearity error as a percentage of full-scale output range, r_o :

$$\%u_{L_{m+r}} = \frac{u_{L_{\infty}}}{r_o} \times 100 \quad (2.10)$$

This is how the linearity error for the pressure transducer in Table 2.4 was estimated. The scatter in the data measured during a calibration affects the precision in predicting the slope of the calibration curve. As shown for the linear calibration curve in Figure 2.3, in which the zero intercept is fixed, the scatter in the data about the curve fit are random errors. The sensitivity error is a statistical measure of the random error in the estimate of the slope of the calibration curve [21].

The static sensitivity of a device is also temperature dependent, and this is often specified. In Table 2.4, the sensitivity error reflects calibration results at a constant reference ambient temperature, whereas the thermal sensitivity error was found by calibration at different temperatures. The slope of a static

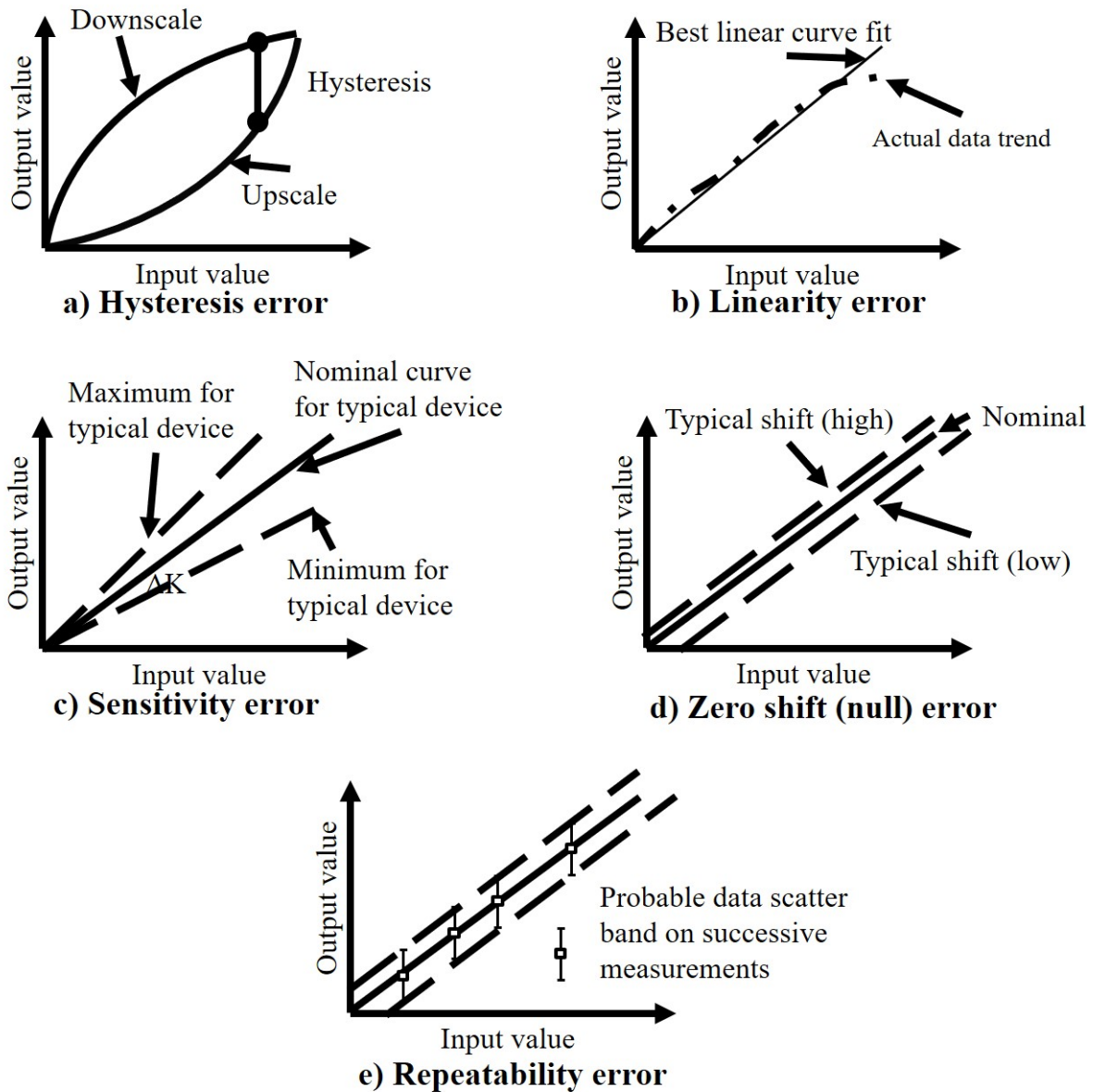


Figure 2.3 – Common elements of instrument error from [12]. a) Hysteresis error b) Linearity error c) Sensitivity error d) Zero shift (null) error e) Repeatability error.

calibration curve provides the static sensitivity K of the measurement system, which is a measure relating the change in the indicated output associated with a given change in a static input.

Uncertainty

The term instrument precision, when reported in instrument specifications, refers to a random uncertainty based on the results of separate repeatability tests. Manufacturer claims of instrument precision must be based on multiple tests performed on different units of the same manufacturer, either performed in the same lab (same-lab precision) or, preferably, performed in different labs (between-lab precision). An

estimate of the overall instrument error is made by combining the estimates of all known errors into a term called the instrument uncertainty. The estimate is computed from the square root of the sum of the squares of all known uncertainty values. For M known errors, the overall instrument uncertainty, u_c , is estimated by:

$$u_c = [u_1^2 + u_2^2 + \dots + u_M^2]^{1/2} \quad (2.11)$$

For example, for an instrument having known hysteresis u_h , linearity u_L , and sensitivity u_K errors, the instrument uncertainty u_c is estimated by:

$$u_c = [u_h^2 + u_L^2 + u_K^2]^{1/2} \quad (2.12)$$

The uncertainty is a numerical estimate of the possible range of the error in a measurement. In any measurement, the error is not known exactly since the true value is rarely known exactly. However, based on available information, the operator might feel confident that the error is within certain bounds, a plus or minus range of the indicated reading. This is the assigned uncertainty. Uncertainty is brought about by all of the errors that are present in the measurement system, i.e. its calibration, the data set statistics, and the measurement technique [22]. Individual errors are properties of the instruments, the test method, the analysis, and the measurement system. Uncertainty is a property of the test result. The systematic uncertainty might be based on a comparison against a concomitant method. The uncertainty values assigned to an instrument or measurement system specification are usually the result of several interacting random and systematic errors inherent to the measurement system, the calibration procedure, and the standard used to provide the known value. An example of the errors affecting an instrument is given for a typical pressure transducer in Table 2.4. The value assigned to each error is the uncertainty.

Sensor design

The choice of an industrial sensor is a compromise between several characteristics that can be contradictory. It requires a good knowledge of the existing devices, their characteristics, advantages and drawbacks. The choice results from the precise definition of the needs. It can be divided into two subparts [14]:

1. definition of the transducer type of material
2. definition of the main characteristics of the sensor

The type of the material concerns first the physical quantity that needs to be measured and then the sensor type (analog, digital or logic) that mainly depends on the output signal desired. It also depends on the use of the measurement signal (monitoring, command, diagnosis, transmission) and the available

Table 2.4 – Manufacturer’s specifications : Typical Pressure Transducer. From [12].

Operation	
Input range	0-1000 cm H_2O
Excitation	+/- 15 V DC
Output range	0-5 V
Performance	
Linearity error	+/- 0.5% FSO
Hysteresis error	Less than +/- 0.15% FSO
Sensitivity error	+/- 0.25% of reading
Thermal sensitivity error	+/-0.02%/°C of reading
Thermal zero drift	+/- 0.02%/°C FSO
Temperature range	0-50°C

FSO : Full Scale Operating range

processing equipment. The metrological characteristics need to be specified, conditions of use, geometric specifications and economical possibilities or even ergonomic. Three main characteristics need to be outlined:

1. the sensing range required according to the range of the common values taken by the quantity being measured
2. the accuracy of the measurement required according to the problem addressed. It is expressed in percentage of the measurement range
3. the speed of the measurement according to the evolution domain of the physical quantity. For a sensor it is expressed in terms of response time or in terms of bandwidth

Four main conditions of use need to be clarified [13]:

1. the ambient temperature range acceptable according to the sensor’s operating range. It is expressed by the extreme values.
2. the tolerable overload according to accidental values taken by the physical quantity due to external causes. This overload is expressed in sensing range times.
3. the lifetime the number of cycles or manipulations applied on the sensor during its use without changing its nominal characteristics.
4. several protections according to the sensors ambient against physical threats: corrosion, dust, tightness, impact, electromagnetic radiation and others more. Most of the physical threats can be thwarted by simply coating or encapsulating the sensor’s main parts.

Figure 2.4 shows the different development steps of a miniaturised sensor.



Figure 2.4 – Development steps of a miniaturised sensor. From [23].

2.2 Gas kinetic theory

When working with MEMS, to which miniaturized sensors belong, several physical and geometric parameters have to be considered in order to accurately model gas microflows. Those parameters describe mainly rarefaction effects, which need to be taken into account when characteristic lengths are of the order of $1 \mu\text{m}$, under usual temperature and pressure conditions. In this section, the figures of merit from gas kinetic theory necessary to understand, analyse and model Pirani sensing are presented.

Modelling gas microflows requires taking into account several characteristic length scales. At the molecular level, we may consider the mean molecular diameter d , the mean molecular spacing δ and the mean free path λ . Figure 2.6 shows all those dimensions together.

The parameters presented here are:

- viscosity
- collision rate
- mean free path
- Knudsen regime
- transition pressure
- thermal conductivity

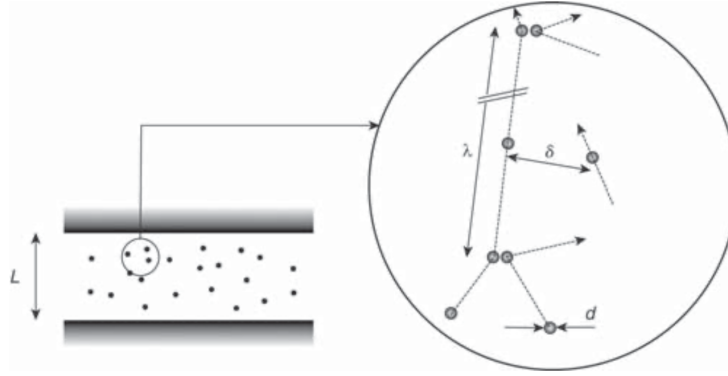


Figure 2.5 – Main characteristic length scales at molecular level. From [24].

Viscosity

The viscosity of a gas can be thought of as a measure of its resistance to flow. Near atmospheric pressure, gas viscosity is weakly dependent on pressure. It is primarily a function of temperature. The viscosity is needed to compute later on the mean free path and therefore the thermal conductivity of a specific gas. The viscosity μ is defined as [24]:

$$\mu = \mu_0 \left(\frac{T}{T_0} \right)^\omega \quad (2.13)$$

with:

- μ_0 – Viscosity at temperature T_0
- T – Temperature in K
- T_0 – Reference temperature in K
- ω – a coefficient that depends on the collision model chosen

According to the collision model adopted the coefficient ω can take several values [24]. For the Hard Sphere Model an ω value of 1/2 is assumed [24].

Collision rate

In the case of dilute gases, most of the intermolecular interactions are binary collisions. A collision model requires the definition of the force exerted between the two considered molecules. This force is repulsive at short distances and weakly attractive at large distances. The collision rate is necessary to compute the mean free path and hence the gas thermal conductivity. From the viscosity value the collision rate can be calculated as:

$$\nu = k_1 \frac{\rho RT}{\mu} \quad (2.14)$$

with:

- ν – Collision rate at temperature T_0
- k_1 – Coefficient of 5/4 for the Hard Sphere model
- ρ – Gas density
- R – Specific gas constant
- T – Temperature in K
- μ – Viscosity at temperature T_0

The estimation of the collision rate and consequently of the mean free path depends on the model chosen for describing the elastic binary collision between two molecules. The simplest collision model is the Hard Sphere Model inferring $\omega = 1/2$ [24]. The Hard Sphere Model was used throughout all the thesis.

Mean free path

The mean free path is the average distance travelled by a molecule between two consecutive collisions. If we consider a simple gas consisting of a single chemical species with molecules having the same structure, then the mean free path depends on their mean diameter d and on the number density:

$$n = d^{-3} \quad (2.15)$$

and the inverse $1/n$ represents the mean volume available for one molecule. For example, a gas in standard conditions (for a temperature of 273.15 K and a pressure of 101325 Pa), has about 27 million molecules in a cube of 1 μm in width and in the case of air for which $d_0 = 0.42$ nm, the mean free path is $\lambda_0 = 49$ nm.

The mean free path represents the distance crossed by a molecule before colliding with another one or with walls which creates heat transfer [5]. That is why it is a figure of merit relevant for the Pirani principle and it appears in all the Pirani heat transfer equations available in the literature directly or indirectly in the expression of the thermal conductivity or conductance of the gas. The mean free path of Nitrogen versus pressure varies between approximately 10 m at 10^{-4} Pa and 10 nm at atmospheric pressure. It allows to identify the flow regime of the gas versus pressure using the relationship between the mean free path and the Knudsen number, introduced in the next section.

The thermal velocity c' of a molecule is the difference between its total velocity c and the local macroscopic velocity u of the flow. The mean free path of the molecules is expressed as the ratio of the mean thermal velocity $\overline{c'}$ to the collision rate ν [24]:

$$\lambda = \frac{\overline{c'}}{\nu} = \frac{\sqrt{8RT/\pi}}{\nu} \quad (2.16)$$

with R the ideal gas constant, T the temperature and ν the collision rate, which leads to:

$$\lambda = k_2 \frac{\mu}{\rho \sqrt{RT}} \quad (2.17)$$

with k_2 equals approximately 1.277 for the Hard Sphere Model [24], μ the viscosity and ρ the gas density.

Knudsen regime

The Knudsen number plays a very important role in gaseous microflows. From the value of the Knudsen number, it is possible to qualify the flow regime of the gas and its thermal properties and later on the relevance of the Pirani sensing principle. The Knudsen number is defined as [24]:

$$K_n = \frac{\lambda}{d} \quad (2.18)$$

with:

- K_n – Knudsen number
- λ – Mean free path
- d – Characteristic dimension of the device

That is why, it is convenient to differentiate the flow regimes in function of K_n , and the following classification is used [24]:

- For $K_n < 10^{-3}$, the flow is a continuum flow and it is accurately modeled by the compressible Navier-Stokes equations with classical no-slip boundary conditions.
- For $10^{-3} < K_n < 10^{-1}$, the flow is a slip flow and the Navier-Stokes equations remain applicable, provided a velocity slip and a temperature jump are taken into account at the walls. These new boundary conditions point out that rarefaction effects become sensitive at the wall first.
- For $10^{-1} < K_n < 10$, the flow is a transition flow and the continuum approach of the Navier-Stokes equations is no longer valid. However, the intermolecular collisions are not yet negligible and should be taken into account.
- For $K_n > 10$, the flow is a free molecular flow and the occurrence of intermolecular collisions is negligible compared with the one of collisions between the gas molecules and the walls.

Their limits are only indicative and could vary from one case to another, partly because the choice of the characteristic length d is rarely unique. For flows in channels, d is generally the hydraulic diameter

or the depth of the channel. Typically, most of the microsystems which use gases work in the slip flow regime, or in the early transition regime.

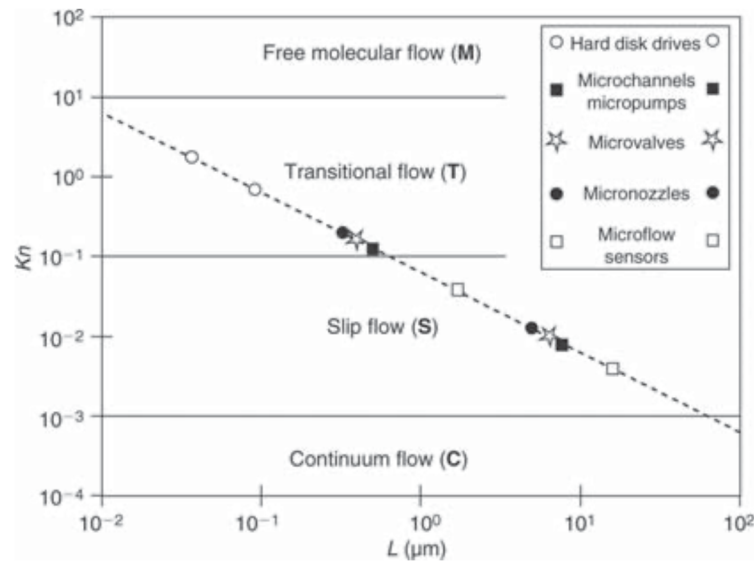


Figure 2.6 – Gas flow regimes for usual microsystems. From [24].

Figure 2.7 shows the Knudsen regime versus pressure versus size of the gas gap.

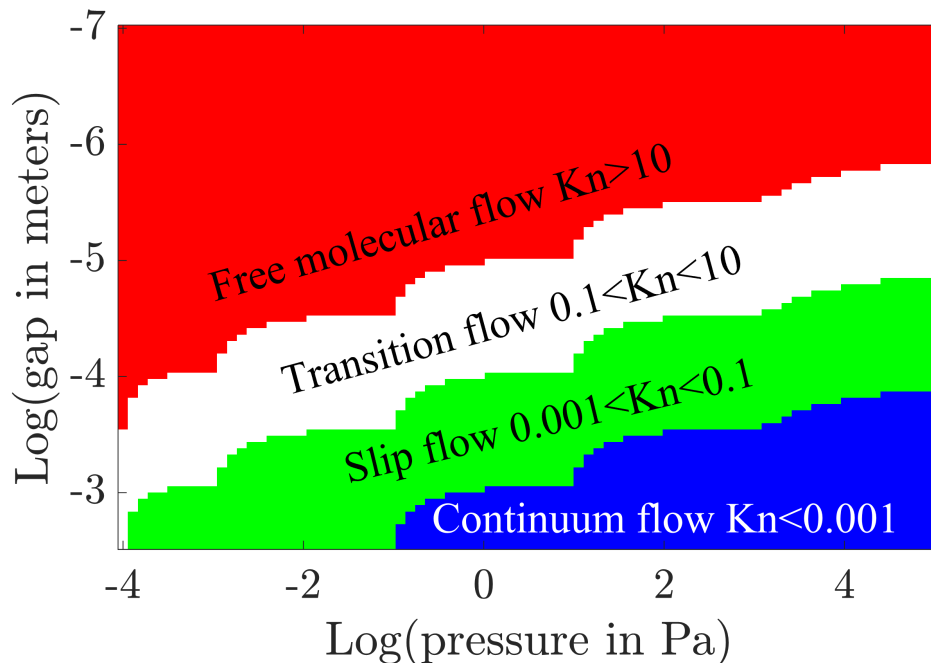


Figure 2.7 – Knudsen number vs pressure vs dimension of the channel. From [25].

Under the effect of both low pressures and small dimensions, more rarefied regimes can occur. First, shrinking system sizes results in an increase of surface over volume effects. This helps for heat transfer

enhancement, but it also requires a reliable knowledge of the velocity, as well as the temperature and boundary conditions.

For any value of the Knudsen number, there is in the neighbourhood of the wall a domain in which the gas is out of equilibrium. This domain is called the Knudsen layer and has a thickness in the order of the mean free path. For very low Knudsen numbers (in the continuum flow regime), the effect of the Knudsen layer is negligible. In the slip flow regime, which is roughly in the range $10^{-3} < \text{Kn} < 10^{-1}$, the Knudsen layer must be taken into account. The value of the Knudsen layer thickness is expressed as [26]:

$$l_c = \frac{kT}{\pi d^2 p} \quad (2.19)$$

with:

- k – the Boltzmann constant
- T – the temperature
- d – the molecular diameter
- p – the pressure

The flow in the Knudsen layer cannot be analysed from continuum by use of the Navier-Stokes equations anymore, for example. But for $\text{Kn} < 10$ its thickness is in the range of $10 \mu\text{m}$ and the Knudsen layer can be neglected, providing the boundary conditions are modified and express a velocity slip, as well as a temperature jump at the wall. Thus, the Navier-Stokes equations remain applicable. Within the scope of this thesis, only stationary flows without macroscopic movement velocity are addressed.

Transition pressure

One figure of merit in the analysis of the Pirani measurement principle is the transition pressure. It corresponds to the pressure for a Knudsen number of 10. The transition pressure corresponds to the transition between the transition flow and the free molecular flow [24]. The transition pressure depends on the gas and the geometry of the device and is a good estimation of the pressure range with the highest sensitivity of the sensor. The transition pressure versus the gas gap, one of the dimensions of the device is plotted in the appendix. In [27], the transition pressure is defined as follows:

$$p_{tr} = \frac{\kappa_{g0} w T_b}{(w+z) d \bar{c}'} \quad (2.20)$$

with:

- κ_{g0} – the continuum thermal conductivity independent of pressure
- w – width of the Pirani gauge
- T_b – temperature of the Pirani sensor
- z – thickness of the Pirani gauge
- d – the gas gap
- \bar{c}' – the average molecular velocity

Thermal conductivity

The Pirani sensing principle is based on the pressure dependence of the gas thermal conductivity that influences the heat transfer balance. The thermal conductivity is expressed in [10] as:

$$\lambda(p, d) = \lambda(p_0) \left(1 + 2 \left(\frac{2-a}{a} \right) \frac{\bar{l}(p) 9.5}{d 6} \right)^{-1} \quad (2.21)$$

where $\lambda(p_0)$ is the thermal conductivity at atmospheric pressure, a is the energy accommodation coefficient which is taken to be 0,77 for Nitrogen in smooth surfaces [10], d is the gas gap, i.e. the distance between the sensor heated area and the "ambient" surface of the rest of the sensor and $\bar{l}(p)$ is the pressure dependent mean free path of the gas molecules. This expression for gas thermal conductivity is used throughout the thesis to calculate the pressure dependent gas thermal conductivity.

The accommodation coefficients depend on various parameters that affect surface interaction, such as the magnitude and the direction of the velocity and usually take values between 0.7 and 1. These coefficients seem to be reasonably constant for a given gas and surface combination [28].

Figure 2.8 shows the gas thermal conductivity versus pressure through the whole target sensing range. The thermal conductivity was computed using the above mentioned expression. The thermal conductivity varies through several orders of magnitude.

2.3 Pressure sensors

Many industrial and research setups need accurate vacuum monitoring for various purposes. The vacuum range is divided into several regimes. The whole vacuum range covers 15 decades of pressure from 10^{-10} Pa up to atmospheric pressure. Table 2.5 describes the vacuum levels.

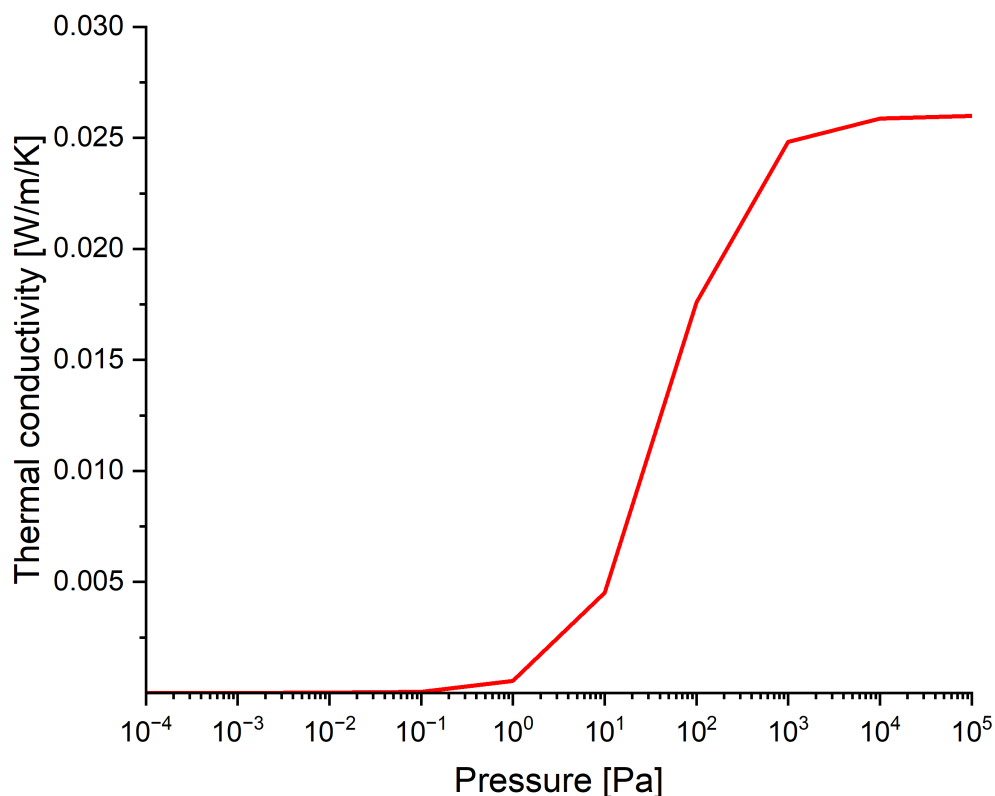


Figure 2.8 – Thermal conductivity of nitrogen versus pressure for the device presented in [10].

Table 2.5 – Vacuum levels according to the ISO 21360 Norm

Pressure range in Pa	Degree of vacuum
10^5 to 3×10^3	Low vacuum
3×10^3 to 10^{-1}	Medium vacuum
10^{-1} to 10^{-4}	High vacuum
10^{-4} to 10^{-7}	Very high vacuum
10^{-7} to 10^{-10}	Ultra-high vacuum (UHV)
10^{-10}	Extreme-ultrahigh vacuum (EHV or XHV)

Several transducing principles are available to sense subatmospheric pressures [5]. In the following sections, some of them are introduced:

- Capacitive Diaphragm Gauges (250 Pa - 7×10^7 Pa)
- Piezoresistive gauges (2000 Pa - 1.5×10^8 MPa)
- Bourdon gauges

- McLeod gauges (10^{-3} - 10 Pa)
- Liquid manometers
- Knudsen gauges
- Thermocouple gauges (10^{-2} - 100 Pa)
- Ionization gauges (10^{-8} - 100 Pa)
- Pirani gauges (10^{-2} - 10^4 Pa)

Capacitive Diaphragm Gauges

CDGs measure pressure via the mechanical deformation suffered by a thin wall or diaphragm that modifies the capacitance of the gauge placed in an electronic circuit. The deflection of a calibrated metallic diaphragm indicates pressure [18]. A CDG measures gas pressure by direct measurement of the applied force on the surface of a thin diaphragm. The mechanical deflection of the elastic sensor diaphragm is a function of the applied pressure. The diaphragm deflection ω in the center of the diaphragm can be calculated by the following equation [29]:

$$\omega(p) = \frac{p \cdot r^4 \cdot 3 \cdot (1 - \nu^2)}{16 \cdot E \cdot t^3} \quad (2.22)$$

where ν is the Poisson ratio, E is the Young modulus, t is the thickness of the diaphragm, and r is the free radius of the diaphragm. The distance change due to pressure change is measured by the resultant capacitance change [29]:

$$\Delta C_{\text{meas}}(\omega) = \frac{\epsilon_0 \cdot A}{d_0 + \omega} - C_0 \quad (2.23)$$

where d_0 is the distance at zero pressure, ϵ_0 is the dielectric permittivity, A is the area of the housing electrode, ΔC_{meas} is the resultant capacitance change, and C_0 is the capacitance at zero deflection. The diaphragm constitutes an electrode and together with an integrated auxiliary electrode it forms a pressure dependent capacitor. Inserted in an electrical measurement circuit, the applied pressure is converted into an electrical signal. Figure 2.10 shows the operating principle of a CDG. CDGs are mechanically simple and robust. They are able to operate over a wide temperature range and are very tolerant of short-term overpressure conditions. They can be used to measure a wide range of pressure from vacuum (250 Pa) to high pressures up to around 70 MPa. They are suitable for both lower-pressure applications and reasonably harsh environments. Since no DC current flows through the capacitor, they are inherently low power. Capacitive sensors exhibit low hysteresis and good repeatability of measurements. They also have low temperature sensitivity. The response time is in the order of milliseconds, and even faster in the case of MEMS devices. One of the main disadvantages of capacitive sensors though is the non-linearity exhibited because the output is inversely proportional to the gap between the parallel electrodes as well as their sensitivity to vibrations.

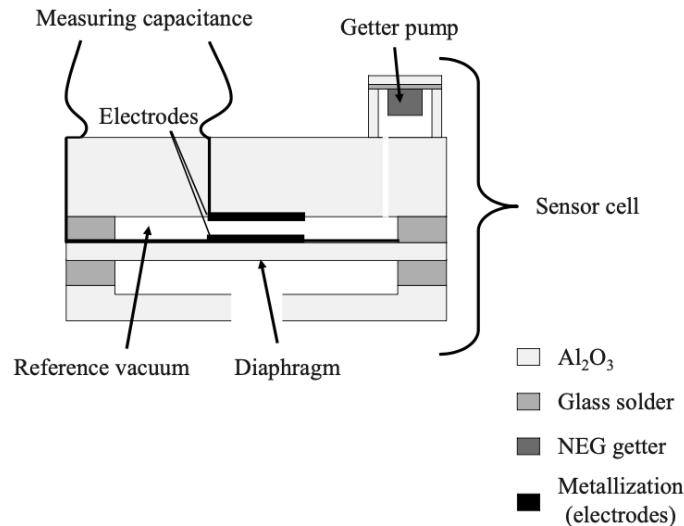


Figure 2.9 – Structure of Inficon ceramic diaphragm gauge. From [29].

Piezoresistive pressure gauges

Piezoresistive gauges use a strain gauge made of a piezoelectric material that changes its electrical ohmic resistance when it is subject to stress. Piezoresistive gauges rely on piezoelectricity similarly. In a piezoresistive strain gauge sensor, the change in electrical resistance of one or more resistors mounted on a diaphragm is measured. The change in resistance is directly proportional to the strain caused by pressure on the diaphragm. The resistors are connected in a Wheatstone bridge circuit, which is a very sensitive way of converting the small changes to an output voltage. In a piezoresistor the resistance R changes linearly with the applied strain:

$$\frac{\Delta R}{R} = G \cdot \frac{\Delta L}{L} \quad (2.24)$$

where G is the proportional gauge factor of a piezoresistor.

Piezoelectric pressure sensors use materials, such as quartz crystals or specially formulated ceramics, which generate a charge across the faces when pressure is applied.

A given force results in a corresponding charge across the sensing element. However, this charge will leak away over time meaning that the sensor cannot be used to measure static pressure. These are one of the earliest and most widely used type of pressure sensors. The simple construction means low cost and durability. The sensors are robust with good resistance to shock, vibration, and dynamic pressure changes. The readout circuits are simple and enable high-resolution measurement. The output is linear with pressure and the response time is typically below one millisecond. They can be used for a wide range of pressure measurements from 21 kPa to 150 MPa. The output is also stable over time. The resistive elements can be bonded to the diaphragm. Alternatively, thin film resistors can be created directly on the membrane. These can operate at higher temperatures and are more suitable for use in harsh environments. The main disadvantage is that the sensor has to be powered. This makes them unsuitable

for low power or battery operated systems. Scaling down the size reduces the resistance and increases the power consumption. The sensor output is temperature dependent. This can be a big disadvantage for applications such as tire pressure measurement where there are large temperature changes over the operating cycle. Silicon strain gauges are much more sensitive and can measure pressures down to 2 kPa.

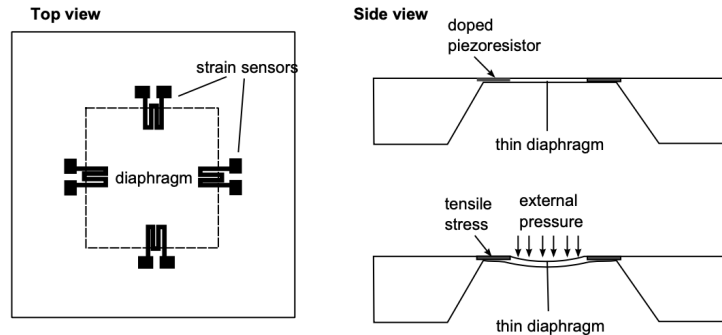


Figure 2.10 – Structure of a piezoresistor based pressure sensor. From [29].

Bourdon gauges

Bourdon gauges have a curved tube with a circular, spiral or coiled shape as a measuring element. This tube moves outwards when the pressure inside the tube is higher than the external pressure, and inwards when the internal pressure is lower. This motion is proportional to the pressure to be measured, and it is coupled to a pointer mechanism. Bourdon gauges give accurate results and are of low cost. They are simple in construction and can be modified to give electrical outputs. They are safe even for high pressure measurement. However, they respond slowly to pressure changes and are subject to hysteresis. They are sensitive to shocks and vibrations. Amplification is also necessary since the displacement of the free end of the Bourdon tube is low.

McLeod gauges

McLeod gauges pressure measurement consists in compressing a given volume V of the gas whose pressure P needs to be measured to a much smaller volume v and observing the resulting pressure p which is given by the relation:

$$p = PV/v \quad (2.25)$$

McLeod gauges are inexpensive devices that measure vacuum pressure without any electronics or sophisticated equipment. They are used for calibrating other low pressure measuring gauges. They are independent from the gas composition and the readings obtained from McLeod gauge do not require any correction. Nonetheless, McLeod gauges are useful for measuring pressures of gases that obey Boyle's law. Condensable gases cannot be used. The gauge can be handled only by skilled technicians due to a

risk of contamination among others. It cannot give continuous output. The McLeod Gauge measures the vacuum pressure in the range between 10^{-3} and 10 Pa.

Liquid manometers

Liquid manometers enable pressure calculation via reading the height of a barometric column or U tube manometer. The equation used to relate the change in pressure to change in height in a manometer is:

$$\Delta P = \rho g \Delta h \quad (2.26)$$

where ΔP is the difference in pressure, ρ is the density of the fluid, g is the force due to gravity (9.81 m/s^2 for Earth), and Δh is the difference in height. Figure 2.11 shows the working principle of liquid manometers. They measure pressures between 100 Pa and 10^6 Pa. They are easy to fabricate and relatively inexpensive while providing good accuracy and high sensitivity. They require little maintenance. They are nevertheless fragile and can cause hazards when exposed to atmosphere in the case of quicksilver manometers for instance.

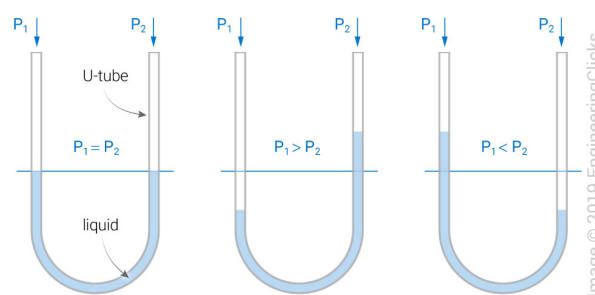


Figure 2.11 – Liquid manometer principle retrieved from www.engineeringclicks.com on 10/10/2021.

Knudsen gauges

Knudsen gauges consist of two parallel metallic strips suspended from the middle of a vertical tube. When one strip is heated electrically in the presence of gas at low pressure, the other strip is pushed away from the heated strip because the molecules hitting it on the side facing the heated strip impart to it more momentum than those hitting it on the other side. The deflection of the unheated strip is a function of the pressure of the gas and can be used for its measurement [30]. Pressures between 10^{-6} and 10^{-1} Pa can be measured independently of the gas composition.

Heat conductivity pressure sensors

In heat conductivity pressure sensors, energy is dissipated from a heated surface in a gas in two ways: by radiation and by conduction through the surrounding gas. At atmospheric pressure the thermal conductivity λ is independent of the pressure. At low pressure, where the distance between hot and cold

surfaces is less than the mean free path, the heat loss by conduction depends on the pressure [5]. Gauges depending for their indication of pressure on the thermal conductivity of the gas are usually operated under conditions in which the energy input is maintained almost constant. The temperature of the heated surface decreases when pressure rises, and the different types of conductivity gauges involve different methods for determining the change in temperature.

Thermocouple pressure gauges

In the thermocouple type, the temperature is determined by means of a thermocouple spot welded at the center of a heated wire; in the resistance type the change in temperature is determined by measuring the resistance change. Besides, since the length of a wire varies with temperature, this constitutes another method of measuring the temperature. In a thermocouple gauge, a wire is heated by means of applying an electrical current. It contains two elements: a heater (filament) and a thermocouple junction which contacts the filament. With the filament current held constant, as the pressure within the tube is decreased the filament will become hotter because of the improved thermal insulation provided by the increasingly rarefied gas. This temperature is sensed by the thermocouple junction. Measurement is accomplished by reading the thermocouple junction voltage on a sensitive meter which has previously been calibrated against a manometer. These gauges consist of the gauge tube itself, a power supply for the filament, and a moving coil meter for displaying the pressure. As different gases have varying thermal conductivities, the gauge will not be accurate when working with argon or carbon dioxide for instance. That is why a compatibility curve like the one shown in Figure 2.13 is used. Thermocouple gauges are typically used to measure pressures in the range between 0.01 Pa and 100 Pa. Despite being cheap, thermocouple are inaccurate and present a burning risk.

Ionization gauges

Ionization gauges are used for measuring pressures in the range 10^{-8} Pa to 100 Pa. Currently, only ionization gauges can measure pressures below 10^{-3} Pa accurately. They exist in two forms known as a hot cathode and a cold cathode. In the hot cathode form, gas of unknown pressure is introduced into a glass vessel containing free electrons discharged from a heated filament. Gas pressure is determined by measuring the current flowing between an anode and a cathode within the vessel. This current is proportional to the number of ions per unit volume, which in turn is proportional to the gas pressure. Cold cathode ionization gauges operate in a similar fashion except that the stream of electrons is produced by a high voltage electrical discharge. These electrons encounter gas molecules as they circulate, ionising them. These ions are attracted toward the negatively biased collector (held at 0 V) and form a small current. This current is proportional to pressure, according to:

$$P = I_c / (sI_e) \quad (2.27)$$

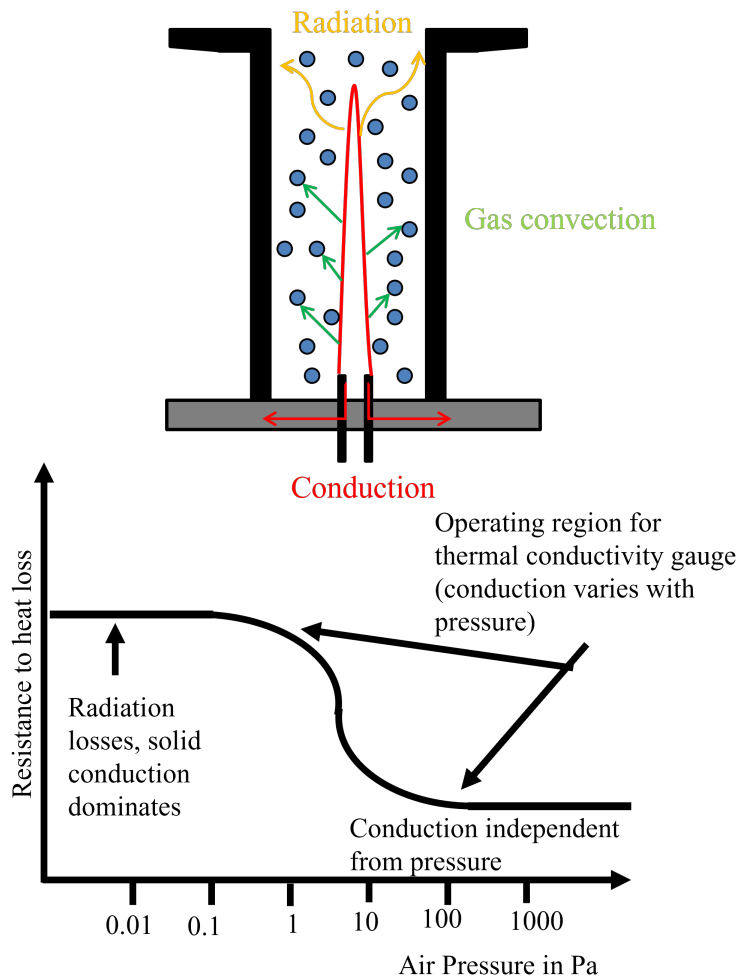


Figure 2.12 – Principle of the thermal conductivity gauge. From [31].

where I_c is the collector current, s is sensitivity and I_e is the emission current.

The high velocity of an electron, when colliding with a gas molecule, drives it out of the molecule, leaving it positively charged. A measure of the ion current to the ion collector then gives an indication of the gas pressure in the device. This is how an ionization gauge operates. Conventional ionization gauges are not able to measure pressures below 10^{-6} Pa. The Bayard-Alpert gauge was designed for this purpose. The voltage applied to the electrodes is much bigger [32] than for conventional ionization gauges. The ionization gauge requires considerable auxiliary electrical equipment and is sensitive to the gas species.

At these pressures the energy transported by molecules of gas is small compared to the momentum transported by photons on account of the comparatively enormous mass of the molecules. The Pirani gauge measures the heat transfer while the Knudsen gauge measures the momentum transport, hence its advantage. The use of a suspension involves difficulties when the gauge is subject to external causes of vibration.

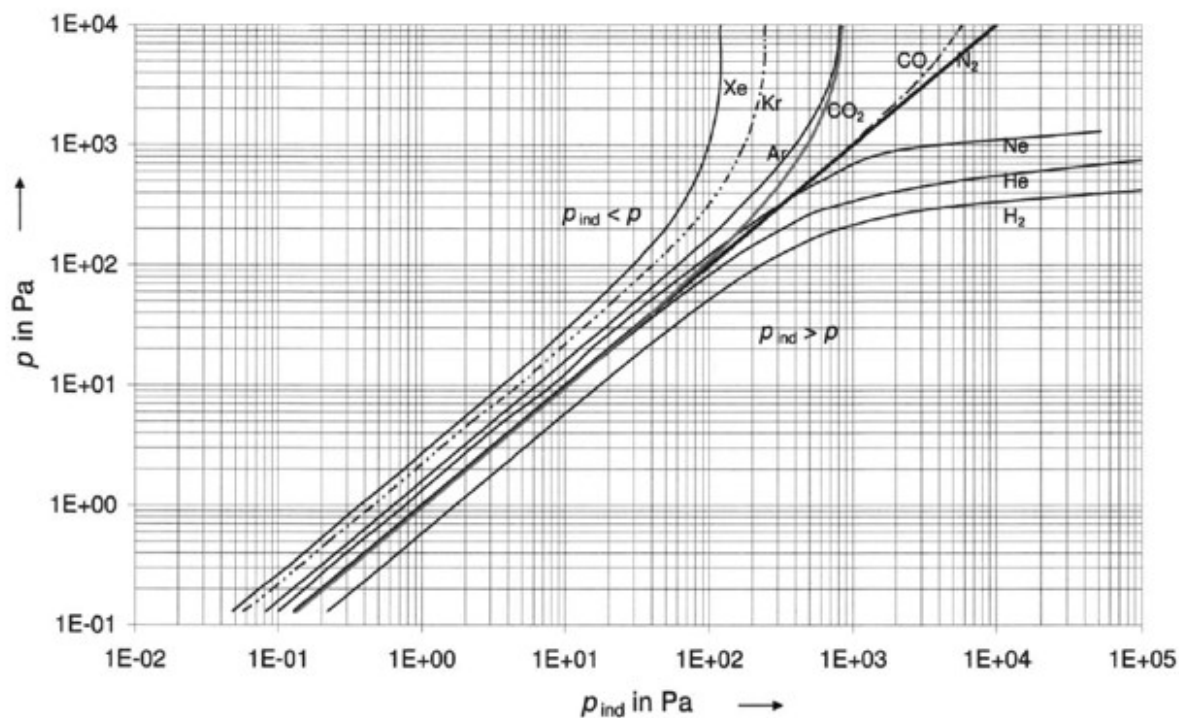


Figure 2.13 – Gas dependence of the Pirani heat transfer gauge. From [33].

Those transducing principles have privileged ranges where their sensitivity is maximal depending on their dimensions. MEMS and miniaturization of devices have been used for pressure sensors in order to be inserted in microfluidic devices on the one hand, on the other hand, it allows to improve the sensing range and sensitivity.

For the measurement of vacuum, different types of gauges may be sorted, according to the transducing principle involved. All the mentioned gauges present assets and drawbacks depending on the application where they are used. The experimenter must decide upon the objective of any set of measurements and then choose the gauge that grants the desired information with the best convenience and the desired degree of accuracy. Many times the order of magnitude of the pressure is sufficient, other times a continuous record of variation in pressure is needed, without any reference to the nature of the gas present.

2.4 Pirani sensors

2.4.1 Pirani operating principle

Pirani gauges have a fine wire filament that has a high temperature coefficient of resistance. The wire acts as both the heater and the sensor. Usually a Pirani gauge is part of a Wheatstone bridge circuit that also

includes a temperature compensating element. Well designed Pirani gauges offer better accuracy and response time than do thermocouple gauges (often tens of milliseconds vs. several seconds). Marcello Pirani pointed out in 1906 that in order to construct a gauge based on the relation between the heat conducted from a wire and the pressure, three different schemes could be used:

- The voltage on the wire is maintained constant, and the change in current is observed as a function of the pressure
- The resistance (and therefore the temperature) of the wire is maintained constant, and the energy input required for this is observed as a function of the pressure
- The current is maintained constant, and the change in resistance is observed as a function of the pressure

The Pirani wire is usually inserted inside a Wheatstone bridge where the signal is taken from. Two elements are used with characteristics matched so that they can be operated in adjacent arms of a Wheatstone bridge. One element is sealed off in good vacuum and gettered. This serves as a temperature compensator for the other element, which is connected to the system in which the pressure is to be determined.

The bridge is balanced under conditions of good vacuum in the pressure sensor, and the off-balance current comes from the pressure. The exact calibration varies with the nature of the gas. Since the linear expansion of a heated wire is a function of the temperature, such consideration may be applied to measure the pressure of a gas in which the wire is located. Gauges with bimetallic strips are used. The gauge can also be a spiral. As the pressure decreases the loss of heat by conduction becomes negligibly small as compared with the radiation loss. No modification in the geometrical design of the gauge can improve the ratio of energy loss by gas conduction to energy loss by radiation since at these low pressures the molecules of gas travel in straight lines between the wire and the walls just as the photons of radiation do. The optimal operation range of a Pirani gauge is between 0.01 Pa and 100 Pa.

2.4.2 Pirani sensor modelling

The Pirani principle operates when a heated element is inserted inside a vacuum chamber. When the Pirani element is supplied with a constant heating power, it will transfer heat to its surroundings and reach an equilibrium temperature characteristic of the pressure and the gas. The efficiency of the Pirani sensing depends on the heat transfer occurring between the Pirani gauge itself and the gas molecules surrounding it that come into contact with it. The quality of this heat transfer is described by the value of the gas thermal conductivity. The Pirani element transfers heat by three means:

1. Solid conduction from the Pirani sensor to its carrier, the value of the thermal conductance depends on the sensor design and its thermal conductivity. For instance the solid conductance between the Pirani transducer and the rest of the sensor core is stated in [34] as:

$$G_S = \left(\frac{1}{4.2k_t d} \frac{B}{A} + 5 \times 10^4 \right)^{-1} \quad (2.28)$$

where k_t is the thermal conductivity of the Pirani gauge material in $\text{W m}^{-1} \text{K}^{-1}$, d the thickness of the sensor heated area, B the gas gap and A the width of the sensor heated area. In [10] for instance, the solid conductance is defined in a complete different way due to a different sensor geometry.

2. Radiation from the sensor's hot surface to the surface of the chamber, its value depends on the emissivity and the exterior surface of the sensor.

The radiation conductance G_r can be deduced from the Stefan–Boltzmann law for the case of radiation exchange between an isothermal surface (temperature T and emissivity ε) and a black ambient environment of temperature T_0 . The radiative thermal conductance is defined as:

$$G_r = \frac{2\varepsilon\sigma (T^4 - T_0^4) A}{(T - T_0)} \quad (2.29)$$

where σ is the Stefan-Boltzmann constant and A the sensor heated area.

3. Solid to gas conduction from the sensor to the gas molecules that contact it which effectively depends on pressure. The solid thermal conductance is very specific to the geometry of the Pirani gauge. In [10], the gas conductance is modelled by the sum of two conducting gas columns of cross section A and lengths d_1 and d_2 :

$$G_g(p) = \lambda(p, d_1) \frac{A}{d_1} + \lambda(p, d_2) \frac{A}{d_2} \quad (2.30)$$

where $\lambda(p, d)$ is the gas thermal conductivity at pressure p for a for a gas column of length d . Figure 2.14 shows the structure of the Pirani sensor presented in [10] with the occurring heat transfers.

The solid to gas conduction between the Pirani gauge and its surrounding gas molecules which effectively depends on the pressure is stated in [34] as:

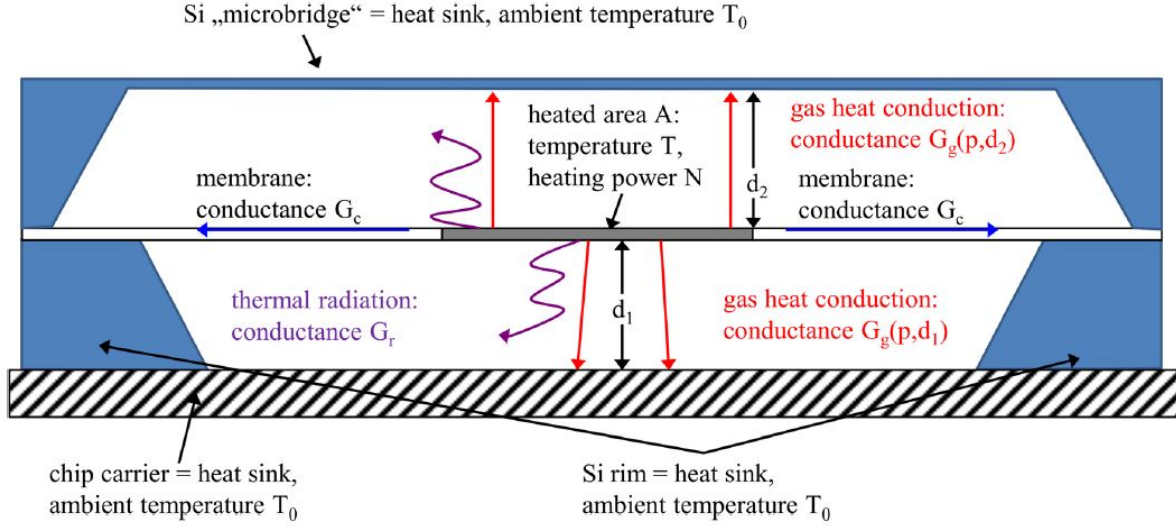


Figure 2.14 – Schematic cross section of MEMS Pirani sensor presented in [10].

$$G_g = \frac{\varphi}{2 - \varphi} G_a A_s P \left(\frac{P_{t1}}{P + P_{t1}} + \frac{P_{t2}}{P + P_{t2}} \right)$$

and

$$G_a = \Lambda_0 \left(\frac{273.2}{T_a} \right)^{1/2} \tag{2.31}$$

where φ is the accommodation coefficient of the gas, G_a and Λ_0 are the gas molecular conductivities at T_a and at 273 K, respectively; A_s is the floating plate area; P is the ambient pressure; P_{t1} and P_{t2} are transition pressures on both sides of the membrane, which are inversely proportional to the effective separations of the membrane from their heat sinks. The article [35] uses the same modelling equations for his Pirani sensor.

The air thermal conductivity with respect to temperature and pressure is expressed in [36] as:

$$k_{air} = k_{air,0} \times \frac{1}{1 + \frac{T \times 7.6 \times 10^{-5}}{P \times g}}, \tag{2.32}$$

where $k_{air,0}$ is the thermal conductivity of air at room temperature and pressure taken as (0.0284 W/(m K)) and g the gas gap between the heated nanowire and its substrate

In some cases, such as in [37] the model of the heat transfer in a Pirani sensor neglects radiation and solid conduction due to the small size of the Pirani sensing wire. The overall thermal conductivity of a gas $k_g(P)$, is a linear function of P at low pressures and limits to a constant at high pressures, and obeys the following equation:

$$k_g(P) = k_c \left(\frac{P/P_0}{1 + P/P_0} \right) \quad (2.33)$$

with:

- k_c – gas thermal conductivity at the continuum regime
- P_0 – empirical transition pressure

Steady state equation

The steady state behaviour of a Pirani sensor is described by the three different kinds of heat transfer that occur between the Pirani gauge and its surroundings, i.e.:

$$T - T_0 = \Delta T = \frac{1}{G} N = \frac{1}{G_r + G_c + G_g(p)} N \quad (2.34)$$

with:

- T, T_0 – Temperatures in K
- N – Power dissipated by the sensor in W
- $G, G_r, G_c, G_g(p)$ – Thermal conductances in WK^{-1} temperature in K

Transient equation

In the paper [38] a model of the thermal response time of a cylindrical wire used as a Pirani sensor is described. The objective from this model was to see the transient behaviour of the Pirani sensor and estimate the time for thermal equilibrium which is the minimum of the response time that can be expected. The geometry modelled is shown in Figure 2.15.

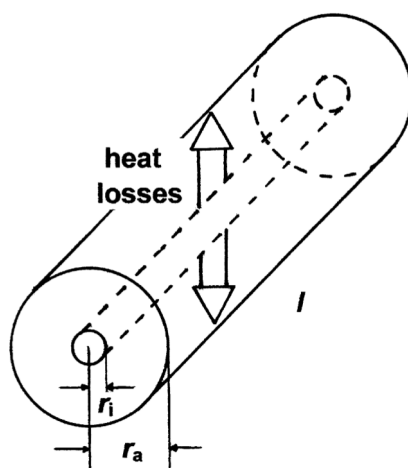


Figure 2.15 – Schematic drawing of a typical Pirani sensor with a thin heated wire mounted on a cylindrical housing. From [38].

Relying on the first principle of thermodynamics, the heat dissipated by the system is:

$$P_{\text{heat}} = c_{\text{wire}} m_{\text{wire}} \frac{dT}{dt} + P_{\text{stat}} \frac{T - T_a}{T_i - T_a} \quad (2.35)$$

where P_{heat} is the heating power supplied to the sensor in W, c_{wire} is the specific heat capacity of the Pirani sensor material in JK^{-1} , T the Pirani sensor temperature, T_i the Pirani sensor operating temperature, T_a the ambient temperature and P_{stat} the power necessary to maintain the Pirani sensor in equilibrium at T_i .

This leads to the equation for the Pirani sensor wire temperature:

$$T(t) = T_a + \frac{P_{\text{heat}}}{P_{\text{stat}}} (T_i - T_a) \times \left[1 - \exp\left(-\frac{t}{\tau}\right) \right] \quad (2.36)$$

where the time constant τ is defined as:

$$\tau = \frac{c_{\text{wire}} m_{\text{wire}} (T_i - T_a)}{P_{\text{stat}}}. \quad (2.37)$$

Electrical output signal

In [10], the relationship between the final output voltage of the sensor and all the intermediate variables (pressure, temperature, resistance, voltage) is established. The previous equations presented above showed the relationship between the pressure and temperature. Now the relationship between temperature and electrical resistance is shown, followed by the relationship between the electrical resistance and the final output voltage.

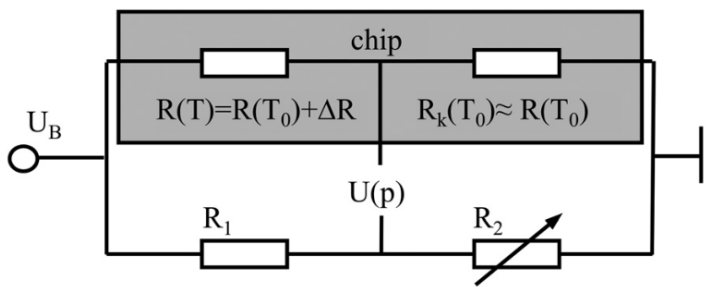


Figure 2.16 – Wheatstone bridge containing the MEMS Pirani sensor. From [10].

For the characterization of the MEMS Pirani pressure response a Wheatstone bridge circuit with a constant voltage supply U_B is used. This Wheatstone bridge is balanced at atmospheric pressure. The pressure decrease to reach vacuum pressures causes a temperature increase of the sensor. This temperature increase is correlated with a resistance increase of :

$$R(T) - R(T_0) = \Delta R = R(T_0)\beta(T - T_0) \quad (2.38)$$

where β is the linear Temperature Coefficient of Resistance (TCR). The signal voltage $U(P)$ is related to the resistance increase by

$$\begin{aligned} U(P) &= \left[\frac{R(T)}{R_k + R(T)} - \frac{R_1}{2R_1} \right] U_B = \left[\frac{R_0 + \Delta R}{2R_0 + \Delta R} - \frac{1}{2} \right] U_B \\ &\approx \frac{1}{4} \frac{\Delta R}{R_0} \left[1 - \frac{\Delta R}{2R_0} + \left(\frac{\Delta R}{2R_0} \right)^2 \right] U_B, \end{aligned} \quad (2.39)$$

where $R(T)$ is the Pirani sensor resistance, R_k , the compensation resistor that has the same resistance as the Pirani sensor at the reference temperature T_0 . Figure 2.17 shows the different steps to model a Pirani sensor behaviour from gas kinetic theory to the final electrical output signal.

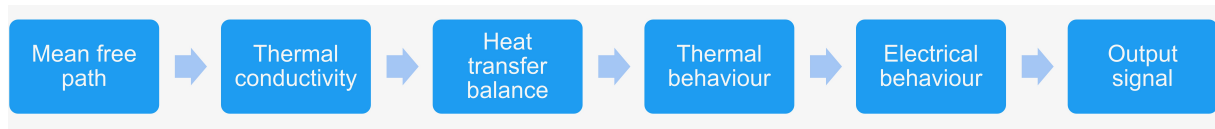


Figure 2.17 – Pirani sensor behaviour modelling.

2.4.3 Pirani sensors state of the art

In a conventional Pirani gauge, the change in pressure vs. wire temperature remains fairly linear over a pressure range of about 0.01 Pa to 100 Pa depending on the wire dimensions typically in tens to hundreds of micrometers. Below this range, heat transfer is dominated by radiation from the wire's surface and conduction from the wire to its carrier. Above this range, heat transfer is ruled by thermal convection. In addition to that, other heat transfer mechanisms, i.e. solid conduction from chip to carrier and radiation, overwhelm the pressure dependent gas heat transfer.

A wide choice of sensors based on the Pirani principle is therefore available in the literature. A list of references is given in Table 2.6 which also includes the measurement principles and the sensing range of the sensors. The devices are often made using microfabrication and semiconductor technologies. These sensors address different pressure ranges: from two decades of pressure up to seven decades of pressure for one single device.

However, systematic investigations of Pirani wires have identified limits of the process corresponding to saturation due to the pressure dependence of thermal conductivity in high vacuum and close to atmospheric pressure [39, 40].

A high vacuum process will need to be provided with gauging that follows the pump down cycle from atmospheric pressure through the volume zone and into the dry down zone. A thermal conductivity

gauge can follow the pressure all the way through the volume zone, but when the system goes into the dry down zone below about 0.01 Pa, where water vapor becomes the predominant residual gas and an ionization gauge is therefore required.

Usually, with the exception of some extended range gauge modifications, these two gauges together can be used to cover the full pump down cycle. This is why several electronic gauge controllers combine both types of gauges in the same unit. For instance, vacuum hybrid sensors such as Pirani Bayard-Alpert and Pirani-Magnetron increase the measurement range from atmospheric to the ultra-high vacuum.

Consequently, the revived development of hybrid sensors combining two or more operating principles has received much attention recently since a lot of combined Pirani gauges are commercialized (Canon Cold Cathode Pirani Gauge M-360 CP or BCG 450 from INFICON for instance).

2.5 Wireless power transfer and wireless sensing

In order to develop a wireless power transfer system based on coupled inductive coils, a preliminary theoretical analysis is necessary to grasp the physical variables involved as well as the sensitive parameters. Figures 2.18 and 2.19 show the magnetic field lines of one and two coupled coils, which illustrates the interaction between the coils during inductive coupling.

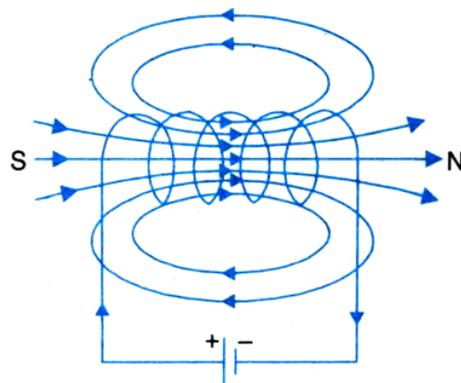


Figure 2.18 – Magnetic field lines of one coil alone. Retrieved from [41]

2.5.1 Coils coupling for wireless power transfer circuit design

In the following, a design-oriented analysis of a wireless power link driving a resistive load is presented as a preamble to the implementation of the wireless heating unit of the sensor developed in this thesis. The standard equation-pair of coupled inductor is employed to analyse the circuit configuration to obtain:

1. the reflected impedance of the secondary circuit detected at the primary side

Table 2.6 – Detection principles and pressure ranges of MEMS Pirani gauges

Researcher	Type of gauge	Pressure range [Pa]
Van Herwaarden and Sarro, 1988	Heated cantilever combined with thermopile	$0.13 - 1.33 \times 10^4$
Völklein and Schnelle, 1991	Heated resistor combined with thermopile	0.13 - 10
Piotto et al., 2017	Heated resistor with thermopile	$0.3 - 1 \times 10^5$
Mastrangelo and Muller, 1991	Microbridge	$10 - 1 \times 10^4$
Swart et al., 1994	Microbridge	$13 - 1.33 \times 10^4$
Chae et al., 2004	Microbridge	2.6 - 267
Moelders et al., 2004	Microbridge	1.33 - 133
Doms et al., 2005	Microbridge	$100 - 1 \times 10^5$
Stark et al., 2005	Microbridge	$1.33 - 1 \times 10^6$
Mitchell et al., 2008	Microbridge	$1.33 - 1 \times 10^5$
Khosraviani and Leung, 2009	Microbridge	$13.3 - 1 \times 10^6$
Li et al., 2010	Microbridge	$106 - 2.67 \times 10^4$
Jiang et al., 2010	Microbridge	$0.1 - 1 \times 10^3$
Chen, 2012	Microbridge	$133 - 1.33 \times 10^5$
Puers et al., 2002	Microbridge	$100 - 1 \times 10^7$
Moutaouekkil et al., 2015	Microbridge	$1 \times 10^3 - 1 \times 10^5$
Mailly et al., 2009	Microbridge	$20 - 2 \times 10^4$
Robinson et al., 1992	Resistor on dielectric membrane	$10 - 1.33 \times 10^4$
Paul et al., 1994	Resistor on dielectric membrane	$100 - 1 \times 10^5$
Shie et al., 1995	Resistor on dielectric membrane	$1.33 \times 10^{-5} - 133$
Chuo et al., 1997	Resistor on dielectric membrane	$13.3 - 1.33 \times 10^7$
Stark et al., 2003	Resistor on dielectric membrane	$1.33 - 1.33 \times 10^4$
De Jong et al., 2003	Resistor on dielectric membrane	$10 - 2 \times 10^4$
Zhang et al., 2006	Resistor on dielectric membrane	$10 - 1 \times 10^5$
Völklein et al., 2013	Resistor on dielectric membrane	$1.33 \times 10^{-4} - 1.33 \times 10^3$
Grau et al., 2014	Resistor on dielectric membrane	$0.13 - 1 \times 10^5$
Xiao	Resistor on dielectric membrane	$1 - 1 \times 10^3$
Kimura et al., 2007	Resistor on dielectric membrane	$2 \times 10^{-3} - 1 \times 10^5$
Jeon et al., 2016	Resistor on dielectric membrane	$1.3 \times 10^{-2} - 1 \times 10^5$
Paul and Balthes, 1995	Resistor on dielectric membrane	$100 - 1 \times 10^6$
Wenzel and Bak, 1998	Resistor on diaphragm	$10 - 1 \times 10^5$
Qui et al., 2009	Metallic wire	1 - 100
Brun et al., 2012	Silicon nanowire	$50 - 1 \times 10^5$
Ghouila-Houri et al., 2017	Microwire	$1 \times 10^4 - 8 \times 10^5$
Schelcher et al., 2011	Ni-microbeam	$3.3 - 1 \times 10^5$ 45
Wang et al., 2011	Microplate	$0.1 - 1 \times 10^5$
Santagata et al., 2011	Tube-shaped	$0.133 - 1.33 \times 10^5$
Mercier et al., 2012	Cr/Au-resistor on LiNbO ₃ -substrate (SAW-device)	$1 \times 10^{-3} - 1 \times 10^5$

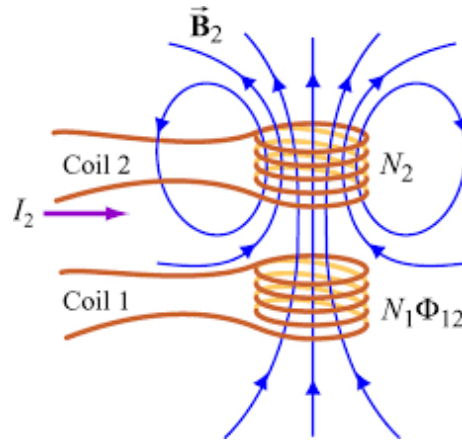


Figure 2.19 – Magnetic field lines of two coupled coils. Retrieved from [41]

- 2. the link voltage gain
- 3. the link efficiency

the following analysis presents the equations with parameters arranged in a way to highlight the physical meaning of the results and help design the coupled coils. In [42], the design of coupled coils with a resistive load is presented in a design oriented way which is very similar to the target configuration used within the scope of this thesis.

An essential aspect of design oriented analysis is to group the terms strategically to expose the physical meaning and the key parameters. Let us start with the ideal transformer and its modelling, as shown in Figure 2.20. The ideal transformer has a turns-ratio of $1 : n$ and its $I - V$ characteristic is described by the following equations:

$$V_2 = nV_1 \tag{2.40}$$

$$I_1 = nI_2 \tag{2.41}$$

with:

V_1, I_1 – Voltage and current at Tx coil

V_2, I_2 – Voltage and current at Rx coil

The input impedance in the s-domain $z_{in}(s)$ is computed as:

$$z_{in}(s) = \frac{V_1}{I_1} = \frac{1}{n^2} Z_L(s) \tag{2.42}$$

with:

z_{in} – The input impedance

Z_L – The output impedance

The ideal transformer is modelled using one current-controlled current source and one voltage-controlled voltage source. The coil system is described in the time domain by the equation pair of the coupled inductors that drive a resistive load. Figure 2.20 shows an ideal transformer while Figure 2.21 shows ideal coupled coils.

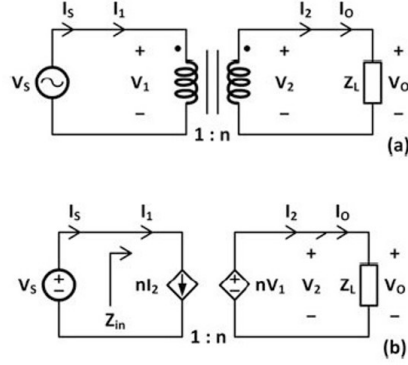


Figure 2.20 – Ideal transformer: (a) circuit; and (b) circuit model. From [42].

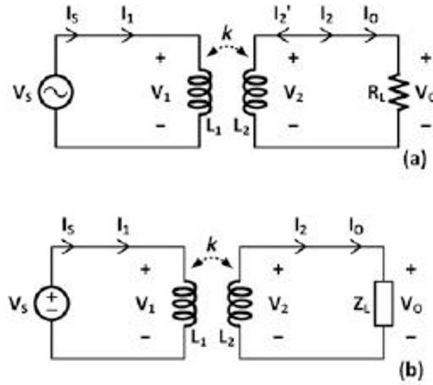


Figure 2.21 – Ideal coupled coils (a) in the time domain with a resistive load and (b) in the s-domain with a load impedance $Z_L(s)$. From [42].

The circuit analysed is a pair of ideal coupled inductors with primary inductance L_1 , secondary inductance L_2 , and mutual inductance M driving a load resistor R_L . The coil system is described in the time-domain by the equation-pair of the coupled inductors that drive a resistive load:

$$\begin{aligned} V_1(t) &= L_1 \frac{dI_1}{dt} + M \frac{dI_2'}{dt} \\ V_2(t) &= M \frac{dI_1}{dt} + L_2 \frac{dI_2'}{dt} = -I_2' R_L \end{aligned} \tag{2.43}$$

The computation in the s-domain is more convenient using $I_2 = -I_2'$. The generic load impedance $Z_L(s)$ is then derived from:

$$\begin{aligned} V_1(s) &= sL_1I_1 - sMI_2 \\ V_2(s) &= sMI_1 - sL_2I_2 = I_2Z_L(s) \end{aligned} \quad (2.44)$$

The mutual inductance is calculated via the coupling coefficient k and the turns ratio n :

$$k = \frac{M}{\sqrt{L_1L_2}}, n = \sqrt{\frac{L_2}{L_1}} \quad (2.45)$$

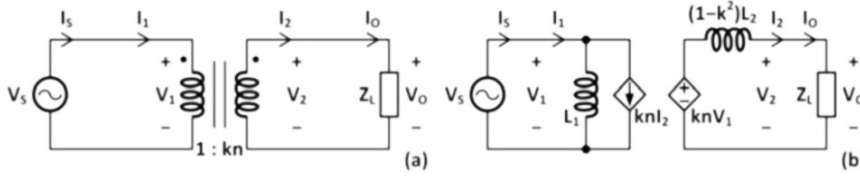


Figure 2.22 – (a) Transformer model of ideal coupled coils (b) equivalent circuits on each side. From [42].

The input voltage $V_1(s)$ and the output voltage $V_2(s)$ shown in Figure 2.22 are given by:

$$\begin{aligned} V_1(s) &= sL_1(I_1 - knI_2) \\ V_2(s) &= knV_1 - s(1 - k^2)L_2I_2 \end{aligned} \quad (2.46)$$

Reinjecting the k and n formulas we have:

$$V_1(s) = sL_1I_1 - sL_1 \frac{M}{\sqrt{L_1L_2}} \sqrt{\frac{L_2}{L_1}} I_2 \quad (2.47)$$

and

$$V_2(s) = \frac{M}{L_1} (sL_1I_1 - sMI_2) - sL_2I_2 + s \frac{M^2}{L_1L_2} L_2I_2 \quad (2.48)$$

Link voltage gain and coupling efficiency

Calculating the voltage gain and efficiency helps define the electronics components properties (inductance, capacitance, resistance) in order to be able to transfer the necessary power to the receiver coil. The link voltage gain A_T from the source to the load is:

$$A_T = \frac{V_o}{V_S} \quad (2.49)$$

and the link efficiency η_T

$$\eta_T = \frac{P_o}{P_s} \quad (2.50)$$

where V_s and P_s are the source voltage amplitude and source power at the primary coil; V_0 and P_0 are the load voltage amplitude and power at the secondary coil.

Considering $s = j\omega$, the equivalent impedance of the secondary circuit reflected to the primary side is defined as:

$$Z_{eq}(s) = \frac{\omega^2 M^2}{R_L + sL_2} \quad (2.51)$$

The quality factor of the inductor of the secondary coil driving the load R_L is:

$$Q_L = \frac{\omega L_2}{R_L} \quad (2.52)$$

The equivalent impedance Z_{eq} can then be written:

$$Z_{eq}(j\omega) = \frac{\omega^2 M^2}{R_L (1 + Q_L^2)} (1 - jQ_L) \quad (2.53)$$

or

$$Z_{eq}(j\omega) = \frac{k^2}{n^2} \frac{Q_L^2}{(1 + Q_L^2)} R_L (1 - jQ_L) \quad (2.54)$$

The link voltage gain can be expressed as:

$$A_T = \frac{V_o}{V_s} = \left| knV_s \frac{R_L}{R_L + j\omega(1 - k^2)L_2} \right| \frac{1}{V_s} \quad (2.55)$$

which leads to

$$A_T = \frac{kn}{\sqrt{1 + (1 - k^2)^2 Q_L^2}} \quad (2.56)$$

The coupling coefficient is smaller than 1 and can be very small. If the load resistance is large the quality factor is small. The average power of the load is given by:

$$P_o = \frac{1}{2} V_o I_o^* = \frac{1}{2} R_L |I_o|^2 \quad (2.57)$$

If the system is ideal it has no parasitic resistance and despite a weak coupling there is no loss. The power is consumed in the primary coil even if there is no load resistance. The model does not account for EM radiation losses. Taking into account parasitic resistance, power transfer calculation is more accurate for a real circuit.

Resonant coupled coils

In wireless power transfer circuits, capacitors are usually added to both the primary and the secondary coil to resonate at the frequency of power transmission. A capacitor can be inserted in series or in parallel to the inductor, and the coils can be made series-resonant or parallel-resonant. The quality factor can be made real at ω_o if:

$$\frac{1}{\sqrt{L_1 C_1}} = \omega_o \quad (2.58)$$

In the next two paragraphs describe the calculation of the resonance frequency in the case of a series-series resonant coupled coils and series-parallel coupled coils.

Series-series resonant coupled coils

If a capacitor is added in series with the primary and secondary coil respectively, the s-domain equations are:

$$\begin{aligned} V_S &= (1/sC_1 + R_1 + sL_1)I_1 - sMI_2 \\ V_2 &= sMI_1 - sL_2I_2 = (R_2 + 1/sC_2 + R_L)I_2 \end{aligned} \quad (2.59)$$

The equivalent impedance is given by:

$$Z_{eq}(j\omega) = \frac{\omega^2 M^2}{R_L + R_2 + 1/j\omega C_2 + j\omega L_2} \quad (2.60)$$

$Z_{eq}(j\omega)$ can be made real at the power carrier frequency:

$$f_0 = \omega_0/2\pi \quad (2.61)$$

if

$$\frac{1}{\sqrt{L_2 C_2}} = \omega_0 \quad (2.62)$$

Similarly $I_1(j\omega_0)$ can be made real at ω_0

$$\frac{1}{\sqrt{L_1 C_1}} = \omega_o \quad (2.63)$$

if:

$$\frac{1}{\sqrt{L_1 C_1}} = \frac{1}{\sqrt{L_2 C_2}} = \omega_o \quad (2.64)$$

Z_{eq} is purely real as well as I_1 while I_2 is purely imaginary. The new link voltage is:

$$A_T = \frac{|V_o|}{V_S} = \frac{\omega_o k \sqrt{L_1 L_2} R_L}{R_L + R_2} \frac{1}{R_1 + \frac{\omega_o^2 k^2 L_1 L_2}{R_L + R_2}} \quad (2.65)$$

The link voltage gain can then be rewritten as:

$$A_T = \frac{knQ_1}{(1 + k^2 Q_1 Q_S)} \frac{R_L}{R_L + R_2} \quad (2.66)$$

The the load power is $P_o = \frac{1}{2} I_o^2 R_L$ and the source power is $P_{ST} = 1/2 V_S I_S^*$. To compute link efficiency η_T we make use of $1/(L_1 C_1)^{1/2} = 1/(L_2 C_2)^{1/2} = \omega_o$:

$$\begin{aligned} P_{ST} &= \frac{V_S I_S^*}{2} = \frac{1}{2} (R_1 I_1 - j\omega_o M I_2) I_1^* \\ P_{ST} &= \frac{1}{2} \left(R_1 \frac{R_L + R_2}{j\omega_o M} - j\omega_o M \right) I_o \frac{R_L + R_2}{-j\omega_o M} I_o^* \\ P_{ST} &= P_S = \frac{|I_o|^2}{2} \left(R_L + R_2 + R_1 \frac{(R_L + R_2)^2}{\omega_o^2 M^2} \right) \end{aligned} \quad (2.67)$$

The link efficiency is given by:

$$\eta_T = \frac{P_o}{P_S} = \frac{1}{1 + \frac{n^2}{k^2} \frac{1}{Q_S^2} \frac{R_1}{R_L} + \frac{R_2}{R_L}} \quad (2.68)$$

Compared to the previous values, the resonant circuit gives a better efficiency.

Series-parallel resonant coupled coils

If a capacitor is added in series with the primary coil and a capacitor is added in parallel to the secondary coil a pair of series-parallel resonant coupled coils is prepared:

$$\begin{aligned} V_S &= (1/sC_1 + R_1 + sL_1) I_1 - sMI_2 \\ V_2 &= sMI_1 - sL_2 I_2 = (R_2 + 1/sC_2 || R_L) I_2 \\ I_o &= \frac{1/sC_2}{1/sC_2 + R_L} I_2 = \frac{1}{1 + sC_2 R_L} I_2 \end{aligned} \quad (2.69)$$

The equivalent impedance is given by:

$$\begin{aligned} Z_{eq}(s) &= \frac{\omega^2 M^2}{sL_2 + R_2 + 1/sC_2 \parallel R_L} \\ Z_{eq}(j\omega) &= \frac{\omega^2 M^2 (1 + j\omega C_2 R_L)}{R_2 + R_L(1 - \omega^2 L_2 C_2) + j\omega(L_2 + C_2 R_2 R_L)} \end{aligned} \quad (2.70)$$

$Z_{eq}(j\omega)$ is designed to be real by assigning the resonance frequency:

$$\omega_r = \sqrt{\frac{1}{L_2 C_2} - \frac{1}{C_2^2 R_L^2}} = \frac{1}{\sqrt{L_2 C_2}} \sqrt{1 - \frac{L_2}{C_2 R_L^2}} \quad (2.71)$$

The definition of the resonant frequencies for each configuration is useful for the design and the optimisation of the coupled-coils.

2.5.2 State of the art of wireless power transfer

A sensor operated wireless needs to be supplied with power wireless. Wireless power transfer methods used for miniaturised sensors were reviewed in literature. The major insights are presented in the following. In [43], an induction power transfer for brain implants is presented. The optimum link design efficiency reached is 80% and an efficiency of 20% is reached at 20 mm coupled distance by self-developed coils. In [43], a mathematical optimisation process of an inductive powering system suitable for implanted biomedical systems is described. The parameters studied are size, energy efficiency, tissue absorption and operation frequency. The design also considers high-permeability structures being applied to the primary coil, enhancing the efficiency by means of an increased mutual inductance. Thereby, a final link efficiency of 80% at a coil separation distance of 5 mm and 20% at 20 mm using a 10 mm planar receiving coil is achieved. Mathematical expressions for designing a highly efficient primary side coil driver and for selecting the components of the secondary side are elaborated. Impedance matching calculation is presented. Near field and far fields are used. A procedure to obtain a wireless powering system with optimum efficiency for a given size constraint identifying the optimum operating frequency according to the coils dimensions with ISM bands taken into account is put forward. The geometrical parameters taken into account are: the number of turns, the outer coil radius, the trace width and the trace pitch. The electronic design and signal conditioning chip electronic design is presented. An FR4-substrate with a copper height of 35 μm is used. S-parameters are captured for different distances adjusted by plastic spacers, allowing to calculate the optimum efficiency for the case of optimum impedance matching. Efficiency levels exceeding 80% are reached. For a 20 mm distance between coils, 20% efficiency is still achievable. The system presented in [43] inspired the design of the heating unit of the sensor developed in the scope of this thesis.

In [44], a fixed-load receiver that can be moved to nearly any position or orientation within the range of the transmitter and still achieve a near constant efficiency of over 70% for a range of 0-70 cm is presented. The analysis performed gives critical insight into the design of practical systems, including the introduction of key figures of merit that can be used to compare systems with vastly different geometries and operating conditions. A circuit model is presented along with a derivation of key system concepts such as frequency splitting and the maximum operating distance. The concept was experimentally validated for 59 cm diameter coils.

In [45], a contactless power transfer technology based on strongly coupled electromagnetic resonators is presented. A quality factor of 1010 at 1.8 K under 1.3 GHz was obtained. The ultra low electrical resistivity of a superconducting material allows an RF resonator to obtain a high quality factor. However, in the radio frequency range the losses remain moderate, some orders of magnitude less than in copper. Styrofoam and steel cooling vessels were placed between the Tx and Rx coil. For a 370 kHz frequency, a 20 cm coupling distance, a 30 cm diameter Tx and Rx coil, 81% efficiency was achieved at 15 cm coupling distance and 17.5% at 30 cm. This article addresses the issue of wireless power transfer in metallic environments, which is a main constraint of the sensor developed, since vacuum chamber are mostly metallic, the wireless transmission of signals in such an environment had to be carefully addressed.

In [46], strongly coupled planar coil structures for the purpose of enhanced induction over large areas is presented. A squircle shape at the outer rim with rounded corners and straight sides evolved into a fully circular shape in the inner side, which proves to be essential to achieve high efficiency in arrays and all-surface inductive heating. The efficiency was shown to be increased overall by 37,4% using outer squircle-inner circular coils instead of conventional circular coils. The efficiency of the power transfer achieved is around 50%. The influence of phase and relative angle between Tx and Rx coil was also assessed. This article deals with the orientation and the respective placing of Tx and Rx coils to optimize the power transfer, which was investigated in the testing phase of our prototype. Several geometries for the inductively coupled coils were considered during the design phase, including squircle-shaped coils although they were not retained for the first prototype due to their big size.

In [47], a wireless temperature measurement induction heating system for hyperthermia is presented. Coupling distances of 1.0, 2.0, 3.0 and 4.0 cm were tested. A signal to noise ratio of 18.3 dB was achieved at 3.0 cm. In addition, the correlation of the voltage with either the temperature or distance was high. A method for estimating the temperature from the voltage measured even if the coupling distance is known is unknown. This article helped estimate and choose the target coupling distance for our developed sensor.

In [48], the thermal responses of nickel, iron and copper heating units were studied by applying an alternating magnetic field as a function of geometry of unit, strength of magnetic field and kind of metal. This paper compares several materials for their heating properties and was used as a reference during the design of the heating resistor of the sensing chip.

2.5.3 Wireless sensors

In order to develop a miniaturized wireless sensor for vacuum sensing, the state of the art of miniaturized wireless sensors was reviewed in order to gain insights on existing solutions and remaining technical challenges.

Wireless technology, enabled by a micro/nano-antenna, is already essential to micro/nano robots, because the scale of the micro/nano robot makes a wire connection impossible, due to the size of the wire. Additionally, various wireless sensors are currently being intensively developed for the Internet of Things, and much smaller wireless components also need to be developed for those applications.

In [49], a wireless thin film transistor structure in which a source/drain or a gate is connected directly to a micro antenna to receive or transmit signals or power. It can be used as an electrical switch, a rectifier or an amplifier, for various electronics as well as microelectronics, since it allows simple connection with other devices, unlike conventional wire connections. An amorphous indium gallium zinc oxide thin film transistor with magnetic antenna structure was fabricated and studied. To enhance the induction coupling efficiency while maintaining the same small antenna size, a magnetic core structure consisting of nickel and nanowires was formed under the antenna. With the micro-antenna connected to a source/drain or a gate of the transistor, working electrical signals were controlled. The results qualified the device as an alternative solution to existing wire connections which cause a number of problems in various fields such as flexible and wearable electronics. A magnetic core structure was added to the micro antenna design to increase the magnetic flux density without changing the size of the antenna structure. The use of nanowires increases the effective area and surface to volume ratio. The coils used have 500 micrometer diameter. This article helped gain insights on the current capabilities of miniaturized antennas.

Most wireless sensing methods for coil coupling are published for medicine applications implantable devices such as in [50]. A prototype of an implantable pressure monitoring device and a 3 T clinical magnetic resonance imaging (MRI) is presented. The pressure monitoring device contains a catheter-mounted piezoresistive pressure sensor, a rechargeable battery, a wireless communication system and an inductive pickup coil. An RF intracranial pressure monitoring available on chip radio communication systems such as the nRF24LE1 from Nordic needs power on the order of 10 mW. The long-term implantable pressure monitor contains: sensor, catheter and electronic module (sensor interfacing, radio, power transfer). An analogy can be made between vacuum and the human body in terms of components size and energy transfer constraints as well as wave interference issues. The electronic unit consists of a rechargeable Lithium ion battery, an inductive power coil for transcutaneous energy transfer, a 2.4 GHz wireless data antenna link, and associated signal conditioning and amplification circuitry silicone jacket to allow for RF transparency. Materials used are Titanium, glass and ceramics. The heat transfer was assessed for both the short and long configuration at 128 MHz. The RF coil was tuned to 128 MHz. This coiled LC setup was tested with 8 cm from sensor tip to coil, 2.25 turns, and 3 cm from coil to electronic unit. The temperature change at the sensor tip was 7.2 °C, where the LC device caused a temperature change of 1.7 °C, after the 15 minutes scan. The same operating frequency of 2.45 GHz was retained

for our sensor, the energy consumption of this device is in the mW range same range as our developed sensor.

According to [49], a wire connection between a device implanted in a body and a control or a power supply system located externally can be a source of infection and an inconvenience for patients, which can be avoided with wireless functions. Likewise, in flexible display systems, which are considered to be the most important hardware component for next generation smart phone systems, damage to the scan and data lines connecting the thin film transistors (TFTs) is one of the significant obstacles to their practical implementation. The lines, in rows or columns, are easily broken by bending or folding, since the electrode shape is narrow (micrometer level) and long (cm to m level). Alternatively, if the signal or the power is supplied using wireless technology, those issues could be easily solved. Therefore, a wireless TFT structure would be an important component, since it could be applied as an important building block in various devices, as an electrical switch, a rectifier or an amplifier, for various electronics with wireless functionality. Here the advantages of wireless sensors are emphasized.

In [51] an UHF RFID Tag with an ultra-low power, small area, high resolution temperature sensor which adopted double voltage-controlled oscillators has been designed. The presented device has a low yield. The core area of the tag is $756.967 \mu\text{m}^2$. The power optimised tag allows a communication range of more than 6 m from a 1 W effective radiated output power reader. The sensor features independence of process, supply voltage and bias current variation for the double voltage-controlled oscillators structure. The area of the sensor is $109.47 \mu\text{m}$ and the power consumption of the sensor is less than 600 nW. These properties allow the use of the RFID as a batteryless sensor in a wireless environment temperature monitoring system. The device contains nonetheless heavy conditioning electronics. The relevance of the RFID function is discussed here, which was implemented as well on our developed sensor. Furthermore, the power consumption is estimated as a function of the transfer signal and the coupling distance.

In [52], the communication protocol between the sensor and the user interface is addressed. Communication protocols can have significant impact on the overall energy dissipation of sensor networks. A Low-Energy Adaptive Clustering Hierarchical method has been developed. Simulations show that this method can achieve as much as a factor of 8 reduction in energy dissipation compared with conventional routing protocols. The communication protocol or signals transferred impact directly the power consumption. It is therefore necessary to find a compromise between all those parameters to make a functional wireless sensor system.

In this perspective, Surface Acoustic Waves are compatible with wireless sensing and can be used as a pressure or temperature transducers. This is why they were considered as an operating principle and their theoretical background is presented in the following section.

2.6 Surface Acoustic Waves

Surface Acoustic Wave (SAW) devices are based on the physical property of piezoelectricity. Some materials are able to convert electrical energy into mechanical energy back and forth. In some cases the mechanical energy is converted into waves propagating within the material. Different kind of waves can be generated during this energy conversion. In a solid material, an acoustic wave generates changes in the relative position of atoms, which is called strain. The position changes are also specified in terms of displacement from the equilibrium state, and the displacement is generally a function of position. In the presence of strains, the material generates internal forces which tend to return the material to its equilibrium, unstrained state. A localised displacement, such as that due to a hammer blow, will cause strains which in turn generate stresses. The stresses generate further strains at more distant points. In this way, the disturbance propagates away from the point of the blow in the form of acoustic waves, which can travel over the whole extent of the solid. Figures 2.23 and 2.24 show the material deformation generated by SAW [17].

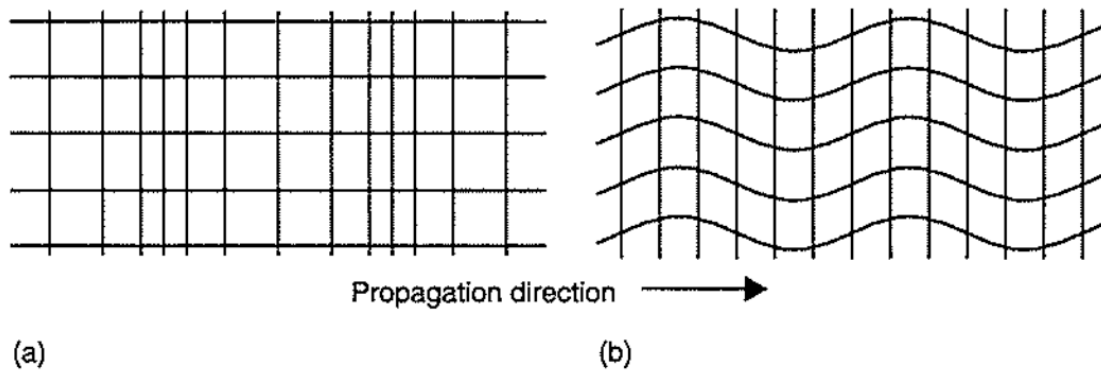


Figure 2.23 – Displacement of a rectangular grid during propagation of bulk acoustic wave. a) Longitudinal wave. b) Transverse wave. From [17].

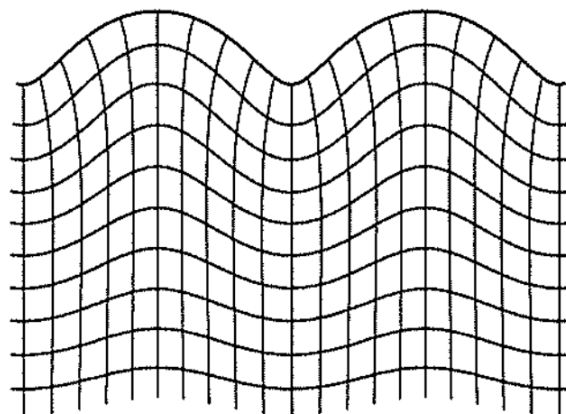


Figure 2.24 – Displacement of a rectangular grid during propagation of a Rayleigh wave. From [17].

The existence of a SAW was shown in 1885 by Lord Rayleigh. The wave, often called a Rayleigh wave, propagates along the plane surface of an isotropic solid half-space, with amplitude decaying exponentially away from the surface. The solution needs to satisfy the condition that there is no traction on the surface, and to do this it has two components corresponding to bulk shear and longitudinal waves. The wave is non-dispersive, with a velocity a little less than that of the bulk shear wave. The motion of individual atoms is elliptical.

Sezawa found that Rayleigh-type waves, with displacements in the sagittal plane, could also exist in a layered system and, like Love waves, they were dispersive and gave a series of modes with different velocities. Rayleigh, Love and Sezawa waves all occur in surface-wave devices, though Rayleigh-type waves are dominant. All of these waves are suitable for surface-wave devices.

Important properties are the wave velocity, piezoelectric coupling, temperature effects, diffraction, attenuation and the level of unwanted bulk-wave generation. It was found that on some crystals the surface-wave propagation was almost ideal, even for frequencies up to 1 GHz. However, even small imperfections can be relevant when exact requirements are to be met, and temperature effects always need to be considered. SAW properties (propagation velocity, resonance frequency and elastic constants) are sensitive to the surrounding environment conditions such as temperature, pressure, and humidity. Table 2.7 shows the sensitivity of SAW resonance frequency to different environmental parameters. Many of the surface-wave properties of a material can be deduced by calculating the wave velocity [17].

The wave velocities for a free surface and a metallized surface are denoted by v_f and v_m , respectively. In the latter case, the surface has an idealised metal coating which shorts out the parallel component of electric field at the surface, but is too thin to have any mechanical effect. The fractional difference between these velocities characterises the piezoelectric coupling to the wave. It is also common to define a coupling constant K^2 as twice this value, so we have:

$$\Delta v/v \equiv (v_f - v_m)/v_f = K^2/2 \quad (2.72)$$

Piezoelectricity can only be present if the material is anisotropic, that is, its properties vary with direction in relation to the internal structure. Nearly always, a single-crystal material is chosen because such materials can also give low losses. Since the material properties vary with direction, it is essential to quote the orientation when specifying a material. For example, a common material is Y-Z Lithium Niobate ($LiNbO_3$), where the notation indicates that the surface is normal to the crystal Y-axis and the wave propagates in the crystal Z-direction. Another case is 128° Y-Z Lithium Niobate. This is a rotated Y-cut. The surface normal makes an angle 128° with the crystal Y-axis, and the wave propagates in the crystal Z-direction. Both of these cases have strong piezoelectric coupling, but the temperature stability is poor. The reverse is the case for ST-X quartz. This is a 42.7° rotated Y-cut, with wave propagation along Z. It has good temperature stability, as quantified by the temperature coefficient of delay (TCD). The delay is maximized at 21°C , where the TCD is zero, and for practical purposes the delay is a quadratic function of temperature.

2.6.1 SAW sensors structure

SAW devices rely on wave motion guided along the surface of a solid material which gives access to the wave within its propagating path and thereby increases their versatility. A method to generate and detect the waves was then required which led to the apparition of the Interdigital Transducer (IDT) in 1965. In 1965, White and Voltmer put forward the IDT as a source or receiver of surface waves. The transducer consists of a sequence of metal electrodes, usually of Aluminum, alternately connected to two bus bars one for the generation and the other for reception of the waves. The SAW device consisted then of a shaped metallic thin film deposited on the surface of a piezoelectric crystal. Typical materials used in this context are quartz and Lithium Niobate. Such devices could be made conveniently using lithographic techniques borrowed from the semiconductor manufacture.

SAW are elastic waves travelling along the surface of solid piezoelectric materials with amplitude that decays exponentially with depth. Using an IDT, these waves can be demonstrated and reproduced. It is also simple to fabricate using lithographic techniques, similar to those used for integrated circuits but simpler because only one layer is involved. A crucial advantage is that the transducer geometry can be varied in an almost arbitrary manner, giving significant versatility. This is well illustrated by the considerable range of surface-wave devices that have been developed subsequently. Besides, further devices were developed such as reflective gratings, delay lines, bandpass filters, resonators, oscillators and matched filters. SAW devices are found in many practical systems such as radars, televisions and smartphones.

SAW devices and sensors are made of a piezoelectric crystal substrate with an IDT on its surface that converts voltage or other signals to SAW and vice versa. When a voltage is applied, the input transducer generates a periodic electric field, and a corresponding elastic stress is set up because of the piezoelectric effect. The IDTs are effective mainly at a frequency where the transducer pitch corresponds to the SAW wavelength. The response is strongest at this frequency and weaker at other frequencies, so the device can also be regarded as a bandpass filter. At the output the receiving transducer acts in a reciprocal manner, converting incident waves to an output voltage. Thus, the device converts an electrical input signal into an electrical output signal. Typically, a transducer might have 20-1000 electrodes. The electrode width is a quarter of the center-frequency wavelength, and the minimum possible width, determined by the fabrication technology, limits the frequency obtainable. In commercial production, the minimum width is about 0.5 μm . For a typical velocity of 3000 m/s this gives a maximum operating frequency of 1.5 GHz, though special techniques can extend this to 5 GHz. The lowest frequencies used are in the region of 20 MHz, because at low frequencies the device size becomes inconvenient. Figure 2.25 shows the structure of an IDT. The dimensions of the IDT electrodes determine the properties of the waves that they will generate, the propagation frequency in particular. When the SAW substrate with the IDT is connected to wireless antenna, the SAW device can be operated wirelessly as well.

Nevertheless, the basic two-transducer surface-wave device has an important limitation arising from reflections of the waves by the transducers. Unwanted reflected waves reach the output after three transits

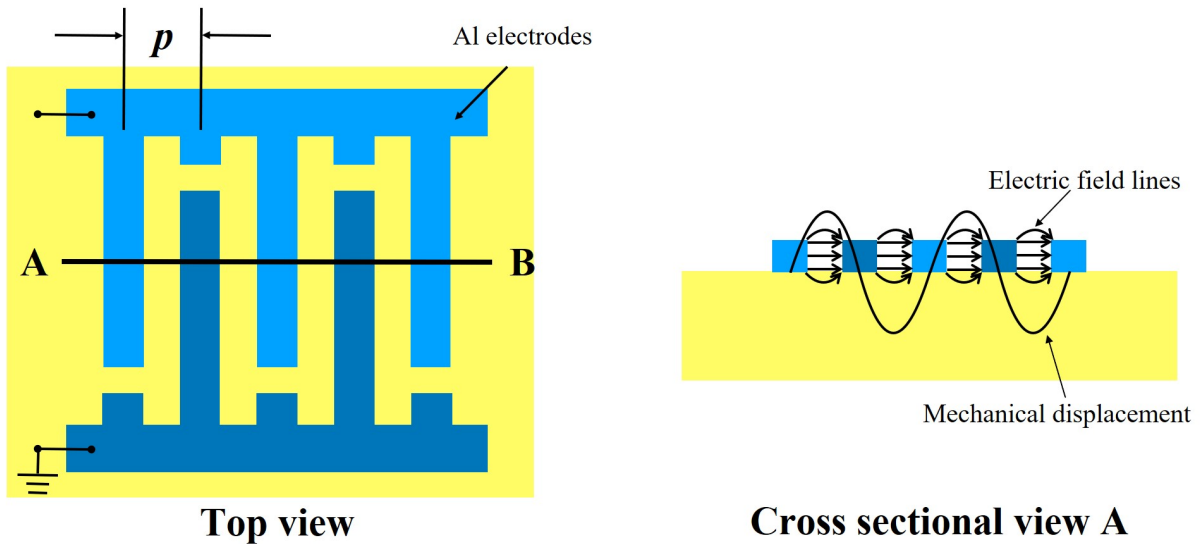


Figure 2.25 – Structure of an interdigital transducer. From [53].

Table 2.7 – Linear coefficient for physical effects on SAW substrate materials.

Physical quantity	Linear coefficient
Temperature	up to 100 ppm/K
Pressure, stress	2 ppm/kPa
Force	10 ppm/kN
Mass loading	30 ppm/ μg^{-2}
Voltage	1 ppm/V
Electric field	30 ppm/V μm^{-1}

of the device, giving a triple-transit signal. Higher-order reflections are also to be observed, called multiple-transit signals. In the device frequency response, these signals cause ripples in the amplitude and phase. In most devices the ripples must be well controlled, and this implies that the triple-transit signal must be minimised either by accepting a large insertion loss or by using a radically different device structure. The problem arises basically because a transducer has three ports. In a two-port device, such as a conventional filter, reflections are eliminated by matching the ports electrically, and this also minimises the insertion loss. To excite the SAWs and detect the changes in the environment properties, two types of device configurations, namely delay lines and resonators are commonly used.

Delay lines

SAW delay lines utilise the SAW propagation time, *i.e.* the ratio of acoustical wavelength L and SAW velocity v_{SAW} . In known sensor applications, L and v_{SAW} , respectively, are changed because of a temperature change, mechanical stress, and strain or because of a mass loading from a thin surface layer. The

delay T_0 of a delay line is affected by the measurand. A typical delay line SAW sensor consists of two IDTs deposited on a piezoelectric substrate at a certain separation, one for input and one for output of the electric signal [16]. This region creates a delay in time between the input and output signals based on its length and the SAW velocity.

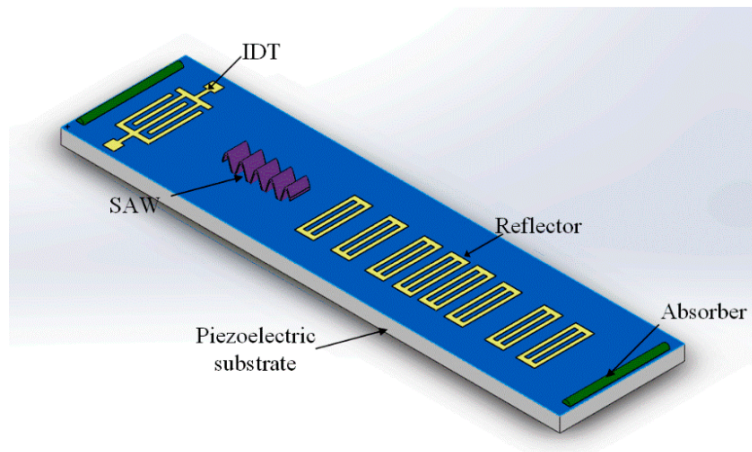


Figure 2.26 – Delay line IDT structure. From [54].

Resonator structure

The second configuration type of the devices is the resonator structure that consists of two IDTs for emission and detection of the acoustic waves and grating reflectors that are placed outside of each IDT so that a resonating cavity is formed in between. This structure is called a two-port resonator. If a single IDT is used for the input and output signals, the configuration is called the one-port resonator. SAW resonators' resonance frequency is influenced by the external measurand. Figure 2.27 shows the structure of a SAW IDT resonator.

2.6.2 SAW sensors applications

Piezoelectric materials are sensitive to environmental conditions such as temperature, pressure, stress, force, mass loading, voltage and electrical field. That is why they can be used to sense those environmental properties directly or other variables indirectly such as humidity, chemical species concentration or rotation velocity of components inside rotating machines.

Several SAW pressure and temperature sensors are available in the literature. They are based on the resonance frequency shift that depends on the pressure and/or the temperature. They use several materials and several configurations to address different ranges with good sensitivity. SAW devices used as temperature sensors have high sensitivity and wide sensing range. Temperatures between 0°C and 5000°C can be detected.

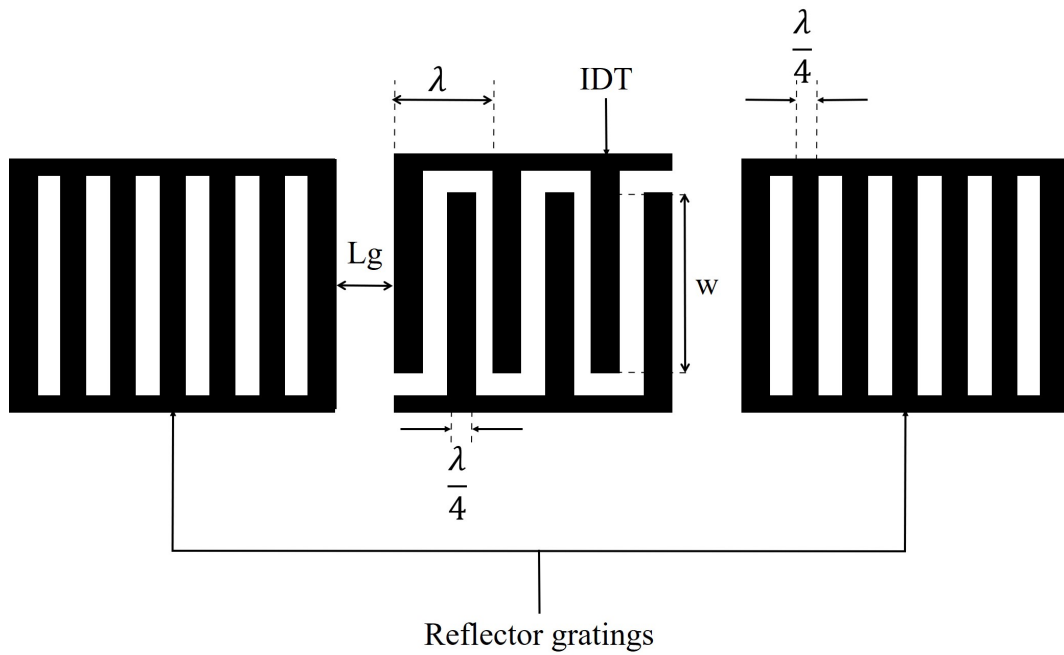


Figure 2.27 – Resonator IDT structure. From [55].

Some piezoelectric crystals are more sensitive to temperature than others, which is used for specific applications. Less sensitive crystals are used for their thermal stability. Table 2.8 shows the temperature coefficient of frequency of the piezoelectric crystals the most sensitive to temperature. These are the maximum sensitivities that can be expected from SAW sensors. SAW sensors were initially used as tire pressure monitoring system for the automotive industry [56]. [55] presents SAW devices used as accelerometers which was one of their first applications.

Table 2.8 – Temperature coefficient of frequency of several piezoelectric materials

Substrate material	Crystal cut	Linear TCF [ppm/K]
Lithium Niobate ($LiNbO_3$)	rotated 128 Y/X cut	72
	Y/Z standard cut	92 ppm/K
Lithium Tantalate ($LiTaO_3$)	X/112Y	18
	36 Y/X rotated cut	30
Langasit ($La_3Ga_5SiO_{14}$)	X/Y cut	24
Quartz (SiO_2)	ST-X cut	0 "Quartz stable"

A very popular application of SAW sensors is the specific detection of a gas species or an organic component [53]. In this case, a top layer of absorbent such as isobutylene or ZnO is placed on top of the IDT. The nature of the absorbent layer is specific to the sensed gas species. When the sensed substance

is in the environment the layer gets enriched, its density changes and the resonance frequency changes. Concentrations of chemical species such as NO_2 and CO_2 , CO , toluene and water are measured this way in the food and chemical industry for instance [57]. An E-Nose is an array of sensors that detects several gas species simultaneously. The sensors inside an E-Nose are often SAW sensors. The other aspect that makes the SAW devices successful is their wireless operability that makes them suitable for sensing of harsh and remote environment such as the underground, inside rotating machines [56] or even inside the human body [43].

For pressure measurements, subatmospheric pressures and overatmospheric pressures are separately addressed. SAW pressure sensors sensing pressure via strain and deformation of a membrane can address limited ranges of pressures because if the deformation range is too big the substrate cracks [58].

The devices operate at different frequencies depending on the range. In [59], a pressure sensor operates between 5 and 11.5 GHz to sense pressures between 1 and 7×10^5 Pa with a sensitivity of 5.37 ppm/kPa. The device described in [60] senses pressures between 0 and 3.5×10^5 Pa and operates at a frequency of 65 MHz using a Lithium Niobate substrate. Diaphragm-based SAW sensors are suitable to monitor pressures higher than 1×10^5 Pa with a precision of around 67 Pa. To reach precisions better than 0.13 Pa another transducing principle is usually required.

Several studies were published on SAW devices simulation using the software COMSOL or theoretical studies [60, 61]. SAW devices show often linear behaviour where the resonance frequency depends linearly on the pressure [59] or temperature. In [62], there is a linear relationship between the resonance frequency and the pressure. In [63] a ZnO/Si substrate is used to sense pressures between 0 and 5×10^6 Pa. Nonetheless, SAW devices used as pressure sensors have limited sensing range in terms of pressure decades.

A very interesting feature of SAW devices is that they can be wirelessly operated which is of major advantages in many applications such as vacuum technology. In vacuum the coupling between temperature and pressure through the Pirani effect is used to measure pressure with higher sensitivity. This explains the emergence of SAW Pirani sensors and why they were selected as an operation principle within the scope of this thesis.

2.7 SAW Pirani sensors

SAW devices are sensitive to both temperature and pressure but are more sensitive to temperature. Using the high sensitivity of SAW to temperature and the pressure dependence of the thermal conductivity of gases to pressure, a SAW chip can be used to measure subatmospheric pressures with better precision using temperature instead of pressure. Nicolay et al. [64] first had the idea to use a SAW temperature sensor as a pressure sensor for subatmospheric pressures. The concept was further developed and many features were integrated [11, 54, 63, 65–67].

The substrate used was Lithium Niobate since it is the most sensitive to temperature with a Temperature Coefficient of Frequency (TCF) approaching 100 ppm/K. Indeed, the TCF of the material needs to be high to observe a high temperature variation with the pressure.

The Surface to Volume Ratio and therefore the dimensions of the sensing chip are also critical parameters for the performances of a SAW Pirani sensor. The surface of the chip reflects the contact and interaction with the sensed gas and the volume reflects the thermal resistance of the device and therefore the response time.

A heated SAW chip in vacuum will show a resonance frequency shift that varies linearly with the temperature and can therefore be correlated to the pressure. This transducing principle allows to extend the range from 10^{-4} Pa up to 10^5 Pa.

For SAW Pirani sensors, wireless interrogation was introduced followed by wireless heating [11]. Different frequencies were tested, among which the 433 MHz and 2.45 GHz ISM bands. However, the developed devices had response times in the order of 1000 s which was a significant drawback compared to conventional capacitive or resistive gauge technologies. The sensor response time depends mainly on its thermal inertia. Miniaturisation is therefore of interest to the efficiency of the measurement. The SAW-Pirani devices presented in the literature showed promising results in terms of sensing range and wireless operation but are still relatively bulky, require a lot of embedded electronics and have poor response time. Moreover, the models presented use no gas kinetic theory and the thermal model is decoupled from the wave model.

SAW-Pirani sensors still have many features that could be improved. There is room left for significant progress in the thermal management (three kinds of heat transfer, radiation by the reduction of the emissivity, the reduction of the thermal contacts which are parasitic heat transfers). Besides, techniques increasing the coupling efficiency all along with device miniaturisation are highly desirable. The present work is a contribution to these.

This was the main motivation to develop a SAW-Pirani sensor for this thesis, which will be elaborated on the next chapters. In the present work, two different measurement techniques will be combined, namely miniaturised Pirani principle and Surface Acoustic Waves.

2.7.1 SAW signal processing

There are different ways to acquire a SAW signal. SAW readers are available off the shelf from companies such as SAW Components (Dresden, Germany). These commercial readers operate only in a predefined frequency and give directly the temperature value for instance. Connecting the SAW device to a Vector Network Analyzer(VNA) allows to extract its frequency response from its scatter parameters. In [9], an interrogator and SAW reader suitable for frequencies between 85 MHz and 6.6 GHz is presented. The device allows the user to set the frequency, power and waveform of the interrogation

signal. The reader developed in the scope of this thesis using a VNA has frequency flexibility between 1 MHz and 3 GHz but no power flexibility, a constant power input of 0.5 dBi. The Radio Frequency Identification (RFID) function allows to identify the chip in the time domain not only in the frequency domain through the resonance frequency. The system presented in this publication is suitable for the designed chip. It has also a plethora of applications. SAW RFID is totally passive and uses pulsed carrier instead of continuous wave as interrogation signal. SAW tags can be read with about 100 times lower power interrogations signals and are 10^5 times smaller in size. They are more robust in high level interference and harsh environments. Experimental results presented compare user defined pulse duration and frequency and measured ones for instance. User parameters available are the carrier frequency, the pulse duration, the silence period, the IQ data and the power of the output interrogation signal. The user can also easily switch between custom waveforms. A SAW reader is made of a transmitting circuit and a receiving circuit. The transmitter circuit sends inquiry pulses to the SAW tag. The receiving circuit demodulates the echo signal received from the SAW tag. The demodulated signal is sampled by high speed ADC and stored in SRAM [68].

SAW RFID is very interesting in terms of energy consumption and power efficiency. SAW RFID readers use low power radio frequency pulses as interrogation signals [9] while other RFID technologies require higher power and continuous request signals.

The reflected SAW pulses return to the IDT and are reconverted into an electrical signal radiated back to the reader by the tag antenna. Each reflector of the tag is placed at a precisely determined position on the chip, that is why each response signal from a SAW tag carries a unique identification code based on the positions of its reflectors. The time delay between two interrogation pulses, also called silence period is set long enough to avoid collision between the response signal from the tag and the next interrogation pulse.

The review paper [69] gives a comprehensive survey of the present state of reader architectures such as time domain sampling (TDS), frequency domain sampling (FDS) and hybrid concepts for both SAW resonators and reflective SAW delay line sensors. Critical performance parameters such as measurement accuracy, dynamic range, update rate, and hardware costs are presented. SAW readers architectures are divided into two categories: time domain and frequency domain. Time sampling also known as wide-band or full band sampling, and frequency domain sampling also known as narrowband or partial band sampling. There are also hybrid architecture concepts such as switched frequency stepped continuous wave (S-FSCW) and pulsed frequency modulation (FM)/amplitude modulation (AM) tracking loops. In [62], a wireless pressure sensor using a Bourdon tube as a primary sensor is proposed. A SAW sensor is integrated on the surface of the Bourdon tube. Due to change in applied pressure a frequency shift is obtained which is transmitted through the antenna of the SAW sensor. This signal is then received by the antenna of the SAW interrogation unit. The sensor shows linear characteristics with respect to the applied pressure. Any portion of the IDT has its equivalent circuit model. The sensing information is extracted from the S_{11} values.

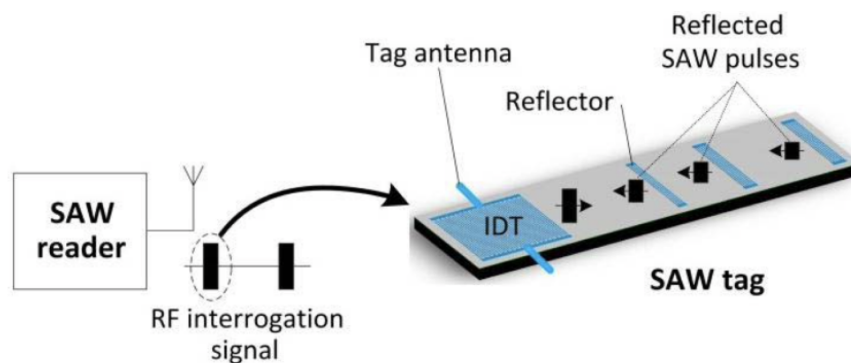
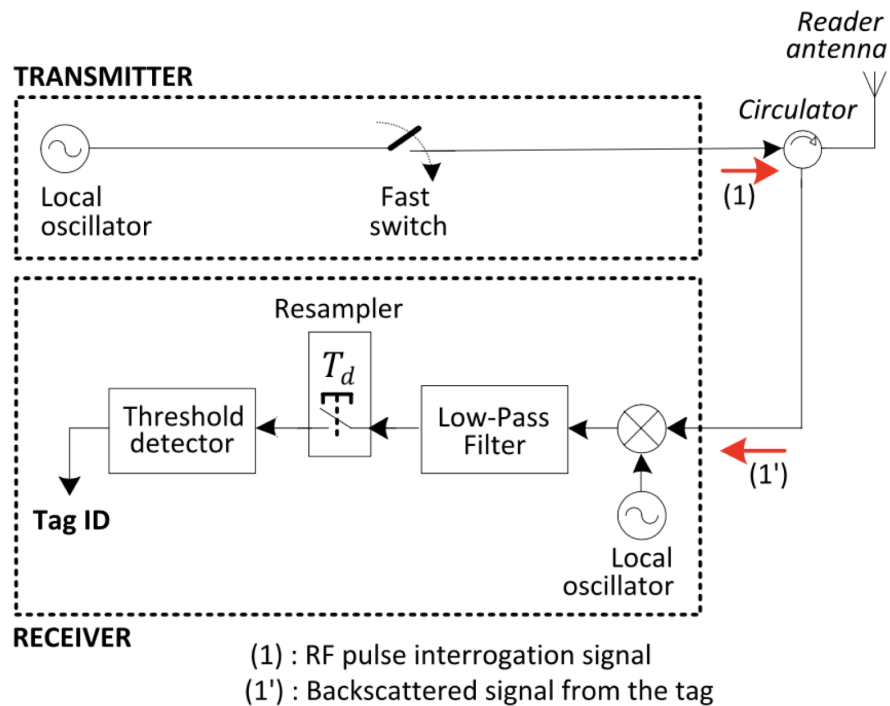


Figure 2.28 – SAW IDT with signal processing circuit from [9].

An operational amplifier can be used to linearise the output signal of a sensor. In [70], a wireless communication network module consisting of an acquisition unit, a wireless control unit and a microcontroller unit is presented. By means of Zigbee and Lora technologies, the module receives and transmits the collected data to a PC work station in real-time. The module can control the sensor array's working mode and monitor the working status. Simultaneously, the testing location is determined by the Global Positioning System (GPS) module integrated into the SAW sensor array. GPSs have been used in wireless sensor networks, enabling the establishment of a wireless sensor communication network to monitor target gases. The components of the detecting and wireless communication system of a SAW sensor array are: the Decision Making User, the Display Platform, the Database Server, the Cloud Computing

Platform, the Server 1, the Application Server 2, the Control Terminal 1, the 8—Database 1, the Database 2, the Cable/Wireless Network, the Control Terminal 2 and the SAW Sensors.

Reference [2] addresses the measurement uncertainty of a sensor. For SAW delay line sensors, the resolution of the measurement is enhanced by phase discrimination. Evaluation of delay from the response signal's envelope only yields a resolution of a few nanoseconds. With phase evaluation, a small time delay corresponding to a phase shift can be detected with a much higher sensitivity. A resolution of 1 degree for phase detection at a 1 GHz frequency corresponds to a time resolution of approximately 3 ps. For a 3 μ s sensor delay interval, the relative resolution is enhanced from 10^{-3} to 10^{-6} , replacing time delay by phase measurement. The actual achieved resolution for the indirectly affected SAW transponders is better than 1% in worst case. In actual systems, errors occur because of the sensor itself, because of the signal processing, and because of external effects from the radio propagation as well as noise and interference. Employing frequency measurement, the relative frequency error $\delta f/f$ can be calculated from the phase error $\delta\phi$. Measurement of one period length is afflicted with an error in frequency of $\delta\phi/2\pi$. If the phase is unambiguous, the number of periods is counted for a time interval T_m , and the relative frequency error is calculated from:

$$\frac{\Delta f}{f} = \frac{\Delta\phi}{2\pi} \cdot \frac{1}{T_m \cdot f} \quad (2.73)$$

In fabrication, tolerances are given to be up to 100 ppm for low cost SAW mass products, representing the accuracy limit for SAW sensors without calibration. For resonant devices, total aging remains smaller than 50 ppm. For delay lines, aging only depends on the almost negligible aging of the crystal substrate and is not specified. This paper offers a detailed uncertainty analysis of SAW signal. [71] reviews non-regenerative and regenerative power supply systems with special emphasis on piezoelectric energy harvesting systems. Besides, the wireless sensor module TICCC2530 TE CORE RF from Micro-pelt Technology can perform 10 degrees temperature difference measurements and radio transmission every 2 s. A software application tracks power, temperature and voltage. Its energy consumption is lower than 90 μ W.

2.8 Microfabrication technologies

In the following sections the technologies for realisation of the components of the sensor developed in this thesis are outlined. These encompass technologies for fabrication of the sensor chip, its electrical connection and its packaging. The technologies presented here are:

- electron beam lithography
- sputtering

- wirebonding
- polymer packaging

These are of course not the only available manufacturing technologies. The interested reader can refer to the book [72] by Marc Madou for a more detailed overview.

Electron Beam Lithography

The sensor chip contains Aluminum electrodes on its top surface. These electrodes form the Interdigital Transducer and are responsible for the generation and the transmission of SAW on the chip surface. The dimensions of the electrodes determine the frequency of the SAW. Since the operating frequency is 2.45 GHz, the thickness of one electrode is 50 nm, the pitch is 400 nm and the length of one electrode is around 100 μm . The technology used to generate the electrode structures is the Electron Beam Lithography.

Electron beam lithography is a direct writing technique that uses an accelerated beam of electrons to pattern features that have been coated with an electron beam sensitive resist. The primary advantage of electron beam lithography is that it can write custom patterns with a resolution lower than 10 nm.

An Electron Beam Lithography system uses hardware similar to a Scanning Electron Microscope (SEM) to guide a nanometer sized focused beam of electrons to form a latent image in a layer of resist. A focused beam of electron is scanned across a substrate covered by an electron-sensitive material, a resist that changes its solubility properties according to the energy deposited by the electron beam [73].

Exposure to the electron beam changes the solubility of the resist, enabling selective removal of either the exposed or unexposed areas of the resist by immersing it in a developer.

The result of this exposure is to render the resist either more soluble (called a positive tone resist) or less soluble (negative tone resist) in a suitable developer solution. The resulting pattern is then transferred via etching or by depositing other materials.

There is almost always a difference between the digital line width in a pattern and the actual developed feature size after processing. This comes about from electron scattering in the resist. For a well-characterized process, there is generally a fixed difference between the digital size and the actual size, known as bias. This can be implemented by altering all the sizes in the design as appropriate.

Sputtering

Sputtering was used to manufacture a heating resistive layer on a chip. The source material is called the target and the emitted atoms or molecules are said to be sputtered off. To perform sputtering, the target material and the substrate are placed in a vacuum chamber. A voltage is applied between them so that the target is the cathode and the substrate is attached to the anode. A plasma is created by ionizing a sputtering gas (generally a chemically inert, heavy gas like Argon). The sputtering gas bombards the

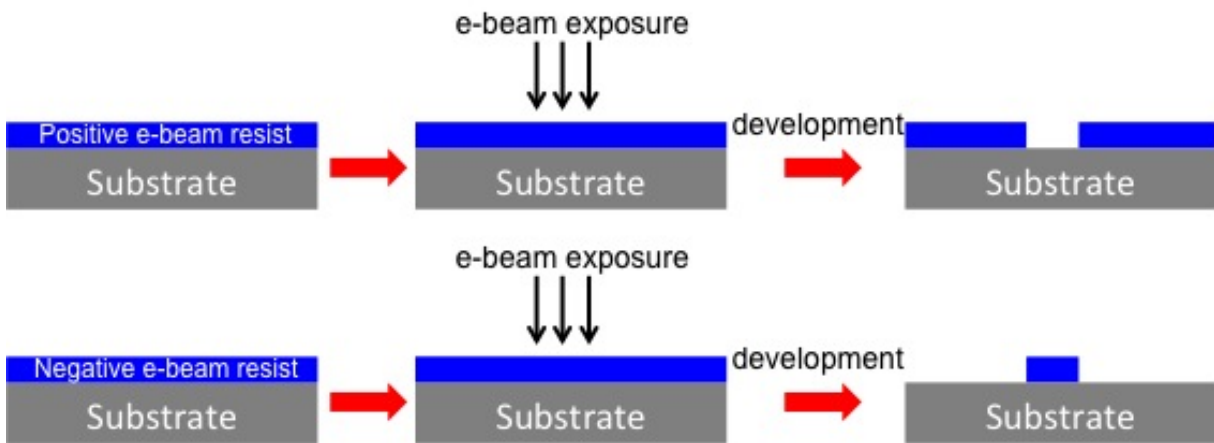


Figure 2.29 – Schematic of the electron beam lithography process. Picture retrieved from [74].

target and sputters off the material aimed to be deposited. Figure 2.32 shows a schematic of the sputtering process.

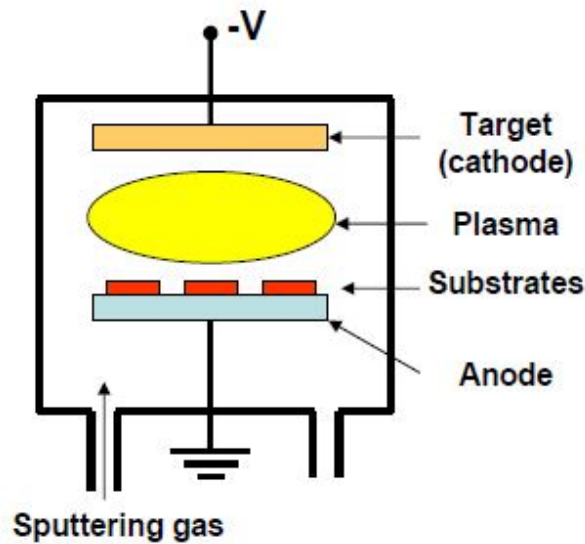


Figure 2.30 – Schematic of the sputtering process.

In order to have a self-sustaining plasma, each electron has to generate enough secondary emissions. Since collisions are desired, the pressure can not be too low. The mean free path should be a tenth or less than the typical size of the chamber. Sputtered atoms from the target make their way on to the substrate through diffusion. Ions and neutralised gas atoms may also embed on the substrate as impurities. The ions incident on the substrate may also re-sputter the surface. Chemical reactions may occur.

Wirebonding

Wirebonding is a process for making interconnections between an integrated circuit (IC) and its packaging [75]. In this thesis, wirebonding was used to connect the sensing chip with the rest of the sensor components. Wirebonding is a back-end process done at the chip level with high reliability and high precision up to $5\ \mu\text{m}$. It is considered as the most cost-effective and flexible interconnect technology available [75]. Wires are bonded using heat, pressure and ultrasonic power. There are two main classes of bonders: ball-bonder and wedge-bonders. Figure 2.31 shows a schematic of ball-bonding. The wires can have a diameter between $10\ \mu\text{m}$ and a few hundreds of micrometers. Wires can be in Gold, Aluminum, Copper and Silver electrically insulated or non insulated.

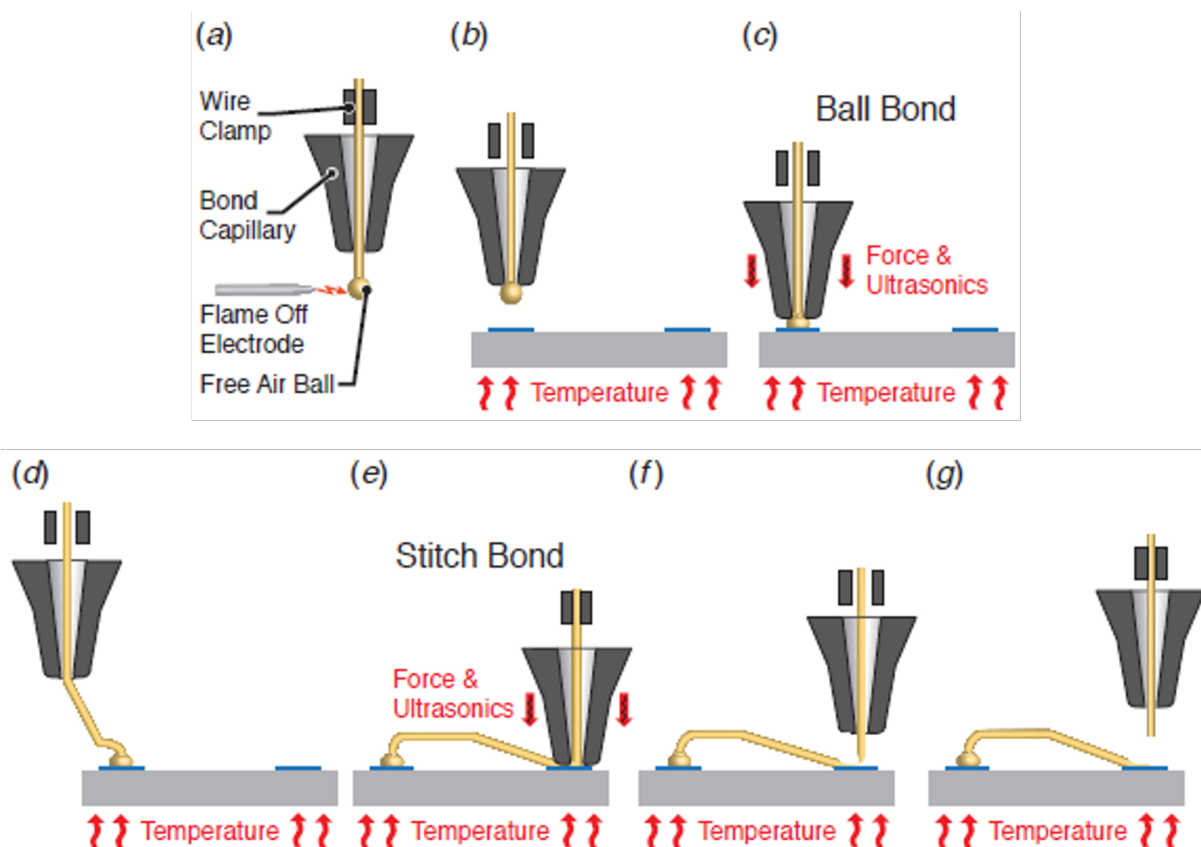


Figure 2.31 – Schematic of ball-bonding process. From [76]

Packaging

Packaging is important to protect the sensor system components from the surrounding environment. Packaging is responsible for the durability and the resistance of the sensor. Several technologies are available for manufacturing. They are subdivided in additive manufacturing and subtractive manufacturing.

For polymer packaging with dimensions in the mm range, which is the solution developed in this thesis, conventional milling remains a suitable choice for rapid prototyping first and later on for serial production.

The milling process uses rotary cutters to remove material. The rotation velocity is usually between 10^3 and 10^5 rpm. It has a resolution down to $50\ \mu\text{m}$ with tolerances up to $1\ \mu\text{m}$ and is compatible with all polymer materials.

It is performed via Computer Numerical Control (CNC). It is low cost and customisable. However, there is limited flexibility to complex shapes, the tool are damaged easily and heat fractures can occur during the process [75]. Other packaging technologies include notably Electrical Discharge Machining, Water Jet Cutter or Laser Machining.

Printed Circuit Board Technology (PCB) mechanically supports and electrically connects electronic components using conductive tracks, pads and other features etched from copper sheets laminated onto a non-conductive substrate [75].

The electrical components usually involved are Surface Mount Devices (SMD), such as capacitors, inductors, resistors, integrated circuits.

The board can have one, two or multiple copper layers. The electrical connection between layers is performed using Vertical Interconnect Access. Typical dimensions for line spacing are $75\ \mu\text{m}$, $10\text{--}100\ \mu\text{m}$ for metallisation thicknesses.

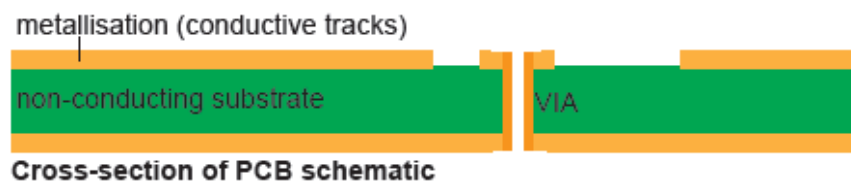


Figure 2.32 – Schematic of PCB cross-section. From [75].

PCB manufacturing costs are low compared to semiconductor substrates for instance and they do not require clean room processing. However, they are sensitive to temperature[75].

In [10], which is the reported Pirani sensor that reaches the smallest vacuum pressure in the high vacuum range, the heating resistor consists of a membrane suspended by 4 beams of $70\ \mu\text{m}$ width and $746\ \mu\text{m}$ length. The chip has a $3\ \text{mm}$ by $3\ \text{mm}$ surface. The membrane material is Silicon Nitride. The heater is a Nickel thin film resistor patterned by lithography. In addition to that, a $100\ \text{nm}$ thin film gold is deposited on both sides of the membrane area to reduce radiative heat transfer. The sensing range of the chip is 1.33×10^{-4} to $1332\ \text{Pa}$. A silicon microbridge acts as a heat sink in the same way as the microchannel in our case. Two different gas gaps are available on top and at the bottom of the chip. The top gap is $50\ \mu\text{m}$ thick and the bottom gap is $300\ \mu\text{m}$ thick.

2.9 Vacuum considerations

This section gives an overview of some best practices based on experience about some vacuum specific phenomena. [77] assesses the outgasing of certain materials in vacuum. Teflon (PTFE) does not outgas in high vacuum. The materials were tested up to ultra-high vacuum (10^{-10} Pa range). The main gases evolved by a sample of extruded Teflon were H_2O , CO and CO_2 . The outgassing from Hialvac glaze and machined Teflon was below the detectable limit. This is why PTFE was selected as a packaging material for our sensor.

In [64], to determine the sensitivity of the device close to the Knudsen regime, the ultimate pressure of the pump was maintained during the whole experiment. The power injected in the heating resistor was increased by threshold. For each threshold, after the thermal equilibrium was reached and the temperature computed, the pressure was varied by a few tenths of Pa. The relative frequency shift generated by this threshold was measured and the ultimate pressure reinstalled. The sensitivities of the device for each threshold were extracted. This article proposes a protocol for the characterisation of a wireless SAW-Pirani sensor in vacuum, which helped us during the characterisation of the prototype in vacuum.

In [78], several low pressure gauges are compared. An uncertainty analysis is presented. The most important source of noise identified was the short term random noise. The short term random noise creates instabilities in zero-pressure readings. Another source of uncertainty is, for heated gauges, thermal transpiration at absolute pressures below 100 Pa. At higher pressures performance is limited by long-term shifts in calibration with time (months to years). Random noise limits the smallest pressure change that can be resolved by a transducer. A measure of the noise-limited pressure resolution is given by twice the standard deviation of repeated readings at a stable pressure. The resolution of different transducers tends to scale linearly with their full scale range. The CDGs have a resolution of about 1 part in one million of full scale (FS) range, quartz based transducers about 1 part in one million to 3 parts in one million of FS and MEMS-type transducers at about 4 parts in one million to 10 parts in of FS. Because of their availability with lower FS ranges, CDGs have the best absolute pressure resolution among the transducers. The zero instabilities in transducers manifest themselves primarily in two ways. They appear either as zero shifts that correlate directly with changes in room temperature, or as zero drifts that vary randomly in both sign and magnitude and are probably due to drifts in electronics and/or mechanical structure of the gauge. This article gives insight about the various sources of noise and uncertainties for pressure sensors and easy ways to calculate them with available measurement data.

A PhD thesis by Ruellan [79] proposes to use the transient regime to reduce response time of thermal conductivity pressure gauges. Using AC signal increases the sensitivity by reducing the noise. Reducing the noise also comes with a reduction of drifts. This can be seen by applying pressure thresholds to the sensing device. The omega method is used to determine thermal conductivity. The small response time can be measured by applying a step current to a nanowire and observing the voltage output. A simple nanowire has a resistance in the range of $k\Omega$. The capacitance of a coaxial cable is in the range of 100 pF. For a 1 m cable of 20Ω , the characteristic response time is $2 \mu s$. This time is close to the thermal

response time of the device. The cabling used for signal acquisition impacts the response time in the μs range. The response time depends on pressure. This thesis identifies the parameters that impact the most heat transfer based pressure sensors.

3 Modelling and Simulation

To design a new improved SAW-Pirani sensor system, a model for the sensing principle and how the sensing signal comes from was built in order to optimize the sensing behaviour afterwards. For this purpose, the Pirani principle was simulated in Matlab using the modelling equations available to identify the key sensitive parameters. Then the geometry of an infinite periodic SAW sensor was taken to model and simulate its thermal behaviour and its response to pressure variations. Later, a first design of the complete sensor was prepared in COMSOL to see the thermal behaviour response to pressure variations between 10^{-4} Pa and 10^5 Pa.

3.1 Matlab simulation of the Pirani principle

Several equations and models that describe the process of the Pirani sensor are available in the literature. Some of these equations were implemented with the Software Matlab in order to perform a parameter sensitivity analysis. The Matlab code developed to compute the curves presented in the following is available in 9.1.

3.1.1 Response time

The transient behaviour of a Pirani sensor was modelled in order to estimate the thermal response time. Figure 3.1 shows the temperature of a Pirani wire versus time. It was computed from the article [38] and the equations are presented in 2.4.2. The thermal equilibrium is reached after 0.25 ms. The response time of a commercial Pirani sensor is in the range of 5 to 10 ms [10]. The time constant of the system is proportional to the mass of the sensor, its thermal capacity, the temperature difference between the operating temperature and the ambient temperature and inversely proportional to the heating power. This gives an indication about how the response time can be controlled. The sensitive parameters are the size and the material of the sensor, the heating power applied and the operating temperature.

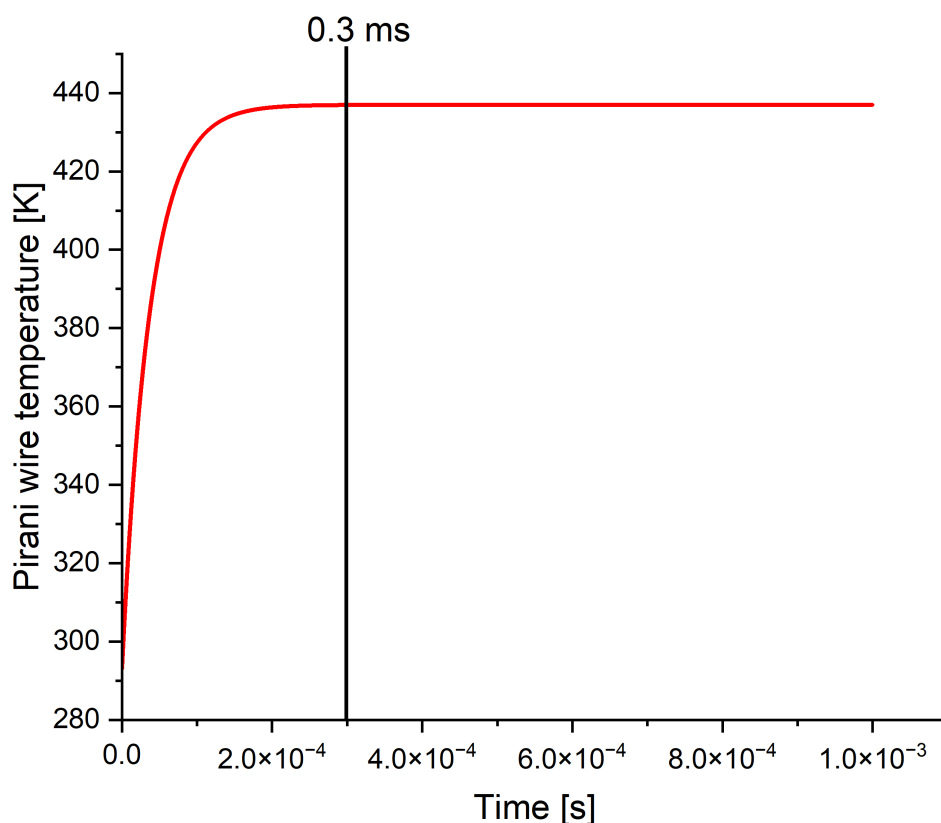


Figure 3.1 – Thermal response of a cylindrical Pirani wire computed from [38].

3.1.2 Initial temperature

The model presented in the paper [36] was used to observe the effect of the initial temperature and of the air gap on the sensitivity of the device. Figure 3.2 shows the thermal conductivity of the gas versus pressure for different initial temperatures.

The initial temperature of the sensor influences the gas thermal conductivity. However, increasing the initial temperature increases the power consumption as well.

3.1.3 Gas gap

Figure 3.3 shows the thermal conductivity of the gas versus pressure for different gas gaps. The gas gap value appears directly in the expression of the gas thermal conductivity as stated earlier in 2.2. A lower gap means a higher value of the Knudsen number.

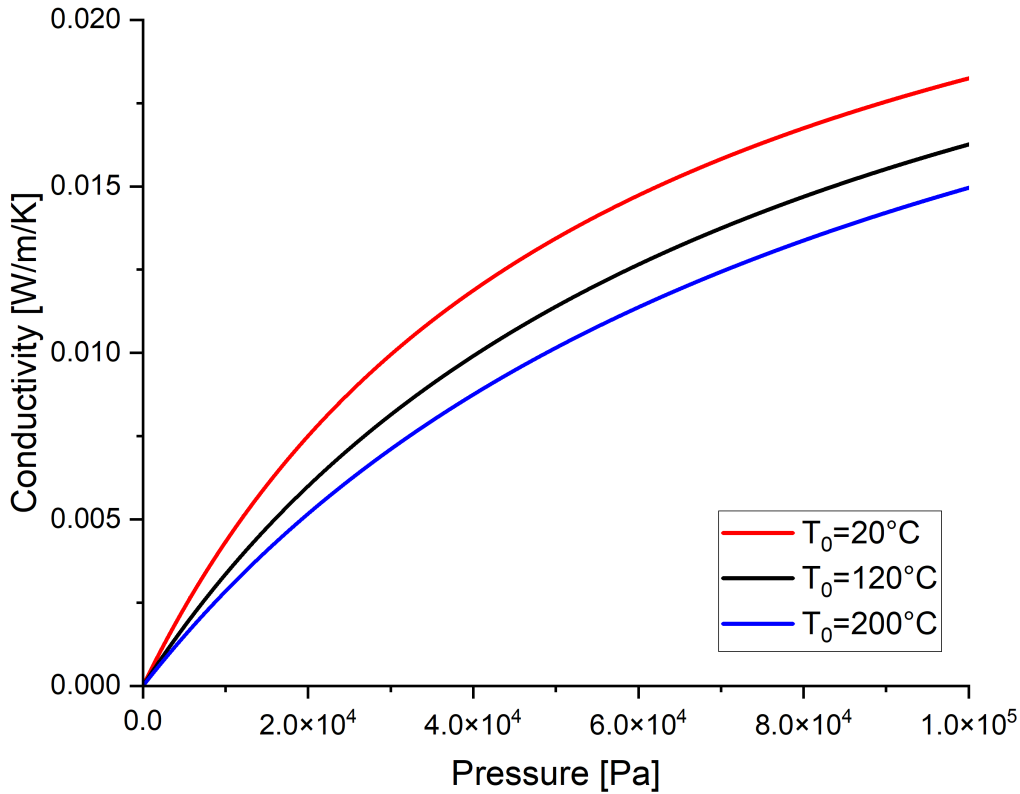


Figure 3.2 – Thermal conductivity of the gas versus pressure for different temperatures from [36].

3.1.4 Gaseous heat transfer over total heat transfer ratio

The articles [10] and [80] present two complementary Pirani sensors that cover the sensing range between high vacuum and atmospheric pressure. The model presented was used to model our own device. The devices presented in [10] are the best sensors available in the literature in terms of performance and sensitivity. Using the equations presented in the papers, many aspects of a Pirani sensor could be analysed.

Figure 3.5 shows the ratio of gas conductance over total conductance versus pressure obtained from [10]. It can be seen that below 0.01 Pa the gaseous conductance represents less than 10% of the total conductance and above 100 Pa it represents more than 99% of the total conductance. Figure 3.4 shows the actual values of the gas conductance and the total conductance computed from [10] as well.

In the rough vacuum region i.e. between 10^4 Pa and 10^5 Pa, the gaseous heat transfer represents more than 99% of the heat transfer balance. Figure 3.5 depicts the same ratio for pressures between 10^{-4} Pa and 1 Pa. In this range, the gaseous heat transfer share rises progressively from less than 1% up to 90%. For a pressure higher than 1 Pa this ratio is higher than 99%.

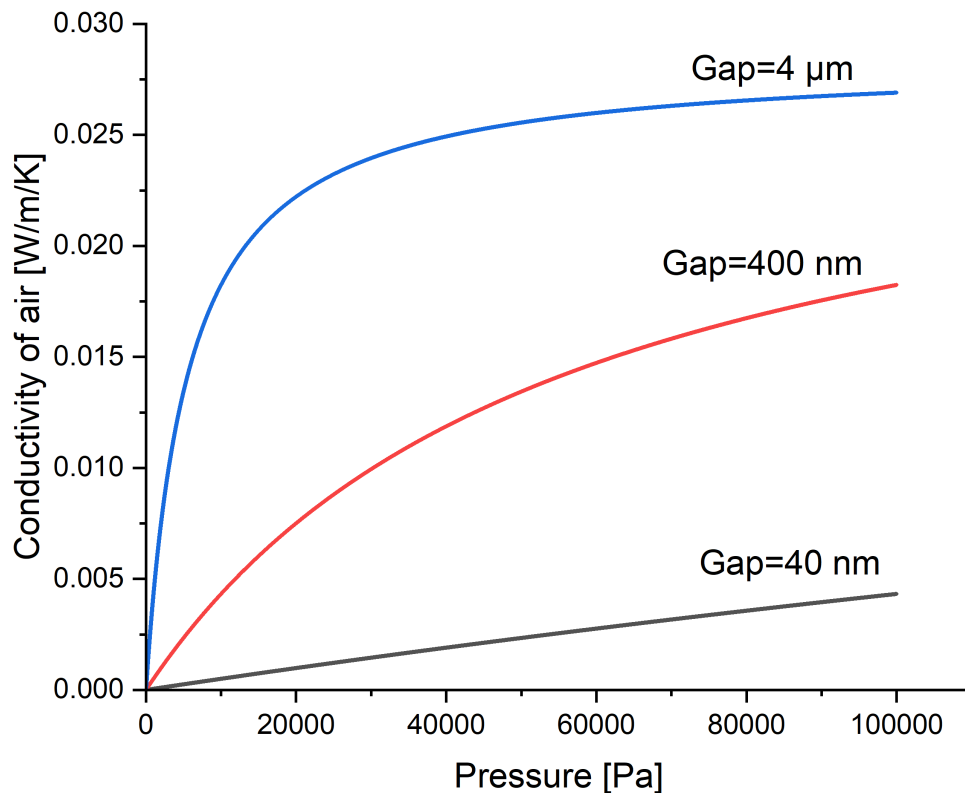


Figure 3.3 – Thermal conductivity of the gas versus pressure for different gas gaps from [36].

3.1.5 Sensor area

Figure 3.6 plots the gaseous thermal conductivity and the total thermal conductivity versus the sensor area from the model presented in [35]. This curve is also an estimation of the signal to noise ratio evolution with miniaturisation. Indeed, miniaturisation is a way to suppress the noise caused by solid conduction and radiation. Besides, to increase the useful signal which is the solid to gas thermal conduction, the Pirani gauge hot surface in direct contact with the gas should be increased.

Figure 3.7 shows the thermal conductivity of the gas versus pressure for different sensor areas. The modelled sensor is the sensor presented in [35]. The modelled areas are the original area of $7.744 \times 10^{-9} \text{ m}^2$ presented in the paper and an area 100 times bigger. For Pirani pressure sensing, the only useful thermal conductivity is the gaseous one, the rest can be considered as parasitic. Reducing the size of the sensor reduces the total thermal conductivity while the gaseous one stays constant. Using a smaller device allows to obtain a higher ratio of useful heat transfer over total heat transfer. The variation of the thermal conductivity with the size shows the interest of the miniaturisation of Pirani sensors. A higher heated

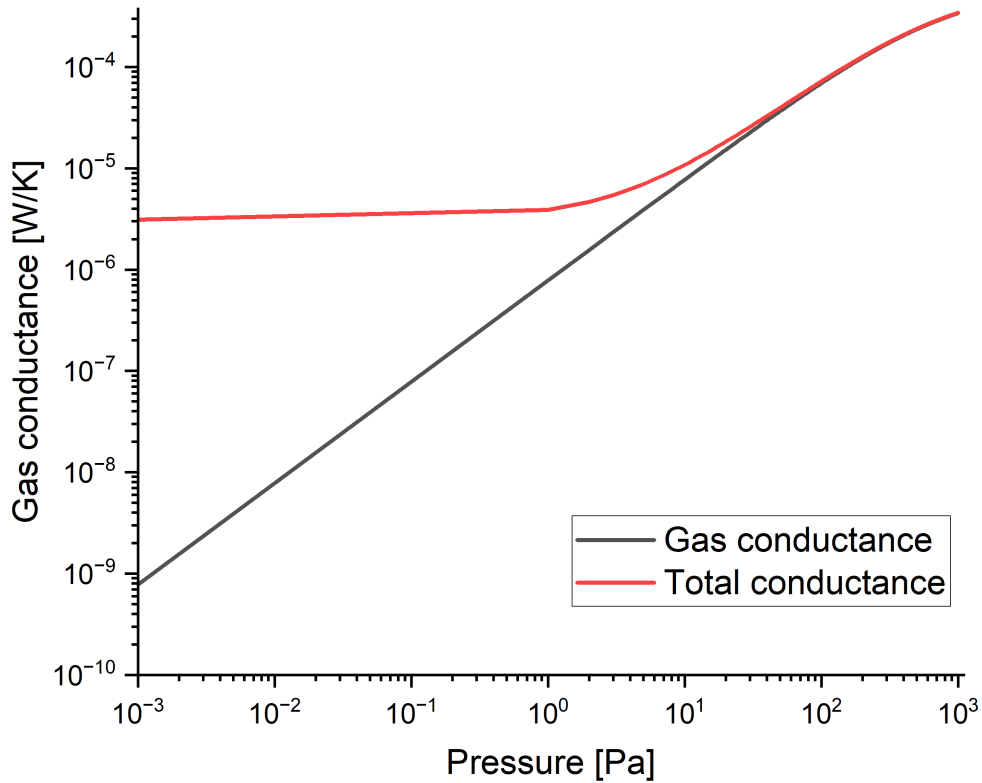


Figure 3.4 – Ratio of gas conductance to total conductance computed from [10].

surface means a bigger heat transfer between the sensor and the measured gas. The gaseous thermal conductivity increases when the sensor area in contact with the gas increases.

3.1.6 Summary

During literature review, several Pirani models were identified. It was deemed relevant to work on and confront the equations and the models to identify the sensitive parameters in order to control and improve the sensing range and the sensitivity.

Some models consider the three different kinds of heat transfer such as [10], while others consider the signal heat transfer only and neglect the rest such as [37]. Neglecting the radiation and solid conduction in the analysis curtails the operating range and the sensitivity of the sensor.

The parameters that increase the gas thermal conductivity at low pressure are the surface of the sensor and the gas gap which corresponds to the surface to volume ratio. The accommodation coefficient of the gas influences the value of thermal conductivity but no equation is available to calculate it for a Pirani

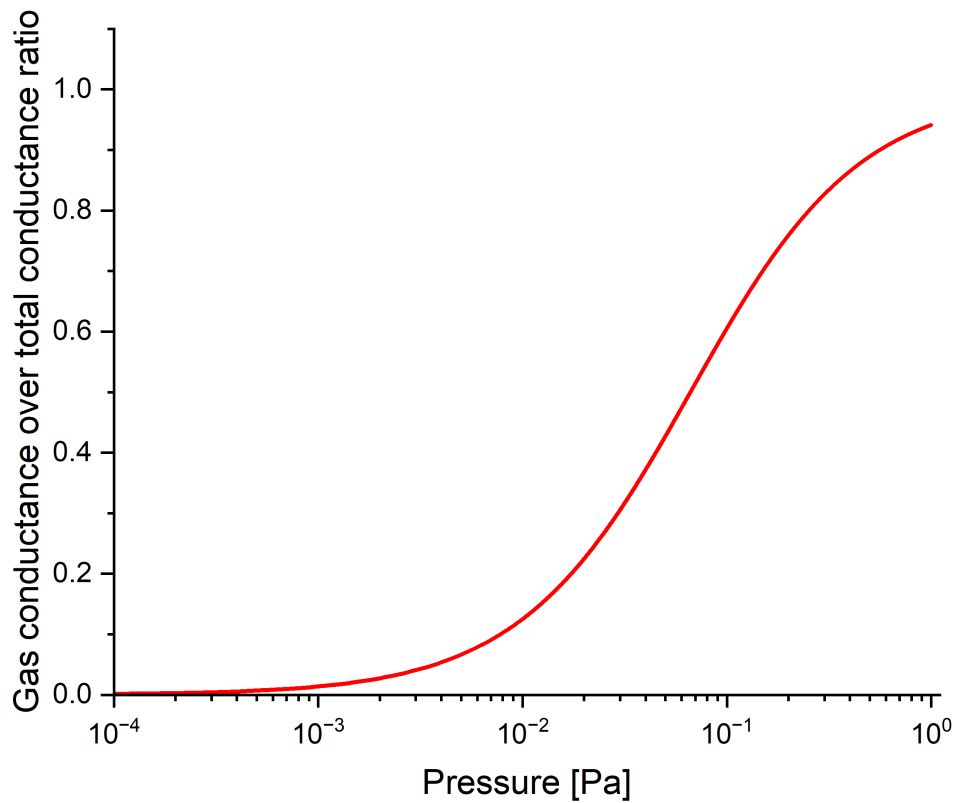


Figure 3.5 – Ratio of the gaseous heat transfer over the total heat transfer in a Pirani sensor in high vacuum computed from [10].

sensor that is why the values taken are all empirical. The article [28] uses MEMS Pirani sensors to calculate their accommodation coefficient with precision.

Besides, the solid conduction and radiative parasitic heat transfer can be reduced by applying some extra processes on the sensor. The surface emissivity of the sensor can be reduced via an appropriate coating such as carbon black coating [81]. The solid conduction of the sensor can be mitigated by reducing the size of the physical contact between the sensing device and its housing [10] or by applying an insulating silicon carbide layer between the Pirani gauge and the sensor core.

3.2 Simulation of the thermal behaviour of a Surface Acoustic Wave sensor

In order to identify the key sensitive parameters of a SAW sensor with respect to the sensed environment, an infinite periodic sensor was modelled in COMSOL and several parameters were varied. The effect

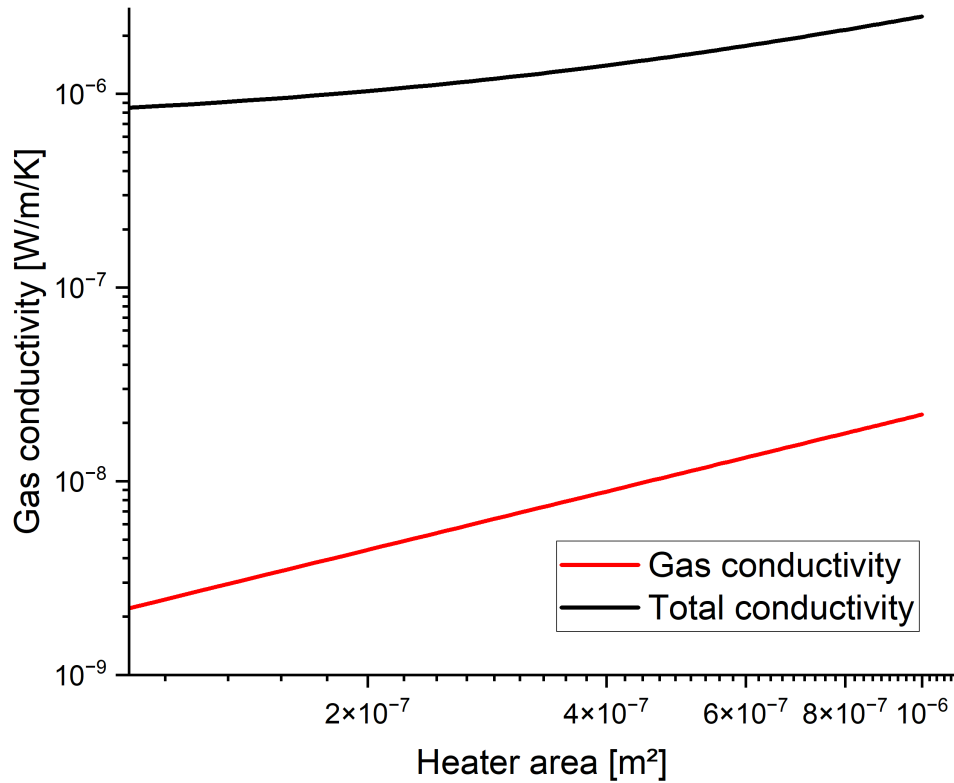


Figure 3.6 – Gaseous thermal conductivity and total thermal conductivity versus sensor heated area. Computed from [35]

of each parameter on the thermal response and pressure sensitivity of the device is presented. The sensor modelled was a basic pair of IDT electrodes on a piezoelectric substrate covered with a coating. A column of nitrogen at low pressure was on top of the sensor and a wall modelled the channel. This sensor was assumed to be an infinite periodic sensor. The model is inspired from a COMSOL tutorial for SAW sensors and is shown in Figure 3.8. The model presented here is purely theoretical and was only used to identify key parameters to improve a SAW-Pirani sensor performances.

The top of the wall is subject to air convection with a coefficient $h = 5 \text{ W m}^{-2} \text{ K}^{-1}$. The left and right of the sensor are insulated. The heating power qb is supplied from the bottom of the sensor. Firstly, a thermal simulation was performed to see the behaviour of the sensor at low pressure (10^{-4} Pa to 1 Pa). The pressure variation was input into the software by changing the thermal conductivity of the gas. The thermal conductivity of the gas was calculated using a formula established by Völklein et al. in [10] and is expressed for low pressures as:

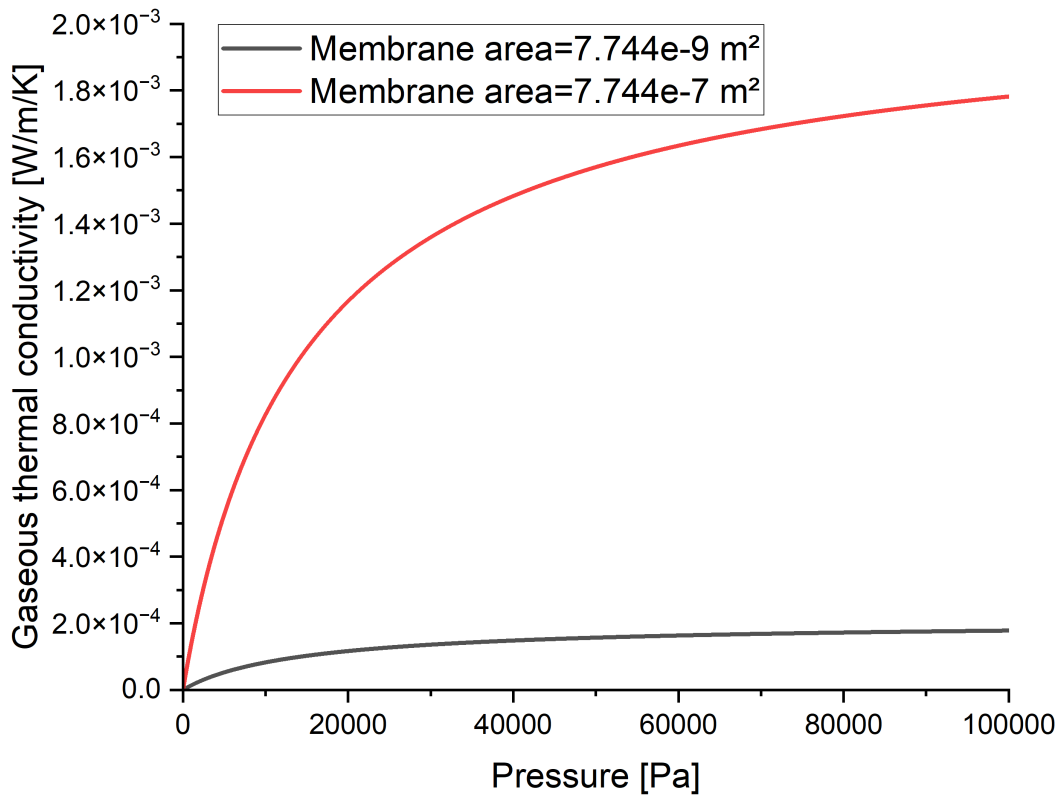


Figure 3.7 – Gaseous conductivity for different heater areas computed from [35]

$$\lambda(p, d) = 92 \frac{W}{mK} \cdot \frac{pd}{m \cdot \text{Torr}} \quad (3.1)$$

with:

p – pressure in Torr

d – distance between the hot sensor and the cold ambient surface

Above 100 Pa another method has to be applied to calculate the mean free path. The values of pressure dependent thermal conductivity of nitrogen input in COMSOL are shown in Table 3.1.

The initial model was tuned to have a response time within 1000 s and a final temperature within 400 K. Then each of the geometric parameters, the power supply, and the emissivities of the radiating surfaces were varied to see their influence on the performances of the sensor.

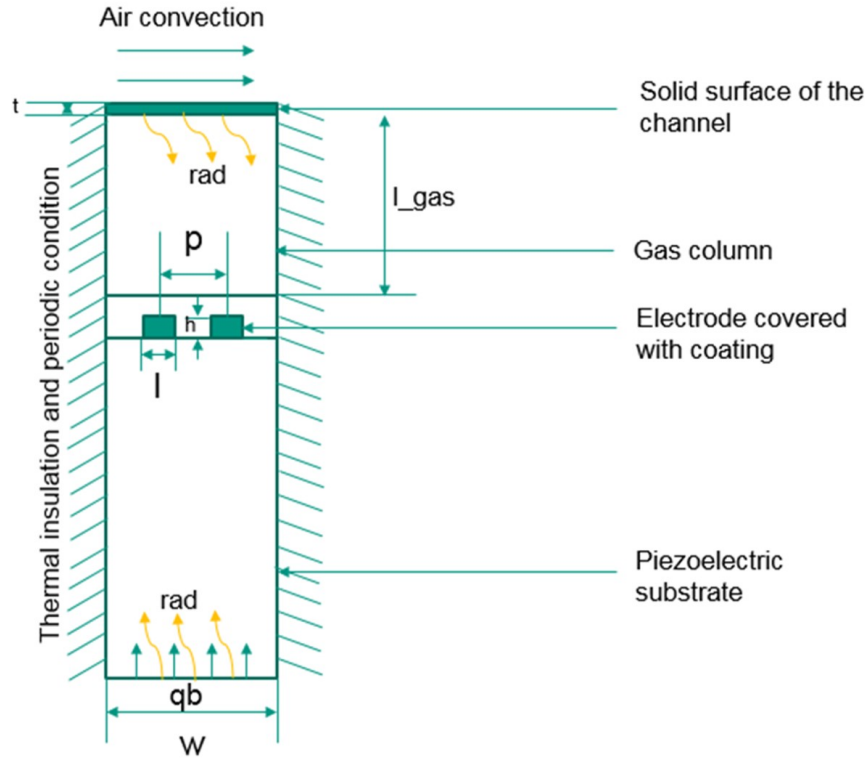


Figure 3.8 – Model used for the parameter sensitivity analysis. From [82].

Table 3.1 – Computed thermal conductivity of nitrogen.

Pressure in Pa	Thermal conductivity in $\text{W m}^{-1} \text{K}^{-1}$
10^{-4}	10^{-7}
0.001	7×10^{-7}
0.01	6.9×10^{-6}
0.1	6.91×10^{-5}
1	6.91×10^{-4}

Effect of the emissivity of the substrate

For this model the emissivity of the substrate was varied and the thermal response observed at the minimum pressure which is 10^{-4} Pa. The tested values of emissivities are shown in Table 3.2 at a pressure of 10^{-4} Pa with their relevance. The final temperature and response time are influenced by the emissivity value. Figure 3.9 shows the thermal response for the substrate emissivities tested.

The emissivity sensitivity analysis shows interesting results. Surprisingly, the smallest possible emissivity increases considerably the response time and final temperature. Higher values of surface emissivities (between 0.1 and 0.4) might be more desirable in terms of response time and final temperature and are

Table 3.2 – Substrate emissivities tested.

Emissivity value	Observation
0.01	minimum possible emissivity of carbon black coating
0.2	1.25°C temperature difference between 10^{-4} Pa and 10^{-3} Pa
0.3	1.94°C temperature difference between 10^{-4} Pa and 10^{-3} Pa
0.4	3.5°C temperature difference between 10^{-4} Pa and 10^{-3} Pa
0.75	Lithium Niobate emissivity

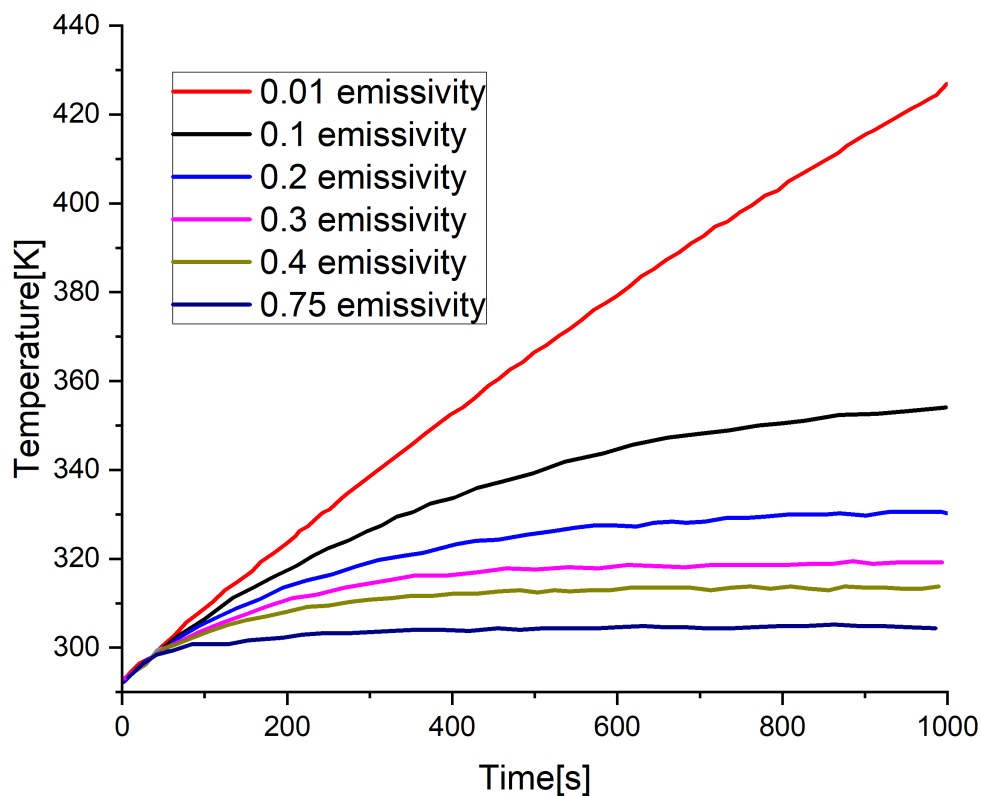


Figure 3.9 – Thermal response of the infinite periodic sensor at 10^{-4} Pa for substrate emissivities of 0.01, 0.1, 0.2, 0.3, 0.4 and 0.75.

easier to achieve. The temperature differences obtained for the relevant surface emissivities are mentioned in Table 3.2. A difference of temperature of 2°C between the final temperatures for 10^{-3} Pa and 10^{-4} Pa should be enough to have a good precision at this range of pressures. Figure 3.10 shows the thermal response at different pressures for an emissivity of 0.4.

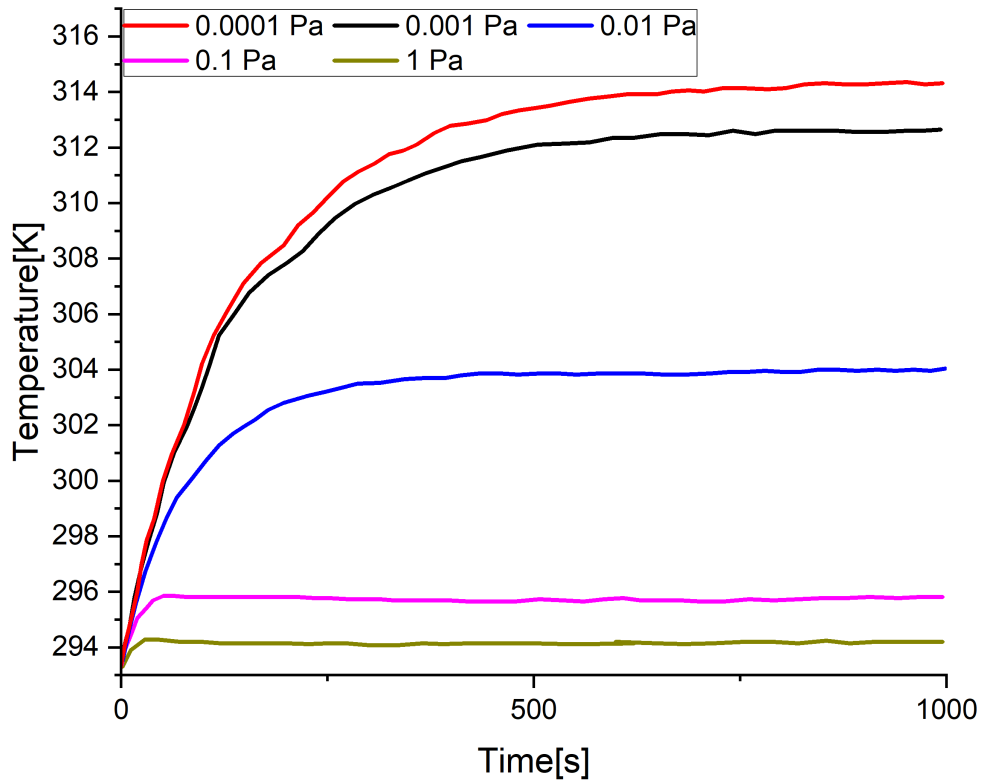


Figure 3.10 – Thermal response at different pressures for an emissivity of 0.4.

Effect of the substrate thickness

The thickness of the SAW chip was then varied. The substrate thicknesses tested were $5\ \mu\text{m}$, $10\ \mu\text{m}$, $15\ \mu\text{m}$ and $20\ \mu\text{m}$. The thickness of the substrate affects the surface to volume ratio of the sensor and therefore the response time. The thickness should be the lowest possible. Attention has to be paid nonetheless to the sensor's fragility and to the manufacturing constraints. A thickness lower than $5\ \mu\text{m}$ cannot be manufactured in practice and would be too fragile. The curves above correspond to pressures of $10^{-4}\ \text{Pa}$ which correspond to the maximal response time observed. For higher pressures, the response time is lower. When the thickness increases the response time and the final temperature increases due to an increase in the thermal capacity. No significant impact on the sensitivity of the device could be observed. Figure 3.11 shows the thermal response of the model for the different thicknesses tested.

Effect of the length of the gas column

The length of the gas column l_{gas} i.e. the gas gap was also varied. However, its variation implies a modification of the thermal conductivity and the flow regime which means the Knudsen number. The values of l_{gas} tested were $25\ \mu\text{m}$, $100\ \mu\text{m}$ and $1000\ \mu\text{m}$. Figure 3.12 shows the obtained results.

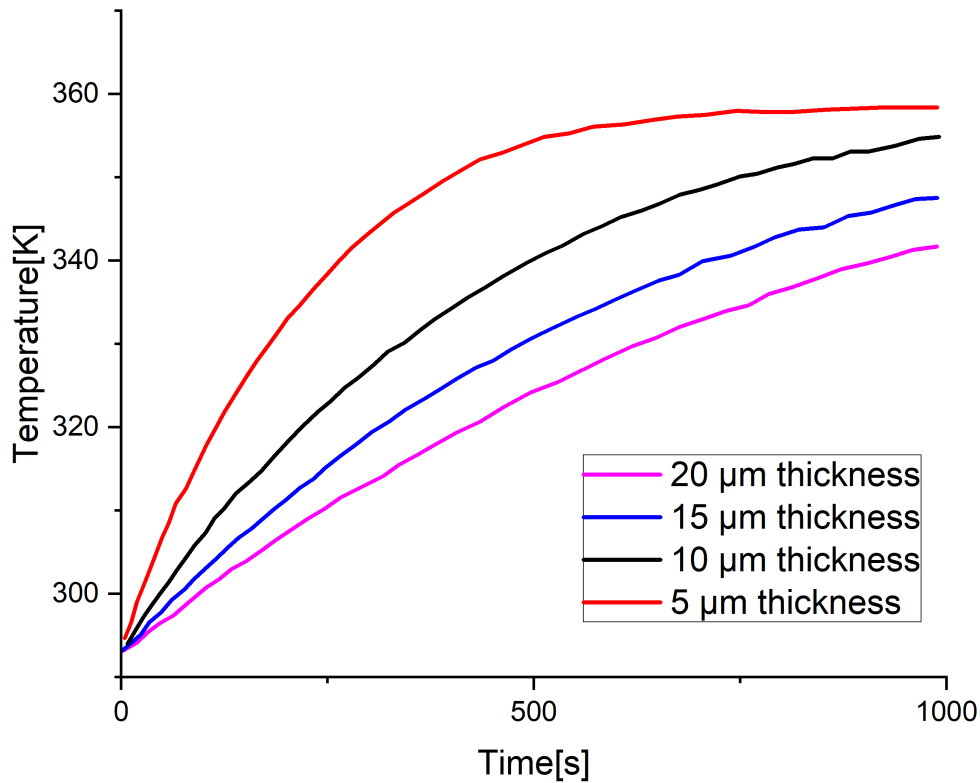


Figure 3.11 – Variation of the SAW substrate thickness.

The value of l_{gas} influences the equilibrium temperature and the response time. When the gas column increases the amount of gas to heat rises therefore the response time rises. The steady state temperature rises as well when the gas column gets bigger. The heat generated by the sensor is aimed to be dissipated in a minimum distance. The thickness of the Knudsen layer has therefore to be calculated. The Knudsen layer thickness is 1.43 m for a pressure of 10^{-4} Pa. The Knudsen layer has the same order of magnitude as the mean free path. The gas gap will always be within the Knudsen layer. The values of the computed thermal conductivities for different sizes of the chamber are depicted in Table 3.3.

Effect of the channel emissivity

The sensor shall be inserted inside a microchannel. For this reason the radiative heat transfer between the sensor and the channel was also simulated. The value of the channel's surface emissivity was varied between 0.1, 0.2, 0.3, 0.4, 0.5, 0.6, 0.7, 0.8, 0.9 and 1. Figure 3.13 shows the obtained temperature response.

The emissivity of the channel's top surface does not influence significantly the final temperature, the response time or the sensitivity at different pressures.

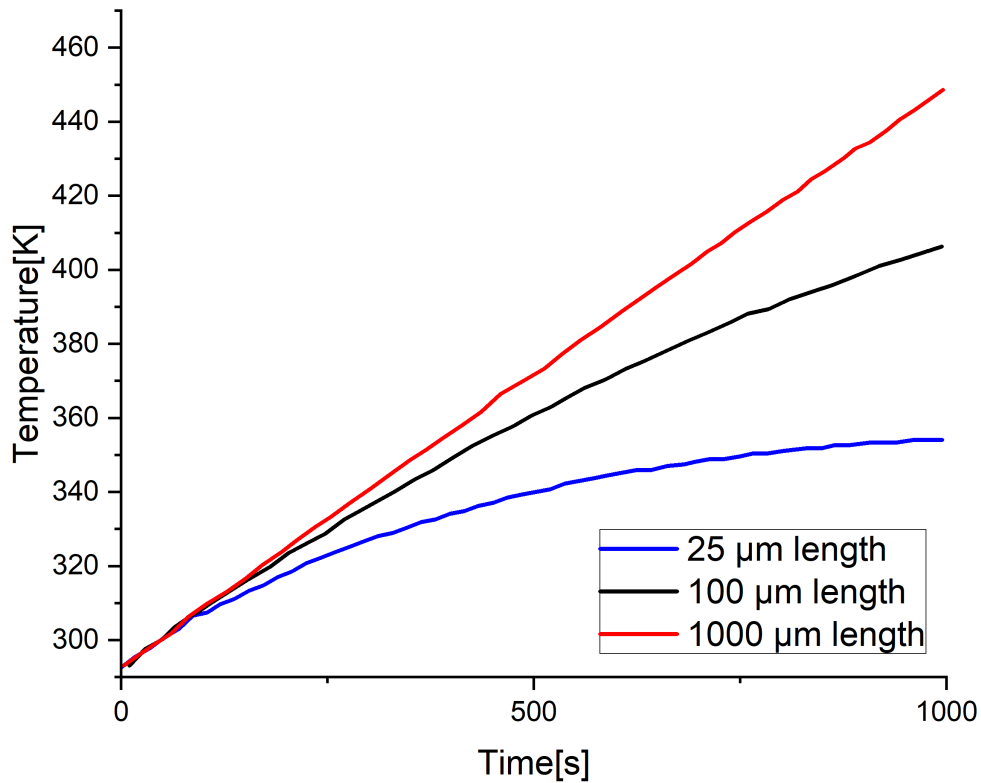


Figure 3.12 – Thermal response obtained for different lengths of the gas column.

Effect of the width of the substrate

The width of the substrate was also varied. The values of the width of the substrate tested were $4\ \mu\text{m}$, $5\ \mu\text{m}$, $10\ \mu\text{m}$, $15\ \mu\text{m}$ and $20\ \mu\text{m}$. This width is the width of one single pair of electrodes. The real width of a sensor chip corresponds to at least the width of one pair of electrodes multiplied by the number of electrodes. Figure 3.14 shows the results of the variation of the substrate width.

The width of the substrate influences the response time and the final temperature. When the width increases, the response time and final temperature decreases. For a thickness of the substrate of $20\ \mu\text{m}$, the final temperature at $10^{-4}\ \text{Pa}$ is $361.38\ \text{K}$ and the temperature at $10^{-3}\ \text{Pa}$ is $357.15\ \text{K}$. The increase of the substrate width is to be seen as an increase of thermal mass of the sensor and therefore an increase of thermal capacity in the heat transfer balance.

Effect of the pitch of the electrodes

The pitch p of the electrodes corresponds to the spacing between the electrodes. The values tested for the pitch were $3\ \mu\text{m}$, $4\ \mu\text{m}$ and $5\ \mu\text{m}$. Figure 3.15 shows the thermal response for these pitch values.

Table 3.3 – Thermal conductivity at pressures between 10^{-4} Pa and 1 Pa for several gas column lengths.

Pressure in Pa	10^{-4}	10^{-4}	10^{-4}	10^{-4}
Gas column length	100 μm	1 mm	100 mm	1 m
Thermal conductivity ($\text{W m}^{-1} \text{K}^{-1}$)	6.91×10^{-9}	6.91×10^{-8}	6.91×10^{-6}	6.91×10^{-5}
Pressure in Pa	10^{-3}	10^{-3}	10^{-3}	10^{-3}
Gas column length	100 μm	1 mm	100 mm	1 m
Thermal conductivity ($\text{W m}^{-1} \text{K}^{-1}$)	6.91×10^{-8}	6.91×10^{-7}	6.91×10^{-5}	6.91×10^{-4}
Pressure in Pa	10^{-2}	10^{-2}	10^{-2}	10^{-2}
Gas column length	100 μm	1 mm	100 mm	1 m
Thermal conductivity ($\text{W m}^{-1} \text{K}^{-1}$)	6.91×10^{-7}	6.91×10^{-6}	6.91×10^{-4}	6.91×10^{-3}
Pressure in Pa	10^{-1}	10^{-1}	10^{-1}	10^{-1}
Gas column length	100 μm	1 mm	100 mm	1 m
Thermal conductivity ($\text{W m}^{-1} \text{K}^{-1}$)	6.91×10^{-6}	6.91×10^{-5}	6.91×10^{-3}	6.91×10^{-2}
Pressure in Pa	1	1	1	1
Gas column length	100 μm	1 mm	100 mm	1 m
Thermal conductivity ($\text{W m}^{-1} \text{K}^{-1}$)	6.91×10^{-5}	6.91×10^{-4}	6.91×10^{-2}	6.91×10^{-1}

For a constant width of the substrate, the value of the pitch does not influence the thermal response of the sensor. This is due to the presence of the coating whose mass and thermal capacity has more influence than the electrodes.

Effect of the width of the electrodes

The width of the SAW IDT electrodes was varied. The values tested for the width of the electrodes are 0.3 μm , 0.5 μm , 1 μm , 1.5 μm and 2 μm . The width of the electrode changes the composition of the substrate and hence the thermal conductivity of the top of the substrate. Figure 3.16 shows the thermal response for the widths tested in this model.

When varying the pitch or the width of the electrodes the width of the substrate has to be kept constant to see only the effect of the pitch and the width of the electrode. The width of the electrodes does not influence response time nor final temperature or precision. However, these parameters are important for

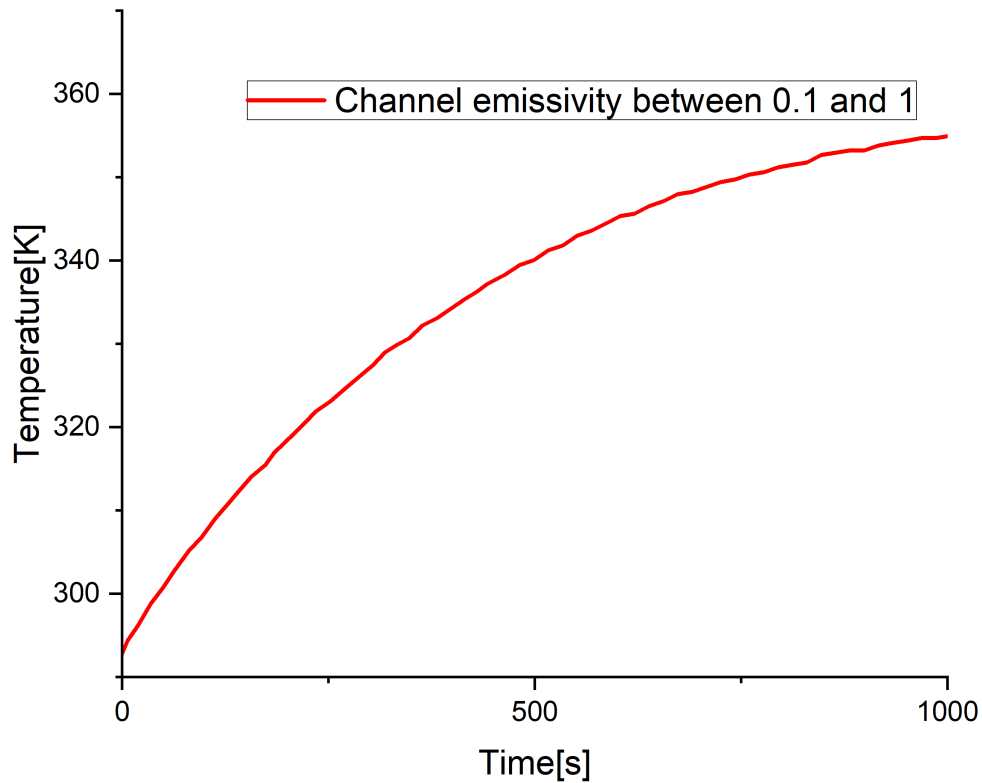


Figure 3.13 – Variation of the microchannel surface emissivity.

the transfer function and signal of the sensor (frequency, scattering parameters). In practice it modifies the wavelength and the frequency of the SAW propagating.

Effect of the presence of a coating

For applications such as specific detection, coating are applied to the metallic electrodes such as Polyisobutylene that absorbs some gases. In the case of a SAW Pirani sensor, the application of a coating would aim to control the surface emissivity value or protect the electrodes against the ambient conditions (corrosion, contamination). The thickness of the coating covering the electrodes was varied between $0.1 \mu\text{m}$, $0.5 \mu\text{m}$, $1 \mu\text{m}$ and $2 \mu\text{m}$. The coatings of $0.1 \mu\text{m}$ and $0.5 \mu\text{m}$ are smaller than the electrodes that is why they show similar behaviour. Figure 3.17 shows the obtained results. $1 \mu\text{m}$ and $2 \mu\text{m}$ show similar response times and equilibrium temperatures. A coating of $0.5 \mu\text{m}$, $1 \mu\text{m}$ or $2 \mu\text{m}$ according to manufacturing capabilities should be enough. Coatings of $1 \mu\text{m}$ and $2 \mu\text{m}$ lower slightly the response time and the final temperature. The coating was assumed to have an emissivity of 0.01.

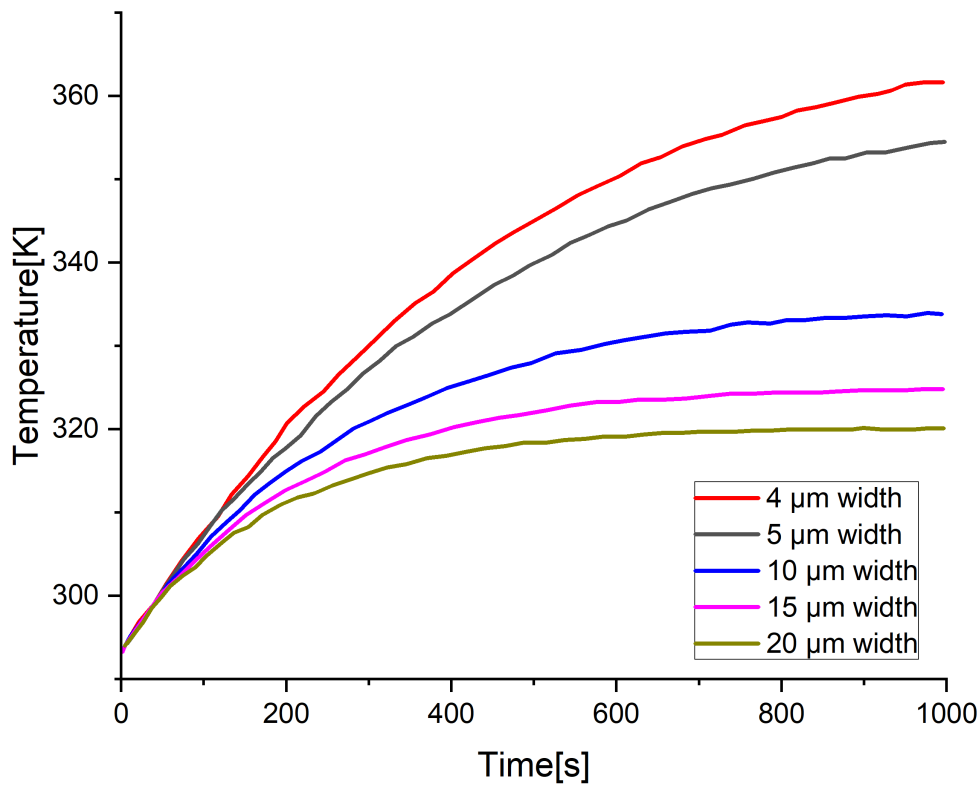


Figure 3.14 – Variation of width of the substrate.

Effect of the height of the electrodes

The height of the aluminum electrodes was varied between $0.1 \mu\text{m}$, $0.2 \mu\text{m}$, $0.5 \mu\text{m}$, $1 \mu\text{m}$ and $2 \mu\text{m}$. Figure 3.18 shows the obtained thermal response. No influence could be observed.

Effect of the thickness of the electrodes

The thickness of the electrodes did not influence either the thermal response of the sensor. It may have no impact in terms of thermal response but the thickness is important in terms of transfer function. The thickness of the electrodes as well as all the geometrical parameters of the electrode are imposed by the nature of the wave and the operating frequency chosen.

Effect of the heating power

In this simulation the heating power (q_b) is supplied at the bottom as a heat flux (in practice we will try to keep it this way as much as possible). There is no real limitation on the maximum amount of the energy supplied but maybe in the minimum amount. The final temperature and the response time are

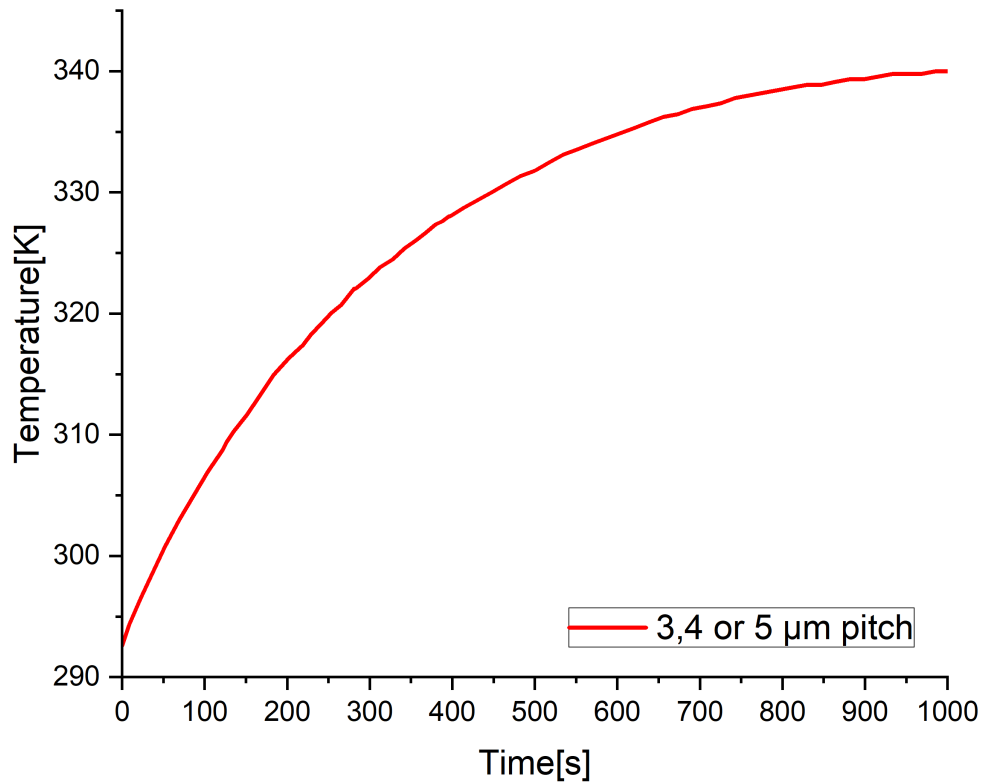


Figure 3.15 – Variation of the pitch of the metallic electrodes.

significantly affected. The nominal amount used for the previous simulations is 15 W m^{-2} . The values of power tested are 0.1, 1, 5, 10, 15, 20, 50 and 100 W m^{-2} . When q_b is high the response time is low. When q_b is high the final temperature is high. The temperature can however not rise indefinitely. Figure 3.19 shows the results obtained.

Summary

The variation of parameters of the simulation allowed to identify sensitive parameters which are:

- power supply: the higher the power the higher the final temperature
- width of the substrate: the higher the surface the higher the contact between sensor and gas
- size of the gas gap: the bigger the gap the higher the contact
- thickness of the substrate: the smaller the thickness, the smaller the response time
- substrate emissivity: the higher the emissivity the lower the final temperature

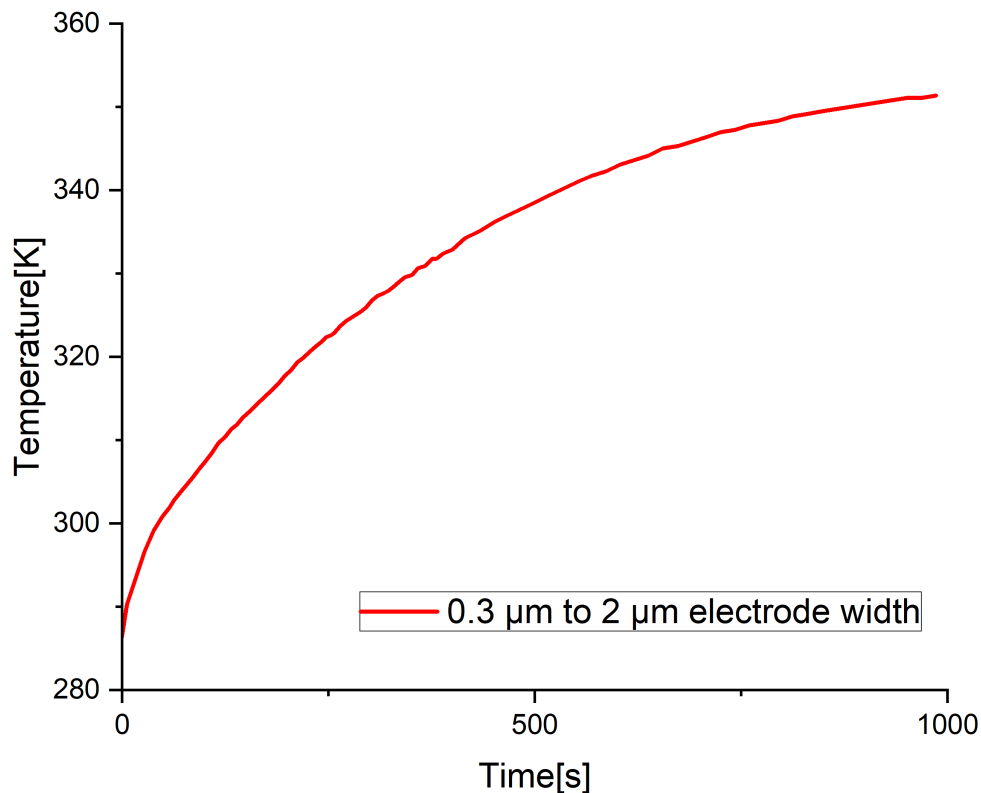


Figure 3.16 – Variation of the width of the metallic electrodes.

The identification of the sensitive parameters was used during the design phase in order to optimise the performances of the sensor. Indeed, only parameters influencing the performances were given priority, which are the length, width and thickness of the chip, while the rest of the parameters was adjusted according to the manufacturing constraints. This COMSOL calculation for an ideal infinite periodic sensor was made to identify the key sensitive parameters. The further sections present simulation of a real design that was used as a starting point for manufacturing.

3.3 Simulation of the packaged sensor in COMSOL

The purpose of the simulation was to model the behaviour of the sensor packaging as a whole and the sensor chip in vacuum. The simulation was used to dimension the sensor's components, i.e. the sensing chip, the microchannel geometry and dimensions in order to increase the sensitivity at high vacuum and close to atmospheric pressure. Several parameters of the simulation were varied in order to identify

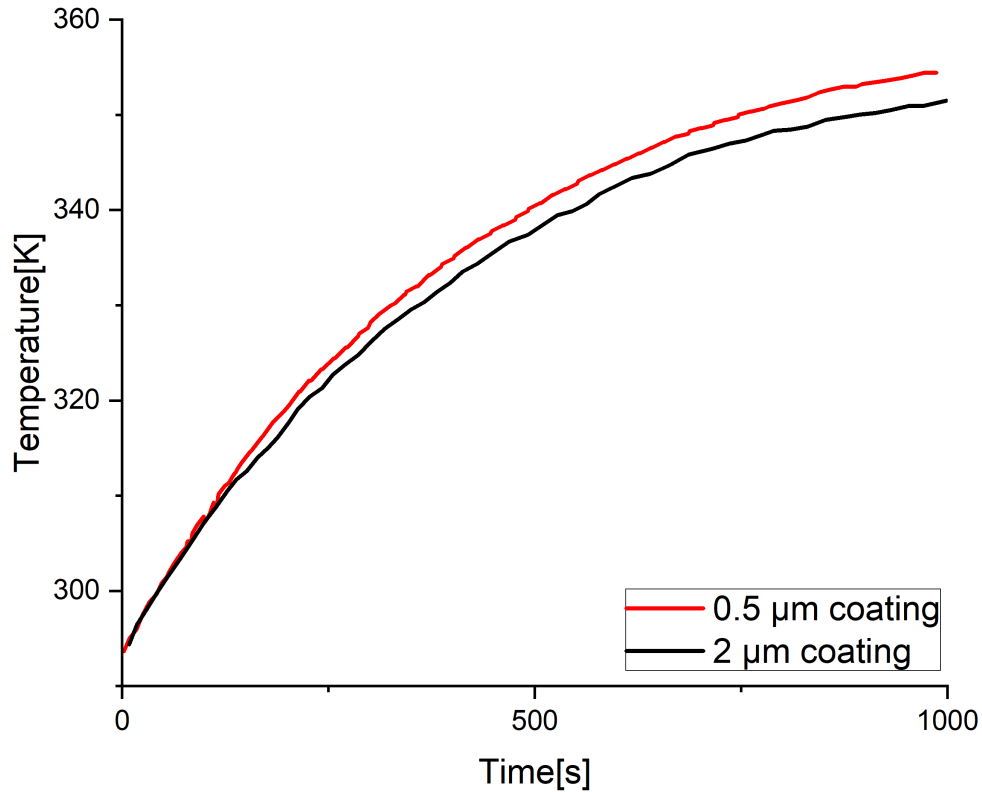


Figure 3.17 – Variation of the coating of the substrate.

the key sensitive parameters that mostly affect the performances of the sensor, i.e. the steady state temperature at different pressures.

3.3.1 Preliminaries

A numerical simulation of the designed sensor package was performed using the software COMSOL Multiphysics 5.3.a (Build 229). COMSOL uses the Finite Elements Method to solve partial differential equations related to electrical, mechanical, fluid and chemical applications. The Finite Elements Method (FEM) is a powerful numerical tool to solve heat transfer problems as well as fluid mechanics, mechanical stiffness and pressure distribution etc. It is based on the numerical solution of the conservation laws of energy for the heat flow through the geometry of interest, taking the form of differential equations. The calculation scheme includes the definition of a geometry, the creation of a mesh for the volume occupied by the device, the definition of the physical models to be applied for the problem and the definition of

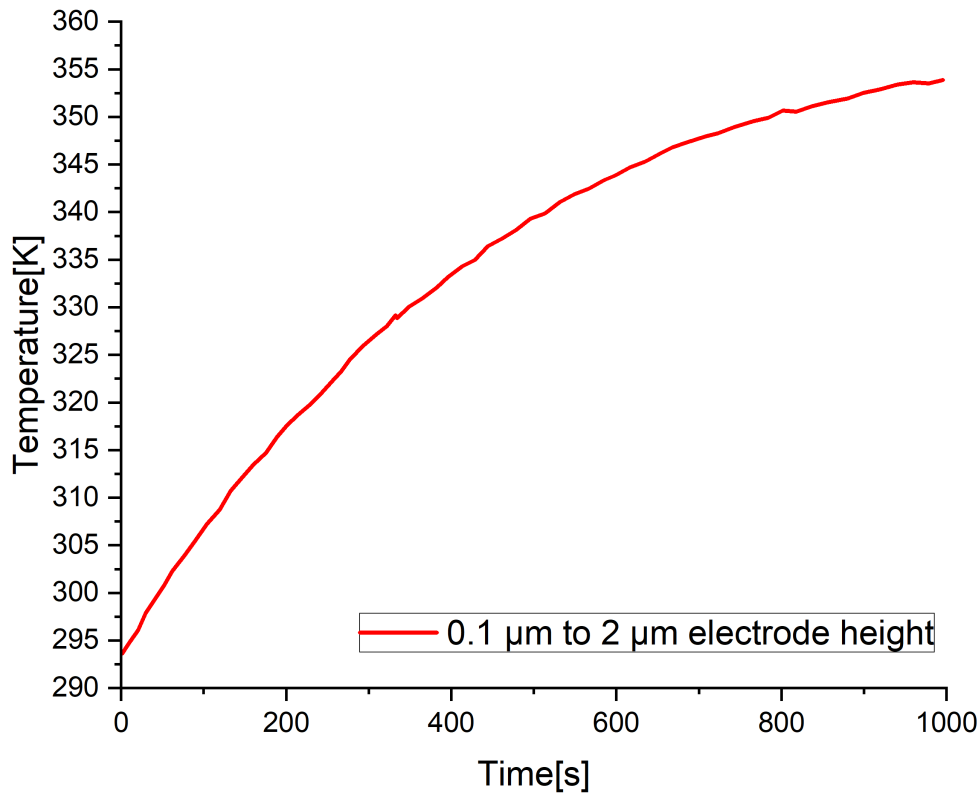


Figure 3.18 – Variation of the height of the electrodes.

the boundary conditions for the geometrical structure. The simulation routine solves the governing equations to calculate the thermal properties for every element of the mesh domain. The underlying partial differential equations are based on the heat transfer equations and the first principle of thermodynamics. COMSOL allows the development of custom designed geometries, the definition of material properties for both solid and fluid parts, impose different types of boundary conditions and eventually prepare a suitable mesh for the problem solved. The software COMSOL was used to design the chip geometry and optimise its thermal behaviour in vacuum. The Heat Transfer in Solids module was used. It includes heat transfer for solids and fluids. Three components were inserted: the packaging variant 1 of the sensor from Table 4.3 represented by a 1 cm³ Polymethyl methacrylate cube, the sensing chip variant 1 from Table 4.1 which is a block of Lithium Niobate and the 600 μm diameter microchannel filled with nitrogen at different pressures. The module heat transfer in solids of COMSOL was used. Conjugate heat transfer between solids (PMMA and Lithium Niobate) and fluids (nitrogen) was implemented. No real flow was modelled only heat transfer which is most relevant to the Pirani sensing principle.

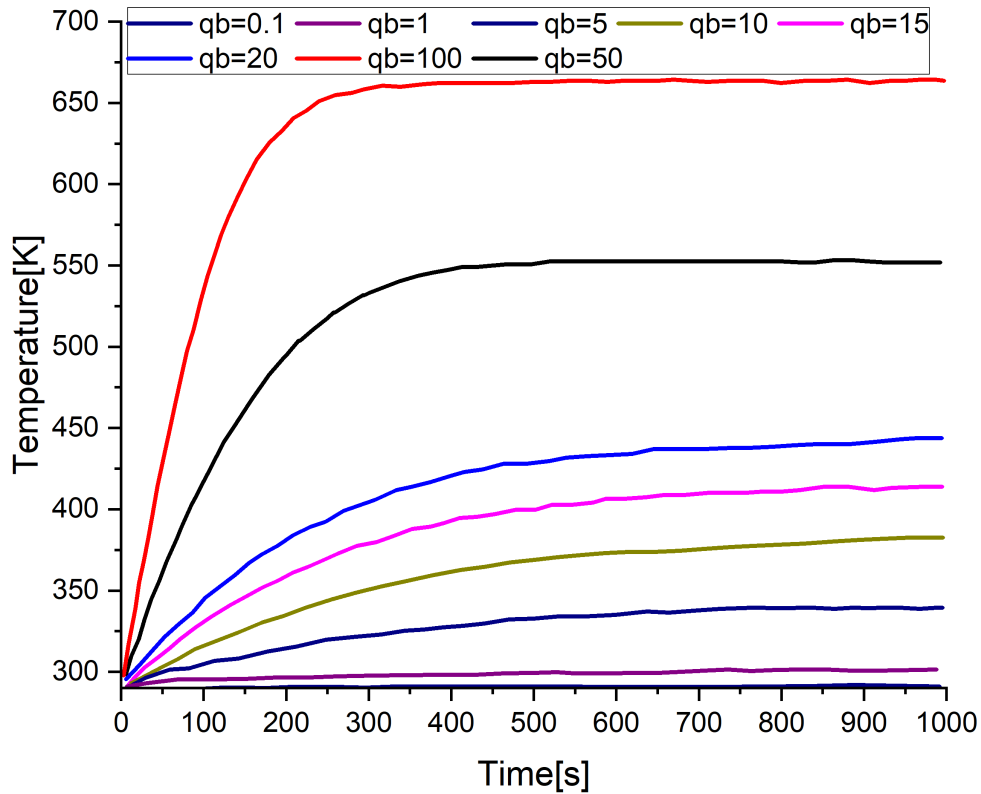


Figure 3.19 – Thermal response when varying the power supply.

3.3.2 Materials and methods

Geometry

The simulated geometry consists of 1 cm^3 of PMMA crossed at its center by a $600 \mu\text{m}$ diameter microchannel. The chip used here is the Variant 1 from Table 4.1. The sensing chip is 1 mm long by $400 \mu\text{m}$ width by $350 \mu\text{m}$ thickness and is located at the center of the channel. The selected thickness of $350 \mu\text{m}$ corresponds to the thickness of the Lithium Niobate substrate wafers available off the shelf and provided by the company SAW components among others that was the supplier of the chips used for the characterization tests.

A schematic view of the developed geometry for the sensor package and chip is shown in Figure 3.20. Figure 3.21 shows the simulated geometry: it consists of a 1 cm^3 cube crossed at its center by a $600 \mu\text{m}$ diameter cylindrical microchannel inside which the chip is suspended without physical contact to the channel. Table 3.4.

Figure 3.22 highlights the microchannel filled with nitrogen. Figure 3.23 shows the complete geometry simulated.

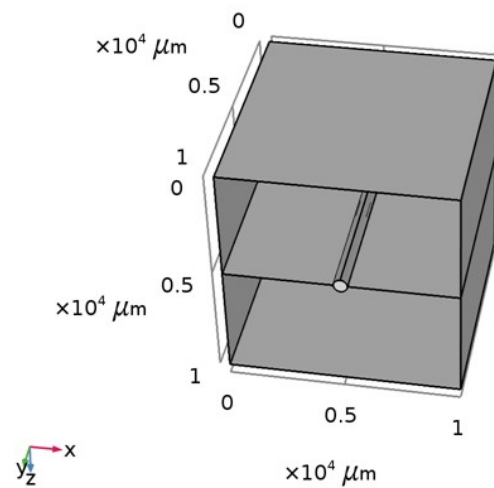


Figure 3.20 – Simulated geometry.

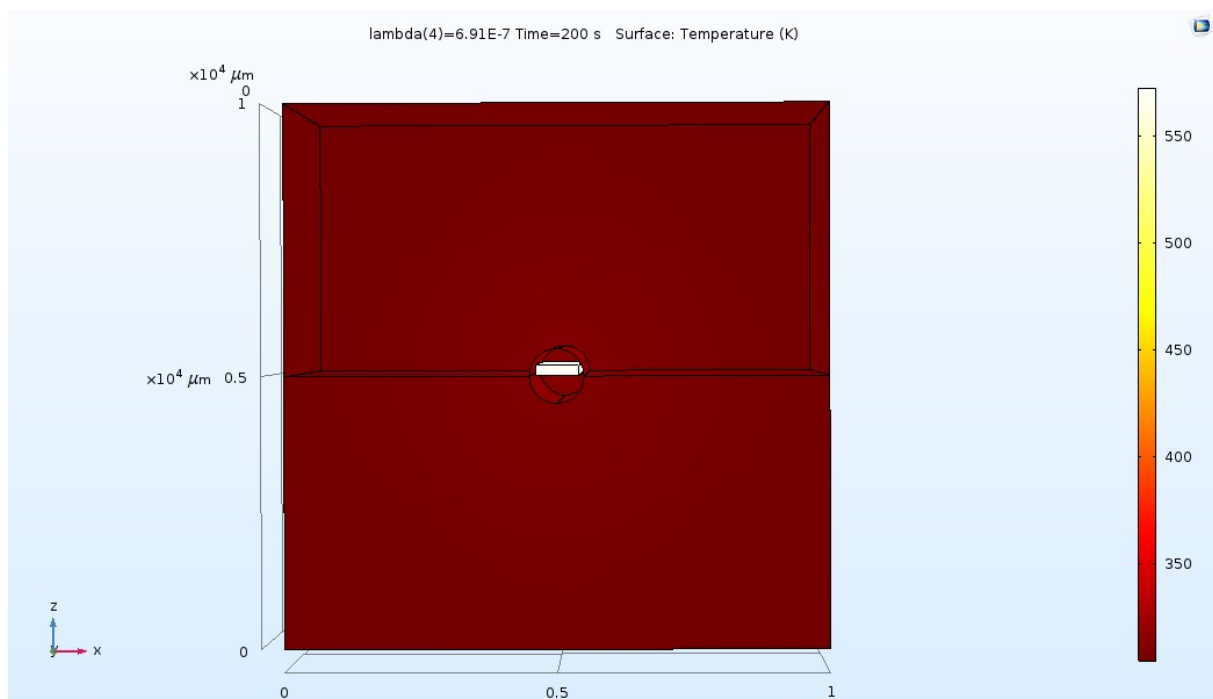


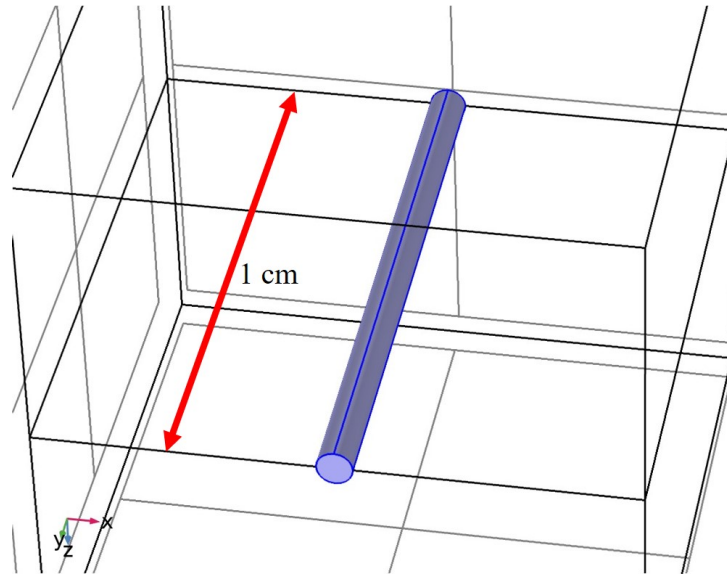
Figure 3.21 – Simulated geometry.

Boundary conditions

After preparing the geometry, it was required to assign specific boundary type for every zone (COMSOL sets them by default to insulated) depending on which different input parameters are required to initiate the calculations. The boundary types listed in Table 3.5 have been assigned. The boundary conditions applied were the thermal insulation of the external boundaries of the sensor and filling the crossing microchannel with nitrogen at different pressures. This allows a preliminary design of the whole sensor

Table 3.4 – Dimensions of the geometry simulated in Comsol.

Symbol	Description	Dimensions
d	Microchannel diameter	600 μm
h	Cube edge length	1 cm
l	Chip length	1 mm
w	Chip width	400 μm
t	Chip thickness	350 μm

**Figure 3.22** – Microchannel filled with nitrogen.

as well as an insight on the heat transfer performances of the assembly. The outside walls of the cube as well as the inlet and outlet of the channel were thermally insulated, the rest of boundaries were all thermal contacts. The chip was heated from its bottom surface with a boundary heat source condition. A power of 10^4 W m^{-2} corresponding to 4 mW was continuously provided. The heating power was tuned to obtain a steady state temperature around 500 K at 10^{-4} Pa and a stable temperature after 100 s. The boundary conditions were designed in a way to avoid unnecessary heat leakages and focus on the useful sensing heat transfer, although radiation cannot be neglected. Figure 3.24 shows the boundary heat source at the bottom of the chip and Figure 3.25 shows the channel diffuse surface used to model radiative heat transfer.

To model radiative heat transfer in Comsol, it is required to choose the nature of the surface radiating and their orientation. The radiative heat transfer here was implemented between the microchannel inner surface and the chip outside surface. The normal vector of the microchannel is oriented towards inside the channel and the normal vector of the chip surfaces are oriented towards outside the chip. The inlet

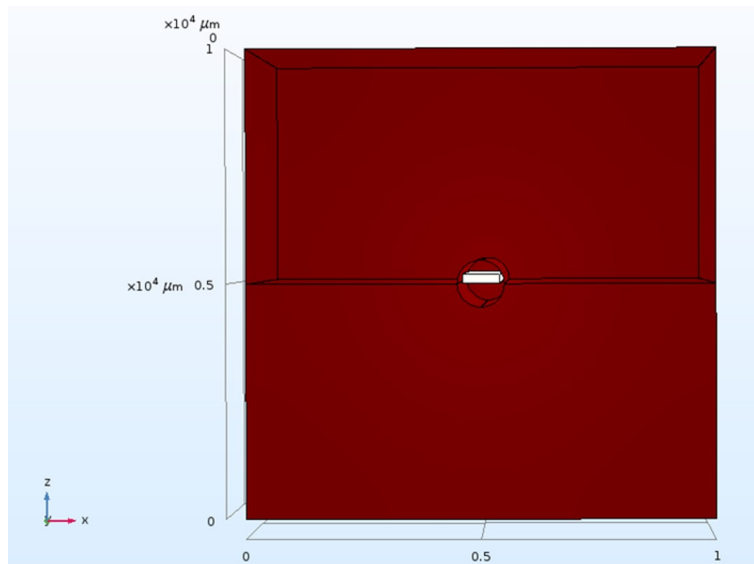


Figure 3.23 – Simulated geometry. A 1 cm³ PMMA cube is crossed at its center by a 600 μm diameter cylindrical microchannel. The 1 mm by 400 μm by 600 μm chip is suspended inside the microchannel. The x and y axes units are identical.

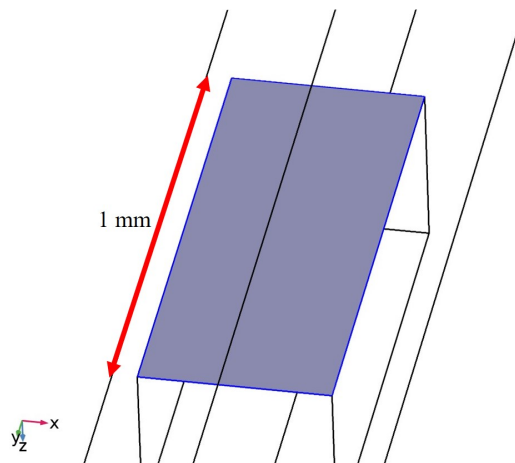


Figure 3.24 – Boundary heat source at the bottom side of the chip.

Table 3.5 – Boundary conditions assigned to the model.

Zone	Boundary type	Input parameters
Cube boundaries	Insulated	Initial temperature
Channel inlet and outlet	Insulated	Temperature
Chip bottom	Boundary heat source	Constant 10 000 W m ⁻² heat source
Channel surface	Continuous conduction	None

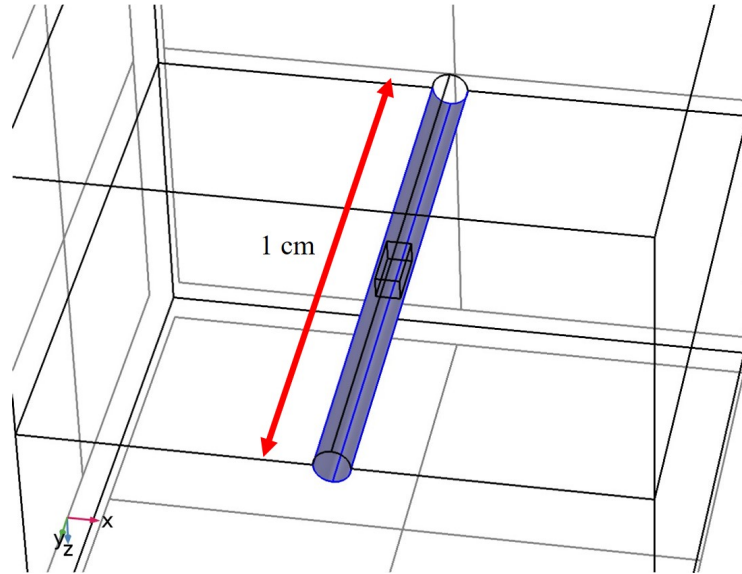


Figure 3.25 – Diffuse surface for radiative heat transfer.

and outlet of the microchannel as well as the cube walls temperature was set to a constant value of 298 K. The ambient steady state temperature was set to 293.15 K.

Material properties

The simulation contains three materials which are Lithium Niobate for the SAW-Pirani sensing chip, nitrogen for the sensed gas and Poly methyl methacrylate (PMMA) for packaging. Table 3.6 describes the properties of Lithium Niobate and Table 3.8 shows the PMMA properties used.

Table 3.6 – Material properties of Lithium Niobate.

Name	Value	Unit
Density	4700	kg m^{-3}
Thermal conductivity	4	$\text{W m}^{-1} \text{K}^{-1}$
Heat capacity at constant pressure	630	$\text{J kg}^{-1} \text{K}^{-1}$
Cube boundaries	Insulated	Initial temperature
Channel inlet and outlet	Insulated	Temperature
Chip bottom	Boundary heat source	Constant 10000 W m^{-2} heat source
Channel surface	Continuous conduction	None

The microchannel is filled with nitrogen. Its properties are shown in Table 3.7. A temperature dependent thermal capacity is assumed for nitrogen. The heat capacity of nitrogen is shown in Figure 3.38.

Table 3.7 – Material properties of nitrogen.

Name	Value	Unit
Ratio of specific heats	1.4	1
Heat capacity at constant pressure	1040	$\text{Jkg}^{-1} \text{K}^{-1}$
Density	1.19	kgm^{-3}

Table 3.8 – Material properties PMMA.

Name	Value	Unit
Heat capacity at constant pressure	1420	$\text{Jkg}^{-1} \text{K}^{-1}$
Density	1190	kgm^{-3}
Thermal conductivity	0.19	$\text{Wm}^{-1} \text{K}^{-1}$

The surface emissivity of the channel surface was taken as 0.9 which is the emissivity of Polymethyl methacrylate (PMMA), the emissivity of the chip was taken as 0.75 [64], which is the surface emissivity of neat Lithium Niobate, the maximum value that could be reached by the chip emissivity.

The values of heat capacity at constant pressure taken depend on temperature. But since the temperature of the device throughout the simulation varies roughly between 300 K and 400 K, the value of the heat capacity can be considered constant.

Physical model

Conductive heat transfer and radiative heat transfer were implemented. The equation solved by COMSOL was therefore the heat equation derived from the first principle of thermodynamics:

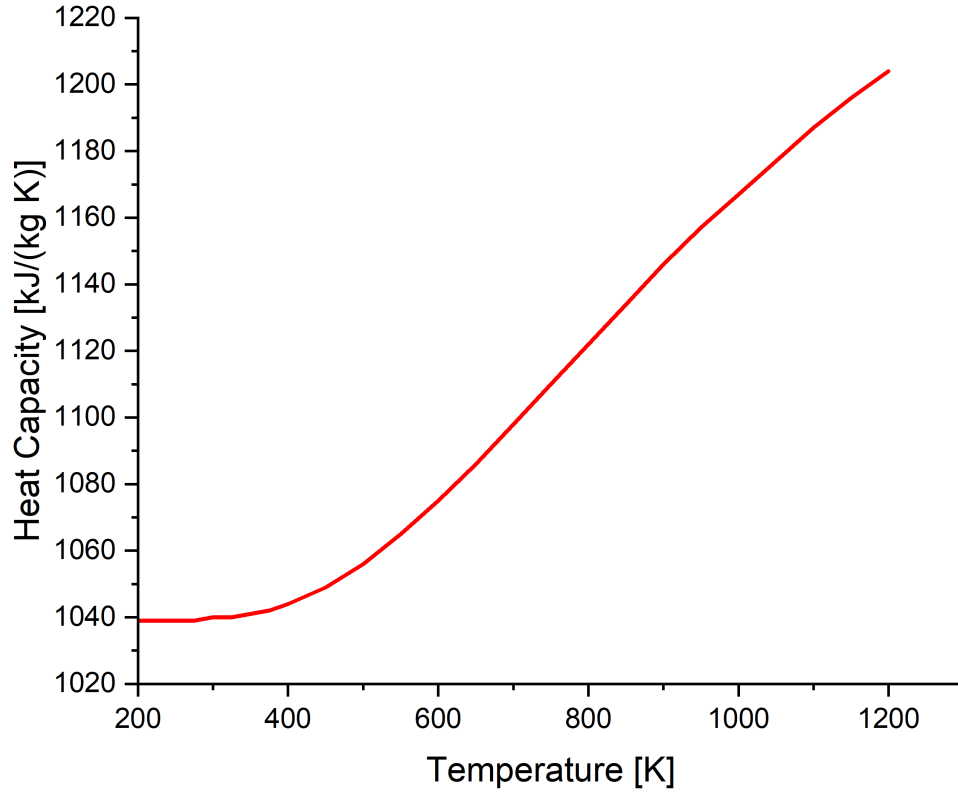


Figure 3.26 – Heat capacity of nitrogen.

$$\rho C_p \frac{\partial T}{\partial \tau} + \nabla \cdot (-k \nabla T) + \rho C_p \mathbf{u} \cdot \nabla T = Q + Q_r \quad (3.2)$$

with:

- ρ – density in kg m^{-3}
- T – temperature in K
- τ – the time in seconds
- C_p – the specific heat capacity (J/kg/K)
- k – the thermal conductivity in $\text{W m}^{-1} \text{K}^{-1}$
- Q – the heating power per unit volume provided at the bottom of the chip in W m^{-3}
- Q_r – the heating power dissipated via radiation per unit volume in W m^{-3}

[83] assesses the reliability of radiative heat transfer with COMSOL comparing it to analytical solutions. Errors lower than 1% are reported in the case of triangular and rectangular geometries. For this reason, radiative heat transfer was also taken into account in the simulation. Radiation is described by surface

to surface radiation between the outer surfaces of the chip and the inner surface of the channel. The equation of the radiative heat transfer is:

$$q_{r,out} = \sum_{S_i} \varepsilon S_i \sigma (T^4 - T_0^4) \quad (3.3)$$

with:

- $q_{r,out}$ – the outward heat flux in W
- ε – the surface emissivity of the chip
- S_i – the surface of each face of the chip
- σ – the Stefan-Boltzmann constant
- T – the temperature of the chip surface
- T_0 – the temperature of the channel which is equal to the ambient temperature

The governing equations of the system show the expression of a time constant. Radiation heat transfer is modelled between the surface of the chip and the surface of the microchannel. The parameter varied was the thermal conductivity of the nitrogen inside the microchannel that reflects the pressure variation. The parametric study was based on the pressure. The effect of pressure variation was simulated by changing the thermal conductivity of nitrogen. The values of the thermal conductivity were computed using the model presented in [10] and adapting it to the dimensions of our design. The values of thermal conductivity computed are presented in Table 3.9.

Table 3.9 – Thermal conductivity values.

Pressure (Pa)	Thermal conductivity
10^{-4}	5.45×10^{-8}
10^{-3}	5.45×10^{-7}
10^{-2}	5.45×10^{-6}
10^{-1}	5.44×10^{-5}
1	5.34×10^{-4}
10	4.51×10^{-3}
100	1.76×10^{-2}
10^3	2.48×10^{-2}
10^4	2.59×10^{-2}
10^5	2.60×10^{-2}

The dynamic viscosity η of the nitrogen depends on the temperature as well as the heat capacity at constant pressure. In this simulation, two different heat transfers are considered, solid to gas conduction and radiation. Heat conduction occurs between all the components in physical contact while surface to

surface radiation is introduced between the chip and the surface of the channel. The ambient temperature is set to 293.15 K. In COMSOL it is necessary to specify the direction of the radiation positive or negative direction or both simultaneously. The radiative boundary conditions taken are summarized in Table 3.10.

Table 3.10 – Radiative heat transfer boundary conditions.

Description	Value
Include surface-to-surface radiation	On
Radiation direction	Positive normal direction
Define ambient temperature on each side	Off
Ambient temperature	User defined
Ambient temperature	293.15 K
Include diffuse irradiance	On
Diffuse irradiance	User defined
Diffuse irradiance	0 W m^{-2}
Surface emissivity	User defined
Surface emissivity	ϵ_{chip}
Surface radiosity	$ht.J_{init}$

Mesh

The mesh used was a physics controlled mesh from COMSOL, different sizes were tested, leading to the same behaviour of the chip. A tetrahedral mesh with fine element size from COMSOL was used for the final simulation. The mesh is finer in the cube part close to the microchannel. Figure 3.27 depicts the mesh. Tables 3.11, 3.12 and 3.13 show the mesh statistics.

Table 3.11 – Mesh statistics.

Description	Value
Minimum element quality	0.2037
Average element quality	0.6709
Tetrahedron	174179
Triangle	12778
Edge element	814
Vertex element	28

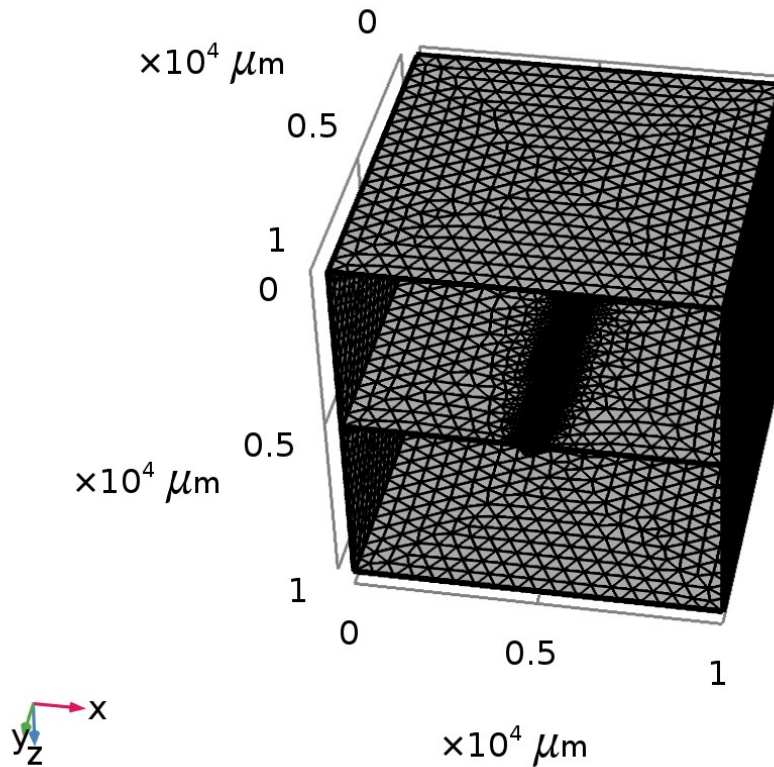


Figure 3.27 – Mesh used.

Table 3.12 – Size.

Description	Value
Maximum element size	550
Minimum element size	40
Curvature factor	0.4
Resolution of narrow regions	0.7
Maximum element growth rate	1.4
Predefined size	Finer

Output solution

A time dependent analysis was carried out in order to determine the pressure dependent steady state temperature and the time to thermal equilibrium. The solver was time dependent from 0 to 100 s with a time step of 0.1 s. The response time being in the range of 60 s, a time step of 0.1 s was deemed reasonable to account for the behaviour variations of the sensor. A transient analysis was performed from 0 to 100 s which is more than the time required by the sensor to reach the steady state temperature.

Table 3.13 – Mesh properties.

Description	Value
Minimum element quality	0.2122
Average element quality	0.6747
Tetrahedron	173912
Triangle	12808
Edge element	814
Vertex element	28

The simulation allowed to estimate the response time of the sensor. Table 3.14 gives the computation information.

Table 3.14 – Computation information.

Computation time	4 h 35 min 3 s
CPU	AMD64 Family 23 Model 1 Stepping 1 8 cores
Operating system	Windows 10

3.3.3 Results and discussion

Temperature

The thermal behaviour of the sensor in vacuum was obtained. Several simulations were undertaken in order to determine the dimensions of the chip that would widen its sensing range and to couple the components together. The output of the simulation was the thermal behaviour of the sensor in vacuum, i.e. the temperature of the surface of the chip versus time amongst others. The steady state temperature at the top surface of the chip was observed and recorded. Table 3.15 lists the final temperature for a range of pressures of interest. Since the waves propagate on the top surface, the resonance frequency depends on its temperature. The objective was to increase the thermal sensitivity of the chip which means, for different pressures, to increase the steady state temperature difference between the different pressure levels. The observed temperature of the chip is uniform. Figure 3.28 shows the variation of

the temperature of the chip vs time at 10^{-4} Pa. The equilibrium is reached after 38 seconds which can estimate the response time of the sensor at high vacuum.

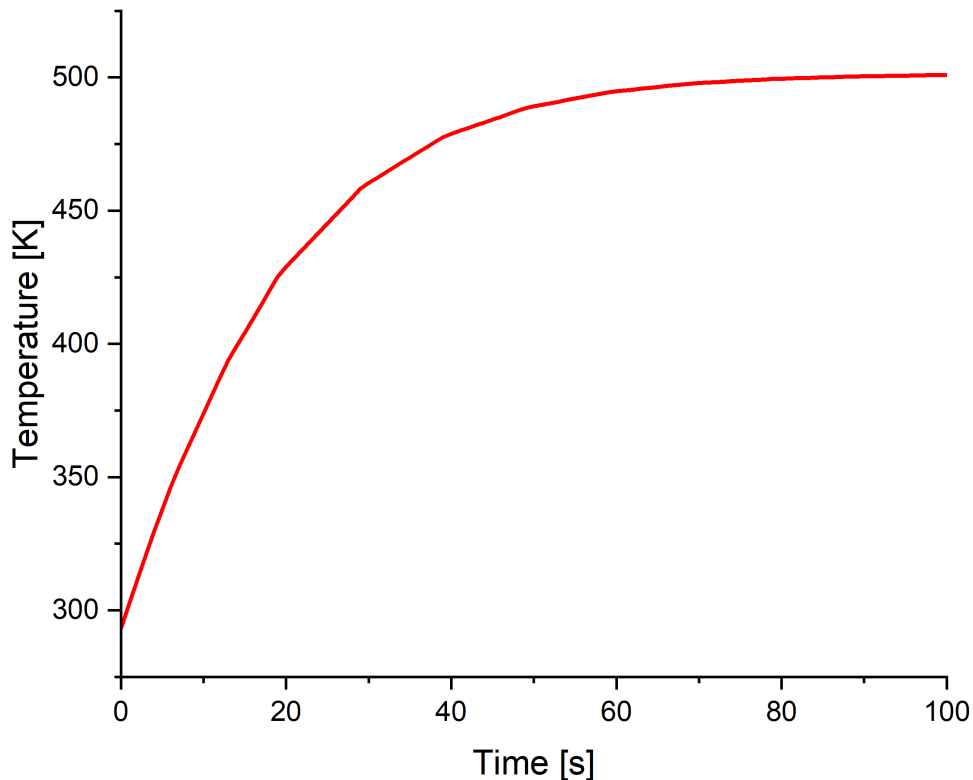


Figure 3.28 – Temperature of the chip vs time at 10^{-4} Pa. The steady state temperature is reached after 38 s.

From the steady state temperature of the chip at each pressure it is possible to calculate the resonance frequency shift. Figure 3.29 shows the steady state temperature of the chip vs the thermal conductivity of the gas. The value of the thermal conductivity is directly correlated and computed from the value of the pressure. The extrema values of 10^{-4} and 10^5 Pa are shown on the curves in addition to other values of pressure. The steady state temperature at 10^{-4} Pa equals to 498 K and at 10^5 Pa it equals 303 K. Figure 3.30 shows the thermal response of the sensor at different pressures between high vacuum and atmospheric pressure.

Figure 3.31 shows the temperature distribution after 200 s of heating. The heat is concentrated at the chip. The temperature of the packaging stays almost constant during the whole simulation.

The temperature distribution along the microchannel, the chip and the radial temperature distribution were observed. The temperature was observed at one fixed point at the centre of the top surface of the chip which is the surface where the electrodes are located and in contact with the gas. Figure 3.32 shows the location of the study point.

Table 3.15 – Simulation results.

Pressure	Thermal conductivity	Temperature[K] at (100s)
10^{-4}	5.45×10^{-8}	498.11
10^{-3}	5.45×10^{-7}	498.04
10^{-2}	5.45×10^{-6}	497.35
10^{-1}	5.44×10^{-5}	490.61
1	5.34×10^{-4}	435.55
10	4.51×10^{-3}	329.13
100	1.76×10^{-2}	305.65
1×10^3	2.48×10^{-2}	303.12
1×10^4	2.59×10^{-2}	302.87
1×10^5	2.60×10^{-2}	302.84

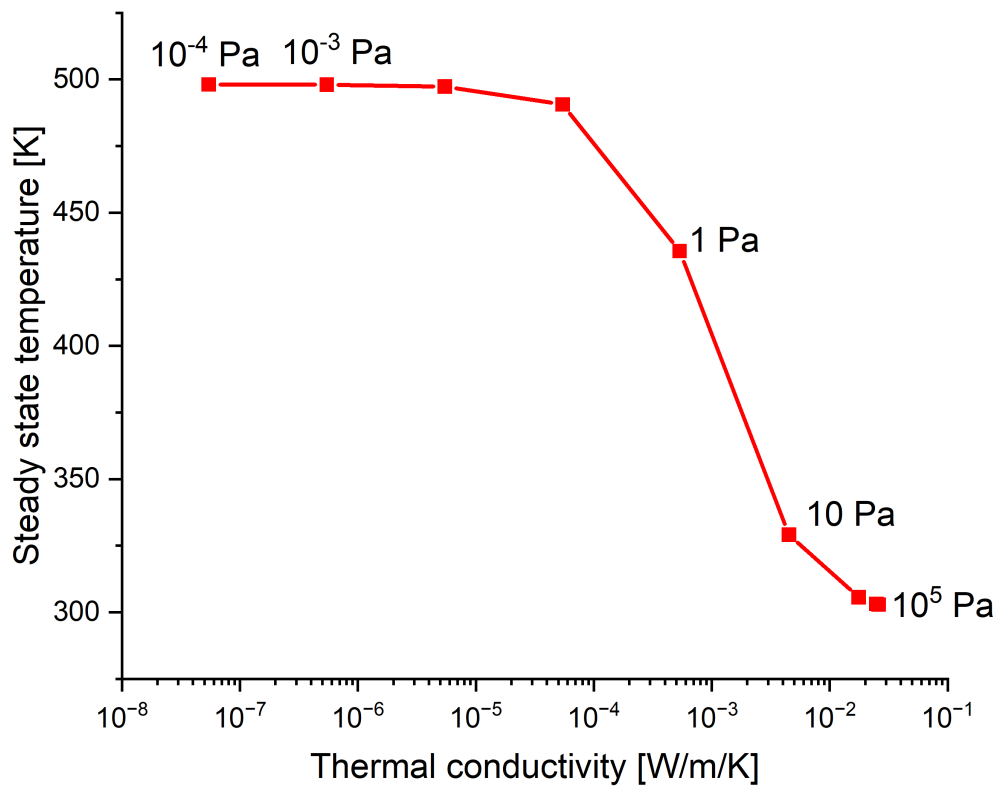


Figure 3.29 – Steady state temperature of the chip in K vs thermal conductivity at different pressures. The thermal conductivity of the gas depends on pressure, which means that the final temperature of the chip also depends on pressure and is used to measure it.

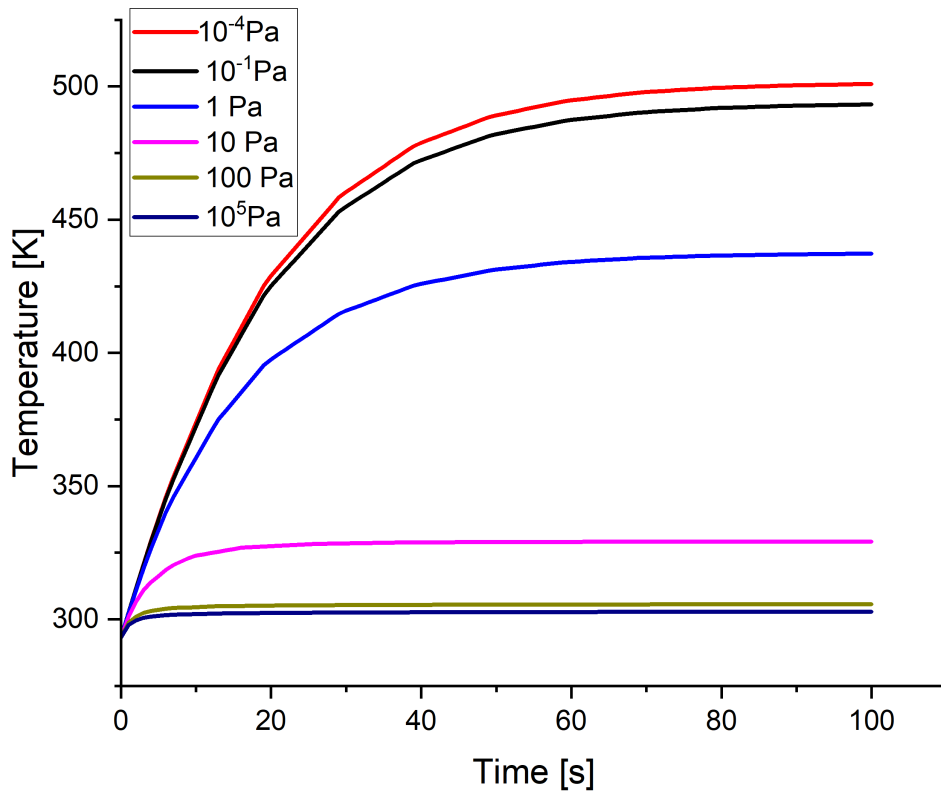


Figure 3.30 – Thermal response of the simulated sensor at several pressures.

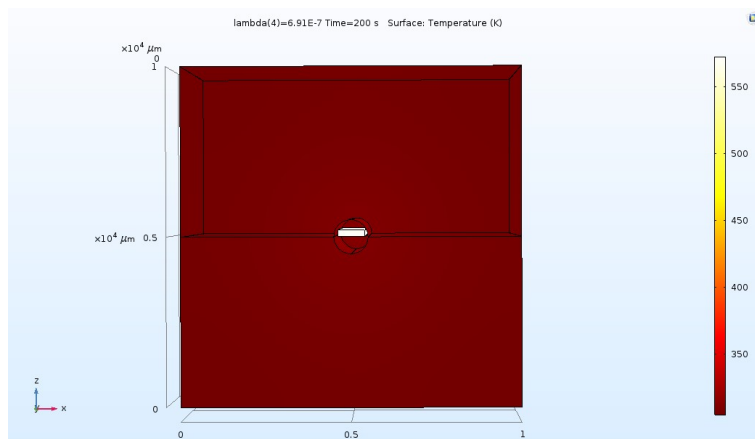


Figure 3.31 – Temperature distribution after 200 s of heating.

The temperature was observed through the axis of the channel. It is uniform at the chip and through the rest of the axis. The transition from the chip temperature to the rest of the axis temperature occurs 0.5 mm before and 0.5 mm after the chip. The transition distance is the same for all the pressures. Figure 3.33 shows the pressure dependent temperature distribution at the sensor axis after 100 s.

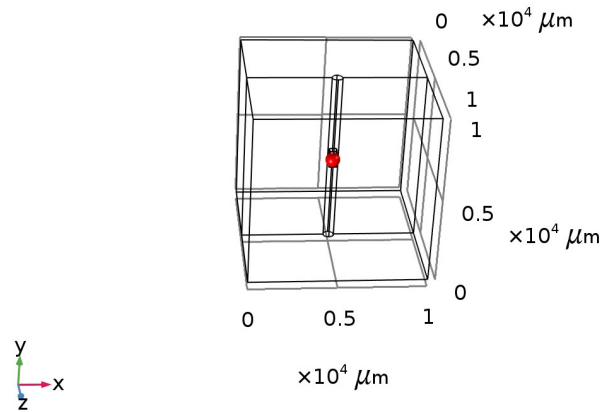


Figure 3.32 – Location of the study point.

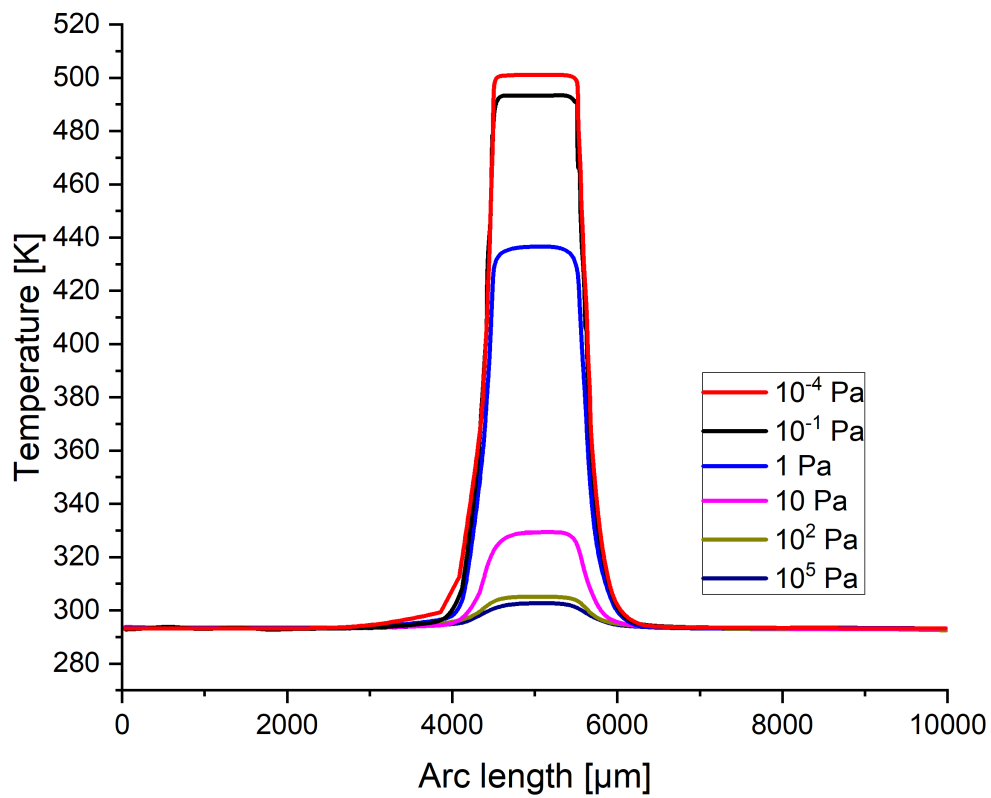


Figure 3.33 – Temperature distribution after 100 s at the sensor axis.

Figure 3.34 shows the chip top surface steady state temperature at 10^{-4} Pa. A uniform uniform temperature can be observed at the surface of the chip. Figure 3.35 shows the chip top surface steady state

temperature at atmospheric pressure. The uniformity of the temperature of the surface of the chip is the same at each pressure.

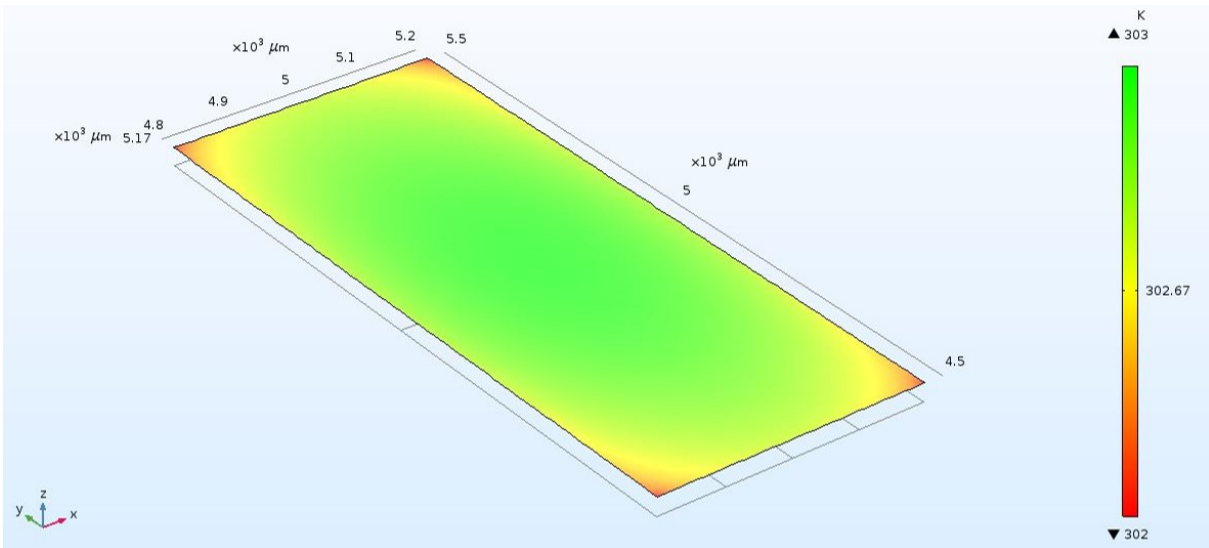


Figure 3.34 – Chip surface temperature at 10^{-4} Pa.

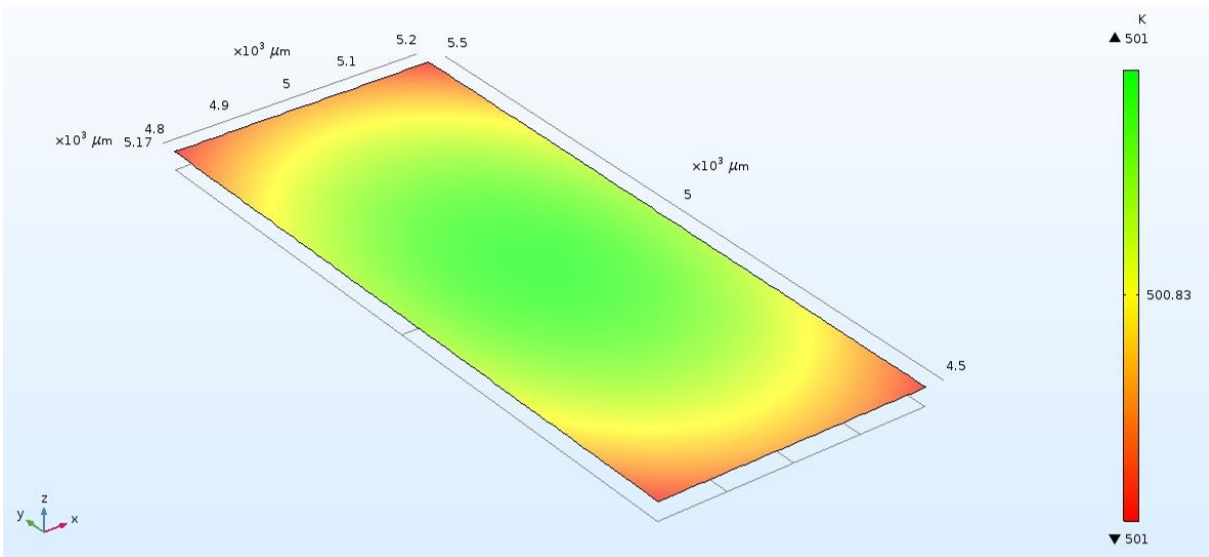


Figure 3.35 – Chip surface temperature at atmospheric pressure.

The radiative heat transfer is different with the pressure. At atmospheric pressure, the radiative heat flux is equal to 445 W m^{-2} . Figure 3.36 shows the radiosity at high vacuum and Figure 3.37 shows the radiosity of the chip and microchannel at atmospheric pressure.

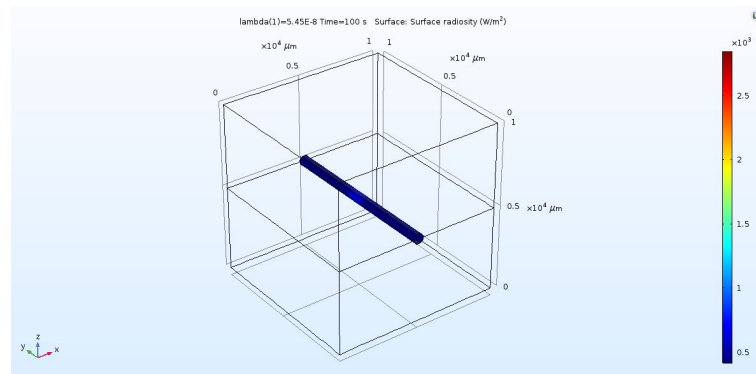


Figure 3.36 – Radiosity at high vacuum.

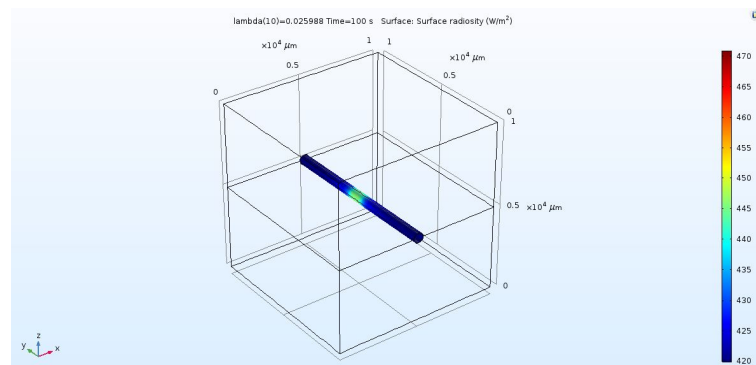


Figure 3.37 – Radiosity of the chip and microchannel at atmospheric pressure.

Assumptions

In the simulation the heat is supplied to the chip from its bottom. It corresponds in practice to the resistive metallic layer that heats the chip when provided with a current. The Lithium Niobate chip is heated from its bottom with a boundary heat source condition that constantly delivers a 10^4 W m^{-2} power i.e. 4 mW of heating power constantly.

A parameter sensitivity analysis was conducted to determine the parameters mostly affecting the sensitivity of the chip. The dimensions of the chip substrate were set by Finite Element Method (FEM) heat transfer simulations, as well as the energy required to heat the chip. An accurate value of the gas accommodation coefficient is a critical parameter to obtain a reliable gas simulation. The accommodation coefficient is used to compute the pressure dependent thermal conductivity of the gas. However, it varies a lot with the gas and the surface contact between the sensor and the gas and all the environment parameters including the pressure [84]. It is important to be aware of the limitations of the simulation. The values used for the simulation were taken from [28]. In this study a Pirani sensor is used to determine accurately the accommodation coefficient of nitrogen for different kinds of surfaces.

One of the most sensitive thermal parameters is the surface to volume ratio. Indeed, increasing the surface of the chip increases the contact between the gas molecules and the chip and therefore the sensitivity of the device on the one hand. On the other hand, reducing the volume and the thickness reduces the heat

capacity of the chip and reduces the response time. Still, the dimensions of the chip need to be set keeping in mind the manufacturing capabilities available and also the mechanical constraints of the chip. A too small thickness would make the chip very fragile. Lithium Niobate wafers with thicknesses of 350 μm being already available off-the shelf, a value of 350 μm thickness was retained.

Using a value of the temperature coefficient of frequency TC_{f_1} of -100 ppm/K [85] for Lithium Niobate the resonance frequency shift from a 2.45 GHz initial resonance frequency at 300 K was calculated. Figure 3.38 shows the calibration curve calculated through the whole sensing range. Table 3.16 shows the frequency shift at selected pressure ranges. The frequency shifts calculated can be measured with a Network Analyzer.

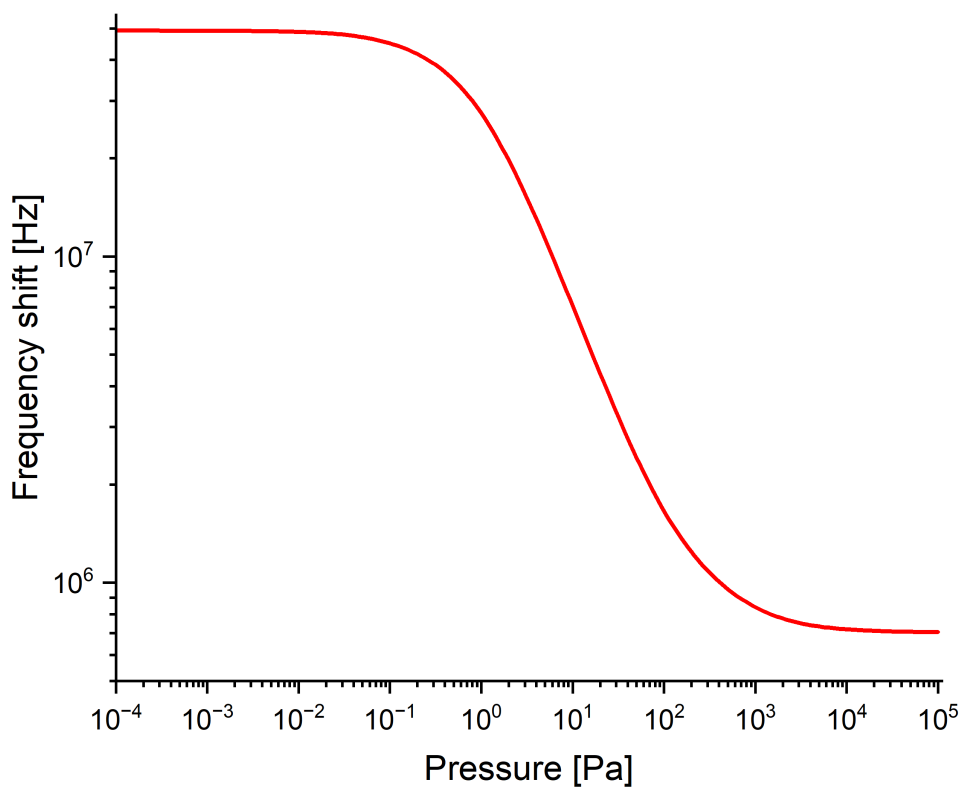


Figure 3.38 – Calculated calibration curve of the sensor. The curve shows the pressure induced frequency shift for an initial pressure of 10^5 Pa and an initial frequency of 2.45 GHz. The characteristic S-shape profile of the thermal conductivity vs pressure can also be observed for the frequency shift but on the opposite direction since the temperature coefficient of frequency is negative.

The sensitivity at high vacuum is higher than the sensitivity close to atmospheric pressure, to increase the sensitivity close to atmospheric pressure the diameter of the microchannel should be reduced.

The specificity of a SAW-Pirani sensor stems from the fact that the pressure induced temperature variation of the chip is transduced in terms of resonance frequency shift. Piezoelectric materials compatible

Table 3.16 – Frequency shift at selected ranges. The frequency shift per decade is in the kHz range or higher and can easily be measured using a Vector Network Analyzer.

Pressure in Pa	Frequency shift in kHz
10^{-4} to 10^{-3}	15.435
10^{-3} to 10^{-2}	152.145
10^3 to 10^4	55.125
10^4 to 10^5	6.615

with SAW have different temperature coefficients of frequency and can reach up to 100 ppm/K for Y, Z cut Lithium Niobate. In this case the frequency shift is computed by multiplying the chip temperature variation of the chip by the temperature coefficient of frequency which allows calculating a preliminary calibration curve for the sensor.

Simulation was in this case used as a qualitative indicator for the design of the sensor i.e. the parameters and dimensions that most affect the sensitivity of the sensor.

The surface to volume ratio of the chip is a key parameter for the efficiency of Pirani sensing. On the one hand, the heat exchange between the sensor and the gas is proportional to the contact surface between the sensor and the gas. On the other hand, the higher the volume, the higher the thermal inertia of the sensor and the higher the time to equilibrium i.e. the response time of the sensor. The surface to volume ratio is independent from the vacuum pressure range addressed.

The diameter of the channel was also among the parameters varied. Other sections of the channel were considered such as rectangular and star section holding the chip for the manufacturing of the prototype. Channel diameters of 1 mm, 800 μm , 600 μm and 400 μm were considered. The size of the microchannel impacts the value of the Knudsen number and therefore the sensitivity of the measurement through the whole sensing range.

The thermal conductivity of the nitrogen was computed using different models and the thermal response of the sensor was computed accordingly. However the different models used show similar orders of magnitude which allows to draw consistent qualitative conclusions concerning the behaviour of the sensor. The thermal conductivity of the packaging and the chip were not varied.

For the Pirani sensing, one of the main limitations is that at low pressures the heat transfer is overwhelmed by solid conduction between the sensor and its carrier and radiation between the sensor surface and the vacuum chamber's surface. In the simulation assessed, solid conduction is completely removed since the chip is suspended in the channel. In practice, the chip is held by four gold thin wires of 25 μm diameter that are not modelled here.

The emissivity of the sensor surface, which is the ratio of the radiated heat compared to the ideal black body model impacts the sensitivity of the chip. Different values of emissivities were tested on both surfaces radiating with each other, i.e. the microchannel and the chip. In practice, the emissivity of the

surfaces can be controlled by applying an appropriate coating with the desired emissivity value such as carbon black that can have an emissivity as low as 0.01. The value of the emissivity of PMMA is 0.9 and the emissivity of neat Lithium Niobate is 0.75 which are common values found in the literature [64].

To see the mesh dependence of the model, 4 different mesh sizes were tested, mainly differing from each other for the element size. The size options coarse, fine, finer and extremely fine from COMSOL were tested. The finer size was retained for the final simulation for the sake of reaching a reasonable compromise between accuracy and computational time.

Different models for the gas thermal conductivity were tested granting different values of gas thermal conductivity at different pressures. The sensitivity of the thermal conductivity of a gas to pressure is the highest at the transition flow and slip flow model i.e. for Knudsen numbers between 10^{-3} and 10. The Knudsen number decreases when the pressure increases. Table 3.17 shows the Knudsen number of the simulated flow. Considering the width of the pressure range sensed, the transition and slip flow of the regime can only be contained within the regimes which corresponds to pressures between 1 Pa and 10^4 Pa which increases the sensitivity towards atmospheric pressure as opposed to a conventional Pirani.

Table 3.17 – Knudsen number of the flow and type of flow according to the pressure value.

Pressure	Knudsen number	Regime
10^{-4}	38145	Free molecular flow
10^{-3}	3813.33	Free molecular flow
10^{-2}	381.33	Free molecular flow
0.1	38	Free molecular flow
1	3.67	Transition flow
10	0.38	Transition flow
100	3.8110^{-2}	Slip flow
1000	3.9210^{-3}	Slip flow
10^4	3.9310^{-4}	Continuum flow
10^5	3.9310^{-5}	Continuum flow

The temperature was observed at the surface of the chip which is the temperature felt by the IDT and reflected in the resonant frequency shift. Quantitative comparisons between the numerical model and the experimental results from the calibrated integrated sensors could be useful to fully validate their measuring principle. However, due to their structural fragility and the lack of compatibility of the available technologies (bonding technologies and sputtering), the exact simulated configuration could not be reproduced in the lab for validation measurements.

The imposed boundary conditions were set taking into account the software. Since the Pirani sensing is a heat transfer process mainly it was deemed more relevant to solve the heat transfer process and not a fluid flow process. A SAW substrate thickness of 200 μm or less is recommended by the simulation to increase drastically the sensitivity.

The simulation shows no physical contact between the chip and the channel in practice the chip was suspended by 4 wires that are also responsible from the electrical connection between and its heating unit on the one hand and its interrogation unit on the other hand. The use of gold wires with a thickness of $25\ \mu\text{m}$ could help avoid a big heat leakage from chip to microchannel in case of direct mechanical contact between them.

The simulation helps estimate the real sensor behaviour although it is difficult to evaluate the discrepancy between the model and the physical conditions. The material choice for the design of micro-structured devices is mainly driven by practical choices (best material withstanding desired working conditions or offering the best compromise between durability and costs). If processes under uniform temperature boundary conditions are to be studied metals with a high conductivity such as copper are the best choice. When thermal transfers need to be studied polymers such as PMMA or PTFE should be studied.

The outer boundaries are all insulated for the three kind of heat transfers. Continuity is applied on all interior boundaries of the chip to ensure the heat transfer between the chip and its surrounding gas. Although the value of the pressure 10^{-4} Pa was introduced in the properties of the fluid, it was not taken into account by COMSOL during the computation.

Many treatments can be applied to optimise the radiative heat transfer. The values of emissivity were voluntarily taken as big, in order to compensate for potential losses in the physical sensor and be able to better estimate the real performance of the designed sensor. The chip surfaces radiate towards outside and the microchannel surface radiates towards the inside i.e. the chip.

The reference device presented in [10] has also been simulated with COMSOL to model accurately solid conduction, gas conduction and radiation. Good agreement was obtained between experimental and numerical results. COMSOL computes accurately the view factors of the radiating surfaces. The device presented here has a response time of 5 ms whereas the response time of our simulated device is 40 s which is almost 1000 times more. A parametric analysis was also performed to optimise the design. The parameters variated were the gas gaps, the width of the chip, the chip dimensions, the thermal conductivity and the bridge voltage. The chip is nonetheless not exactly in the middle which means that d_1 is different from d_2 in the simulation presented in [10].

The boundary conditions can be varied for every studied problem to match the same conditions recorded during the experiments and allow for comparison between numerical and experimental results.

3.4 MOSFET circuit

Following the selection of the components of the sensor's heating unit, the wireless power transfer system had first to be simulated. This section provides a description of the design of the wireless power transfer circuit and the antenna impedance matching circuit. The simulations were performed by M.Sc Suparna Sundarrayyan during her Master thesis. The TINA simulation software from Texas Instruments was used

for the purpose of design and simulation of the circuit discussed below. It is a power circuit simulator and a PCB design software package for analyzing, designing and testing.

The wireless power transfer circuit was designed based on some preliminary requirements which are:

1. A fixed receiver coil of 7.2 μH .
2. A current of 300 mA across a resistance of 1 at the receiver side.
3. The primary and the secondary coil should be placed at a distance of 5 to 10 mm from each other.

The wireless power transfer circuit was designed using a Metal Oxide Semiconductor Field Effective Transistor (MOSFET). The MOSFET IRLIZ44N was used in the transmitter circuit as an amplifier and the circuit was initially simulated using the transmitter coil of 33.6 μH and the receiver coil of 7.2 μH as shown in Figure 3.39.

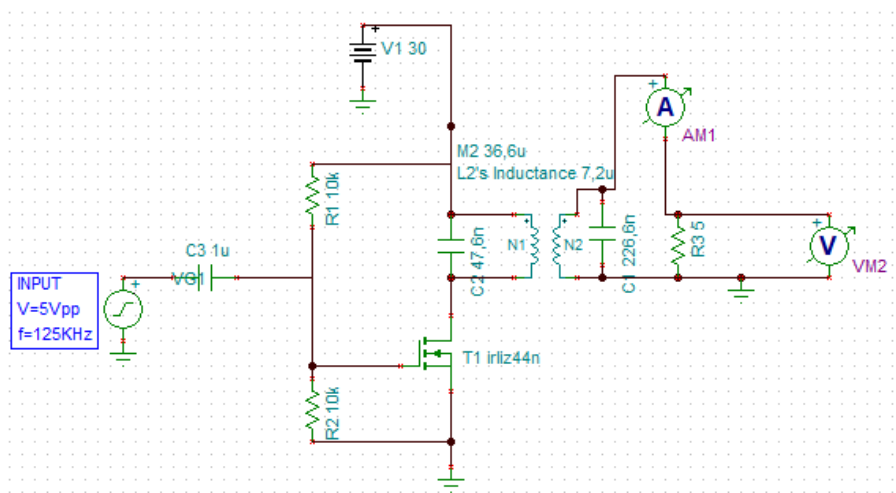


Figure 3.39 – MOSFET circuit simulated.

The circuit was provided with an input sine wave of 5 Vpp at a frequency of 125 kHz. By means of a voltage divider circuit, the required amount of voltage is given to the gate of the MOSFET to increase the voltage beyond the threshold value between 1 V and 2 V. The drain of the MOSFET was powered with a constant 30 V supply. The transmitter coil was connected to the drain of the MOSFET in parallel to a capacitor and the receiver coil was connected in parallel to the capacitor and resistor of 5 Ω . Two outputs were observed which are the voltage across the output resistor and the current flowing through the output circuit. Out of all the signals, the current was the most relevant to the study.

Figure 3.40 shows the output current of 600 mA RMS across the 3 Ω resistor which is more than what was expected. Later on, the output current was set to vary based on changes in the output resistance value. The resistance value was changed over a range of 1 Ω to 10 Ω and the corresponding change in the output current was simulated. Therefore, the current decreases when the resistance value increases. The final circuit was made based on this simulation results.

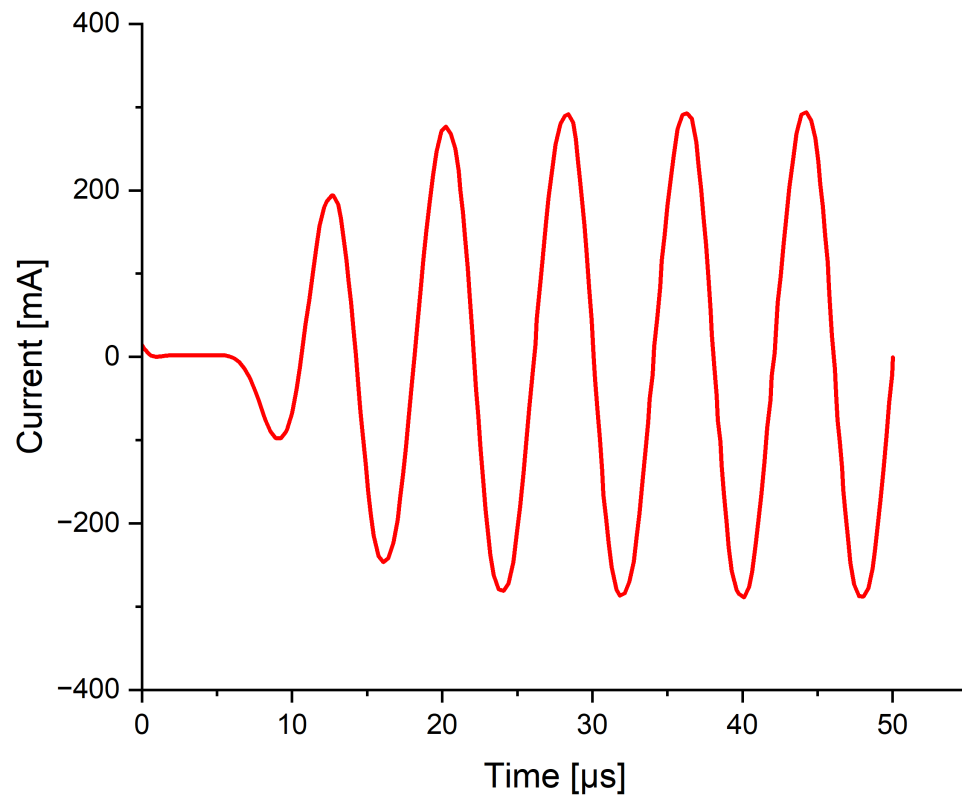


Figure 3.40 – Output current across the 5 Ω resistor.

4 Design of the sensor

Following the simulation of the preliminary design, a complete sensor system was designed based on the findings of the simulation and the manufacturing capabilities in view of manufacturing a prototype. First, the system design is presented with the choice of the technical solutions and the preliminary dimensions for each sensor component. The system is divided into four units : a heating unit, a sensing unit, an interrogation unit and the packaging. Figure 4.1 shows the SAW-Pirani sensor system components. Each unit had first to be designed separately and then combined with the rest. In the following, the role and design of each component are detailed.

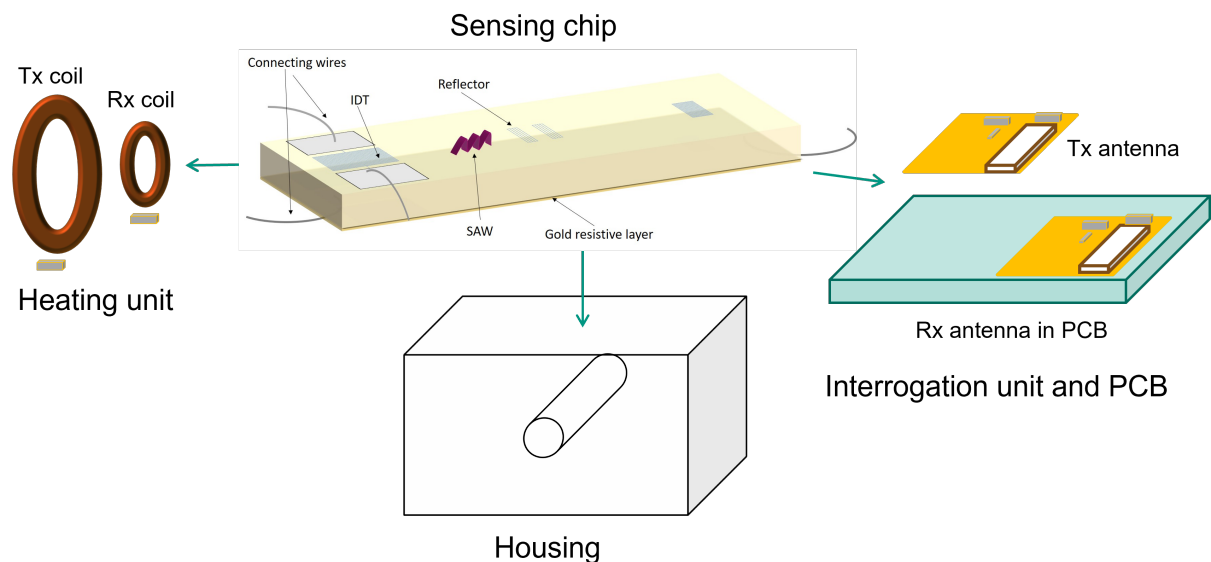


Figure 4.1 – Schematic explosive design of the SAW-Pirani sensor system designed containing: the sensing chip, the heating unit, the interrogation unit and the packaging

In the following tables the variants for each sensor components are presented. Table 4.1 shows the chip variants used in this thesis in the simulation, manufacturing and testing. Table 4.2 lists the interrogation unit variants. Table 4.3 lists the packaging variants. Table 4.4 contains the PCB variants containing the Rx coil from the heating unit and the Rx antenna from the interrogation unit. For the heating unit, only one variant was used that was compatible with all the variants of the other components. The critical component of the heating unit was the receiver coil to insert inside vacuum. The used receiver coil is the WE-WPCC 760308101216 Wireless Power Charging Receiver Coil. The corresponding transmitting coils are presented in the experimental chapter.

Table 4.1 – Chip variants used in the thesis.

Variant	Length	Width	Thickness	IDT type	f_{res}	Application
1	1 mm	400 μm	350 μm			Chip simulated in Comsol for thermal behaviour
2	1 mm	400 μm	350 μm	resonator	2.45 GHz	SCD bare die on foil used to test sputtering, soldering, wirebonding Designed chip, material geometry, resonance frequency, electrodes dimensions designed by Sofia Toto, electrodes placing for delay line and RFID designed by Dr. Pascal Nicolay
3	6 mm	400 μm	350 μm	delay line	2.45 GHz	
4	3 mm	3 mm	1 mm	resonator	2.45 GHz	SCD packaged chip used for characterizing the sensor system at ambient conditions and in vacuum

Table 4.2 – Interrogation antennas used in the thesis.

Variant	Reference	f_{res}	Dimensions[mm]	Application
1	WE-MCA 7488930245 from Würth Elektronik	2.45 GHz	3.2x1.6x1.3	Integrated in PCB and tested. Provided sufficient sensing signal in vacuum
2	P/N 2450AT18B100 2450 MHz Antenna from Johanson	2.45 GHz	3.6x1.6x1.3	Integrated in PCB and tested. Provided insufficient signal in vacuum

Table 4.3 – Sensor packaging used in the thesis.

Variant	Microchannel	Dimensions[mm]	Material	Application
1	Cylindrical 600 μm diameter	10x10x10	PMMA	First design simulated in Comsol
2	Cylindrical 600 μm diameter	19x15x11	PTFE	Manufactured to contain the components and the PCBs in particular

Table 4.4 – PCBs manufactured in the thesis.

Variant	Dimensions[mm]	Material	Application
A	15x11x1.3	FR4	PCB manufactured for the Johanson antenna
B	15x11x1.3	FR4	PCB manufactured for the Würth Elektronik antenna

4.1 Heating unit

The heating unit is responsible for providing the chip with the heating current at its bottom in order to heat it.

For Wireless Power Transfer (WPT) applications, trade-offs among various parameters such as transmission frequency, process technology, resonator topology and output regulation method were necessary which made the design challenging. Since it is a wireless power transfer, it is made of a transmitting part (Tx) located outside vacuum and a receiving part (Rx) located inside the vacuum environment to be sensed. The chip needs 4 mW of power to reach the desired temperature for sensing. This value was determined thanks to the simulation of the chip done with Comsol, presented later on.

When designing a wireless power system, coil specific considerations are necessary. It is important to be aware of the coil system requirements which are:

- available space within the Rx device
- thickness of the Rx coil
- distance between Tx and Rx

- freedom of the positioning of Rx
- electrical performance (efficiency, Q-factor, RDC, shielding...)

In order to wirelessly transfer the heating power to the sensing chip, several power transfer modes were considered. Considerations for different power levels are quite different. Electromagnetic wireless power transfer systems are divided into two main categories: near field and far field systems [42]. Figure 4.2 depicts the difference between a near field and a far field transfer system.

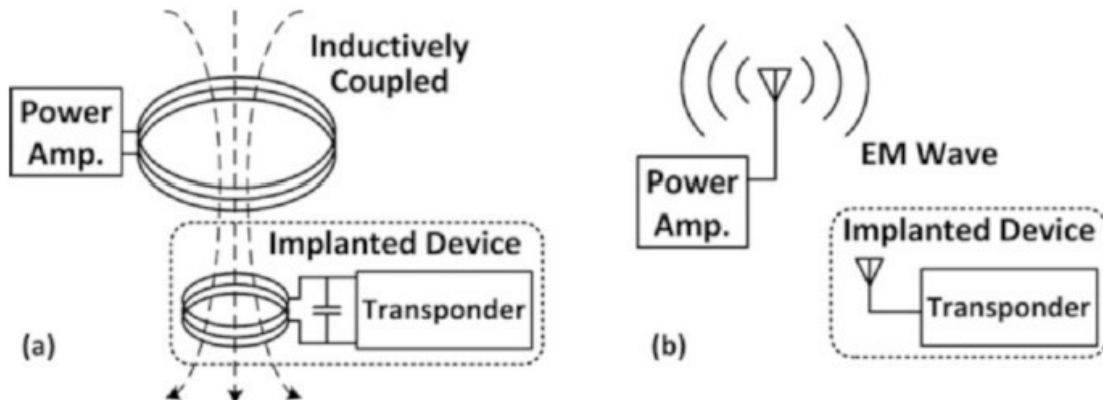


Figure 4.2 – Block diagrams of (a) near field and (b) far field wireless power transfer system. From [43].

In the case of near field operation, the transmission distance d is much shorter than the wavelength λ , both transmitting and receiving devices are coils. The energy transfer is operated via magnetic flux only. The optimum transmission distance is related to the radius of the transmitting coil [42]:

$$x_{opt} = \frac{R}{\sqrt{2}} \quad (4.1)$$

with:

- x_{opt} – Optimum transmission distance
- R – Radius of the transmitting coil

On the other hand, for far field operation, the wavelength is much shorter than the transmission distance and the energy transfer devices are antennas using electromagnetic waves. If the transmitting coil is too large, the field strength becomes very weak. If the coil is too small, the magnetic field strength drops at a fast rate that is inversely proportional to x^3 . The size of the transmitting coil should be designed according to the desired coupling distance. For far field operation, focusing the transmitted energy to a targeted location is rather challenging. For this reason antenna arrays are used to increase the directivity of the power transmission and achieve higher coupling efficiencies. A simplified formula for the path loss between two isotropic antennae is [42]:

$$A_{path} = -20 \log \left(\frac{4\pi d}{\lambda} \right) \quad (4.2)$$

with:

- A_{path} – Path loss in dB
- d – Distance between antennae in m
- λ – Wavelength in m

The path loss is inversely proportional to the wavelength and therefore to the frequency. To reduce path loss, lower frequency bands are used for long distance RF transmission. Resonant circuits give a better link efficiency.

Considering the coupling distance in the cm range and the power transfer needed in the range of tenths of watt magnetic induction between two coils was retained since it has the highest efficiency considering the constraints.

Figure 4.3 depicts the relationship between the coil diameter, the coupling distance and the coupling efficiency. When the coupling distance increases, the efficiency of the coupling decreases. For the same coupling distance, increasing the coil diameter decreases the efficiency. For the same efficiency, increasing the coil diameter allows to increase the coupling distance.

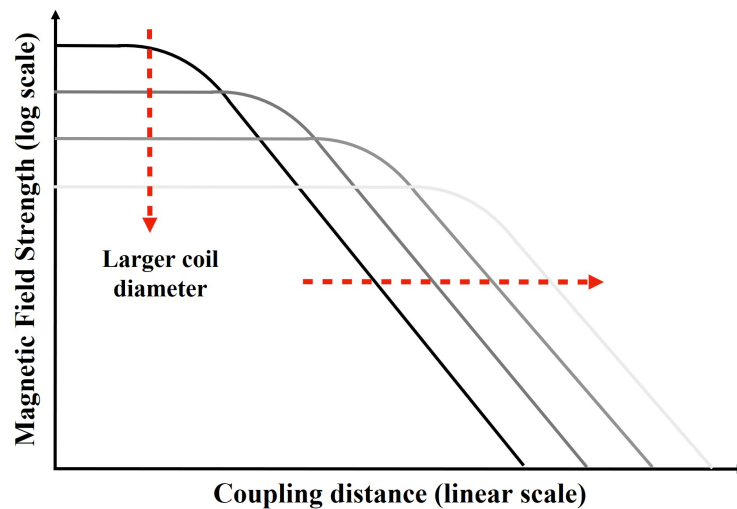


Figure 4.3 – Relationship between coupling distance and coil diameter. From [42].

The quality of the coupling of a wireless power transfer can be described by the coupling coefficient k and the distance d between the coils. A coupling factor of 1 is ideal. In the situation where the two coils are of comparable sizes and placed very close to each other, they are tightly coupled. A higher coupling coefficient k improves the wireless power transfer efficiency hence reducing the losses and heating. Good coupling and maximum energy transmission depends on the size of the effective area of the receiver coil in the magnetic field and the distance in the direction normal to the coil's plane.

In a tightly coupled system, the transmission frequency is designed in a way that it is different from the receiver self-resonance frequency to be able to control the power output while maintaining a high efficiency. For a loosely coupled system, the transmission frequency is well tuned at the receiver self-resonance frequency to induce sufficient power and achieve the best efficiency at increased distance.

The receiver coil is aimed to have a maximum quality factor Q and efficient power transfer is reached if the transmission frequency exactly corresponds to the receiver resonance frequency. Yet, resonant excitation is sensitive to the circuit's components properties which means that additional resonant tuning circuits are required. Increasing the transmission frequency reduces the size of the passive components. Increasing the resonance frequency reduces the value of the inductor and capacitor. High frequency wireless power transfer reduces the volume of the LC resonant circuit. This enables the integration of an entire Wireless Power Transfer system on a chip or on a package.

The model presented earlier in 2.5 was chosen for its simplicity and its closeness to the real situation. Indeed, the load of the receiver circuit is only one resistance corresponding to the heating resistance of the SAW chip. The developed circuit is relatively simple and straightforward, one power source and transmitting coil on the one hand and one receiver coil and a resistive load on the other hand, which corresponds exactly to the ideal transformer structure in first approach since no parasitic loads values are calculated nor available nor other electronic components are inserted such as further inductors, resistors or capacitors. The model was used to calculate the value of the inductances of the Tx and Rx coil, the operation frequency for optimised coupling and the voltage power supply necessary [42]. The use of the equation gives a reasonable estimation of the link voltage gain to determine the voltage that needs to be supplied to the Tx coil and if a power amplification is necessary.

An inductor was selected to perform wireless heating via induction coupling. The WE-WPCC 760308101216 Wireless Power Charging Receiver Coil manufactured by Wuerth Elektronik was chosen for its size and power capacity. Indeed, it has an outer diameter of 6 mm and 2 mm height can receive a current of 500 mA maximum and receive 0.11 W. The received power is sufficient to heat all the chip variants mentioned in this thesis. After the coil was chosen, the wireless power transfer circuit was built. A target of 300 mA rms current to be received by the coil was set. A suitable transmitting coil had to be found and the value of the matching capacitors needed to be calculated.

Capacitors are also usually added to the primary and secondary coil to resonate at the frequency of power transmission. A capacitor was used to tune the resonance frequency of the Rx part, to smoothen the voltage and avoid voltage discontinuities at the load resistor. The value of the resonance frequency of such a circuit is given by:

$$f_{\text{res}} = \frac{1}{2\pi\sqrt{LC}} \quad (4.3)$$

A MOSFET and a Zener diode were used in the transmitting circuit. A diode forces the direction of the current. A Zener diode is a type of diode that allows current to flow not only from its anode to its cathode, but also in the reverse direction, when the Zener voltage is reached. They are used to generate

low-power stabilised supply rails from a higher voltage and to provide reference voltages for circuits, especially stabilised power supplies. They are also used to protect circuits from over-voltage, especially electrostatic discharge. The MOSFET was used as a power amplifier.

The designed circuit was simulated and the values of the electronic components were optimised to achieve the best power transfer prior to manufacturing and testing. Figures 4.4 and 4.5 show the layout designed for the Tx circuit of the heating unit.

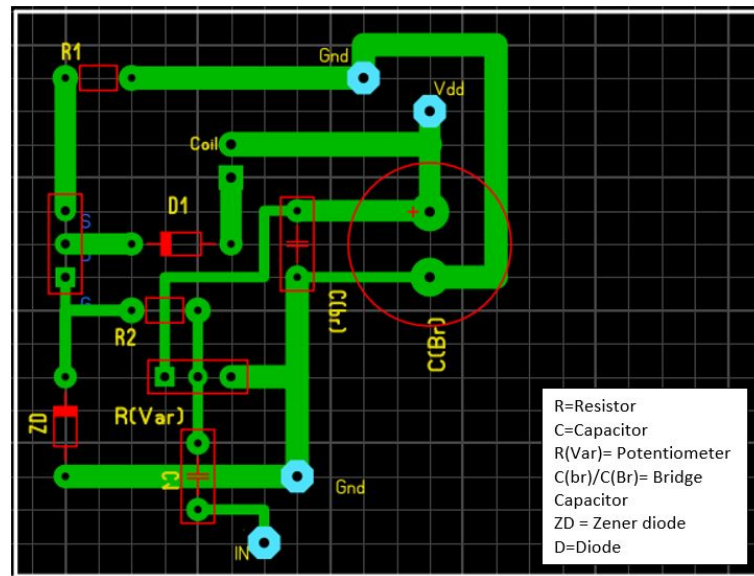


Figure 4.4 – MOSFET Circuit Layout designed with the software Sprint Layout.

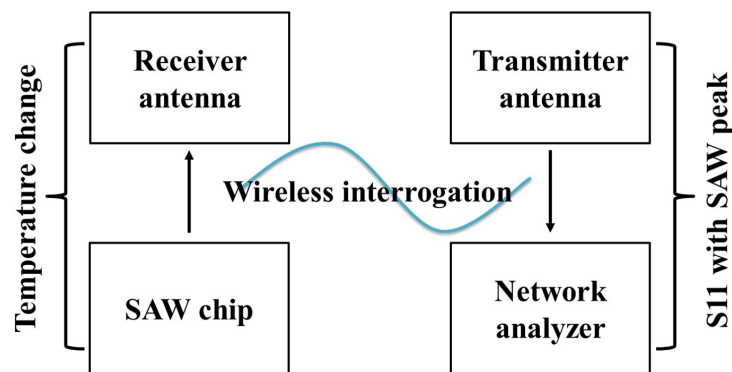


Figure 4.5 – Schematic of the signal transmission between SAW chip and the respective antennae.

In [86], a wireless power transfer circuit is introduced. The size of the setup is big and most of the work was done on the conditioning electronics whereas in our work, miniaturisation was a priority as well as simple electronics.

4.2 Interrogation unit

The theoretical analysis conducted to design the interrogation unit is similar to the one for the heating unit since it is also about wireless power transfer using electromagnetic waves. However, the interrogating unit operates using a Tx and Rx antenna and not via coils. The necessary information is conveyed by the scatter parameters.

The main basic parameters that need to be considered while working with antennas are:

1. Frequency
2. Wavelength
3. Impedance matching : it is when the approximate value of the impedance of a transmitter when it equals the approximate value of the impedance of a receiver. The impedance (in Ohms) of the antenna and the power line should be matched for an effective power transfer between the transmitting antenna and receiving antenna. Antennas are such resonant devices whose impedance if matched, deliver a better output.
4. Voltage Standing Wave Ratio (VSWR) and reflected power : The ratio of the maximum voltage to the minimum voltage in a standing wave is known as Voltage Standing Wave Ratio (VSWR). If the impedance of the antenna and the transmission line do not match with each other, then the power will not be radiated effectively. Instead, some of the power is reflected back. The higher the impedance match, the higher the value of VSWR. Reflected power is the power wasted out of the forwarded power.
5. Bandwidth : the interval of frequencies over which a signal is transmitted.
6. Antenna Gain : the forward gain of an antenna, measured in decibels (dBi) reflects the antenna's directional characteristics, i.e., directional as opposed to omnidirectional: the higher the gain in dBi, the narrower the beamwidth and the more directional the antenna.
7. Directivity : it is a measure of how directional an antenna's radiation pattern is. An antenna that radiates equally in all directions would have effectively zero directionality, and the directivity of this type of antenna would be 1 (or 0 dB).

The scattering parameters (S parameters) describe the relationship between two ports in an electrical network. They are measured with Vector Network Analyzers (VNA) and describe the change of the reflected wave and the transmitted wave with respect to the incident wave of the device under test (DUT) by amplitude and phase at different frequencies. The S-parameter matrix provides a relationship between the reflected wave and the transmitted wave with respect to the incident wave of the DUT at each port and for each operating frequency. For example, for a two-port device, four S-parameters representing the bidirectional behaviour of the network as a function of frequency. The S-matrix terms are:

1. S_{11} = input port reflection
2. S_{12} = reverse gain
3. S_{21} = forward gain (linear gain/insertion loss)
4. S_{22} = output port reflection

In practice, the most commonly used parameter is S_{11} and it implies how much power is reflected from the antenna. Hence it is also called as a reflection coefficient or return loss. To be more precise, if the S_{11} equals to 0 dB, then all the power is reflected from the antenna and nothing is radiated. If $S_{11} = -10$ dB, this implies that if 3 dB of power is delivered to the antenna, -7 dB is the reflected power. The remainder of the power was delivered to the antenna. This delivered power is either radiated or absorbed as losses within the antenna. Since antennas are typically designed to be a low loss, ideally the majority of the power delivered to the antenna is radiated.

Commercial SAW sensors are usually sold with their reader that directly gives the temperature value. No further access to the other signal information in the back end of the device is possible.

The interrogation unit of a SAW-Pirani sensor is responsible for measuring the vacuum pressure. It consists of one transmitter antenna which is connected to a Vector Network Analyser and the receiver antenna which is connected to the SAW chip under measurement. Any variation in the temperature of the SAW chip is then captured as a corresponding SAW peak in the S_{11} plot of the transmitter antenna.

Contrary to wireless heating, wireless interrogation of SAW devices is more widespread and commonplace and the technology is already established for macroscopic devices. The wireless interrogation of the SAW device needs an interrogation antenna outside the vacuum chamber and a receiving antenna physically and electrically connected to the SAW device. Several frequency bands are available for SAW devices operation among which 433 MHz, 865 MHz and 2.45 GHz. The higher the operation frequency, the higher the frequency shift that can be observed during SAW pressure sensing. That is why the highest operation frequency of 2.45 GHz was selected. Furthermore, this frequency corresponds to the Bluetooth and WiFi frequency, which keeps options open for the potential transmission of other signals with the same device.

However, the receiving antenna still had operating frequency and size requirements to fulfil in order to be able to communicate with the SAW chip and fit inside the designed housing. The chip operation frequency being 2.45 GHz, the resonance frequency has to be 2.45 GHz and the antenna with its matching circuit needs to fit inside the allocated space. The Tx and Rx antennae also needed to face each other. For this purpose, two ceramic antennae were found and selected to be implemented in the prototype :

1. Chip-Antenna WE-MCA 7488930245 from Würth Elektronik
2. P/N 2450AT18B100 2450 MHz Antenna from Johanson

Both antennas have the same working frequency range between 2.4 GHz and 2.5 GHz but have different dimensions. Figure 4.6 shows the dimensions of the Johanson antenna and Figure 4.7 shows the dimensions of the WE antenna.

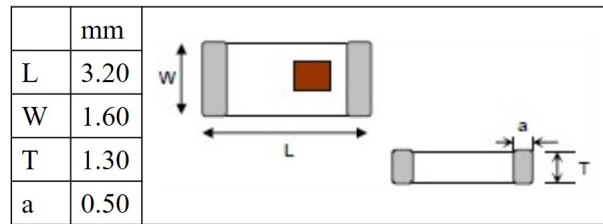


Figure 4.6 – Johanson antenna dimensions extracted from its technical sheet.

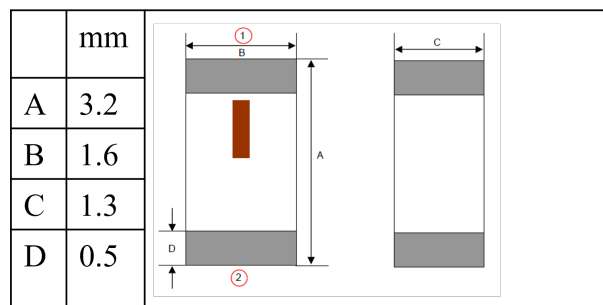


Figure 4.7 – WE antenna dimensions extracted from its technical sheet.

The antenna needs a no ground surface around it of 6.5 mm^2 and a 50Ω feed line. The advocated no ground surfaces for each antenna are available in their respective datasheets provided in appendix.

In telecommunications, a ground plane is a flat or nearly flat horizontal conducting surface that serves as part of an antenna, to reflect the radio waves from the other antenna elements. The plane does not necessarily have to be connected to ground to be used as a reflecting surface for radio waves. Ground plane shape and size play major roles in determining its radiation characteristics including gain. To function as a ground plane, the conducting surface must be at least a quarter of the wavelength $\lambda/4$ of the radio waves in radius.

In microstrip antennas and printed monopole antennas an area of copper foil on the opposite side of a printed circuit board serves as a ground plane. The ground plane must have good conductivity; any resistance in the ground plane is in series with the antenna, and serves to dissipate power from the transmitter. At high frequencies, ground planes are a very good protection against unwanted signal coupling that one can build into a PCB. Other techniques include twisted-pair wiring, coaxial cables and stripline wiring (which uses both a ground plane and some wiring dimension control). Ground planes are also important in low-frequency circuits, because any high-frequency components can accidentally couple (and oscillate).

To be correctly operated those two antennas need a no ground surface around them in addition to a 3.3 nH and 2.7 nH coil and a 1.2 pF capacitor to achieve the 50Ω . The sensitive properties of the antenna are

the bandwidth and the return loss. This antenna has a peak gain of 2.0 dBi and an average gain of 0.5 dBi against a peak gain of 0.5 dBi and an average gain of -0.5 dBi for the other P/N 2450AT18B100 antenna from Johanson. The Wuerth Elektronik antenna is bigger than the Johanson antenna but does not need any matching circuit to have its resonance close to the SAW peak, that is why the size of the PCB is identical for both antennas although they are not the same size. No information about the coupling distance of the antenna is given in the datasheet that can be found in appendix, it was directly tested during the experimental phase.

The return loss is lower in dB for the Johanson antenna without matching circuit (-22.1 dB) which means that the resonance frequency of the antenna can be detected more easily. The passband at -10 dB is 2.36 GHz to 2.59 GHz. For the second Wuerth Elektronik antenna the return loss at resonance is -17.7 dB. Tables 4.5 and 4.6 compare the properties of both antennae.

Table 4.5 – Comparison between Wuerth Elektronik and Johanson antenna.

Antenna	Return loss at resonance	$f_{min}(-10 \text{ dB})$	$f_{max}(-10 \text{ dB})$
WE (without matching circuit)	-17.7	2.31 GHz	2.62 GHz
Johanson (with matching circuit)	-18.5	2.36 GHz	2.59 GHz

The Johanson antenna without matching circuit has a resonance frequency of 2.760 GHz which prevents the detection of any SAW signal in this situation. The coupling of those antennas inside the packaging consisted in preparing the no ground surface, obtaining the coils and capacitors with the right values and ensuring a non metallic path between the transmitting and receiving antenna.

Table 4.6 – Comparison between Wuerth Elektronik and Johanson antenna gains.

Antenna	Peak gain (dBi)	Average gain (dBi)
WE (without matching circuit)	2.0	0.5
Johanson (with matching circuit)	0.5	-0.5

The peak gain of the WE antenna is much higher than the Johanson antenna. The WE does not need any coupling circuit to be operated. That is why the WE antenna was retained for the prototype. For

characterisation at ambient conditions with no size restrictions, antennas were prepared at IMT and designed with the antenna calculator website everythingrf.com.

4.3 Sensing chip

Different materials have been investigated for the substrate and for the IDT electrodes including Lithium Niobate with different cuts, Ti/Au and Aluminum electrodes. Lithium Niobate wafers are available off the shelf but the electrodes are usually manufactured with e-beam lithography. The sensing unit consists mainly of the SAW-Pirani custom designed chip. Different aspects had to be addressed during the design of the chip to optimise its sensitivity through the whole pressure range targeted. To initiate the sensing process, the SAW-Pirani first needs to be heated. This would require a Joule heating resistance physically connected to the chip. The value of the power needed to heat the chip was determined by the simulation, the current provided by the heating coil. The value of the joule resistance had to be aligned with these values. The heating method, the structure of the resistive layer and its position with regards to the chip had to be selected. Based upon the available equipment and the size of the chip, the technical solution selected was sputtering a gold layer at the bottom of the chip. Sheet resistance is applicable to two-dimensional systems in which thin films are considered two-dimensional entities. The gold layer resistance was computed using the formula:

$$R = \rho \frac{L}{A} = \rho \frac{L}{Wt} = \frac{I\rho l}{Pw} \quad (4.4)$$

where ρ is material resistivity which equals $2.44 \times 10^{-8} \Omega\text{m}$, A is the cross-sectional area, L is the length, W is the width and t the sheet thickness. Figure 4.8 plots the thickness of the layer versus the power needed for a defined supply current of 300 mA.

A thickness of 100 nm was selected. In addition, a 5 nm Chromium adhesion layer was inserted. Figure 4.9 shows the designed layer structure of the chip.

The material of the chip had to be chosen among piezoelectric materials. Several piezoelectric materials are used in SAW devices and have different sensitivities to the temperature. Table 4.7 shows the properties of some of them, highlighting Lithium Niobate and its different crystal cuts. Quartz and Lithium Tantalate have a Temperature Coefficient of Frequency (TCF) of 0 ppm/K which means that the resonance frequency does not change with temperature, they are therefore privileged materials for applications that require temperature stability. The TCF indicates gradual changes of the resonant frequency with changing temperature. The material with highest sensitivity to temperature is Lithium Niobate. Different crystallographic cuts lead to different TCF. The electromechanical coupling coefficient reflects the conversion rate of electrical energy into mechanical energy for wave propagation.

The crystal structure of a material changes at the Curie temperature from piezoelectric (non-symmetrical) to a non-piezoelectric (symmetrical) form, and the material loses its piezoelectric properties. This phase

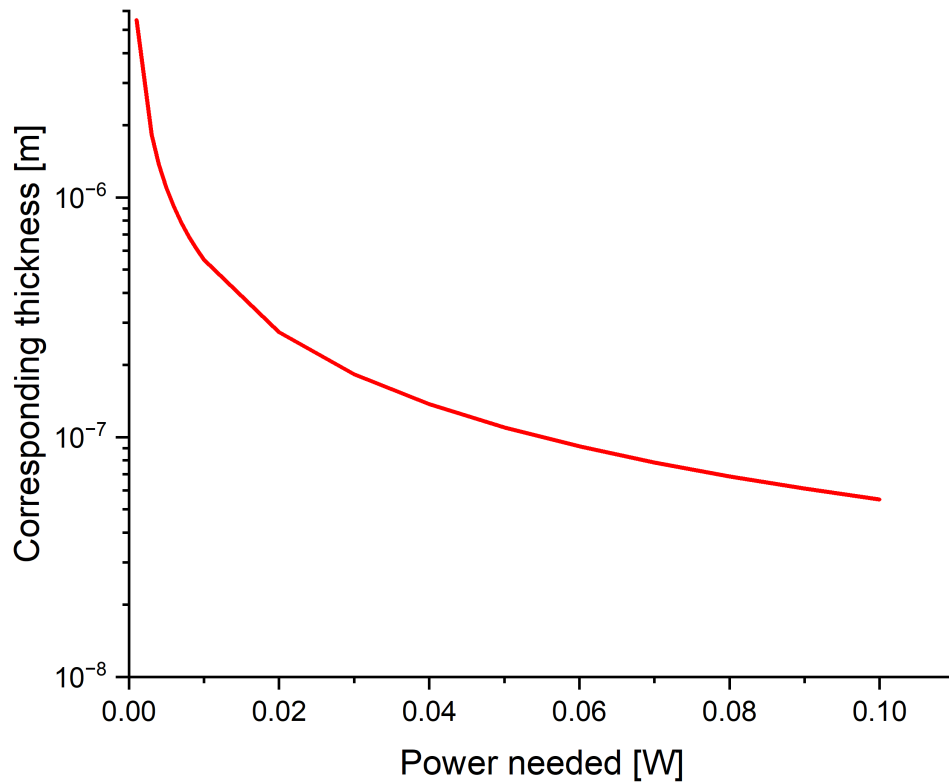


Figure 4.8 – Thickness versus power for a constant supplied current of 300 mA.

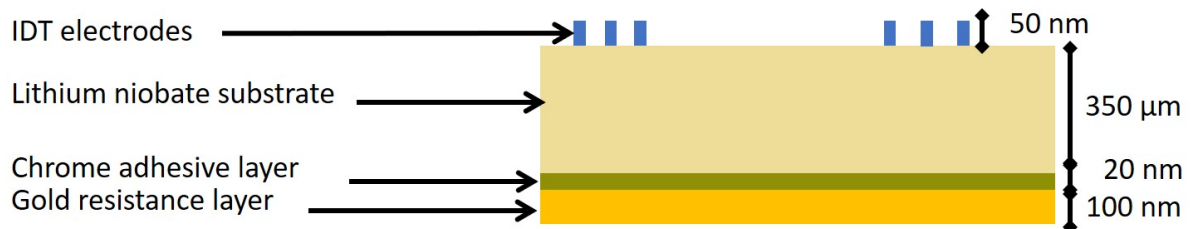


Figure 4.9 – Layer structure of the designed chip.

change is accompanied by a peak in the dielectric constant at that temperature. The Curie temperature, T_c , is expressed in degrees Celsius. The SAW device shall not be used under temperatures higher than its Curie temperature. The Curie temperature of Lithium Niobate is around 1140°C.

The coupling coefficient (sometimes referred to as the electromechanical coupling coefficient) is defined as the ratio of the mechanical energy accumulated in response to an electrical input or vice versa.

The structure of the IDT on top had to be chosen between delay line or resonator. The operating frequency of the chip had to be selected. The operation frequency chosen was the 2.45 GHz ISM band. Selecting the highest frequency available would increase the pressure induced frequency shift, which

Table 4.7 – Piezoelectric materials properties.

Substrate	Wave velocity $V_0[m/s]$	Electromechanical coupling coefficient k_2	TCF[ppm/K]
Quartz, STX	3158	0.16%	0
LiNbO ₃ , Y, Z	3488	4.80%	-94
LiNbO ₃ , 128 rot Y, X	3992	5.30%	-75
LiNbO ₃ , 132 rot Y, X	4000	5.60%	-72
LiTaO ₃ , Y, Z	3230	0.90%	0

would make detection of smaller pressures easier, especially below 0.01 Pa. Besides, this would allow to find coupling components such as transmitting antennas easily.

Resonators are relatively small, usually 1 mm long or less. Delay lines are bigger, at least 6 mm long but enable RFID identification. SAW based RFID tag uses time modulation by reflecting the interrogation signal in a coded waveform that carries the identification information. SAW tags have a simple structure based on delay lines. A SAW tag is composed of an antenna, an IDT and a set of reflectors. Each tag is assigned a unique set of reflectors called code reflectors. Both IDT and reflectors are periodic-structure based and consist of several metallic finger pairs electrodes. The resonance frequency of a SAW-based RFID is:

$$f_0 = \frac{v_{SAW}}{\lambda} \quad (4.5)$$

with:

- f_0 – Resonance frequency
- v_{SAW} – SAW velocity
- λ – SAW wavelength

The SAW wavelength is determined by the periodicity of the IDT.

$$T_i = \frac{2L_i}{v_{SAW}} \quad (4.6)$$

mit:

- T_i – Period in s
- L_i – One way path length in m
- v_{SAW} – SAW velocity in $m s^{-1}$

For the chip variant 3, the electrodes are regular with same width and constant pitch. The metallization ratio, which is the fraction of the IDT surface covered with metal equals to 0.5. The main IDT has a width of $41.508\ \mu\text{m}$ and a length of $30.4392\ \mu\text{m}$. The resolution of the e-beam lithography is $1\ \text{nm}$. The first reflector is located $2\ \text{mm}$ away from the main IDT and has 5 fingers. The second reflector is located $2.1920\ \text{mm}$ from the main IDT and is identical to the first one. The third and last reflector has 20 fingers and is located $3.920\ \text{mm}$ from the main IDT. Figure 5.3 shows the IDT structure. The Aluminum thickness is set at $50\ \text{nm}$ as a trade-off between large reflection coefficient and bulk wave suppression. The dimensions were provided by Dr. Pascal Nicolay that designed the delay line.

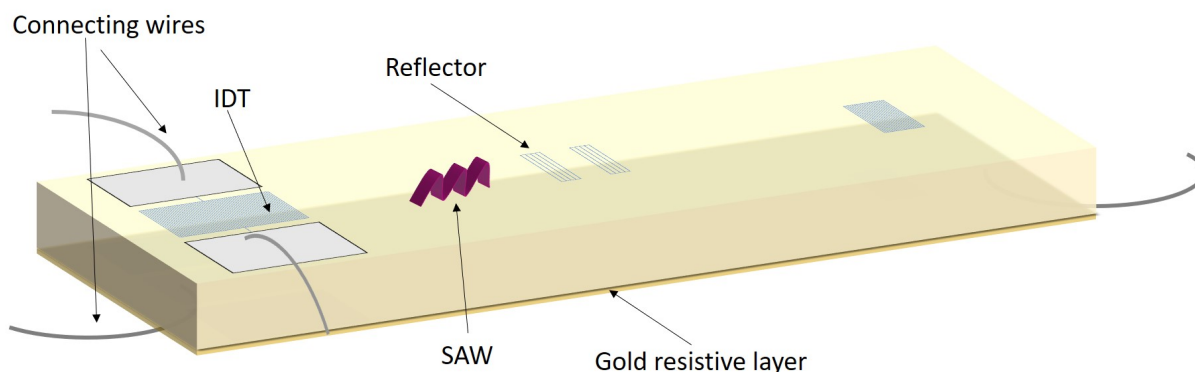


Figure 4.10 – Structure of the designed chip. The Lithium Niobate substrate has a gold resistive layer sputtered and 2 wires for electrical connection at its bottom. On top of the substrate the IDT structure made of the main IDT and 3 reflectors is etched via e-beam lithography. Bonding pads on the top and bottom of the main IDT are electroplated for the electrical connection.

The length, width and thickness of the chip were selected. The sensitivity of the chip to vacuum was optimised. For this purpose the difference of steady state temperature corresponding to each pressure from pressure to pressure has to be as big as possible especially at high vacuum and close to atmospheric pressure. This was the goal of the simulation. The resulting dimensions are $6\ \text{mm}$ by $400\ \mu\text{m}$ by $350\ \mu\text{m}$. The relevance of a coating on top of carbon black to reduce the radiative emissivity was considered [81]. However, the SAW chips are processed in a way during their manufacturing that they already contain carbon black, which applies to the SAW chips used for this thesis as can be seen in the microscope pictures. It protects them at high temperature and it can be seen through their dark color. Nonetheless, simulations showed that a too low value of emissivity would increase the response time and the final temperature without increasing the sensitivity. In the scope of this thesis, several chip variants were used due to practical reasons and design modifications throughout the design, simulation and experimental work. The designs remain similar. The variant 1 is the simulated chip in COMSOL to optimize the thermal behaviour, it was completely designed by Sofia Toto. The variant 2 was ordered from the company SAW Components to perform electrical contacting and the sputtering of the heating resistor. The variant 3 is the chip designed similarly to the one simulated in Comsol but with the length of $6\ \text{mm}$ to be able to contain the RFID function, all the features of the chip were designed by Sofia Toto, except the spacing between the electrodes leading to the RFID function that was designed by Dr. Pascal Nicolay.

The packaged chip variant 4 was ordered from the company SAW Components as well and was used for the characterization measurement at ambient conditions due to the incompatibility of the manufacturing processes applied on the variant 2. The chip variants are summarized in Table 4.1.

4.4 Packaging

A CSSP (Chip Size SAW Package) technology was developed similarly to the system presented in [87]. Following the design of each component, a compact comprehensive design of the sensor housing enclosing all its components (heating unit, interrogation unit, sensing unit and packaging) was imagined. From the beginning the goal of a 1 cm^3 compact cube containing the components was set. The design and selection of all the components was done accordingly, so that they all fit together inside the cube. Figure 4.11 shows the ideal structure of the sensor imagined. The electronic components of the heating and interrogation unit would be in a PCB and a microchannel would cross the cube and contain the sensing chip in contact with the sensed gas. Different geometries were considered for the sensor. First, an empty box with the SAW-Pirani chip at the bottom was implemented in COMSOL.

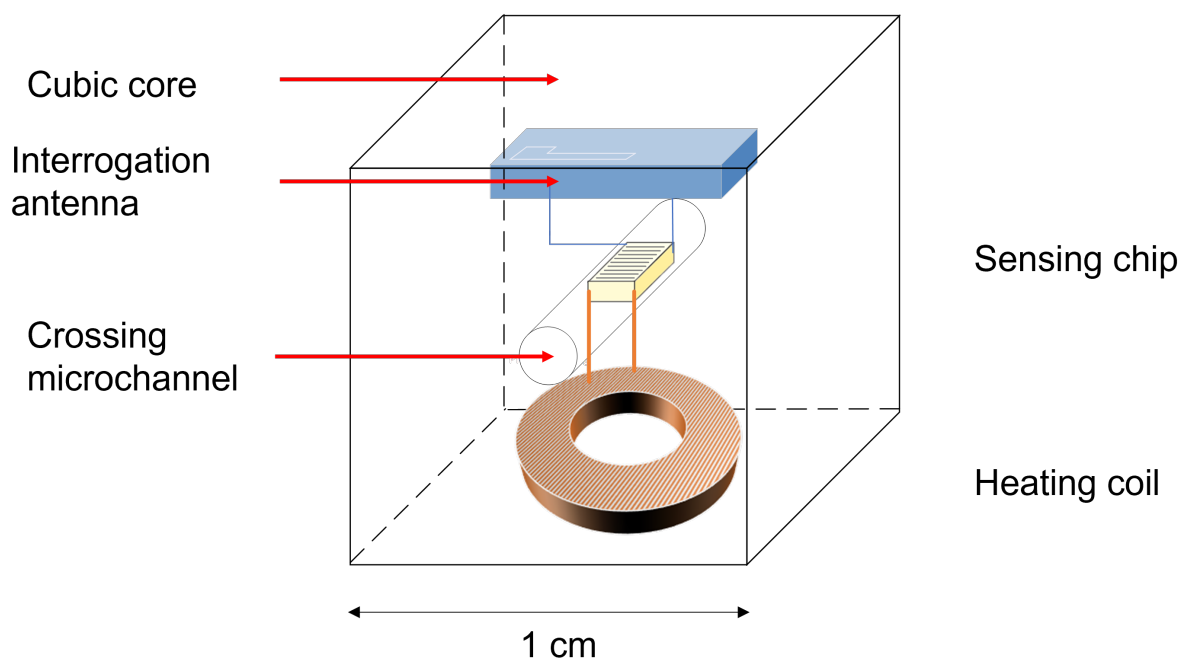


Figure 4.11 – Structure of the wireless vacuum sensor. The design shows a $1 \times 1 \times 1\text{ cm}^3$ Polymethylmethacrylate (PMMA) cube crossed at its center by a microchannel corresponding to the packaging variant 1. The sensing SAW–Pirani chip (variants 1,2 or 3) is inserted inside the microchannel. The heating coil and the interrogation antenna are buried inside the core of the sensor.

Different geometries were also considered for the cross section of the microchannel: circular, quadratic with holding cavities and quadratic with size matching. Figure 4.12 shows the different geometries. For

manufacturing concerns and to reduce solid conduction, the circular section was retained for the first prototype.

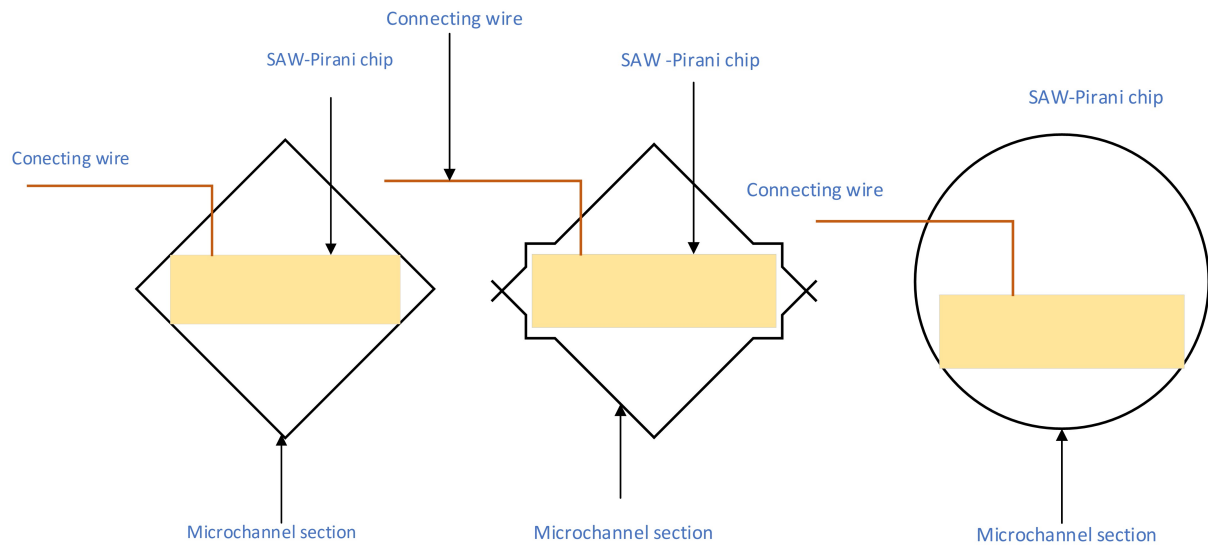


Figure 4.12 – Possible cross sections for the microchannel crossing the sensor: quadratic with holding cavities, circular and quadratic and size-matching.

After testing the components individually, adjustments had to be made to the ideal design to make the components fit. The PCB containing the heating and interrogation unit had 11 mm by 15 mm by 1.3 mm thickness which required a bigger housing. The packaging was designed using the CAD software AutoCAD Inventor. Two different designs were prepared according to the positioning of the coil. The first option consisted in a containing hole for the coil. The objective was to reduce the size of the sensor in case a lateral positioning of the coil was possible. The second alternative was the retained solution which is a 19 mm by 15 mm by 11 mm PTFE block. Figure 4.13 shows the final packaging.

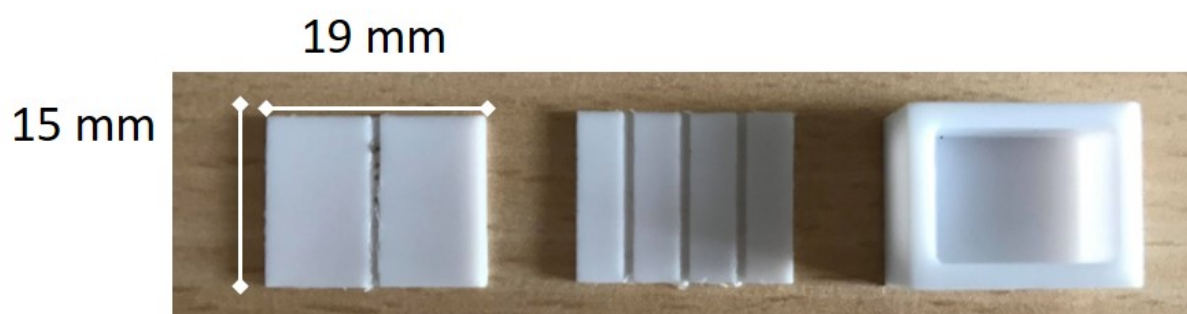


Figure 4.13 – Possible cross sections for the microchannel crossing the sensor: quadratic with holding cavities, circular and quadratic and size-matching.

The final design containing the adjustments was the one of the first prototype and is shown in Figure 4.14.

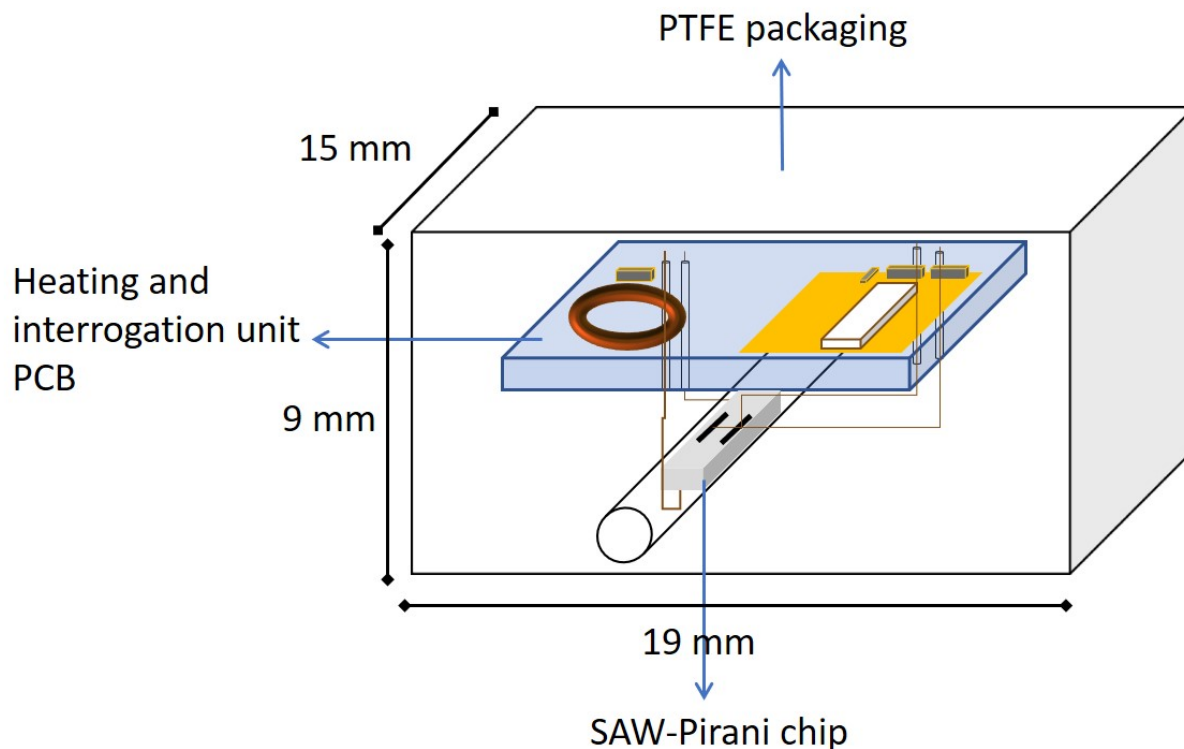


Figure 4.14 – Packaging variant 2 with chip variant 3, antenna variant 2, PCB variant B combined.

4.5 PCB

The heating unit of the sensor and the interrogation unit were inserted together inside a Printed Circuit Board (PCB). Certain factors had to be considered before proceeding to the final PCB:

- The orientation of the secondary coil (planar or lateral)
- Separate PCBs for two different antennae based on the size requirements to fit inside a cubic packaging
- Arrangements to test two types of SAW chips, one which is attached to the back of the PCB (this is for the testing purpose) and the other which is outside the PCB (the main SAW chip which is inside the micro-channel)
- Preparation for the position of other components such as capacitors and inductors for impedance matching and resonance frequency tuning
- Finding the position of holes for the connection of the PCB to the SAW chip placed outside

The receiving part of the heating unit placed on the PCB consists of the receiver coil and its coupled 220 nF SMD capacitor. The final PCB contains the receiver coil, the coupling capacitor for the coil, the antenna, the matching circuit for antenna and the SAW chip. Thus, both the heating unit and the

interrogation unit were placed on a single PCB of 15 mm length and 11 mm width. Based upon size and bandwidth requirements, two antennas were selected. Figure 4.15 shows the two alternative layouts, A and B designed for each antenna.

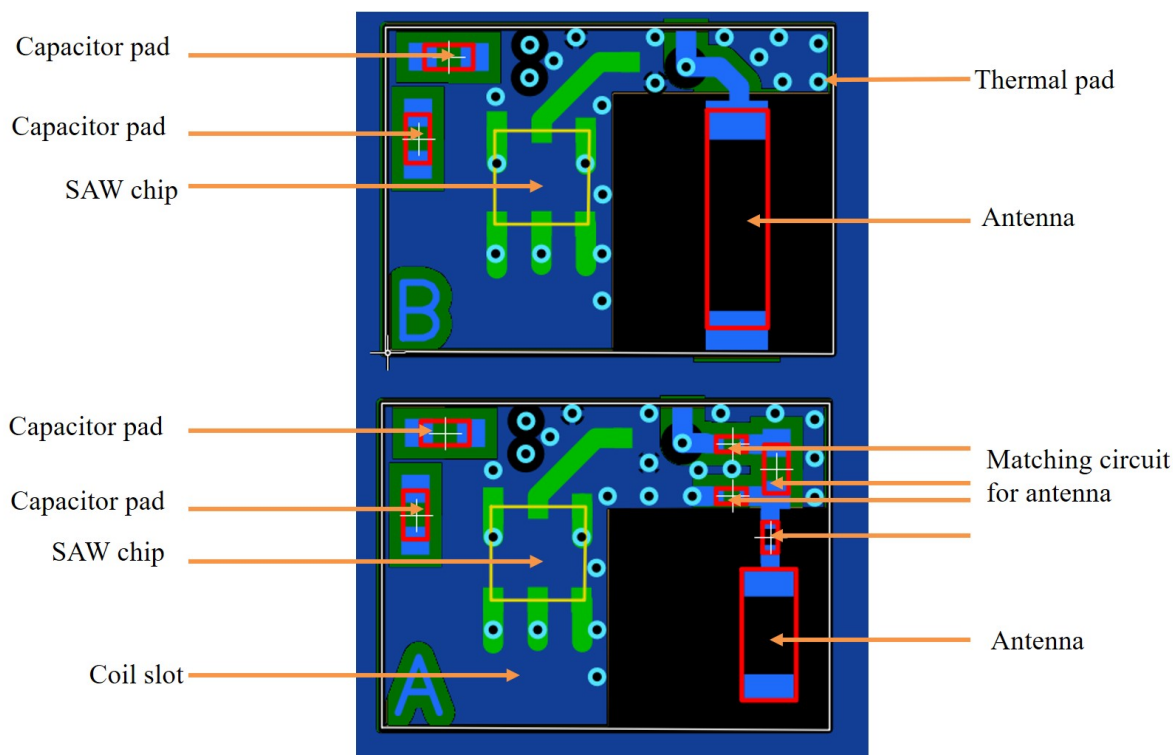


Figure 4.15 – Two PCB layouts designed with Sprint Layout.

The alternative B was designed for the Wuerth Elektronik antenna and the alternative A was prepared for the Johanson smaller one. Additional pads were included for capacitors. The black surfaces correspond to the non ground surfaces required by the antennae. The receiver coil is connected at the left side of the PCB.

Four holes are crossing the PCB. Two holes aim to enable the connection of the secondary coil to the SAW chip for heating via thin gold wires and the other two aim to connect the SAW chip to the antenna measuring the frequency shift.

Matching the impedance between the source and the load is important to obtain a better power transmission. In the PCB design for the antenna, the SAW chip and the receiver antenna should be perfectly matched to 50Ω . The SAW chip and the antenna should be connected with a 50Ω impedance trace. The track width corresponding to this was calculated using the following equation (obtained from <https://www.everythingrf.com/rf-calculators/microstrip-width-calculator>):

$$w = \frac{7.48 \times h1}{e^{\left(z_0 \frac{\sqrt{\epsilon_{r0} + 4i}}{87}\right)}} - 1.25 \times t \quad (4.7)$$

with:

- z_0 – single ended impedance
- ϵ_{r0} – is the dielectric constant
- w – width
- t – trace thickness which equals 35 μm
- $h1$ – dielectric thickness of 0.38 mm

The resulting thickness is 0.642 mm.

5 Experiments

5.1 Manufacturing

The manufacturing process aimed to prove that the miniaturized wireless vacuum sensor is manufacturable. The aim of the manufacturing operations carried out was to manufacture and assemble a working prototype of the sensor designed and simulated. This chapter assesses all the manufacturing processes applied in order to obtain the sensor prototype.

5.1.1 Experimental procedure

The sensor consists of four main subsystems: the sensing unit, the heating unit, the interrogation unit and the packaging. Each subsystem contains a few elements and required several manufacturing operations. The elements were individually manufactured and assembled:

1. The heating unit is made of a Tx part outside vacuum and an Rx part inside vacuum.
2. The interrogation unit is also made of a Tx part outside vacuum and an Rx part inside vacuum.
3. The sensing unit consists of the sensing chip and the wires that connect it to the rest of the sensor.
4. The packaging is made of several parts in polymer.

A small PCB was designed to include the Rx part of the heating unit, the Rx part of the interrogation unit and the sensing unit. This compact structure gathers all the components inserted inside vacuum. First the manufacturing of this PCB is explained, followed by the manufacturing of the sensing chip, the heating unit Tx part, the interrogation unit Tx part and finally the packaging.

PCB manufacturing and soldering

The PCB was designed in a way to contain all the components of the heating unit Rx, the interrogation unit Rx and the sensing unit. It had also to comply with requirements for positioning such as no ground surface and $50\ \Omega$ feed line for the antenna as well as contain the right coupling capacitor for the receiver coil of the heating unit Rx. The result was a 15 mm by 11 mm by 3 mm PCB track. Figure 5.1 shows the manufactured PCB prior to the soldering of the components. The circuitry of the sensor, consisting

mainly in the heating and interrogation unit was manufactured. The structure of the PCB was designed using the software Sprint Layout and ordered for manufacturing from the company Beta Layout.

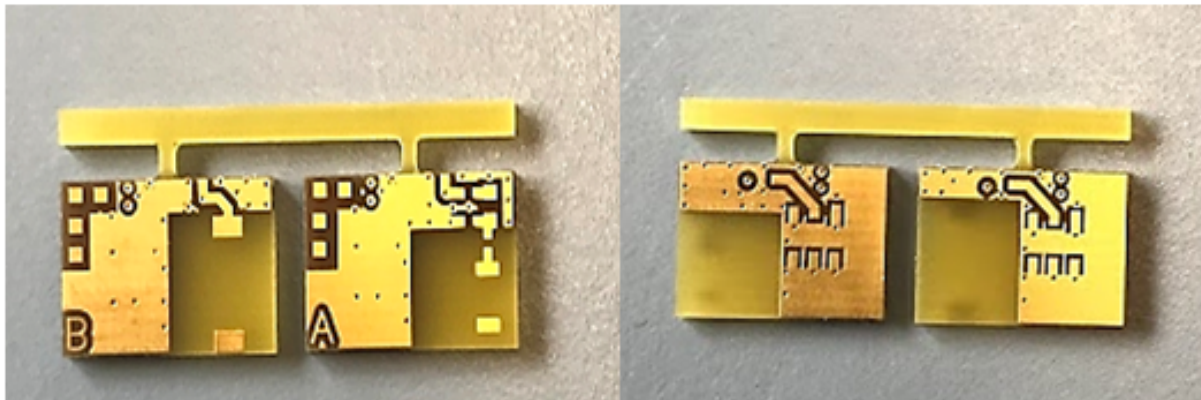


Figure 5.1 – Manufactured PCB prior to soldering. On the left side, the top surface of the PCB is depicted, on the right side the bottom surface of the PCB is depicted. Two different alternatives for two different antennas were prepared. The alternative A was prepared for the antenna P/N 2450AT18B100 from the company Johanson Technology and the alternative B was prepared for the antenna WE-MCA 7488940245 from Wuerth Elektronik. The image on the left side shows the top layer with the pads for the antenna and the coil. The image on the right side shows the soldering pads for the SAW chip. On the top layer, the receiver coil and the receiver antenna were connected and at the bottom layer, the SAW chip was connected to the receiver antenna.

The components were soldered using the Stannol KS100 soldering machine at a temperature of 300 °C. Figure 5.2 shows the complete PCB with all the components soldered. The image on the left side shows the top layer with the pads for the antenna and the coil. The image on the right side shows the soldering pads for the SAW chip.

The PCB consists of four layers. On the top layer, the heating unit and the interrogation unit were placed and at the bottom layer the SAW chip was placed. Figure 5.2 shows the complete PCB with all components soldered. The antennas prepared at IMT were designed with the antenna calculator website <https://www.everythingrf.com>.

Sensing chip

The chip variant 3 from Table 4.1 is 6 mm long, 400 μm wide and 350 μm thick. The length and width were set with the simulation for optimised thermal behaviour while the thickness corresponds to lithium niobate wafers available off the shelf for further clean room processing. The structure of the IDT electrodes on top of the chip is a delay line. The IDT metallic electrodes are aluminum electrodes etched on top of the piezoelectric substrate via e-beam lithography. To assemble the first prototype, the SS2452BB2 chip manufactured by the company SAW Components (Dresden, Germany) with similar properties was used, which corresponds to the chip variant 2 in Table 4.1. Figure 5.3 depicts the SAW Components selected chip.

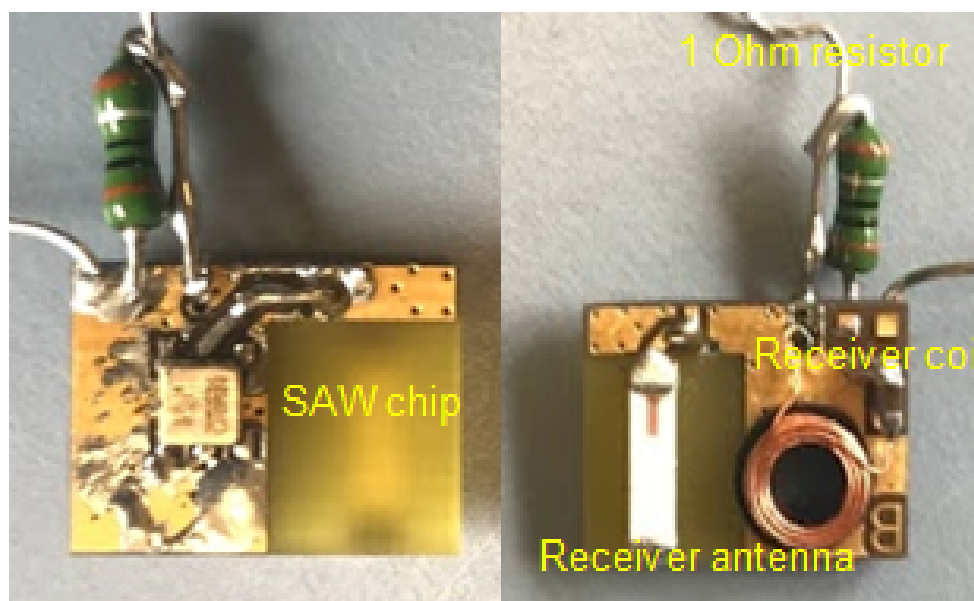


Figure 5.2 – PCB with soldered components. On the left side the bottom part of the PCB containing the SAW chip, on the right side the top part of the PCB containing the heating unit Rx part and interrogation unit Rx part.

It is a 2.45 GHz resonator structure made of lithium niobate that has the same width and thickness as the designed chip i.e. $400\ \mu\text{m}$ by $350\ \mu\text{m}$. Only the length of $1\ \text{mm}$ instead of $6\ \text{mm}$ is different which makes the power transfer constraints for the first tests less stringent, since 6 times less energy is necessary to heat the chip. The bare die on foil chip was ordered and modified prior to its insertion inside the sensor. Three main operations were applied to it:

- the sputtering of a $100\ \text{nm}$ thick gold resistive layer at the bottom of the chip
- the soldering of the resistive layer to the rest of the sensor
- the wirebonding of the SAW IDT to connect it to the rest of the sensor

Figure 5.4 below shows the microscope picture of the chip before the processing. A Keyence Digital Microscope VHX 600 was used here.

The three processes need to be compatible with each other [88]. This induces several constraints:

1. thickness of the gold layer needs to be compatible with the soldering
2. adhesion between the gold layer and the lithium niobate crystal needs to be sufficient to avoid delamination during the soldering

A gold layer of $100\ \text{nm}$ thickness was sputtered at the bottom of the chip. An adhesion Chromium layer of $20\ \text{nm}$ thickness was evaporated between the gold and the Lithium Niobate substrate which enabled the soldering. Figure 5.5 shows the layer structure of the chip. The Figure is repeated for the reader's

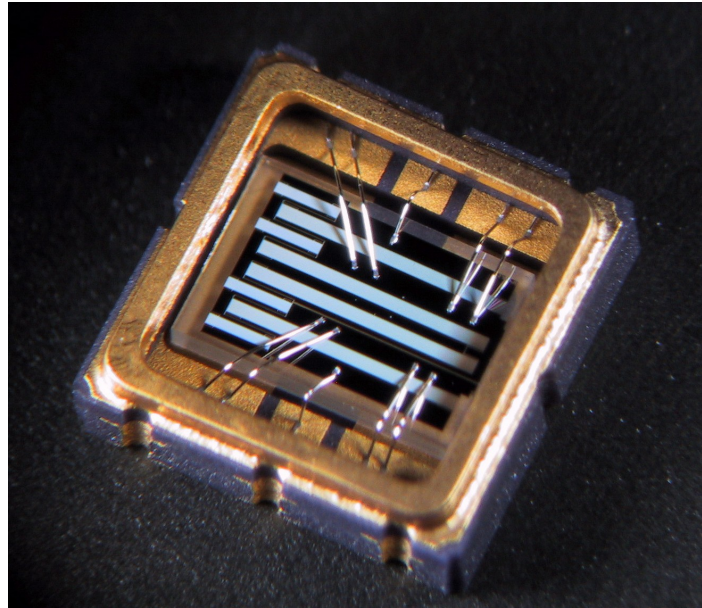


Figure 5.3 – Packaged SS2452BB2 SAW chip from SAW Components.

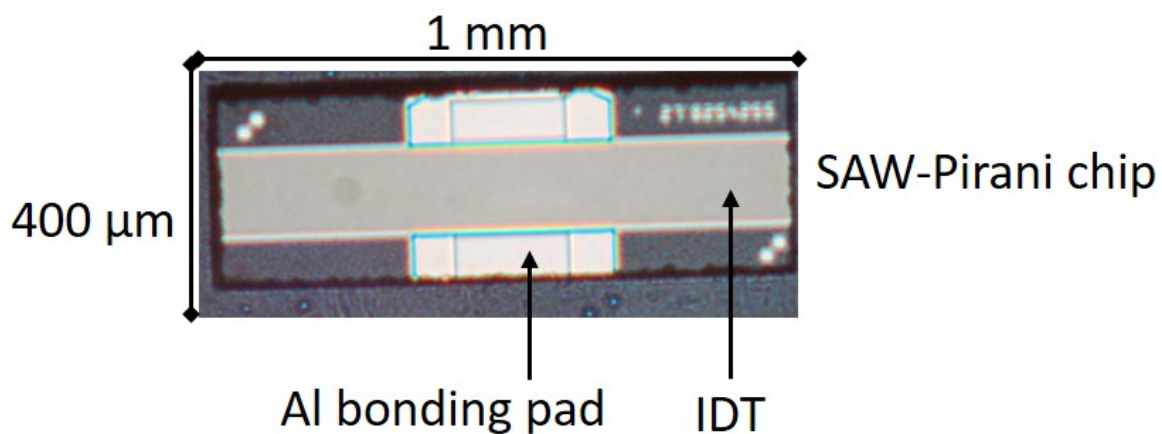


Figure 5.4 – SAW chip with IDT resonator structure prior to manufacturing.

convenience. The gold layer (Figure 5.11) was sputtered using an UNIVEX 400 from the company Leybold using the electron beam evaporator Ferrotec-EVM-6. 20 nm of Chromium then 100 nm of gold at a speed of 10 rpm were sputtered with no tilt angle.

The soldering was performed at the bottom side of the chip using a 100 μm thick Aluminum wire which was rather challenging due to the size of the chip, which is shown in Figure 5.10. The SAW IDT was connected to the rest of the sensor via ball wedge bonding. The chip was bonded to the PCB with a TPT Wirebonder. A 25 μm diameter wire at a temperature of 180 °C was wired by applying a force of 84 mN during 100 ms (Figure 5.12).

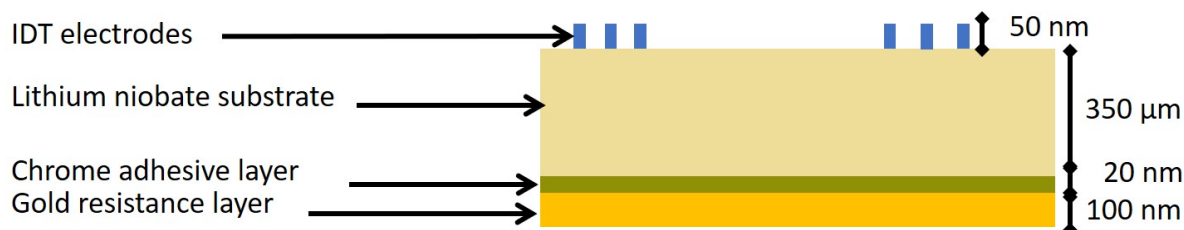


Figure 5.5 – Layer structure of the chip. On the bottom a 100 nm gold layer. On top of it, a 20 nm Chromium layer. On top of it, the Lithium Niobate substrate. On top of it, the Aluminum IDT electrodes.

Heating unit Tx part

The heating unit is responsible for providing current to the Joule resistive layer of the chip that heats it. It is materialised by a transmitting unit and receiving unit. The transmitting unit is located outside the vacuum chamber and consists of a Tx coil and its power supply circuit. The power circuit consists of a power source and an amplification MOSFET circuit. The receiving unit is located inside the vacuum chamber and consists of a receiver coil, its coupling capacitor and the chip. This wireless power transfer circuit was designed and simulated using the TINA software prior to its manufacturing. The layout of the circuit was generated with the software Sprint Layout. Table 5.1 shows the components that were used for the MOSFET circuit design. The two main components of the Tx circuit are the Tx coil coupled to the Rx coil inside vacuum and the MOSFET which is used as a power amplifier. The MOSFET IRLIZ44N from Infineon was used in the transmitter circuit as a power amplifier and the circuit was initially simulated using a transmitter coil of 33.6 μH and the receiver coil of 7.2 μH . A heat sink was prepared for the MOSFET and a fuse that turns the MOSFET off when its temperature exceeds 70 °C. A fuse is an electrical safety device that operates to provide overcurrent protection of an electrical circuit. Its essential component is a metal wire or strip that melts when the temperature exceeds a certain level. When too much current flows through it the current is interrupted. The fuse is a passive component. Table 5.1 contains a description of the complete equipment used for induction coupling.

Table 5.1 – Components of the MOSFET circuit.

Components	Values
MOSFET	IRLIZ44N
Resistor	12 k Ω , 1 k Ω , 1 Ω
Zener Diode	6.8 V and 5.1 V
Capacitor	100 μF , 478 μF , 47 μF , 220 nF
Inductor coil	6.4 μH , 7.2 μH , 10 μH
Potentiometer	100 k Ω

The final circuit was created using the components and devices available at the electronics lab of the KIT IMT. An Tektronix AWG610 arbitrary waveform generator from operating between 1 kHz and 3 MHz was used. An oscilloscope from Memoryrime Voltcraft VDO-2152 A was used to monitor the output signal.

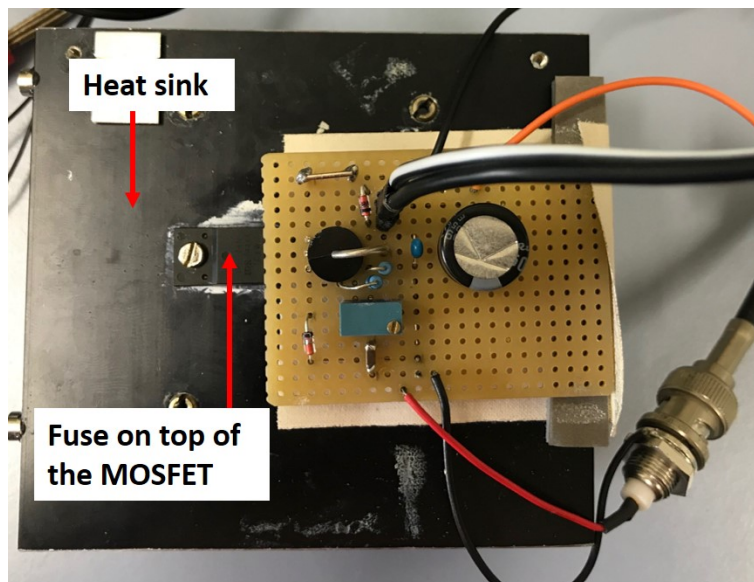


Figure 5.6 – PCB for the MOSFET.

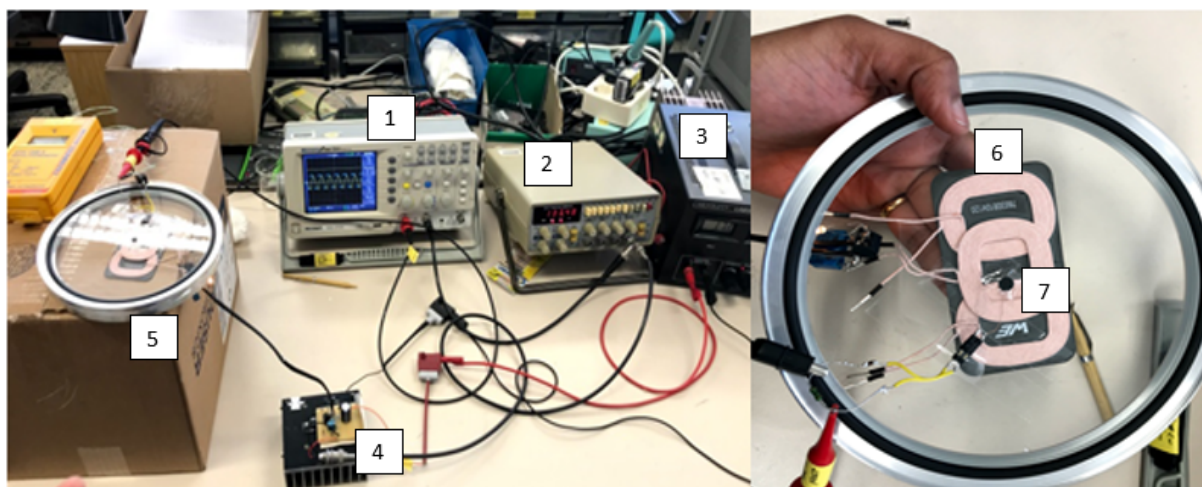


Figure 5.7 – Complete heating unit. On the left side the Tx part and on the right side the Rx part. (1) Oscilloscope (2) Arbitrary Waveform Generator (3) Power source (4) MOSFET circuit (5) Tx and Rx coils (6) Tx coil (7) Rx coil.

Interrogation unit

In order to interrogate the prototype, a transmitting antenna connected to the Network Analyzer is necessary. For this purpose, the WE-MCA 7488940245 from Wuerth Elektronik antenna was soldered on the PCB structure used for the sensor and connected to the Vector Network Analyzer via SMA cable.



Figure 5.8 – Transmitting antenna connected to the Mini VNA Tiny.

Packaging

The packaging was designed in a way to enclose the PCB and the sensing chip. It was manufactured in three parts to allow a flexible mounting of the components. The lateral channels are made for gluing. The central channel has four holes for the wires to cross it. Figure 5.9 shows the manufactured packaging. The figure is repeated for the reader's convenience. The packaging was manufactured using an FP3 NC Dialog 11 milling-machine. Prerequisites for this machine include a minimum thickness of 2 mm for the material to mill and a minimum diameter of 100 μm . After the packaging was manufactured, four 600 μm diameter holes were drilled in the middle of the microchannel to allow the wires to cross the packaging. The polymer housing was made with Polytetrafluoroethylene (PTFE). This material has been selected due to its self-lubricating, electrical insulating and low outgassing properties. Its electrical insulating properties are interesting for wireless operation since it does not absorb the energy radiated to the coil and antenna. The packaging has been designed based on the geometry requirements of the PCB and its components.

5.1.2 Results

In Figures 5.10 and 5.11, the results of the applied processes on the chip are depicted. The pictures were taken with a Keyence Digital Microscope VHX 600 microscope.

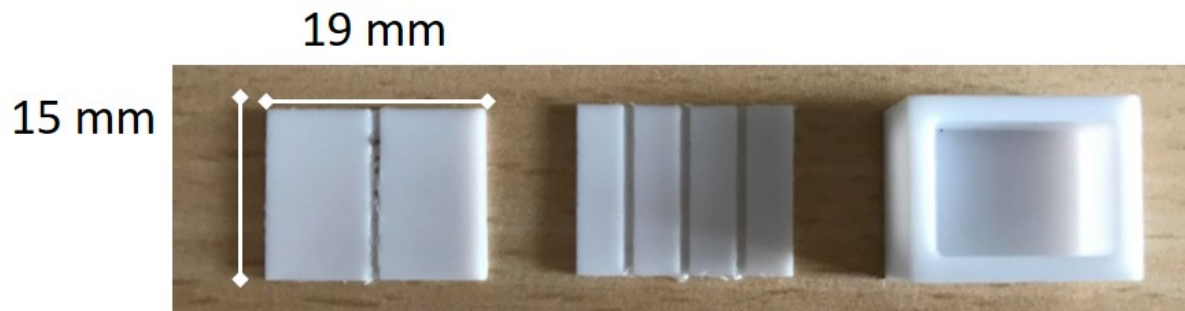


Figure 5.9 – Sensor PTFE packaging. The left piece represents the top part of the channel containing the 4 holes at its middle. The middle part corresponds to the bottom part of the channel with the 2 lateral channels for the glue. The right part corresponds to the top cover of the sensor covering the PCB.

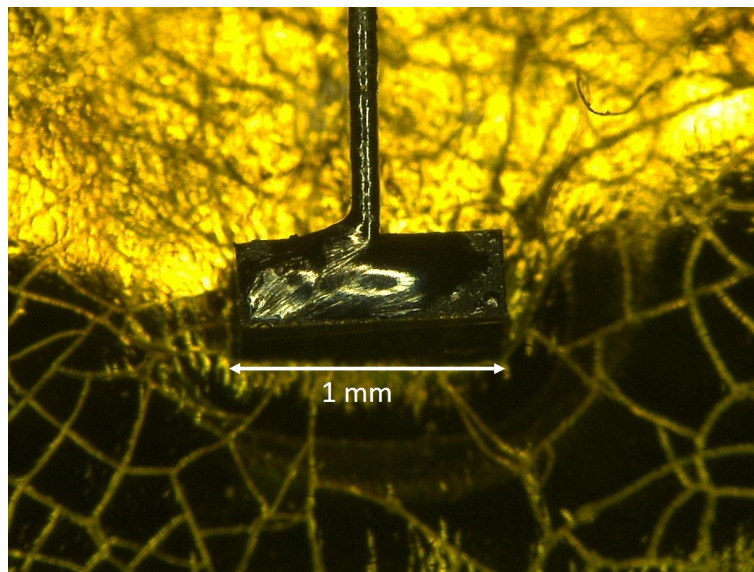


Figure 5.10 – Manufacturing of the heating resistive layer and electrical contacting of the chip. Soldering a $100\ \mu\text{m}$ diameter aluminum wire on the gold layer at the bottom of the chip. The chip is located at the center and placed on a metallic film for protection purposes.

The manufacturing resulted in the assembly of all the components together. The packaging, the PCB with the chip and both Rx parts, the heating unit Tx circuit connected to power source and oscilloscope, the interrogation antenna connected to VNA.

5.1.3 Discussion

Many parameters had to be taken into account and several compromises had to be found during the manufacturing and assembly of the prototype. After the design and the simulation were finalised, a prototype was manufactured using the available equipment and technologies. A compromise had to be

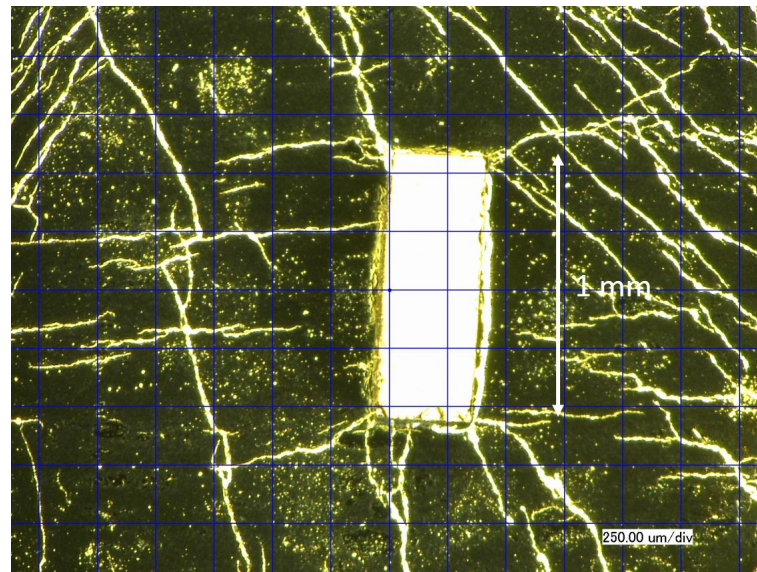


Figure 5.11 – Sputtering of the gold layer at the bottom of the chip.

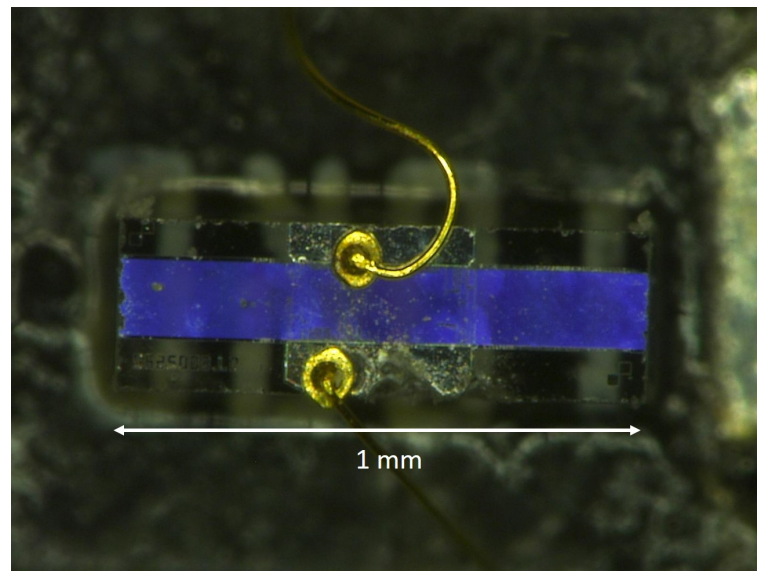


Figure 5.12 – Wirebonding 25 μm gold wire on aluminum pad(c).

found between all the equipment and technologies available. Several manufacturing processes and technologies were combined to assemble the prototype of the sensor. Their compatibility with one another was assessed.

Electrical contacting of the chip

To be able to provide power to the chip and obtain the measurement signal, it has to be electrically contacted to the rest of the sensor core. For this purpose, using the resources of semiconductor packaging, several processes were applied and critical parameters were identified. The chip needs to be soldered in order to be suspended without any substrate. This way, all the heat is transferred to the chip and not

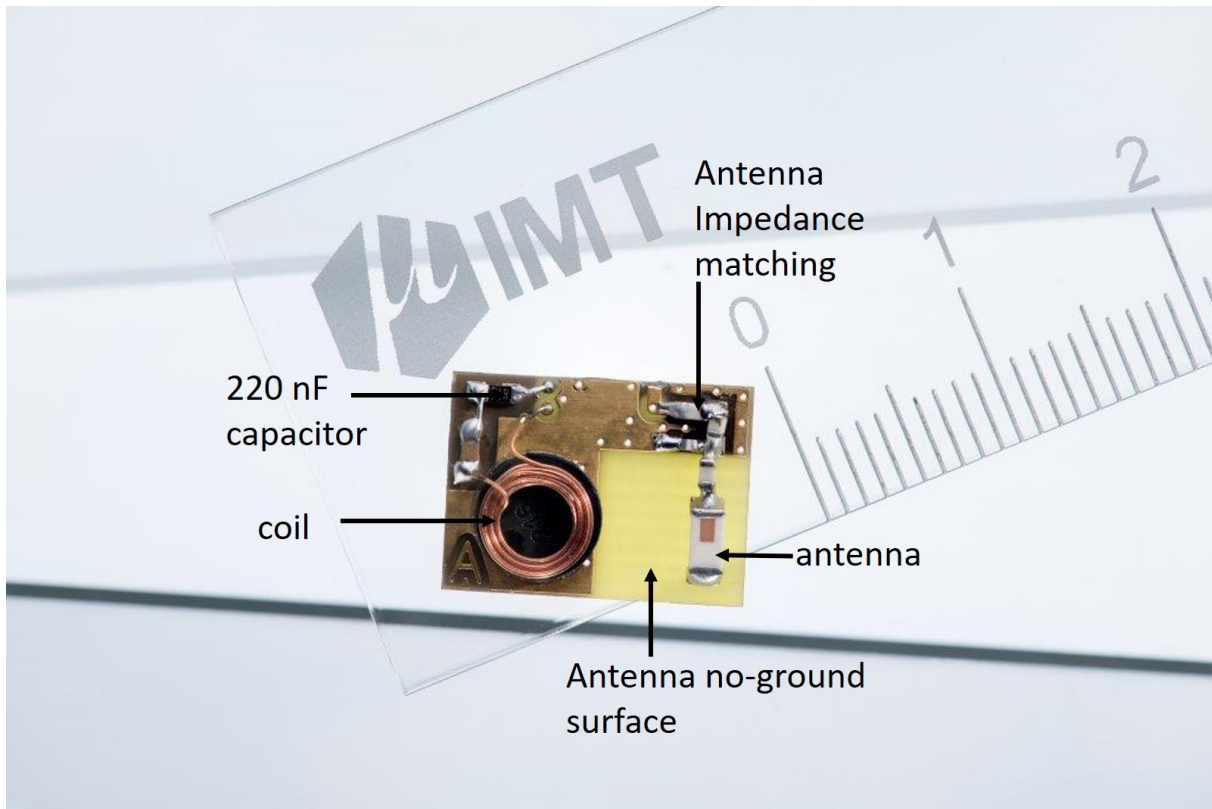


Figure 5.13 – PCB containing the heating unit and interrogation unit of the sensor.

dissipated in the substrate. Usually, chips are soldered on a much larger substrate providing mechanical stability so that relatively big soldering pads compared to the chip size are also possible. The Joule resistive layer at the bottom of the chip needs to be soldered and connected to the receiver coil. The top of the chip containing the SAW IDT already has Aluminum bonding pads and needs to be wirebonded to the receiver antenna.

The properties of the bonding pads on the top close to the SAW IDT have to be taken into account. Several electrical contacting technologies are available at the IMT and at the KIT in general which include automatic wirebonding machines, hand wirebonders and hand soldering as well as experienced technicians. A wide range of wire materials and thicknesses is also available. The pad and surface materials have to be compatible with the wire and the process used. In our design, the gold bonding wires have two functions: electrical connection of the chip to heating and interrogation units and mechanical support of the chip. The electrical connection is a conventional function of wires. However the mechanical support function induces supplementary requirements on the wires and the wirebonding process itself. It is still a challenge to suspend such a tiny chip just using bonding wires. The first constraints for the electric contacting are the dimensions of the chip which are already demanding. The SAW chip substrate is too small to be held with any support. The manufacturing possibilities for the resistive gold layer at the bottom of the chip were investigated. This corresponds to the maximum thickness that could be sputtered by the available machine.

The quality and success of the hand soldering process depends mainly on the experience and the skill of the technician performing it more than the equipment used. Broadly speaking, the wirebonding machine constraints are more stringent than hand soldering, this is why hand soldering was used. In many cases like ours, hand soldering remains the best solution for electrical contacting in comparison with all the machines that impose many constraints. The conventional wirebonding process on a PCB is between two points one on the chip and one on the PCB. The challenge in our case is to leave the wire suspended in the air. In [89], process optimisations are performed on gold wirebonding in order to increase the yield and bond strength. Hardbaking and surface activation of the bonding pad improve the metal adhesion. In order to avoid failure modes such as delamination, optimised processes using commercial wirebonding technologies with no need for more equipment should be sufficient.

Copper wire is well identified as a harder material compared to gold wire in nanoelectronic packaging. However, many companies operating in microtechnologies offer tools that can assist hand soldering like micromanipulators or gamepad control for microstructure that facilitate the soldering process and increases the success chances. The German company Kleindiek Nanotechnik released a soldering system for microfabrication using a gamepad control to monitor the position and the movement of the soldering head, which could make the soldering operation on tiny surface easier, more convenient less risky and less dependent on the operator's manual know-how.

Several attempts to sputter were done. But afterward the soldering took place. The thickness of the gold layer and the adhesion chromium layer are influencing parameters for the success of the soldering later on. The soldering succeeded after the chromium layer on top of the gold was inserted.

IDT

The operation frequency of the SAW IDT was selected for its availability, its convenience and its compatibility with the transmission of other kinds of signal such as Bluetooth and WiFi. The frequency determines the dimensions of the IDT electrodes. The dimensions of the IDT electrodes determine the manufacturing process that needs to be used. A new IDT was designed tailored to the dimensions of the chip extracted from the simulation ; still the dimensions of the electrodes are a standard for the 2.45 GHz frequency range ISM band and should not raise any manufacturing challenge [54]. The dimensions of the electrodes determine the manufacturing process required. In the present case, it is electron beam lithography that needs the preparation of a mask. The choice of a delay line as the SAW IDT structure increases the length of the chip and therefore the Surface to Volume ratio and enables the identification of the sensor within a network. Indeed, the delay of the peaks due to the reflectors enables the RFID function. In [56], the SAW IDT fingers were manufactured via e-beam lithography with Crestec CABL-9500C equipment.

Packaging

The minimum thickness of the packaging possible to manufacture at the IMT facilities was 2 mm, which increases slightly the interrogation distance compared to the nude PCB without packaging. Still, the packaging protects the sensor from contamination and especially the chip in the case of a regular operation of the sensor in harsh conditions. PTFE as a packaging material was a reasonable choice for a first prototype, however an improved version of the prototype could be made of Code 9658 ceramic for better stability in vacuum and a better protection of the chip. [77] assesses the outgasing of certain materials in vacuum. Teflon (PTFE) does not outgas in high vacuum.

Wave propagation

The sensor operates via the transmission of two distinct waves. The antenna wave being in the Gigahertz range is more sensitive than the coil wave in the Kilohertz range. Indeed, during the experimental phase in the lab, finding the right position for the interrogating antenna was more delicate than for the coil and the signal from the interrogation antenna was easily lost, unlike the induction coupling.

That is why position of the antenna inside the vacuum chamber is more critical and should be the closest to the outside environment. A coupling distance of 1 cm was reached between the Tx coil and the Rx coil but the coupling coefficient was very poor around 5%. Since the chip needs very few energy for heating, this is not an issue for operating the sensor.

The innovation and the challenge brought by this new design is the processing of the chip from both sides from the top and the bottom which is not common in semiconductor technology and wafer front end processes. The chips are usually glued or attached from their bottom to the wafer or to a substrate and only the top part is processed.

However, in order to be able to miniaturize significantly the sensor and to eliminate solid conduction from the heat transfer balance a suspension of the chip is required, which in practice can be achieved by using thin wires that suspend mechanically the chip from 4 sides in addition to the electrical contact providing the heating current to the joule resistance directly at the bottom of the chip.

Long term durability

After achieving successful processes such as bonding and soldering and assembling a working prototype, one may ask himself how the sensor will behave in the long term. The insertion inside a remote vacuum chamber, the contamination from the environment and corrosion may become issues. Nevertheless, providing a plasma cleaning step (typically a combination of argon and oxygen) can enhance the bondability of gold wirebonding onto aluminum bondpad [90].

Putting the work into perspective

To put this work into perspective, the prototype developed here is the smallest SAW chip being used as a pressure sensor for SAW-Pirani sensing. No attempt to suspend a microchip by only wires was mentioned in the literature. In [11], Nicolay et al. implemented a 10 mm by 3.1 mm by 1.8 mm SAW tag with a resistor glued on top of it which is more than 10 times bigger than the chip presented here. The heating is also performed by means of induction coupling providing current to the 35 Ω heating resistor. The transmitting coil is provided with a 10 V AC supply voltage at a frequency of 125 kHz. The receiving coil has an inductance of 10 μ H and is connected in parallel to a 0.1 μ F capacitor to achieve the 125 kHz desired resonance frequency. The heating power provided to the resistor equals to 1.5 W whereas it equals 100 mW in our case for chip variant 4 from Table 4.1. The coupling distance between the Tx and Rx coil is 15 mm against 10 mm in our case. In [11], the material of the vacuum window is fused quartz which has a dielectric constant of 3.78 whereas in our case, a PMMA window is used which has a dielectric constant of 3. The response time in [11] equals to 5 min whereas in the presented case it equals to 1 min approximately. Besides, according to the computations, the designed sensor should show a much higher sensitivity in the low pressure range.

In [10], a silicon microbridge acts as a heat sink in the same way as the microchannel in our case. Two different gas gaps are available on top and at the bottom of the chip. The top gap is 50 μ m thick and the bottom gap is 300 μ m thick against twice 125 μ m in our case.

In [43], the optimum link design efficiency reached is 80% and an efficiency of 20% is reached at 20 mm coupled distance by self-developed coils whereas in our case a 10% efficiency is reached at 10 mm distance due to the small size of the receiver coil.

In [91], during wafer manufacturing, higher processing temperature yield darker wafers. For a given processing temperature, wafers with ground surfaces darkened more than polished wafers. The darkness affects the surface emissivity of the chip and therefore its radiative heat transfer.

Recommendations for future work

Several manufacturing processes and technologies were combined to assemble the prototype of the sensor. Their compatibility with one another was assessed. All the designed components were manufactured and assembled. All the operations performed on the chip were successful. However, the soldering at the bottom of the chip destroyed the IDT structure at the top. The wires were able to sustain mechanically the suspended chip. The holes drilled on the packaging allowed the wires to connect the chip to the antenna and the coil. The PCB was designed in a way to minimize the length of the wires connecting the chip. Figure 5.13 shows the manufactured PCB. This means that the organization of the manufacturing steps that was adopted was not suitable. The main limitations and constraints came from the size of the chip. The chip was processed at its top and bottom side outside a clean room but preliminary results show that the designed structure is feasible. Indeed, the wirebonding, soldering and sputtering were challenging

mostly due to the small size of the chip and many other technologies like electroplating were not possible for such a small chip.

The gold layer used as a resistive heating resistance is connected in series with the receiver coil which has a 0.44Ω internal DC resistance at 293 K which implies that the resistance of the gold layer has to be at least one order of magnitude higher in order to obtain significant signal and heat the chip, which means a value of the resistance higher than 4Ω . If the resistive layer is too thin the resistance value is sufficient but the wirebonding is not possible, if the resistive layer is too thick the wirebonding is possible but the value of the resistance is too low. The maximum thickness corresponding to a resistance of 5Ω is 150 nm. Higher thicknesses could be electroplated but a larger surface is needed that is why if this is done at the wafer level higher values of thicknesses can be reached. This means that a front end process performed at the wafer level and a better organisation of the manufacturing steps is required. A solution to increase the resistance and the thickness at the same time is to make a meander resistor instead of a resistive layer.

This means that a front end process performed at the wafer level and a better organisation of the manufacturing steps is required. A solution to increase the resistance and the thickness at the same time is to make a meander resistor instead of a resistive layer. The Ohmega Ply Embedded Resistor Technology, which corresponds to electrodeposited thin film resistive material for planar resistors, can be considered to manufacture the meander resistor. It is a standard subtractive PCB processing for surface or embedded resistors. It is a mature technology (over 30 years), field proven with an excellent long term reliability. It is performance enhancing, a cost effective resistor technology in high speed and high density circuit designs. The tolerance increases with the sheet resistivity. The resistance of an OhmegaPly resistor is expressed by:

$$R = R_S \frac{\text{Length of Resistor}}{\text{Width of Resistor}} \quad (5.1)$$

with:

R_S – sheet resistance in ohms per square

The resistance value of the resistor can be determined by sheet resistance and the geometry of the resistor according to the formula above.

$$R = R_S \times N \quad (5.2)$$

with:

N – number of squares

$$(N = L/W) \quad (5.3)$$

mit:

N – number of squares

L – length of the resistor

W – width of the resistor

Basically, a meander resistor can be considered as a bar resistor with the exception of the corner squares (right-angle bends). Due to the change in current density at right-angle path, the effective number of square is 0.56. Since the IDT electrodes seem to be more fragile than the gold layer, they should be etched at last. The manufacturing steps of the chip could be:

1. Manufacture the meander resistor by laser etching
2. Wirebond the resistor and leave the wires suspended
3. Flip the wafer to process the top
4. Etch the IDT electrodes by ebeam lithography
5. Wirebond the IDT to the PCB

PTFE as a packaging material was a reasonable choice for a first prototype, however an improved version of the prototype could be made of Code 9658 ceramic for better stability in vacuum and a better protection of the chip.

All the designed components were manufactured and assembled. The antenna and coil were tested. The SAW chip was interrogated by means of the antenna using a frequency sweep between 2 and 3 GHz and the minimum of the reflection coefficient corresponding to the resonance frequency could be observed. The coil was tested and the output current of up to 1.2 V peak to peak could be measured at a 1 Ω resistance in series with the coil. The coupling distance between the transmitting and receiving coil was 6 mm. The device was tested at room conditions and still needed to be characterized in vacuum to determine its actual performances. All the operations performed on the chip were successful. However, the soldering at the bottom of the chip destroyed the IDT structure at the top. The wires were able to support mechanically the suspended chip. The holes drilled on the packaging allowed the wires to connect the chip to the antenna and the coil. The PCB was designed in a way to minimise the length of the wires connecting the chip. Figure 5.13 shows the manufactured PCB. Figure 5.12 shows the processing of the chip at its top and Figure 5.10 shows the processing of the chip at its bottom. Indeed, the wirebonding, soldering and sputtering were challenging mostly due to the small size of the chip and many other technologies like electroplating were not possible for such a small chip.

The gold layer used as a resistive heating resistance is connected in series with the receiver coil which has a 0.44Ω internal DC resistance at 293 K. This implies that the resistance of the gold layer has to be at least one order of magnitude higher in order to obtain significant signal and heat the chip, which means a value of the resistance higher than 4Ω . If the resistive layer is too thin the resistance value is sufficient but the wirebonding is not possible, if the resistive layer is too thick the wirebonding is possible but the value of the resistance is too low. The maximum thickness corresponding to a resistance of 5Ω is 15 nm using equation (9). Higher thicknesses could be electroplated but a larger surface is needed that is why if this process is applied at the wafer level higher values of thicknesses can be reached. The sensor operates via the transmission of two distinct waves. The antenna wave being in the Gigahertz range is more sensitive to the environment perturbations than the coil wave in the Kilohertz range. The position of the antenna inside the vacuum chamber is more critical and should be the closest to the outside environment. A coupling distance of 1 cm was reached between the Tx coil and the Rx coil but the coupling coefficient was very poor around 5 %. Since the chip needs very few energy for heating, this is not an issue for operating the sensor.

A miniaturised wireless compact vacuum sensor was designed, simulated and a prototype was manufactured. The miniaturisation of the heating and interrogation units in addition to the sensing chip raised some manufacturing and assembly challenges considering the semiconductor technologies currently available. All in all such a sensor is feasible provided a better manufacturing process is prepared. The obtained prototype shall be tested in vacuum and the best operating mode still needs to be determined by acting on the input signal. Parameters of the input signal that ought to be varied are the AC signal form and the power input.

Next step was to test the prototype at ambient conditions.

5.2 Measurements outside vacuum

Different heater configurations and relative positions between the heater and the chip were presented. Prior to the testing of the prototype in vacuum, its assembly required the characterisation of each component separately and then combined at ambient conditions. The assembled prototype was tested at ambient conditions prior to insertion and test inside vacuum. The objective of the series of measurements outside vacuum was to achieve the right power transfer for the heating and interrogation unit and to obtain the needed measurement signal from the SAW chip. A transmitting and receiving antenna need to be properly coupled to ensure that enough power is received by the Rx antenna, transmitted to the chip and reflected back. The antennae need to have the appropriate resonance frequency, dimensions and to be properly placed in order to be correctly coupled together.

5.2.1 Experimental procedure

The receiver coil was tested with different transmitter coils. The PCB was characterized under different conditions. To enable the transmission of the electromagnetic waves, PMMA windows with different thicknesses were prepared. The Rx coil, the SAW packaged chip and the Rx antenna were soldered on the PCB. The coil induced temperature rise of the chip was recorded as well as the resulting resonance frequency shift. The coil heats up during its operation. Due to its vicinity with the SAW chip, the chip also heats up which induces its resonance frequency shift. This frequency shift was measured. The relative position of the Tx and Rx antennas directly influences the shape of the SAW signal. For this reason the optimum position of the antenna granting the sharpest SAW peak was identified and fixed using Kapton tape. The test rig contains an arbitrary waveform generator and a power source. The IMT lab where the measurements were performed had a 21 °C controlled temperature with a 1 °C drift. Under this initial conditions, a frequency sweep between 2 GHz and 3 GHz with a network analyzer gave a SAW peak frequency of 2458836092 Hz, which is the resonance frequency of the chip at ambient conditions. The maximum voltage measured at the Rx coil of the heating unit is 1.2 V.

In order to protect the MOSFET from over heating, a passive fuse was added to it. When the MOSFET temperature exceeded 70 °C it stopped working. During the operation of the MOSFET circuit, the MOSFET was never turned off the temperature, i.e. its temperature never exceeded 70 °C.

Heating unit

The receiver coil of the sensor needs to receive power from an appropriately coupled transmitting coil connected to power supply. There need to be enough current at the receiver coil when inserted inside the vacuum. The power received at the coil depends on the coupling distance and the materials in between. The 1 Ω resistor connected to the secondary coil was provided with a 300 mA (RMS) current wirelessly using a transmitter coil in order to heat it. An Arbitrary Waveform Generator (AWG) generates the input square wave with a 157 kHz frequency. This wave is an input of the MOSFET. The output of the MOSFET is delivered to the Tx coil. Prior to working with the MOSFET, a few steps were undertaken to activate it.

1. The gate of the MOSFET was be provided with an input voltage superior to the threshold voltage (between 1 and 2 V for the used MOSFET IRLIZ44N).
2. The gate voltage was given through a potentiometer of 100 k Ω .
3. The potentiometer was adjusted to ensure a voltage across the gate higher than 2 V. Then the voltage was fixed to 5 V with a current of 0.2 A.
4. To identify the performance of the MOSFET, a lamp was connected across the drain.

5. For this setup, an input square wave of 10 V peak to peak was given across the gate and the lamp started blinking.

For the final circuit, a transmitter coil of 10 μH was connected in series to a 220 nF capacitor. Initially, the secondary coil was made to couple broadband with the transmitter coil. For a frequency of 158 kHz, a capacitance value of 139.75 nF was calculated using Equation 5.4. The 140 nF capacitor, the 7.2 μH receiver coil and a 1 Ω resistor were connected in series.

$$f = \frac{1}{2\pi\sqrt{LC}} \quad (5.4)$$

with:

- f – frequency in Hz
- L – inductance in H
- C – capacitance in F

The circuit was tested several times with different transmitter coils of various shapes, sizes and inductances of 6.4 μH , 10 μH , 24 μH , 26 μH and with 33 μH .

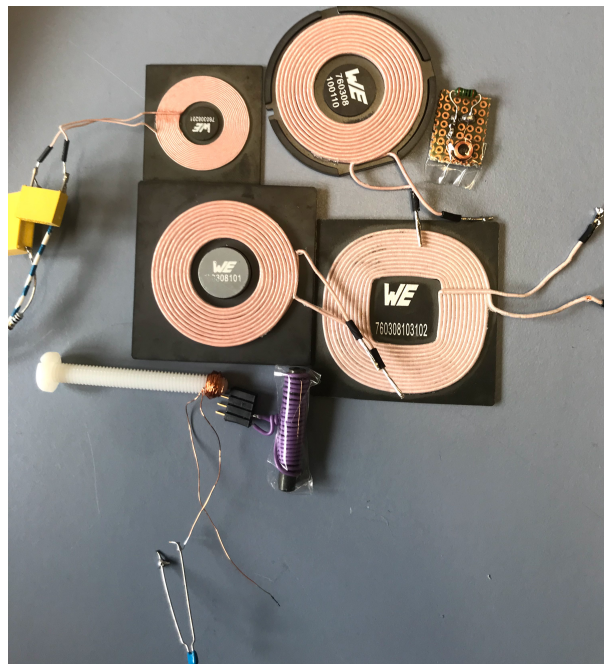


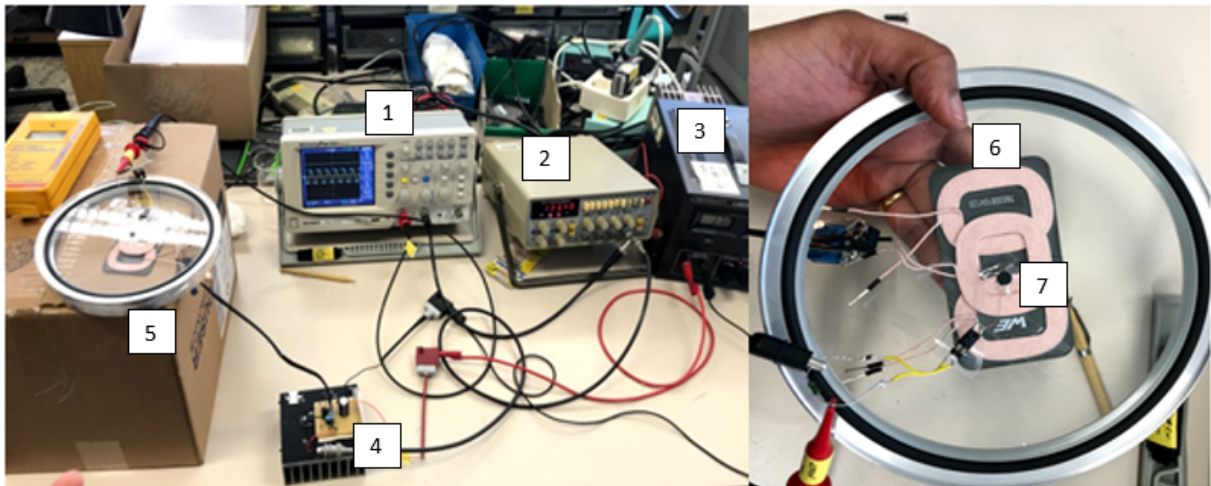
Figure 5.14 – Coils with different sizes and inductances.

During the testing, series and parallel connections of the receiver coil with its coupling capacitor were alternated. For each configuration, the current was measured across the 1 ohm resistor. The primary and secondary coil were placed facing each other and separated by a 5 mm distance. Table 5.2 shows the current measured across the 1 ohm resistance for different types of resonances.

Table 5.2 – Current across the receiver coil based on position and type of resonance.

Type of resonance at the receiver side	Distance between two coils	Current across 1 Ω resistor
Series	Less than 1 mm	492 mV
Series	5 mm	270 mV
Parallel	Less than 1 mm	247 mv
Parallel	5 mm	138 mV

The 6.4 μH coil was giving the best results. Indeed, for a resonance frequency of 125 kHz, the secondary coil was able to generate 423 mV across the 1 Ω resistor at a distance of 5 mm. Both coils were separated using a glass window of 5 mm thickness as shown in Figure 5.7 on the right side.

**Figure 5.15** – Complete heating and interrogation unit setup.

SAW signal vs material and distance

Similarly to the transmitting coil, different transmitting antennae were tested. Figure 5.16 shows the different antennae that have been used to measure the SAW signal during the experiments. Two PCB housings for two different antennas were prepared for the prototype (WE-MCA 7488940245 from Wuerth Elektronik and P/N 2450AT18B100 antenna from Johanson). The one retained was the SMD Antenna WE-MCA 7488940245 from Wuerth Elektronik, which is the antenna with the highest gain at resonance and that did not require any matching circuit components apart from the 50 Ω transmission line. This antenna has a peak gain of 2.0 dBi and an average gain of 0.5 dBi against a peak gain of 0.5 dBi and an average gain of -0.5 dBi for the other P/N 2450AT18B100 antenna from Johanson.

The components were connected for the testing. In order to interrogate the prototype, a transmitting antenna connected to the Network Analyzer is necessary. For this purpose, the same PCB structure as for

the prototype was used containing only the antenna as a transmitter and was connected to the Network Analyzer. The relative position of the transmitter and the receiver antennas was carefully maintained to ensure repeatable measurements and significant measurement signal. Several transmitting antennas were tested. They are depicted in Figure 5.16. All the antennas were showing a distinct SAW peak when they were facing the receiver antenna. However, the only antenna showing a distinct SAW peak beyond a 3 mm coupling distance was the prototype antenna when used in the sensor and interrogation antenna.

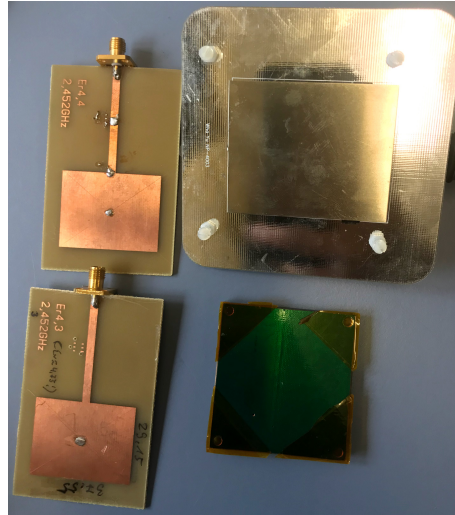


Figure 5.16 – Transmitting patch antennae tested.

The S_{11} curve has mainly two peaks, the peak on the left side shows the resonant frequency of the antenna and the peak on the right side is the SAW peak, the signal from the SAW chip. It can be clearly seen that the peak was generated at a frequency of 2,45 GHz. Hence the SAW chip was properly working and generated the SAW peak at the expected frequency range. All these antennae allowed to identify a SAW peak when they were close to each other. But only with the small antenna, as shown in Figure 5.8, the SAW peak was clear enough at a distance of 3 mm. The set up in figure 5.7 was finalised to achieve the required amount of current as well as the perfect SAW peak. Several experiments were conducted with it.

Testing of different materials between the primary and secondary part

Initially, a circular glass window of 160 mm diameter and 5 mm thickness available in the INFICON catalogue was used and enabled the generation of the required current of 300 mA. However, the antennae were not working due to the material and to the width. Since the material of the window is crucial in order to obtain the aimed result, different types of material needed to be tried after the work with the INFICON glass window was not successful.

Polymethylmethacrylate (PMMA) and quartz were tested for the circuit. Any window with a thickness below 2 mm was not possible to use in the vacuum as it may break due to a large pressure difference between both sides of the window. The main requirements of the window are the thickness, the mechanical stability and the compatibility with EM waves transmission and vacuum.

PMMA window with different thicknesses

PMMA is a clear plastic acrylic material that can be used as a replacement of glass. It has good impact strength, higher than glass. For this experiment, the following thicknesses of the PMMA window were used. Figure 5.17 below shows the SAW peak obtained with PMMA windows of different thicknesses (x-axis is the frequency in Hz and the y-axis is the return loss in dB).

The window was kept between the primary and secondary part. The current obtained across the secondary coil for all the tested thicknesses was higher than 300 mA. In this case, the sharpness of the SAW peak was only influenced by the thickness of PMMA. From the figure 5.17, it can be seen that at a width of 2.5 mm, the SAW peak was large and at 3 mm, a SAW peak of medium size was visible. PMMA width of 5 mm literally gave no SAW peak. Since Quartz is also suitable for radio waves transmission, different thicknesses of quartz were tested to obtain the SAW peak. Figure 5.18 shows the SAW peak obtained for quartz windows of different widths.

From the images, with a quartz thickness of 1 mm and 2 mm, the SAW peak was visible. But as soon as the thickness was increased beyond 2 mm, the SAW peak was not visible anymore. The network analyzer was only able to detect the noise. When comparing both materials based on the quality of SAW peak, the PMMA was better at a width of 3 mm. Indeed, with a PMMA window of 3 mm thickness, it was possible to generate the required amount of current at the resistor as well as a clear SAW peak. Afterwards, finding a suitable position for both the coil and antenna was rather challenging to keep minimal distances between both Tx and Rx parts and to avoid any interference of wave or material since every mm counts. Since the antennae are very directional, both Tx and Rx antennas should be kept at a defined location to obtain a sharp peak. Based upon those observations, a tailored PMMA window was prepared for the interrogation inside vacuum. The devices were placed in a way first to put the antennae facing each other at a minimal distance, then the coils were placed to keep minimum distance between them as well.

To sum up, the measurements performed outside vacuum are :

1. SAW signal acquisition with different antennae
2. Testing different materials of different thicknesses between the transmitting and receiving parts

The antenna used and its size impacts the strength of the signal.

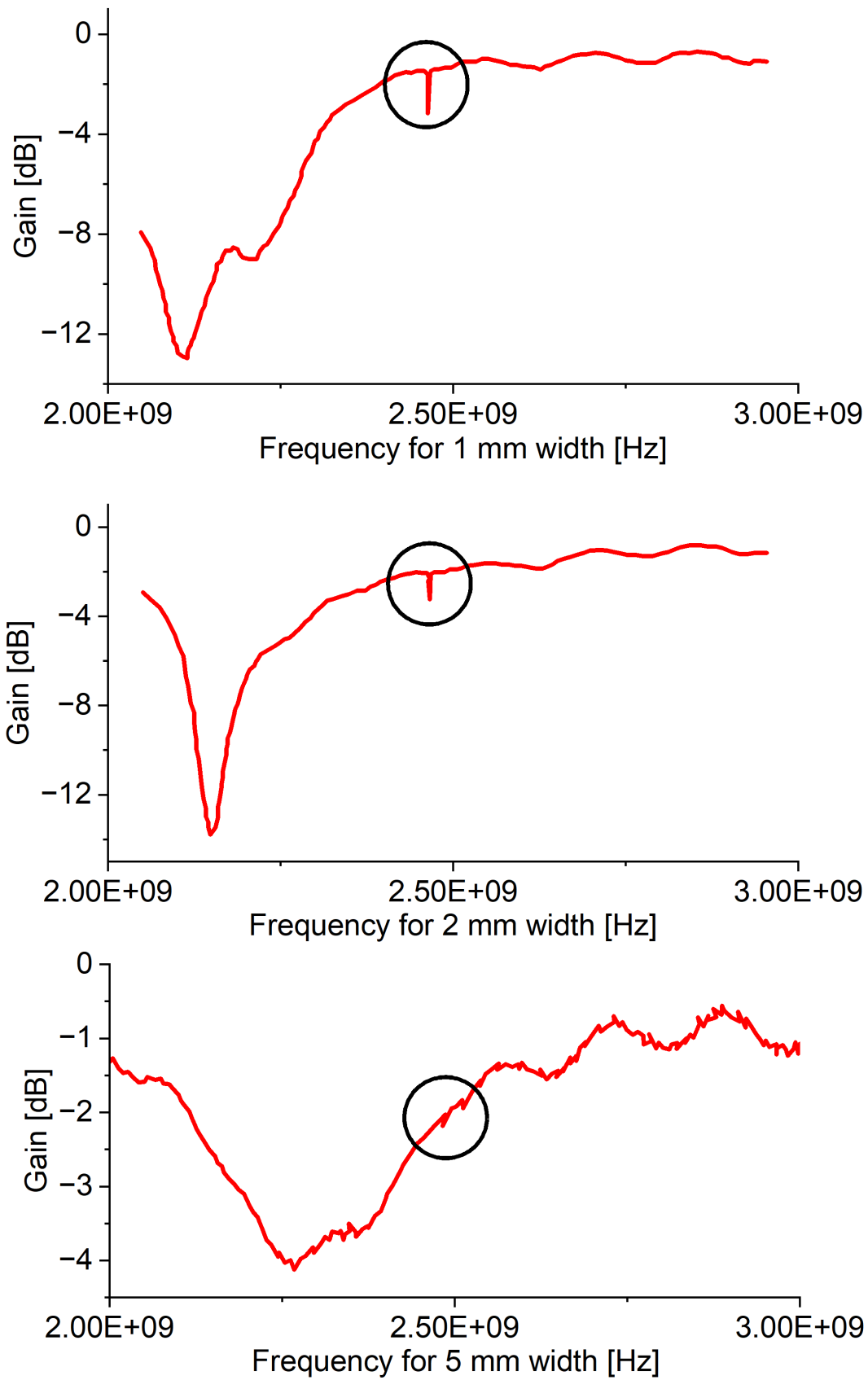


Figure 5.17 – SAW peak obtained with different PMMA window thicknesses.

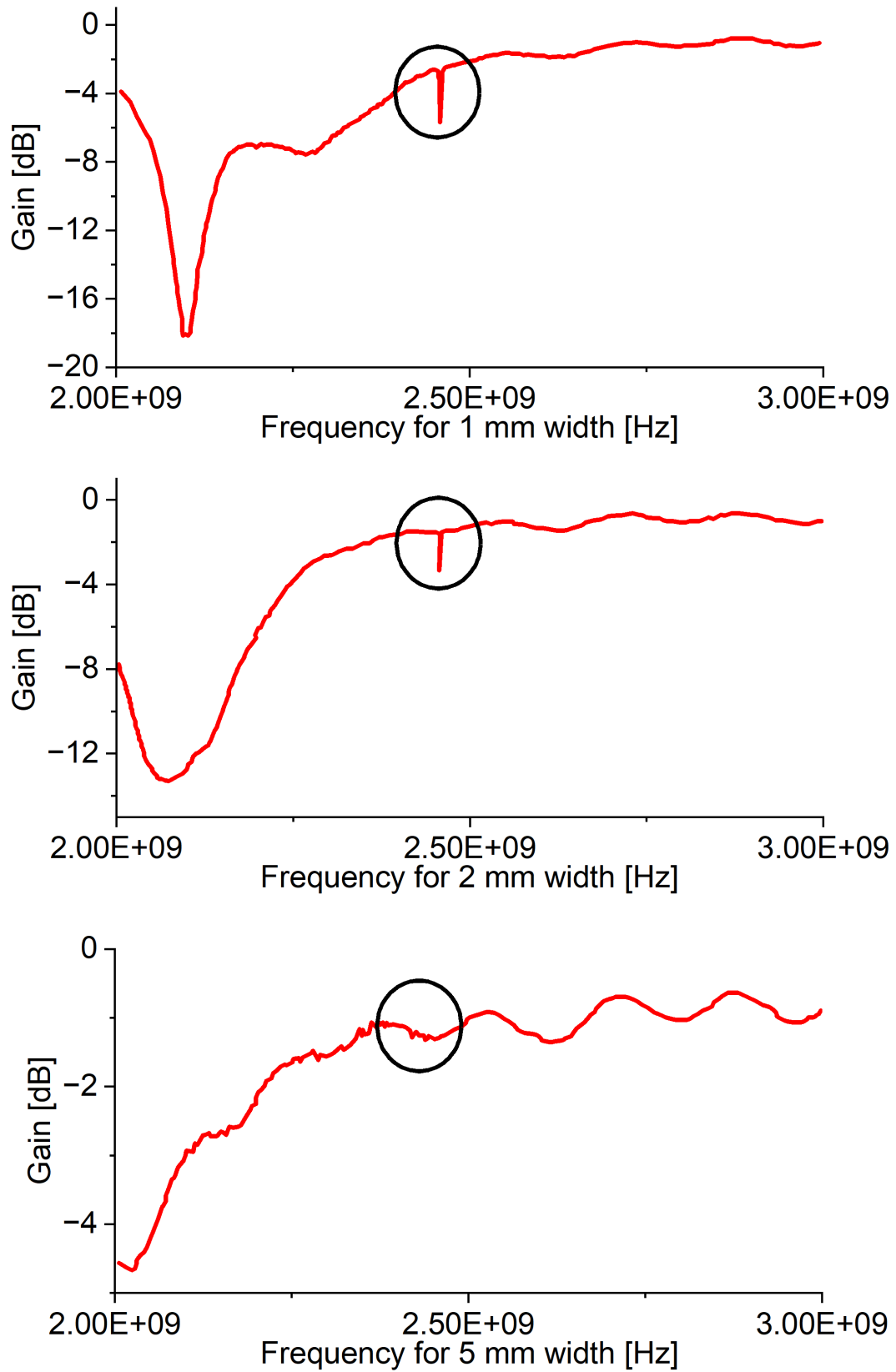


Figure 5.18 – SAW peak obtained with different Quartz window thicknesses.

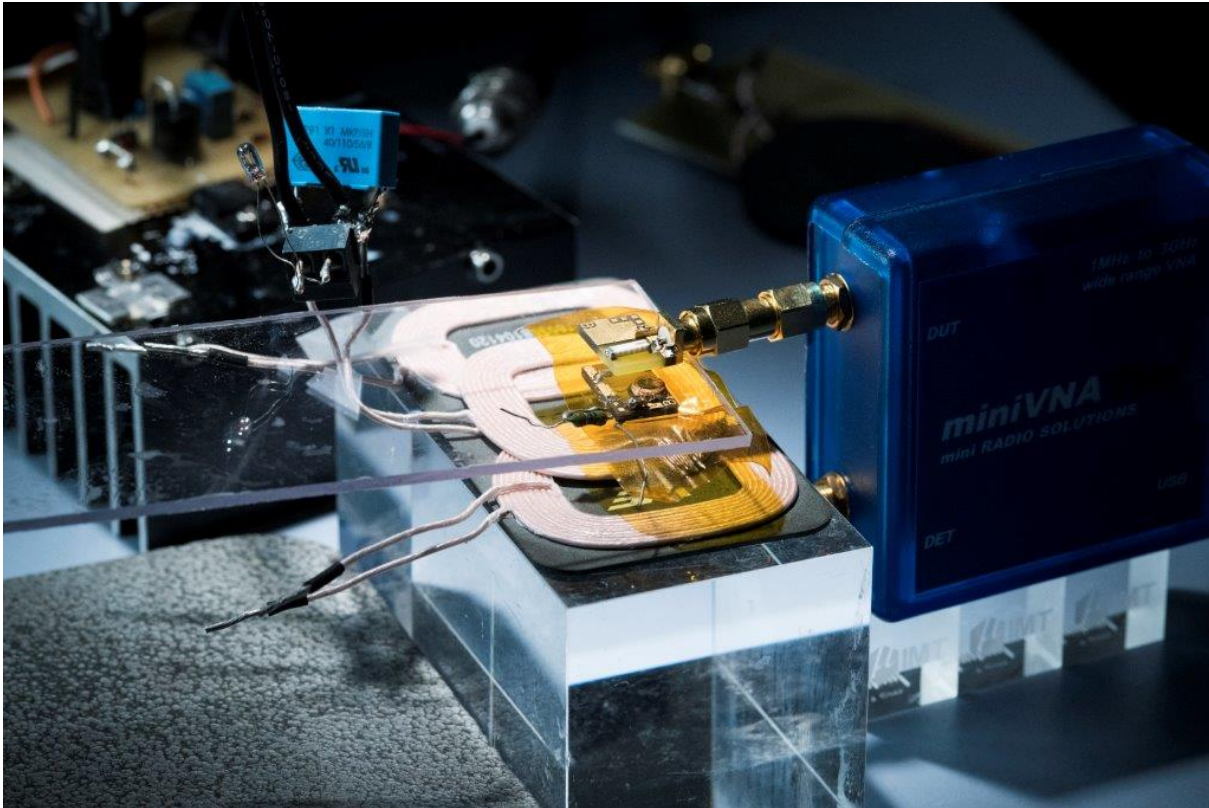


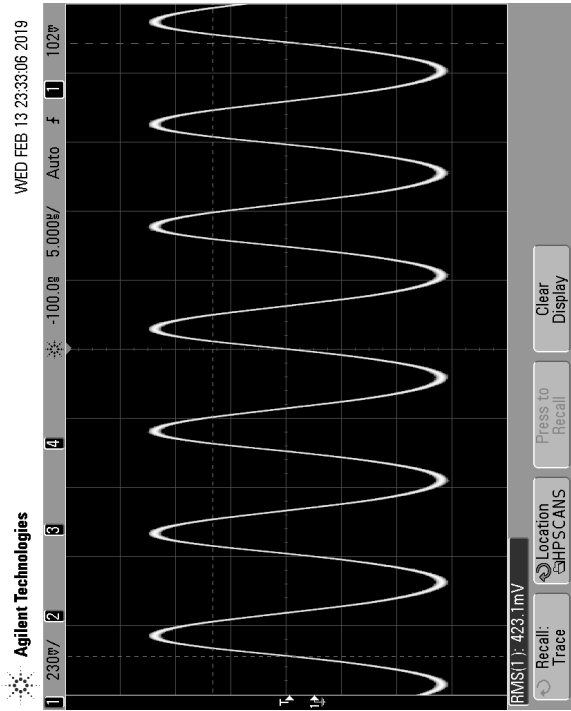
Figure 5.19 – Prototype characterisation with different materials in between outside vacuum.

Induction current vs distance

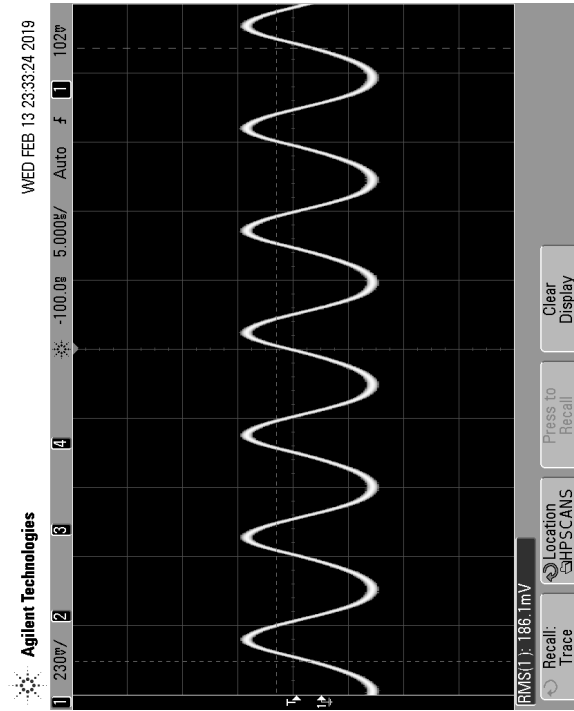
Among the experiments made with the MOSFET circuit, the coupling distance between the Tx and Rx part was varied. The output current across the $1\ \Omega$ resistance was measured for different distances separating the primary and secondary coil. Logically enough, when the distance between the coils was increased, the current across the receiver coil decreased.

Figures 5.20a to 5.20d show the output current signal for the tested positions. Figure 5.20a shows the output current of 535.6 mA when the primary and secondary coil were superimposed. Figure 5.20b represents the graph when the primary and secondary coil are separated by 5 mm. Likewise, Figure 5.20c and Figure 5.20d show the output current across the secondary coil when the Tx and Rx coils were separated from a distance of 8 mm and 1 cm respectively. At a frequency of 158 kHz and with an input of 16 V peak to peak, the secondary coil was able to generate a voltage of 1.17 V at a position close to the transmitter coil and at a distance of 1 cm, a voltage of 625 mV was generated.

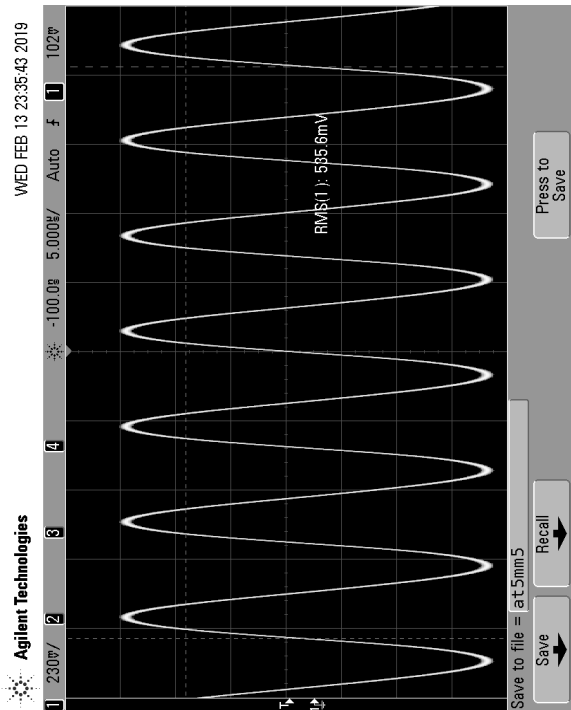
For each configuration, the current was measured across the $1\ \Omega$ resistor. The Rx coil was placed close to the Rx coil and at a distance of 5 mm. Table 5.3 shows the measurement of current across $1\ \Omega$ resistor for different types of resonances. The orientation of the coils was chosen taking into account the magnetic field lines and the receiver coil was placed in the plane where its current output was the highest.



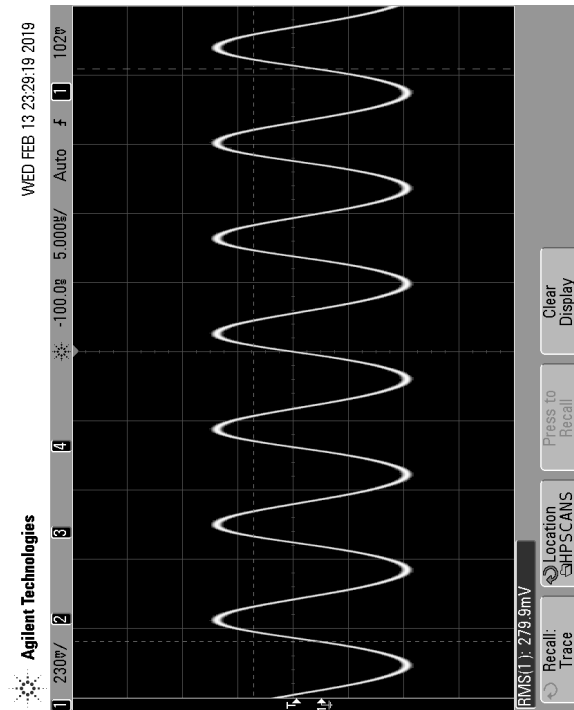
(b) Current = 423.1 mA, distance = 5 mm.



(d) Current = 183.9 mA, distance = 1 cm.



(a) Current = 535.6 mA, distance < 5mm.



(c) Current = 279.5 mA, distance = 8 mm.

Figure 5.20 – Current across the $1\ \Omega$ resistance according to the coupling distance.

Table 5.3 – Current across the receiver coil based on position and type of resonance.

Type of resonance at the receiver side	Distance between two coils	Current across 1 Ω resistor
Series	Less than 1 mm	492 mV
Series	5 mm	270 mV
Parallel	Less than 1 mm	247 mV
Parallel	5 mm	138 mV

SAW peak temperature induced frequency shift

The SAW chip needed to be connected to the interrogation antenna. The SAW chip needed to be characterized and the SAW peak identified and tracked through temperature changes to identify the frequency shift. Later on, the SAW peak had to be generated for pressure induced temperature change. The SAW peak was identified using the network analyzer Mini VNA-Tiny and its Java based application software VNA/J. The Network Analyzer had to be systematically calibrated before performing the measurements. For the measurements the Network Analyzer takes a minimum and maximum frequency as input and gives the gain and phase of the scatter parameters of the device vs frequency as an output. In our case, only the reflection coefficient S_{11} was relevant. The gain amplitude is plotted in decibels and the phase in degrees. The Network Analyzer can be operated in reflection or transmission mode, it is operated in reflection mode in our case. The SAW peak frequency is always situated between 2.4 and 2.5 GHz. That is why the start and stop frequencies were set at 2 GHz and 3 GHz for the first measurements. The chip interrogation was done by performing a single scan of the Network Analyzer (Figure 5.21).

The SAW chip was heated using a heating gun between 25 °C to 110 °C. with a step of 10 °C between each measured temperature. For each 10 °C increase, the corresponding SAW peak was captured using the Network Analyzer. The Network Analyzer was configured in such a way to capture the SAW peak 3 times for every 10 °C change of the temperature. The data was acquired as an excel file and as an image. The SAW peak was identified and tracked by plotting the return loss S_{11} (dB) versus frequency (Hz) from the points available in the Excel file (Figure 5.21).

The SAW peak was identified by plotting the return loss versus frequency. The return loss corresponding to the edge of the SAW peak was identified and the corresponding frequency was recorded. For each temperature change, the excel file was automatically created and the SAW peak frequency was retrieved from it. This way, the SAW frequency corresponding to several intermediate temperatures was identified. Based on that a graph plotting the temperature change vs frequency shift was prepared. Figure 5.22 shows the change in the SAW peak frequency shift versus temperature.

It can be seen that the SAW peak frequency decreases when the temperature increases. When the setup is inserted inside vacuum chamber, the change in the temperature shall be the result of a change in the vacuum pressure.

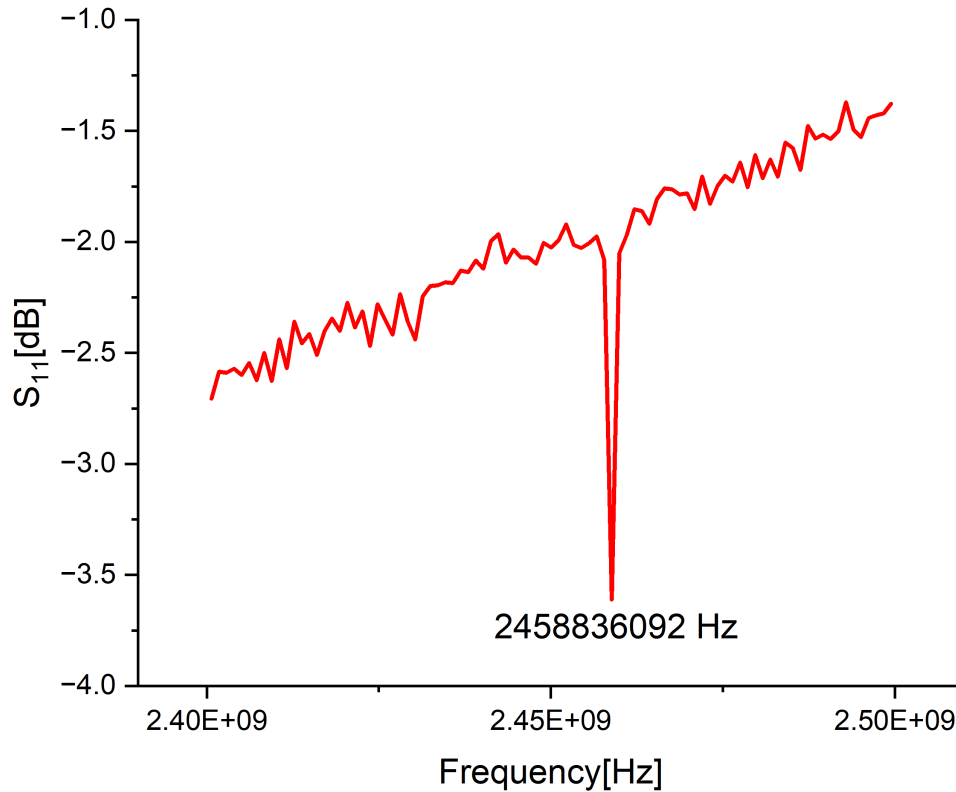


Figure 5.21 – Identification of the SAW signal.

5.2.2 Results

The sensor was characterized under various temperature and pressure conditions starting with ambient conditions. It was then inserted inside vacuum. Quality of the SAW signal obtained was assessed. The propagation of the SAW and EM waves through different materials was compared. Quality of the inductive power transfer was observed. Resonance frequency shift was characterized. Wireless heating was combined with wireless interrogation. The small coil would eventually be placed inside the vacuum chamber connected to the bottom of the SAW chip for heating. Out of all the coils, the $6.4 \mu\text{H}$ coil was giving the best results. At a resonance frequency of 125 kHz, the secondary coil was able to generate 423 mV across the 1Ω resistor at a distance of 5 mm. Basically, both coils were separated using a glass window of 5 mm thickness as shown in Figure 5.15. The change of current across the 1Ω resistance connected to the secondary coil was measured for different positions with respect to the primary coil. If the distance between the coils increases, then there is a decrease in the current across the receiver coil. The right position of the Rx coil had to be determined.

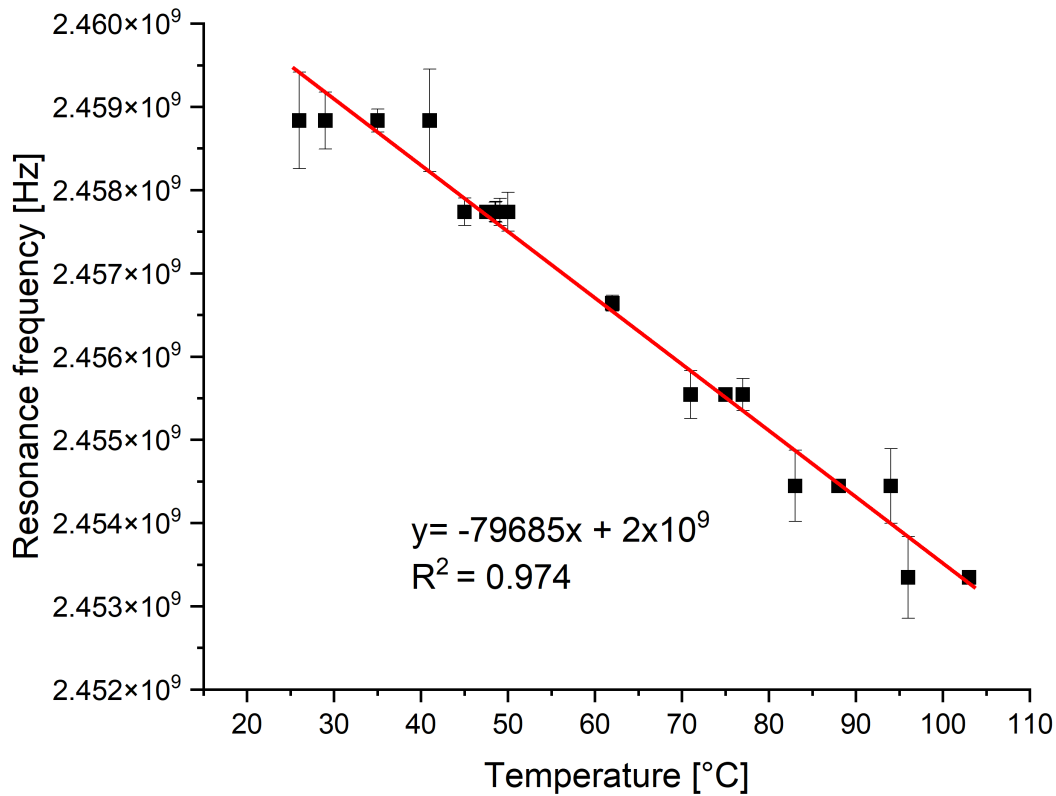


Figure 5.22 – SAW peak frequency versus temperature measured.

The heating unit was tested first with a 10 mm thick borosilicate window as a worst case scenario approach.

Output current at the Rx coil terminals was 300 mA RMS. Then, the heating unit i.e. Tx and Rx coil and the interrogation unit i.e. Tx and Rx antenna were tested together. The optimal solution was achieved with a frequency of 157 kHz.

5.2.3 Discussion

The small coil will be eventually placed inside the vacuum chamber and connected to the bottom of the SAW chip for heating. The small PCB with the secondary coil, receiver antenna, and the SAW will be placed inside the vacuum chamber covered with a polymer block packaging. The Tx coil and Tx antenna will be kept outside of the vacuum chamber separated from their Rx counterparts by a window. The characteristics of the antennae that determine their efficiency are the resonance frequency, the gain, the directivity and the size. The spatial configuration of all the components (alignment, distances) is crucial

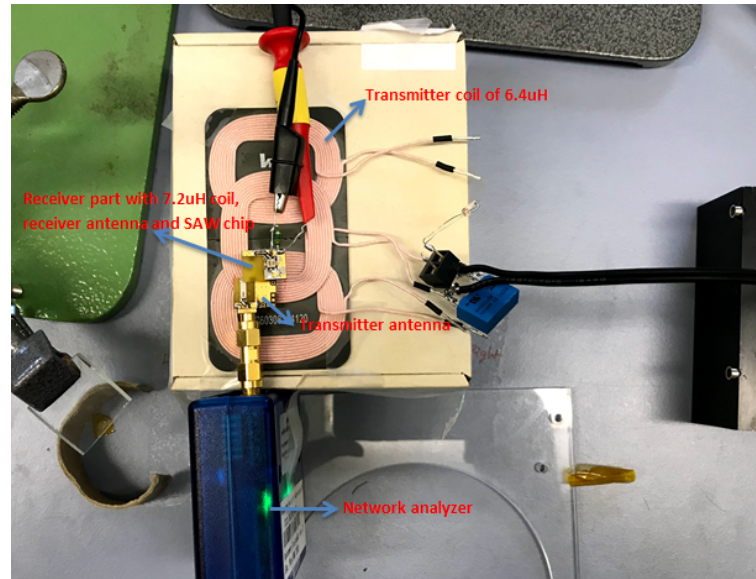


Figure 5.23 – Testing the heating and interrogation unit together. The transmitter coil can be seen on the top, the transmitting antenna in the middle and the VNA on the bottom. In the left part, the receiver unit with the receiver coil, the receiver antenna and the SAW chip can be seen. The clamps visible were occasionally used to check the current values.

for a correct operation of the sensor. The relative position of antenna peak and SAW peak also influences the sharpness of the SAW peak. The main challenge of the prototype assembly was to find the position of all the components to be able to work simultaneously. The positions of the primary and secondary coils as well as the transmitter and receiver antennae were crucial for testing the prototype. The components were all coupled together. The spatial configuration of the setup is critical for the successful obtention of the measurement signal. Since the antenna is very directional, both the antennae have to be placed in such a way that the sharpest possible peak can be seen. Finding a suitable position was a challenging task. The Yageo antenna, considered at the beginning of the development, is omnidirectional and wastes energy in unnecessary directions. The ratio of the radiated interrogation signal received by the antenna is proportional to the surface of the antenna. The power provided by the Mini VNA Tiny is rather low (0,5 dBi). If it is distributed through a large antenna the power received by the small receiver antenna is smaller than when the Tx antenna is of similar size and directivity.

The aim of the antenna coupling was to identify the SAW peak in the reflection coefficient values obtained after a frequency sweep between 2 GHz and 3 GHz. If the antennas were not properly coupled the SAW peak was just not visible. Two peaks can be observed from the S_{11} curve : the peak due to the antenna self-resonance and the SAW peak. It is advisable to make both peaks as close to each other as possible. The resonance frequency of the chip can not be modified it only depends on the temperature. However, the resonance frequency of the antenna can be tuned by adding a matching circuit, switching a feed or short or applying mechanical modifications to the antenna [92]. A reconfiguration possibility of the antenna can be the switching of a parasitic patch under the antenna to obtain a frequency adjustable antenna. Some difficulties encountered during the practical implementation of the devices were unexpected. More

problems were expected with the coils than with the antennae. The required power transfer via induction was relatively quickly reached including for a relatively big distance between Tx and Rx coil.

Though, the implementing of the antennae was more delicate. The coupling distance was much shorter than what could be expected from the data sheet. This could partly be explained by the losses induced by the circuitry, the window size and material. It can also be explained by the size of the antenna that captures a small portion of the electromagnetic energy radiated. The target interrogation distance of 2 cm could not be reached with the components chosen for the first prototype but the first prototype confirmed that the idea is feasible, heating and interrogating through a vacuum window having been achieved.

This implies that using a bigger Rx antenna and a bigger Rx coil could help increase the coupling distance to 2 cm. For instance using a precisely positioned pair of Tx and Rx coil compatible with the Qi standard could help solve this issue although the Rx coil would be much bigger than the one used so far.

The results were analyzed in comparison with the expectations. The experiments taught many things that influenced the sensor design. The experimental results were compared with the chip specifications. The VNA calibration and operation protocol impact the accuracy of the measurements in different ways. The SAW measurements performed are repeatable in the sense that the SAW peak frequency stays stable at the Hz scale, due to the chip itself or to the discretization of the frequency sweep. Using twisted lead wires cancels the induced voltage. A material used as a magnetic shield needs to have a high ferromagnetic permeability. One immediate solution to increase the coupling distance is to use a bigger Rx antenna. The amplitude of the frequency sweep influences the precision of the SAW frequency peak measurement. A narrower frequency band between 2.3 GHz and 2.5 GHz delivers a more precise identification of a SAW peak frequency than a sweep from 2 GHz to 3 GHz. Multiple scans and averaging were made to obtain a smoother signal. The choice of the frequency of the Arbitrary Waveform Generator (AWG) impacts the output voltage resonance frequency.

The echo signal from the SAW tag contains a lot of noise. That is why 10 times averaging is necessary to obtain correct signal. Preliminary Tests were made with an IR camera to identify wireless heating.

5.3 Measurements in vacuum

The purpose of the measurements inside vacuum was to check if the prototype delivers a pressure dependent measurement signal. After characterising the prototype at room temperature and pressure, the prototype was tested and characterized inside a vacuum chamber. The objective of the measurements performed in vacuum was to be able to measure a resonance frequency shift vs pressure through the vacuum pump pressure range.

5.3.1 Experimental setup

Description of the test rig:

The vacuum test rig shown in Figure 5.24 is made of the following components:

- vacuum pump: a TSH071E Turbocube from Pfeiffer Vacuum was used to generate subatmospheric pressure conditions
- metallic ISO KF pipes were used to connect the components
- a VAT gate valve was used to protect the Turbo pump in the rough vacuum region between 10 Pa and atmospheric pressure since it cannot operate under a pressure higher than 10 Pa.
- a BCG 450 triple gauge from INFICON was used as a pressure sensor to monitor the pressure: it contains a Bayard Alpert gauge, a Pirani gauge and a capacitive diaphragm gauge with automatic switch to measure pressures between 5×10^{-8} Pa and 1.5×10^5 Pa. The pressure sensor contains a display indicating the real time pressure and is connected to a LabVIEW user interface via an RS232 to USB cable.
- a needle valve was used to control the pressure
- a Window box was prepared to operate the prototype. The sensor was placed inside the box against the window from inside whereas the interrogation antenna and Tx coil were placed against the window from outside. The PMMA window enabled the propagation of the waves towards and from the vacuum.

In order to test the prototype in vacuum, adjustments to the vacuum chamber were required. It mainly consisted in the preparation of a vacuum PMMA window. Due to the fact that the vacuum viewports available off the shelf are made of borosilicate with a metallisation layer, they are not suitable for SAW interrogation. Companies like VACOM or INFICON commercialize viewports for vacuum optics of several materials and dimensions. The standard viewports are made of borosilicate or fused silicate and show transmission spectra for wavelengths between 0.2 μm and 5 μm . The 2.45 GHz SAW wavelength is 1.3836 μm . The wavelength of the induction wave for coils coupling is in the kilometer range. At first glance the viewport should allow the propagation of the SAW and not the induction wave. However, to prevent tensions occurring during heating, cooling or installing, the viewport contains an intermediate metallisation layer of Kovar (an iron-nickel-cobalt alloy) that prevents electromagnetic waves propagation.

For this reason, a customised PMMA window was manufactured to test the prototype in vacuum. The PMMA circular window had an outer diameter of 160 mm corresponding to the previous viewport diameter and the chamber diameter. The central part of the window, i.e. its 5 cm diameter central circle, had a 2 mm thickness. The transmitting (Tx) coil and Tx antenna were placed outside facing the prototype and the receiving (Rx) coil. Reducing the thickness to 2 mm was done to increase the quality of the signal delivered by the antenna. Since the structure of the chamber did not allow to put the transmitting coil and

the interrogation antenna at different sides, the heating power transfer was separated from the antenna interrogation. The receiver coil was connected to a $10\ \Omega$ surface mounted device (SMD) resistor which was soldered on top of the chip.

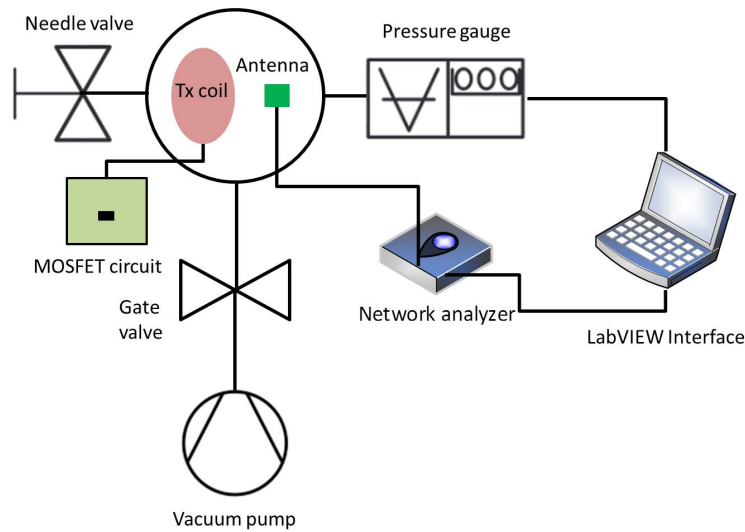


Figure 5.24 – Schematic of the vacuum test rig showing its components.

The prototype inserted inside vacuum consisted mainly of a PCB. On top of the PCB the receiver coil and antenna were mounted. At the bottom of the PCB, the SAW chip was placed. The SMD resistor soldered on top of the SAW chip and connected to the receiver coil was acting as a Joule heating resistance. The soldering of the resistor provided a good thermal contact between the resistor and the SAW chip. A photo of the setup is shown in Figure 5.25.

Since the structure of the chamber did not allow placing the transmitting coil and the interrogation antenna at different sides, as could be possible using a smaller ceramic or glass box with an ISO KF or CF junction, the receiver coil was separated from the rest of the PCB. The heating was performed via an SMD resistor to substitute the direct heating of the chip via a gold metallic layer joule resistance at its bottom. The temperature was measured by placing a Pt1000 sensor in the vicinity of the chip inside vacuum.

Experimental procedure

The objective of the test rig was to measure the resonance frequency of the SAW chip versus pressure. After the assembly of the test rig the vacuum pump was turned on. When the ultimate pressure was reached, the pressure was gradually increased by turning the needle valve. The corresponding resonance frequency of the chip was recorded. Figure 5.26 shows the complete setup.

The pressure was varied between $0.9\ \text{Pa}$ and $10^5\ \text{Pa}$ and the behaviour of the chip was observed during one hour by means of a VNA. Each pressure was maintained over the course of one hour and VNA interrogations were performed every 5 min in order to obtain 10 measurement points for each pressure. Two

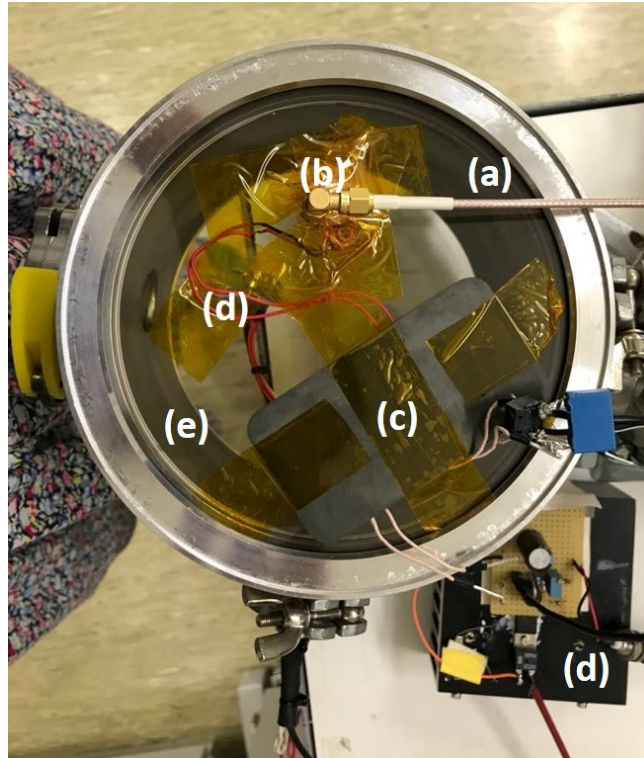


Figure 5.25 – Top view of the test rig showing the window. The Tx coil and the Tx antenna are placed on top of the window: (a) SMA cable going to the Network Analyzer. (b) Sensor PCB. (c) Transmitting coil. (d) Cable inside vacuum connecting the receiver coil and the heating resistor. (e) PMMA window.

points per pressure decade were measured. For each pressure value, the measurements were performed when the pressure was stabilized i.e. 5 min after turning the needle valve to modify the pressure.

The stabilisation of the SAW peak frequency was tracked. The SAW peak was identified from the reflection coefficient S_{11} vs frequency curve via a gain local minimum and a phase local maximum. The MOSFET of the heating unit Tx circuit outside the chamber was supplied with a 16 V square wave at 157 kHz and 0.84 A. The measured output at the receiver coil and heating resistor was 700 mV RMS and 2 V peak to peak. The power provided to the heating resistance was calculated from the voltage measured which equals:

$$P = \frac{U^2}{R} = \frac{0.7^2}{10} = 49\text{mW} \quad (5.5)$$

with:

- P – Power in W
- U – Voltage in V
- R – Resistance in Ω

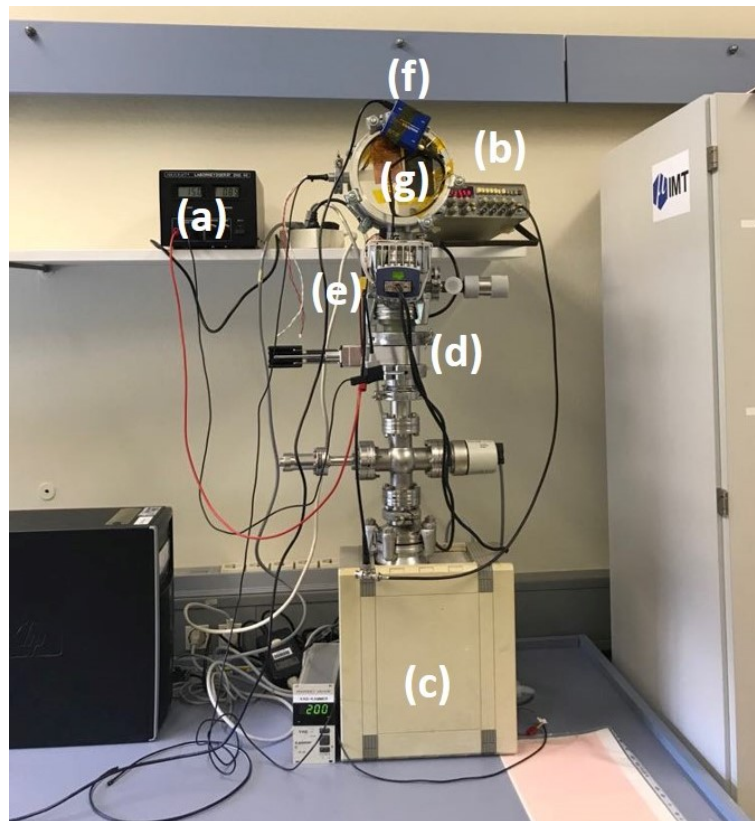


Figure 5.26 – Complete test rig: (a) Voltage source. (b) Arbitrary Waveform Generator. (c) Vacuum pump. (d) Valve to protect the turbo pump. (e) Pressure sensor. (f) Vector Network Analyzer. (g) Window setup shown in Figure 5.25.

Calibration

Prior to the chip interrogation, the Network Analyzer had to be calibrated. Through the use of scattering parameters, the device under test (DUT), i.e. the SAW chip, could be characterized by determining its resonance frequency. At high frequency, scatter parameters are directly related to gain, return loss and reflection coefficient. A VNA's performance depends on the accuracy of its measurements, which require a preliminary calibration. The calibration process aims to perform a vector error correction to remove errors from actual measurements. An analogy to a VNA calibration process is the zeroing out of a test-lead resistance from an ohmmeter to remove the offset caused by the lead resistance.

The error model of a VNA includes multiple terms for every frequency at which measurements are made. The frequencies where the calibration measurements are made must be carefully chosen in coordination with the frequency range where the VNA is to be used. The calibration process determines the error terms, requires a VNA, cables, and standard probes with known impedance. The calibration is performed by sequentially making measurements using calibration standards. Reliable and suitable connectors and cables handled with care are critical components of the calibration setup. No stresses exceeding their specifications should be applied on them. These calibration standards are one-port and two-port networks that have known characteristics. The one port network is used for reflection mode and the

two port network is used for transmission mode. The characterisation of the SAW chip needed only the reflection coefficient S_{11} , hence a reflection mode with one port network. For this purpose, a three steps calibration standard using a coaxial cable was applied. The three steps are:

- short (S): a coaxial short has a total reflection of magnitude 1. The reflection coefficient of the short is dependent only on its length offset, which represents the length between the reference plane and the short. The loss occurring over this length can generally be ignored. Modelling the short in a VNA requires that only its electrical length be entered into the instrument, but in some cases the model can be extended using the polynomial coefficients to account for parasitic inductance.
- open (O): a coaxial open standard is constructed using a closed design to avoid effects caused by entry of stray electromagnetic energy. At the open end of the inner conductor, a frequency-dependent fringing capacitance is formed. Even if an open standard could physically be constructed with a length of 0, fringing capacitances would result in a negative imaginary part for S_{11} at higher frequencies.
- match (M): a match is a precision broadband of 50Ω impedance that has a value corresponding to the system impedance.

The open-short-match technique described above is the most popular for one-port calibration. It uses the three standards connected one after the other to the test port and the relations occurring for wave-quantities a_1 to b_1 are determined. The behaviour of the individual standards is assumed to be known. The corresponding descriptive models are stored in the VNA. Based on the three derived values, the three unknown quantities (source match, directivity, and reflection tracking) can be calculated.

The three calibration probes were included with the VNA. A calibration was performed for every new set of measurements (position changing, modification of the test rig). The SAW peak frequency was always situated between 2.4 GHz and 2.5 GHz. The frequency sweep was performed first between 2 GHz and 3 GHz and then between 2.4 GHz and 2.5 GHz. The calibration was adjusted accordingly, i.e. the number of calibration points were increased from 1000 to 30000 between 2 GHz and 3 GHz in the calibration file of the VNA. Frequency steps of 1 kHz were generated. A smoothing algorithm was applied to all the measurement points. A smoothing algorithm is an averaging function that works over a single sweep. The percentage, or aperture, is adjustable up to a maximum of approximately 20-25% of the span (depending on the specific network analyzer). The result is a smoothing of the trace by the VNA and the outcome is similar to video bandwidth filtering in a spectrum analyzer. The smoothing reduces the noise and increases the signal to noise ratio(SNR).

For each frequency point and its associated window the algorithm normally looks for the mid-point using adjacent data. However, at the beginning and end points (of the measurement span), the algorithm performs a look ahead and look behind. This provides the smoothing function the same number of points for the smoothing window at the beginning and end of the sweep. For noise reduction, averaging is more appropriate, allowing noise to be averaged out. The main disadvantage is that increased averaging

factors increase the required measurement time. For averaging, VNAs use sweep-to-sweep averaging in which each data point is computed based on an exponential average of consecutive sweeps weighted by a user-specified averaging factor. Each new sweep is averaged into the trace until the total number of sweeps is equal to the averaging factor for a fully averaged trace. Each point on the trace is the vector sum of the current trace data and the data from the previous sweep. A high averaging factor gives the best signal-to-noise ratio but slows the trace update time. Averaging applies to each s-parameter per measurement channel, no matter which s-parameters are actually displayed. Regardless of the sweep type, the results of the averaged/corrected trace were placed in the analyser's internal data arrays.

5.3.2 Results

The first characterisation of the prototype in vacuum aimed to evidence a pressure dependent behaviour. This setup allowed to obtain wirelessly a pressure dependent measurement signal via the use of a miniaturised coil and antenna in vacuum and validates the sensor feasibility and concept of miniaturised wireless vacuum sensor.

Different windows were tested. The standard viewport from INFICON made of borosilicate with a metallisation layer and 10 mm thickness did not grant any SAW signal. The rest of the measurements were performed using the custom made PMMA window described in the materials and methods section. The operating frequency chosen for the heating unit, 157 kHz, is the one that gave maximum output voltage at the heating resistor. The voltage output at the receiver coil that is directly provided to the $5\ \Omega$ heating resistance equals to 0.7 V RMS, which corresponds to 100 mW of power approximately. The simulated chip needs 4 mW. The requirements of the heating unit were fulfilled. No SAW peak frequency shift was observed if there was no heating. The observed response time is 1 min approximately. The SAW peak frequency was stabilised one minute after the pressure was modified. The response times calculated (100 s) are therefore realistic.

At some pressures, two SAW peaks instead of one were observed in a repeatable way as can be seen in Figure 5.27. The sharpest peak, which is the main SAW peak is always located between 2.4 GHz and 2.5 GHz. When looking at a broader frequency spectrum 2 GHz to 3 GHz for instance, the antenna self resonances can be observed but not inside the frequency bandwidth of interest between 2.4 GHz and 2.5 GHz. This second resonance may be due to reflection effects inside the SAW chip

An S_{11} value of -10 dB means 10% of the incident power is reflected back towards the source from the device (antenna, junction, amplifier etc) under consideration.

A pressure dependent signal was obtained. When the pressure increases the temperature of the chip decreases. When the temperature decreases the resonance frequency increases. When the pressure increases the resonance frequency increases as well. The criteria to identify the SAW peak frequency was a local minimum of the gain and a local maximum of the phase. The sensitivity is higher between 0.1 kPa

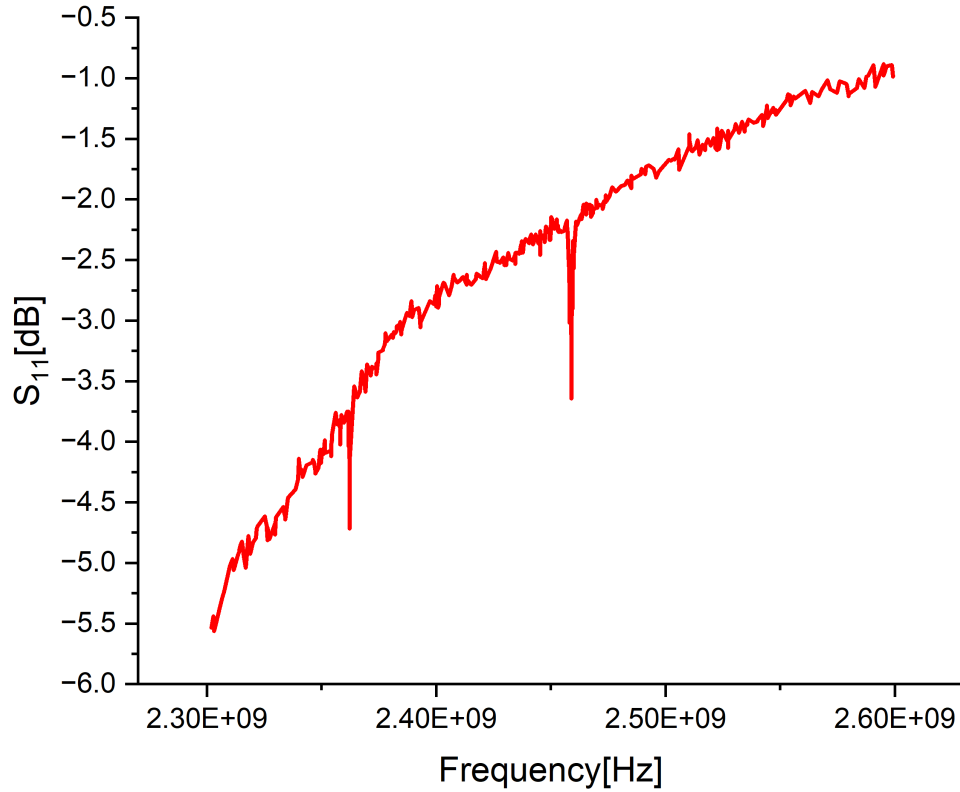


Figure 5.27 – Frequency sweep between 2.3 GHz and 2.5 GHz obtained from the software interface of the mini VNA Tiny. 2 SAW peaks can be distinguished. The sharpest peak corresponding to the first resonance of the SAW chip is always between 2.4 GHz and 2.5 GHz as indicated in the data sheet of the chip The blue curve represents the S11 amplitude in dB and the red curve represents the S11 phase in degrees .

and 1 kPa than close to atmospheric pressure. The results obtained with the prototype are shown in Figure 5.28.

The sensitivity s_P of the sensor to pressure is defined as:

$$s_P = \left. \frac{df_{res}}{dP} \right|_{T=\text{const}} \quad (5.6)$$

with:

- s_P – sensitivity in Hz/K
- f_{res} – resonance frequency in Hz
- T – Temperature in K

The pressure coefficient of frequency PCF is:

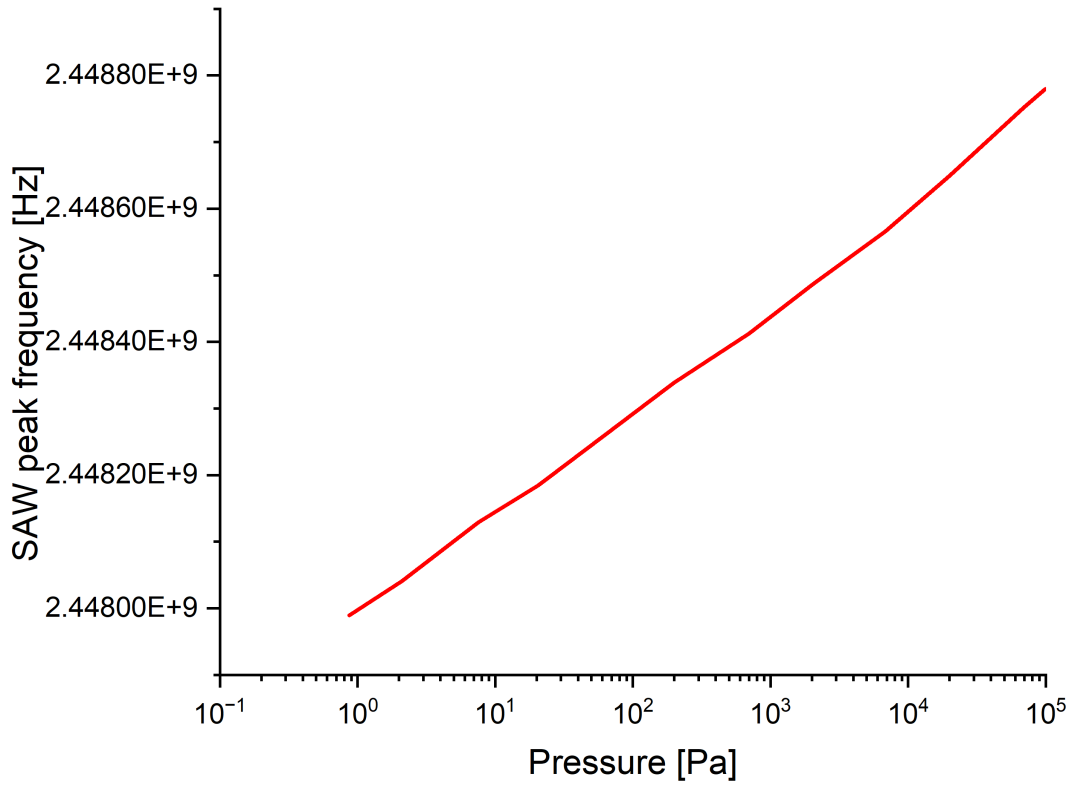


Figure 5.28 – SAW peak frequency vs pressure.

$$PCF = \frac{1}{f_{res}} \frac{df_{res}}{dP} \Big|_{T=const.} \quad (5.7)$$

with:

f_{res} – resonance frequency in Hz

T – Temperature in K

P – Pressure in Pa

The temperature sensitivity s_T is defined as:

$$s_T = \frac{df_{res}}{dT} \Big|_{P=const} \quad (5.8)$$

with:

f_{res} – resonance frequency in Hz

T – Temperature in K

The temperature coefficient of frequency TCF is defined as:

$$TCF = \frac{1}{f_{res}} \left. \frac{df_{res}}{dT} \right|_{P=const.} \quad (5.9)$$

with:

- f_{res} – resonance frequency in Hz
- T – Temperature in K

If the frequency shift vs. pressure and temperature is linear, the resonance frequency can be expressed as:

$$f = f_0 + s_T (T - T_0) + s_P (P - P_0) \quad (5.10)$$

with:

- f_0 – resonance frequency at the temperature T_0 and the pressure P_0 in Hz
- T – temperature in K
- s_T – temperature sensitivity in Hz/K
- s_P – pressure sensitivity in Hz/Pa

The sensitivity in Hz/Pa changes for the different pressure ranges and is reported in Table 5.4. The average sensitivity is 5880 Hz/Pa i.e. 2.4 ppm/Pa between 0.9 Pa and atmospheric pressure. Inside vacuum, the resonance frequency of the SAW chip measured changed with respect to pressure. The resonance frequency increased with the pressure between 2447989448 Hz at 0.871853 Pa and 2448780148 Hz at 99722.23 Pa. The sensitivity constantly decreased with the pressure according to the expectations between approximately 42 kHz/Pa at 0.9 Pa and 1 Hz/Pa at atmospheric pressure. The sensitivity is higher in the rough vacuum area between the minimum pressure and 200 Pa approximately corresponding to the limit between the Knudsen regime and the transition regime [93], which corresponds of Knudsen number close to 1 [64]. The Knudsen regime is not explained in detail here but in [24]. The uncertainty of the pressure sensor used as a reference is 15% and the uncertainty of the frequency was taken as a first approximation as the double of the standard deviation of the measurements. Since those measurements constitute only a proof of concept, no extended uncertainty analysis was performed. The objective was to observe the rough signal measured in vacuum and determine if the behaviour of the chip is influenced by the value of the vacuum pressure. Table 5.4 and Figure 5.30 shows the computed sensitivity of the sensor.

Table 5.4 – Computed sensitivity of the resonance frequency to pressure.

Pressure (Pa)	SAW peak frequency (Hz)	Sensitivity(Hz/Pa)
0.87	2447989448	2807800681
2.10	2448040611	41662.52
7.53	2448128983	16277.52
20.54	2448184797	4290.37
70.44	2448268518	1677.79
198.86	2448338286	543.25
698.50	2448412705	148.95
2058.71	2448487124	54.71
6849.31	2448566194	16.51
20070.38	2448649915	6.33
69677.32	2448752241	2.06
99722.23	2448780148	0.93

The values of the gain at SAW peak frequency are similar and do not really depend on the pressure level. The mean value of the gain at the SAW peak frequency is -3.85 dB and the standard deviation is 0.18. Figure 5.31 shows the values of the gain of the SAW peak versus pressure.

The values of the gain at the SAW peak frequency are shown in the graph between -4.04 dB at 2058.71 Pa and -3.42 dB at 99722.23 Pa. No real trend could be observed despite a continuous increase of pressure. The standard deviation of the gain is stable for each value of the pressure around 0.15%. The value of the phase at the SAW peak frequency shown in Figure 5.32 also does not show any obvious trend, have values between 15° and 25° with a mean value of 23.53° and a standard deviation of 3.05°. The values of the phase at peak frequency are situated between 15.87 at 99722.23 Pa and 26.37 at 69677.32 Pa. The standard deviation of the pressure reported in Table 5.5 increases with the pressure level, which consolidates the statement of the manufacturer that the uncertainty of the sensor represents 15% of the value of the measurement. The standard deviation of the pressure is always lower than 2% which is much beneath the uncertainty claimed by the manufacturer of the measurement value in any case. The sensitivity decreases when the temperature increases.

The S_{11} gain which is the insertion loss in dB takes values between -1 and -5.5 dB in the frequency range 2.4-2.5 GHz. For the SAW peak it is always below -3 dB, which means it is effectively in the antenna bandwidth.

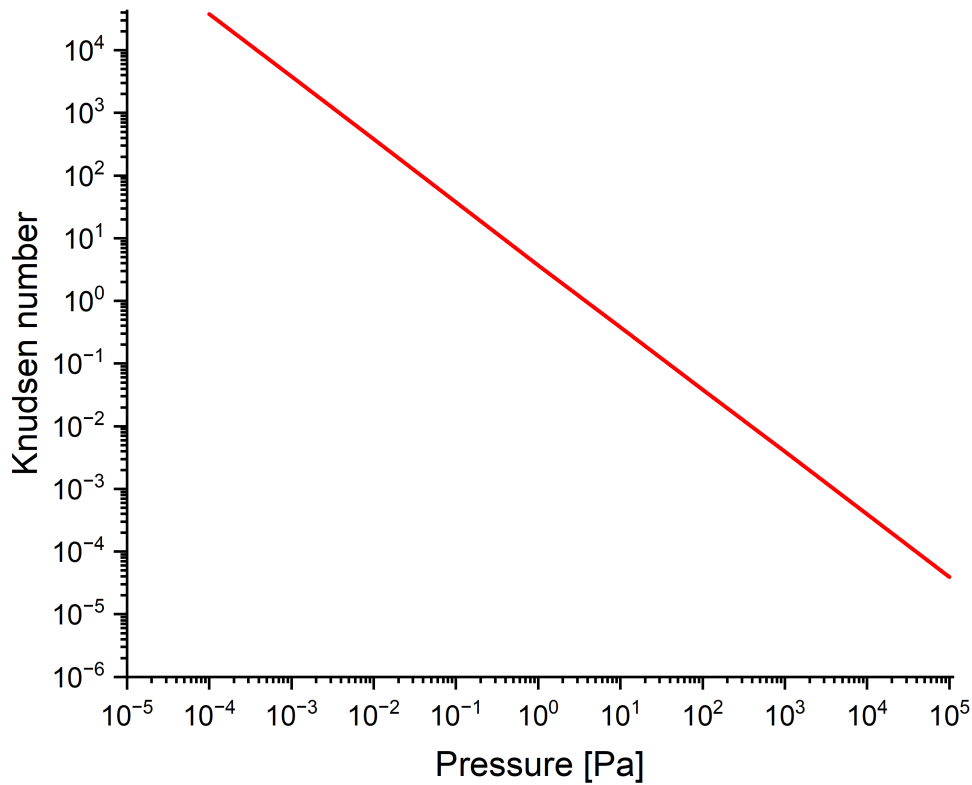


Figure 5.29 – Knudsen number of the flow simulated.

5.3.3 Discussion

Sensitivity

The sensitive device, corresponding to the chip Variant 4 from Table 4.1 is made of lithium niobate $Y+41^\circ-X$ and has dimensions of 3 mm x 3 mm x 1 mm which corresponds to the SMD 3x3 mm packaging. The SAW wave generated has a temperature coefficient of frequency (TCF) of 19 ppm/K. The equilibrium temperature is 65 °C for a pressure of 0.9 Pa. The heating capacity is 49 mW. Figure 5.33 shows the equilibrium chip temperature corresponding to each pressure value. Three regimes can be distinguished in the output curve:

- Knudsen regime from 0.9 Pa up to 200 Pa approximately, where the highest sensitivity is reached
- transition regime from 200 Pa up to 7000 Pa approximately where the sensitivity takes intermediate values
- convection regime approaching atmospheric pressure where the sensitivity is even lower than in transition regime in the range of 1 Hz/Pa

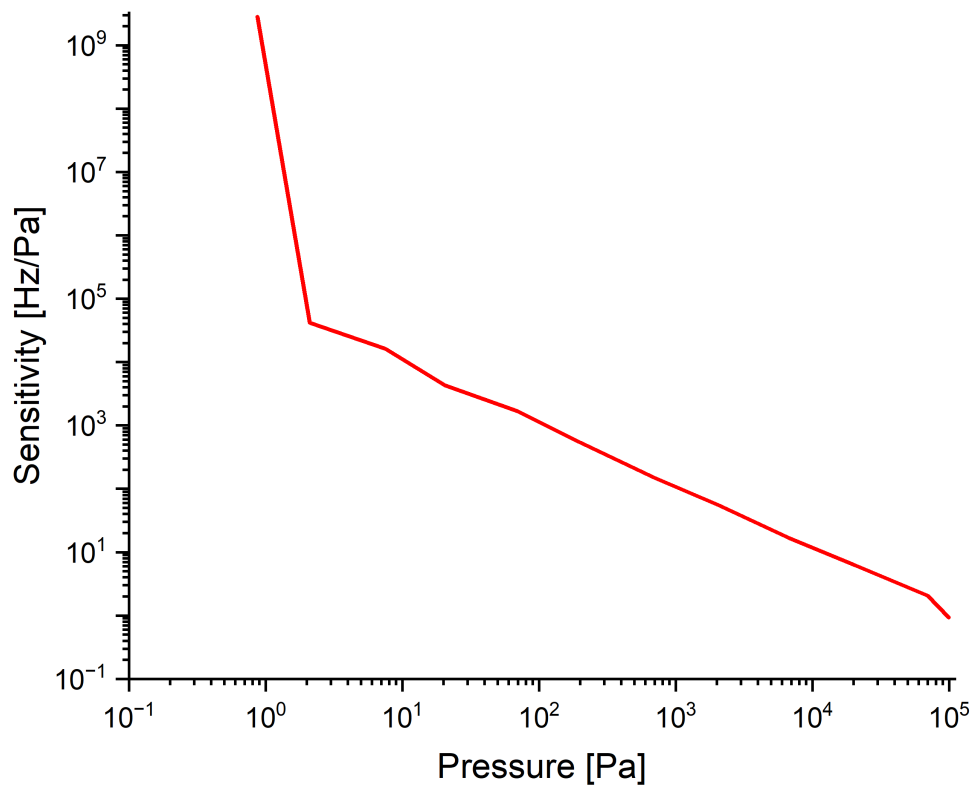


Figure 5.30 – Sensitivity of the SAW chip resonance frequency vs pressure in Hz/Pa. A logarithmic scale for the pressure axis was used for the sake of clarity.

The sensitivity rapidly decreases when the pressure increases. This was expected. It is due to the exit of the Knudsen regime as pressure increases and the corresponding evolution of the gas thermal conductivity towards a constant asymptotic value. The mean free path of the gas molecules at ambient temperature decreases very quickly between 0.01 Pa and 100 Pa from 0.1144 m to 1,144 μm which corresponds to a Knudsen number from 0.715 to 7.15. Considering the dimensions of the chamber whose diameter is 0.160 m, the pressure range tested corresponds to the transition from the Knudsen regime to a regime with a constant thermal conductivity hence the observed responses. The experimental curve of the sensitivity versus pressure is shown in Figure 5.30. It was obtained by deriving the values of resonance frequency with respect to pressure. The equilibrium temperature of the chip for each pressure is shown in Figure 5.33. The equilibrium temperature was computed from the value of the resonance frequency using the temperature coefficient of frequency provided in the technical sheet of the chip which is 18.857 ppm/K. The experimental points obtained are compatible with the theoretical expectations in their trend. This means that the SAW peak frequency increases when the pressure increases with a higher sensitivity in the fine vacuum region between 0.1 Pa and 1000 Pa than between 1000 and 10⁵ Pa in the rough vacuum area. It is to be expected from the Knudsen regime analysis since the thermal conductivity tends towards

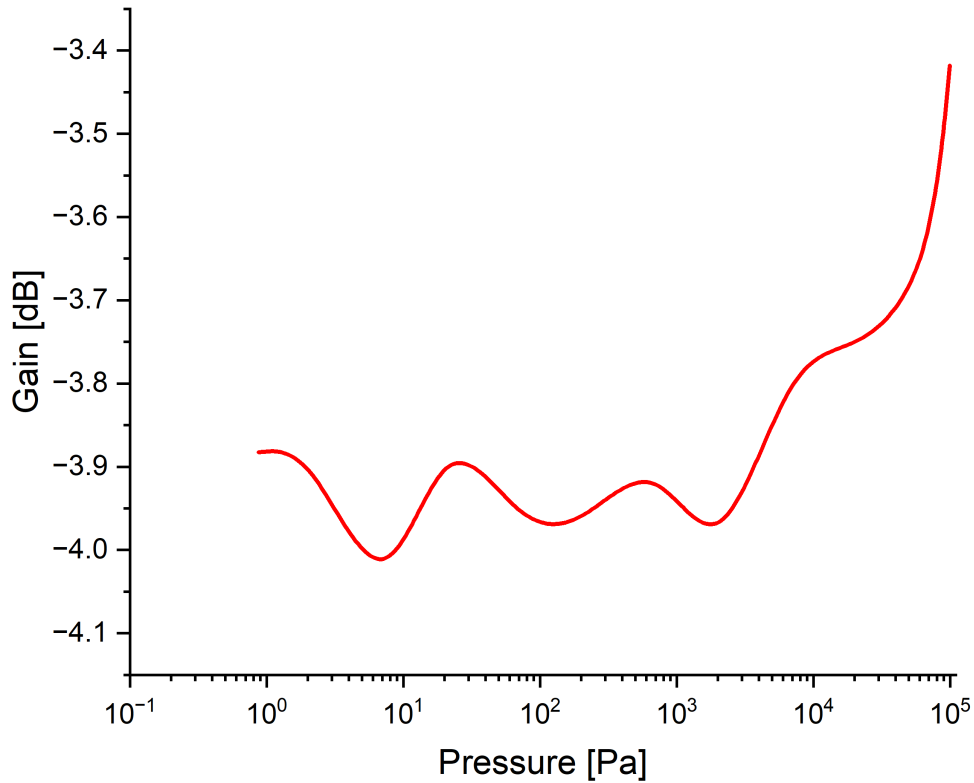


Figure 5.31 – S_{11} gain at the SAW chip resonance frequency vs pressure in dB.

a constant value approaching atmospheric pressure. Another phenomenon less impacting can explain the decrease of sensitivity when the pressure increases. The sensitive device cools down when the pressure increases. The sensitivity of the device to the pressure decreases when its temperature approaches the ambient temperature. This phenomenon is nonetheless less influencing than the exit of the Knudsen regime.

Uncertainty

Every measurement is subject to measurement uncertainty, which is the statistical deviation of the measured values from their true value. There are two types of measurement uncertainty: random uncertainty and systematic uncertainty. Random uncertainties vary with time and are thus unpredictable. While they can be described by statistical analysis, they cannot be removed by calibration. Common random uncertainties include those related to instrument noise and the repeatability of switches, cables, and connectors. On the contrary, systematic uncertainties occur in a reproducible way. They are caused by imperfections in the VNA and can be taken into account by means of calibration. The severity of the random uncertainty can be mitigated by adopting careful and meticulous measurement practices, such as

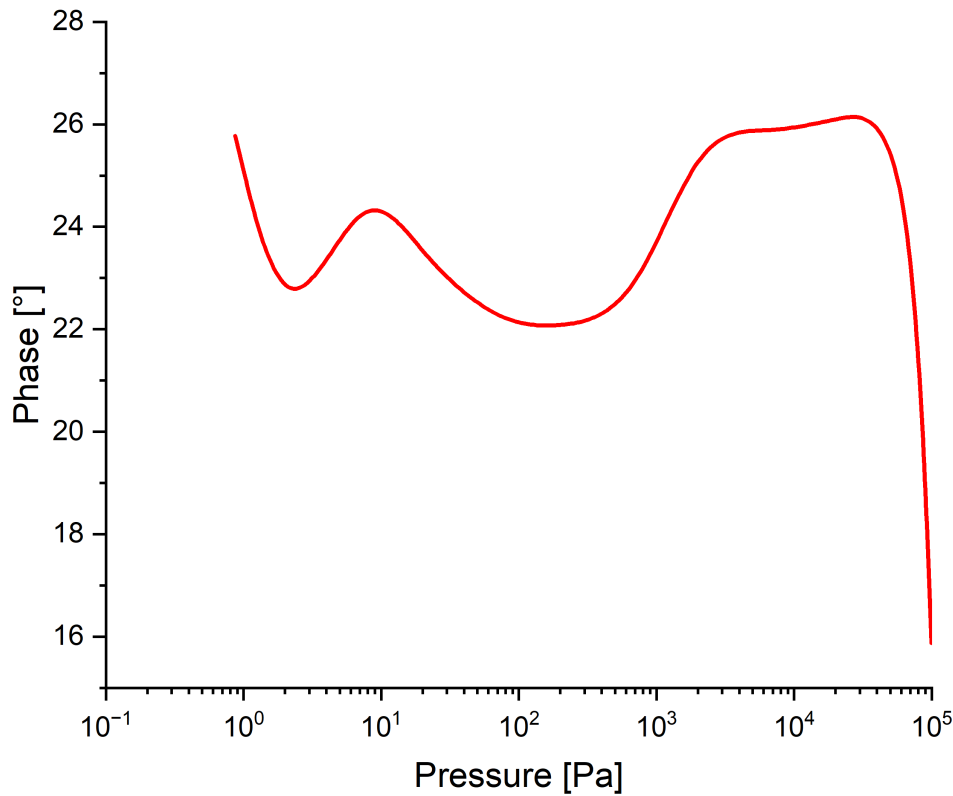


Figure 5.32 – S_{11} phase at the SAW chip resonance frequency vs pressure in degree.

allowing the instrument to achieve thermal equilibrium, using high-quality cables and connectors, selecting a small frequency bandwidth, and using averaging. This was attempted by working in a temperature controlled environment, using thick cables less vulnerable to bending, working on a restricted frequency range corresponding to the location of the SAW signal and using averaging algorithms. A VNA is also sensitive to its surrounding temperature, which can cause a drift. This was addressed by working in a temperature controlled lab with 1°C drift.

An uncertainty analysis and a statistical analysis were performed. The error bars were computed based on the standard deviation (shown in Table 5.5). The sample mean value and standard deviation were computed. This uncertainty remains acceptable given the uncertainties on each system parameter (pressure, TCF, and heating power). The agreement between the theoretical curve and the experimental response is within a range of $\pm 20\%$. This allows to validate the dynamic model of the SAW-Pirani developed. Variations of 1 Pa can be clearly detected. A zoom on the noisiest SAW peak makes it possible to estimate the limit step of measurement at about 1.5 kHz.

The experimental points are compatible with the theoretical expectations. The similarity between theory and experimental results validates the theoretical model to compute the sensitivity of a SAW-Pirani

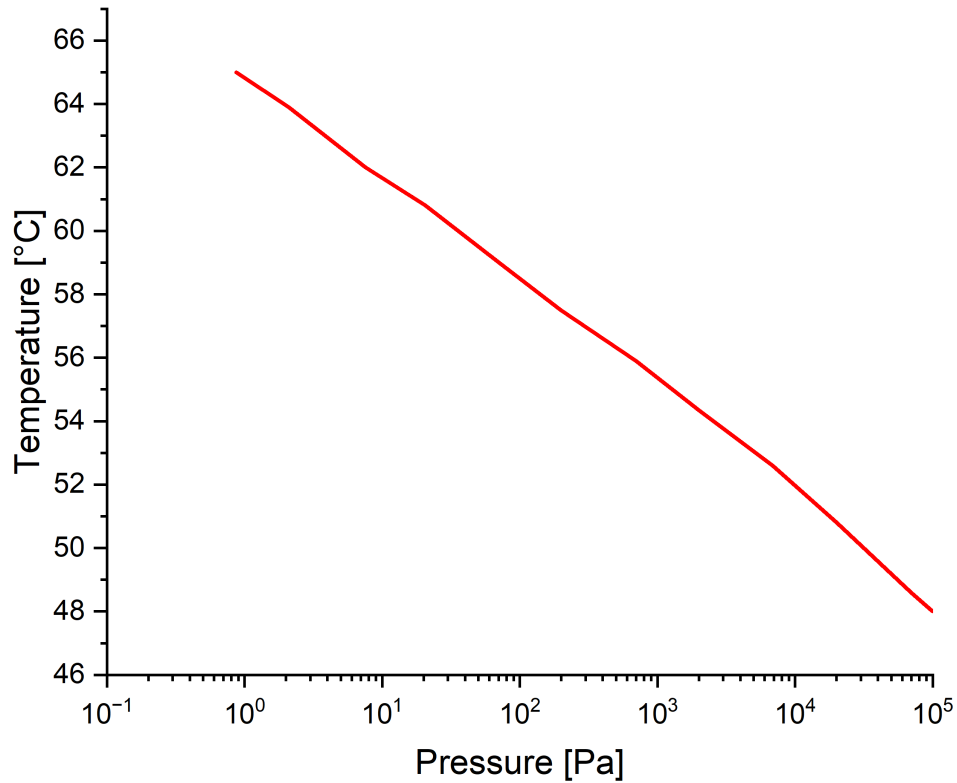


Figure 5.33 – Equilibrium temperature of the chip versus pressure.

sensor. The precision of the reference sensor is not constant and depends on the pressure range. The sensitivity decreases continuously through the pressure range. The uncertainty of the gauge is 15000 Pa close to atmospheric pressure and 1.5×10^{-5} Pa at high vacuum. This diminution also accounts for the discrepancy observed between the experimental results and the theoretical curve computed for a gas in the Knudsen regime. The theoretical curve corresponds to the maximum sensitivity. It was therefore expected that experimental results would be of a lower quality. There are also other sources of uncertainty among which the equilibrium temperature that depends on the pressure, the ambient temperature and the input voltage fluctuations. No frequency counter was used since there was more interest in the shift than in the actual value itself. The basis frequency depends on the thermal resistance and the size of the device. However, no extended uncertainty analysis was carried on. The analysed system is a prototype, many practical aspects were validated and a qualitative result was expected: the trend of the resonance frequency versus pressure. Extensive uncertainty analysis should be performed at a later development stage of the prototype or demonstrator presumably prior to market introduction.

Table 5.5 – Sensitivity of the prototype.

Pressure (Pa)	Pressure standard deviation	Sigma/P(%)
0.87	0.0020	0.22
2.10	0.0136	0.65
7.53	0.103	1.37
20.54	0.4161	2.03
70.44	0.1681	0.24
198.86	1.07	0.54
698.50	5.06	0.73
2058.71	16.07	0.78
6849.31	16.92	0.25
20070.38	15.04	0.075
69677.32	115.33	0.17
99722.23	126.83	0.13

Signal processing

In the Pirani sensing the thermal losses are conduction losses and then gaseous thermal transfer losses. Since the gaseous heat transfer is faster, the response time decreases. When AC current is applied, the response time generates a phase between the input signal and the temperature rise.

A method to reduce noise is to reduce the VNA's intermediate frequency (IF) bandwidth (BW). The IF bandwidth is a digitally implemented variable filter used to reduce noise. Narrower IF BW's result in additional data samples at each frequency point sample. The effect is similar to averaging. However, IF bandwidth reduction results in an increase in point-to-point averaging. Normal averaging is a sweep-by-sweep or trace-by-trace average. The minimum measurable frequency step is 1 kHz, this is the sensitivity of the Network Analyzer. Measurement performance depends on the calibration standard chosen, and on the repeatability of the measurement system itself. A visual criterion was used to identify the SAW peak, an algorithm is needed with clear conditions to identify the SAW peak. These points can be compared to the curve obtained with the simulation of 100 ppm/K calculated with a surface emissivity of 0.75. The experimental values follow the expected trend but are quite far from the orders of magnitude expected.

Outlook

Considering all the limitations and adjustments currently required, it can be asked whether the designed sensor and prototype represents an advantageous solution for the future. The commercially available viewports do not allow the transmission of either waves. Besides, to prevent tensions occurring during heating, cooling or installing, the viewports contain an intermediate metallization layer of kovar

(an iron-nickel-cobalt alloy) that prevents electromagnetic waves propagation. PMMA is not the best material to use in vacuum due to its poor mechanical stability. When vacuum was applied it was systematically bending which presented a risk of failure for such a small thickness. Viewports of ceramics without metallization or quartz should be considered for further tests. In [64] a fused quartz window is used to perform transvacuum measurements. Other distances due to the interrogation antenna and PCB were introduced. The reference [94] highlights the wireless charging procedure of a metallic device. It addresses the issue of electromagnetic waves transmission in metals. In vacuum most equipment is in stainless steel or aluminum, using the surrounding metals as an intermediate coil for induction coupling could be a solution. If this method can also be transposed to antenna operation, there will be no need for windows anymore.

The sensitivity and repeatability of the measurements were assessed. The presettings of the VNA software influences the quality of the measurement signal without modifying the hardware structure. A VNA of better signal quality and denser frequency sweep should be used to obtain a better precision. Since the prototype tested is not a final product, there is no use of an extended calibration according to international standards yet. For this purpose, a pressure calibrator (AMETEK JOFRA AP010C, AMETEK, Inc., U.S.A.) [56] could be used. The final setup in vacuum aimed to operate the prototype wirelessly and see its response. The position of each of the components strongly influences the measurement signal. All the components impact the measurements. In [95], an ultrasonic interferometer is presented. Factors for accurate low pressure manometry include the control of thermal and mechanical instabilities. The sensor itself shall have higher performances thanks to successful manufacturing processes. In order to enhance the performances of the prototype, many improvements in the manufacturing should be made. The SAW device should directly be suspended by wires to the substrate to eliminate the solid conduction heat losses. The heating resistance should be etched around the IDT directly in contact with the gas during the lithography process prior to the dicing.

The PCB containing the heating and interrogation unit should also be adapted to support the suspended chip by containing a hollow at its center aligned to the position of the microchannel. The SAW chip of the sensor is made of Lithium Niobate $Y+41^\circ-X$. However, using the YZ cut of the same Lithium Niobate crystal increases the temperature sensitivity up to 100 ppm/K which increases the temperature sensitivity by approximately five times. The results presented so far can be compared to the theoretical sensitivity curve mentioned above. For this purpose the experimental sensitivities should be multiplied by a correction factor to take the TCF difference into account. This factor equals to $100/19=5.3$ approximately. In order to improve the SAW Pirani performances, a more robust and easier to manufacture prototype should be produced. The IDTs can be in Ti/Au or in Ta/Pt. The Ti/Au electrodes can be used at low temperature. A diffusion phenomenon followed by the oxydation of titanium in gold at higher temperature forbids their use beyond 300 °C. The Ta/Pt structure is not subject to this issue and can be operated at very high temperatures. The use of a Pt heating resistor enables the direct measurement of the substrate temperature with conventional Pt 100 gauge for instance. A dynamic model needs to be validated now to forecast the response time of the sensor with respect to its geometry and its thermal

resistance. It might then be possible to detect 10^{-4} Pa. Finally, the sensitivity can be increased and the limit step further reduced by metallizing the surface of the sensing element. The experimental results also confirm the theoretically planned measurement range. Figure 5.28 shows the response of the SAW-Pirani over a wide range of pressure values, without forced convection device. Further experiments would have to show whether it is possible to remove the zero sensitivity area (regime 2) by means of a forced convection device.

6 Discussion of results

This chapter intends to discuss all the results obtained and to put them into perspective. Based upon the knowledge acquired with simulation, manufacturing, integration and measurements made, a final optimised design taking into account the manufacturing possibilities is proposed.

6.1 Working design

In order to heat the chip it is not necessary to sputter a metallic resistive layer at the bottom of it and process the chip then with many difficulties on both sides, top and bottom. The heating resistance and the SAW IDT shall be both manufactured on the top surface of the chip. The resistance and the IDT with their bonding pads shall be simultaneously produced by lithography. The wirebonding would then be less challenging. Four perpendicular directions would provide enough mechanical support while still mitigating solid conduction. Figure 6.1 shows the new design of the chip based upon the experience acquired with manufacturing equipment available. Only the top side of the piezoelectric substrate is processed. The IDT and reflector structures were maintained the same. However the heating resistor meander structure is placed around the IDT electrodes. Bonding pads are placed in a way that the four needed bonding wires are perpendicular to one another for mechanical support of the chip.

The material of the heating resistor is still flexible. A resistance in the range of $10\ \Omega$ is desirable to heat the chip properly. The value of the resistance can be adjusted by the thickness of the meander. When the resistor is manufactured early enough, bonding pad with according dimensions can also be suitably prepared to be compatible with the wirebonding machine.

Figure 6.2 shows the improved sensor core design. The main modifications are the insertion of a hole in the PCB where the chip is placed and bonded to it. The chip is protected by a microchannel hollow in the polymer package. The closed space protects the chip and allows entrance of the gas.

Packaging of the devices should be compatible with interrogation distances. Protection of the chip from the environment is also not addressed enough. A protection boxing should also be prepared. Contaminations could indeed come from gases, liquids or even small particles. Besides, the use of liquid polymer gel to cover the coil, the antenna and related SMD components would act as a seal, stabilise their position and control their temperature. The transmission of electromagnetic waves enabling Wifi and cell phone communications differs from the wave transfer developed for our sensor by many aspects. First of all, the transmitting antennae used for WiFi and cell phones are much bigger and radiate much more power,

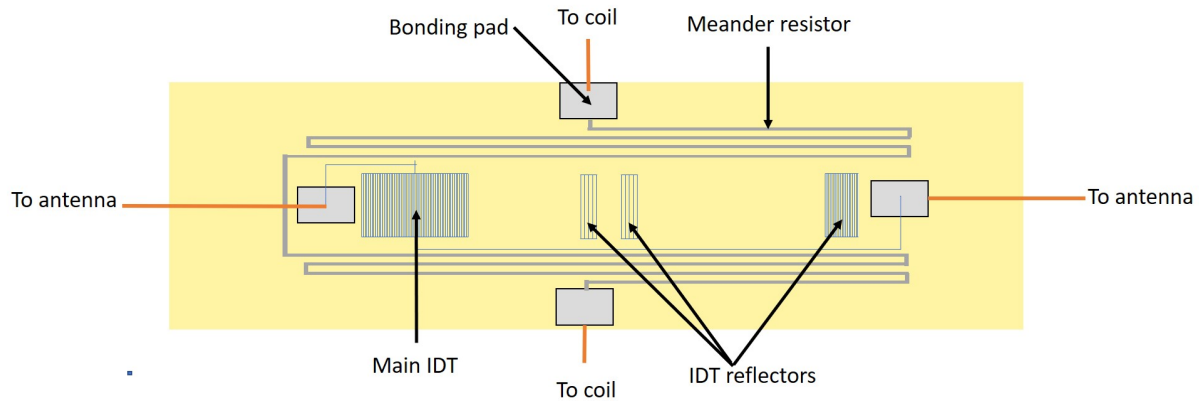


Figure 6.1 – New chip design.

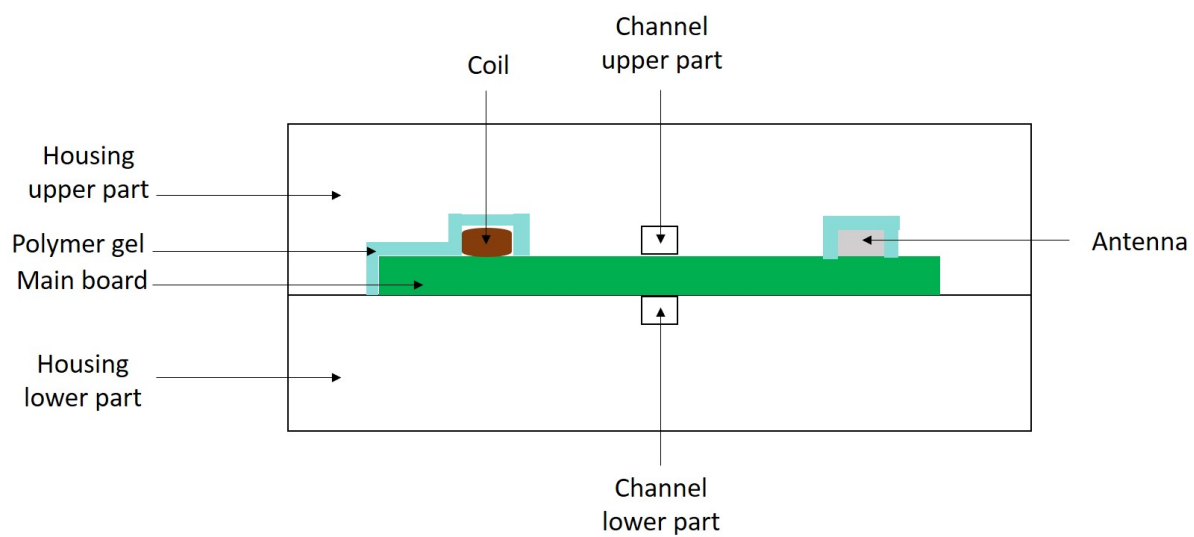


Figure 6.2 – New packaging design.

far field communication and different frequency bands are used. The energy of the receiver units such as a laptop or a cell phone has much more internal energy stored in the battery to amplify the signal received than a MEMS device. Moreover, the transmission signal being omnidirectional, the position and the orientation of the device is not as critical as the position of the micro patch Tx and Rx antenna used in the our sensor.

Considering the low power needs of our sensor, energy harvesting from the surroundings could be considered. The TGP 651 Micropelt thermogenerator generates power voltage from waste surrounding heat. It is suitable for milliwatt applications such as wireless sensor networks. It has dimensions of 15x10x9.5 mm and a weight of 2.2 g which makes it compatible with our sensor dimensions up to a certain point. However, micro thermogenerators still have a low and instable energy output. In [96], the surface resistance of currently available epitaxial HTS thin films at 77 K and for frequencies below 10 GHz is investigated. The resistance is lower by at least a factor of 100 than that of Copper at the

same temperature. This allows microwave components for the lower frequency regime (0.1 to 10 GHz) to be miniaturised without a degradation of their relevant electrical properties. An optimum substrate thickness with respect to the radiation efficiency exists.

Conventional microstrip patch antennas are usually operated at resonance, which results at centre frequency in a real input impedance at the feed point without the need for an additional matching network. The miniaturisation is due to both an increased permittivity and a change in the patch shape. To obtain the same miniaturisation factor without changing the rectangular patch shape, a permittivity of about 110 would be required. At very low temperatures the power efficiency of antenna is very high. The geometric size of resonant planar antennas in the VHF or UHF regime can be considerably reduced by means of a modified “patch shape” including small-width transmission line sections. Owing to both the increased radiation quality factor and increased losses in the small strip conductors, this miniaturisation results in a very low (few percents) value of the radiation efficiency in the case of normal conducting antenna structures. The utilisation of HTS thin films together with low-loss substrates allows the radiation efficiency to be increased to values which are typical for the much larger normal conducting conventional patch antennas.

Heating power could also be modulated by the power supply. Heat management remains one of the main issues of the sensor. Heating occurs in many undesired places. This heat should be harvested or produced in a more useful place. The heat produced at the coils is parasitic. Harvesting the produced heat could save a lot of energy. Considering the size of the Tx coil and the Rx coil, more than one Rx coil can be powered using the same Tx coil. More sensors can be placed, powered and operated in a similar way with a reasonable coupling distance.

Moreover, the RFID function introduced in the chip allows identification of the sensors. After the development of our sensor it is still possible to ask whether the sensor presents in practice an attractive solution compared to the state of the art. The answer remains yes because it offers many new opportunities in terms of miniaturisation, reduced price and wireless operation and extension of the sensing range using one single device. A new sensor was designed and simulated. A first prototype was assembled and tested. It improves the sensing range and avoids the use of bulky wires to acquire measurement signal. The SAW-Pirani developed extends the sensing range in a compact design.

6.2 Simulation

Simulation is a powerful tool but it is very important to be aware of its limits. It provides a qualitative description and analysis of the physical phenomena that can be used as guidelines to improve designs. Nonetheless, precise numerical values should not be given excessive importance whereas trends and tendencies for optimisation can be used. In the present study, the effect of many parameters on the device sensitivity was observed. In the case of a sensor development for industrial applications, parsimonious

effort should be invested on the simulation. The simulation should enable the manufacturing of a prototype, which means the manufacturing capabilities especially dimension limitations should be taken into account at the early stages of the simulation. Heat transfer and electronics simulations were performed, no SAW propagation simulation was conducted. COMSOL should be used to couple SAW and temperature effects as well as mechanical effects together on the sensor due to pressure variation. Simulation should also be used to assess the mechanical stability of the wire suspension. A simulation of the stress due to pressure on the chip and the wires should help to determine easily the optimum diameter value for a stable setup through the whole target range. The mechanical stability of the suspension through the wires should be simulated to determine the optimal length and thickness of the wires. There is less flexibility in the choice of the wire material. The disposition of the wires supporting the chip is critical for the mechanical stability and to eliminate solid conduction losses.

6.3 Manufacturing

The SAW IDT electrodes are manufactured via e-beam lithography. They constitute the smallest and most fragile component of the sensor. They should be manufactured as late as possible in the process and protected as efficiently as possible. Since the IDT electrodes seem to be more fragile than the Gold layer, they should be etched at last. A final process flow for the chip is proposed:

1. Manufacture the meander resistor by laser etching
2. Wirebond the resistor and leave the wires suspended
3. Flip the wafer to process the top
4. Etch the IDT electrodes by e-beam lithography
5. Wirebond the IDT to the PCB

6.4 Vacuum integration

Integration of the sensor inside a vacuum environment in a sustainable way, although it is the essence of the measurement, poses major challenges. The development of our sensor faced several confrontations. First of all the miniaturisation of such a device: while current commercial vacuum sensors have the size of a coffee mug in addition to all the bulky wiring needed for power supply and signal acquisition, the future sensor shall not be larger as 2 cm^3 . The miniaturisation of such a system and the integration of its components altogether in a restricted volume was addressed. Afterwards, wireless operation was implemented to eliminate the necessity of bulky wiring. Wireless operation implementation had to achieve

induction coupling of very small coils through a significant distance in a mainly metallic environment. The extra difficulty due to vacuum is that all the pipelines are in metal which is not helpful for the propagation of EM waves. For this reason, another material had to be used at the interface between the sensor inside vacuum and the transmitting antenna and coil situated outside vacuum. The preparation of a suitable window with an appropriate material in terms of transmissibility and thickness was required. The thickness of the window directly impacted the coupling distance between the induction coils. Quartz, non-metallized borosilicate, ceramics and sapphire were considered. Generally, this interface can either be a window, a viewport or a hollow volume that could also act as a protection and packaging of the sensor. The sensor box would be connected to the chamber via a vacuum fitting.

The Qi standard is a wireless charging standard for providing 5-15 W of power to small electronics. It is mainly used to charge smartphones but it is suitable for consumer devices. For charging cell phones, the coils are much bigger and the coupling distance rarely exceeds 5 mm for an efficiency around 55%. The coils selected in the development of our sensor comply with the Qi standard. A better selection of the coil pair from what is available off the shelf might help find a better compromise between coupling distance, coil size and power transfer efficiency.

In [10] the chip is suspended by 4 solid beams of 30 μm width by 65 μm length. The air gap is between 6 μm and 10 μm for a 300 μm chip. Our developed chip is 400 μm by 6 mm and should be supported by 4 gold microwires of maximum diameter 200 μm . Our sensor does not use any Wheatstone bridge anymore for temperature compensation.

An immediate solution to increase the performances of the sensor would be to use a larger antenna and a larger coil. This would give more flexibility for the interrogation distance and provide a higher current to the heating resistance but sacrifice the miniaturisation and compactness of the sensor. The remaining question is how large the antenna can be and if it is already commercially available. The quality of the interrogation signal received by the sensor inside vacuum depends on the interrogation antenna and the VNA. The antennae selected from Wuerth Elektronik and from Johanson are small and absorb a small portion of the received power and radiate it back. The power transmitted to the antenna and its efficiency is proportional to its size. The power supplied by the Mini VNA Tiny is also very small. Using a more powerful Network Analyzer should already help a lot. A balance should be found between the interrogation distance and the size of the Tx and Rx unit. The higher, the coupling distance, the bigger the size of the Tx and Rx needed to obtain a reliable measurement signal. The minimum coupling distance is determined by the vacuum installation where the sensor is inserted, i.e. the thickness of the vacuum viewport and some distance due to the SMD cable connections outside and the coil geometry inside the vacuum chamber. 1 cm could be a good compromise distance for a start. The PCB size is small enough. Its thickness is a reasonable compromise between small and still mechanically stable and supporting all the components on top of it.

7 Conclusion and outlook

Summary

This research work assesses the feasibility and interest of a wireless compact miniaturised vacuum sensor combining the Pirani principle and Surface Acoustic Waves. The ability to enhance the performances of an existing sensor as well as the combination and miniaturisation of several functionalities in one compact device was addressed. Micro-fabrication and semiconductor technology were used to miniaturise the sensing device and increase its efficiency.

The operation of vacuum pressure sensors manufactured using micro-machining and microfluidics relies on heat transfer effects which are characterized by the variation of thermal conductivity of a gas along the pressure range covered. The thermal conductivity variation can lead to different pressure dependent steady state temperatures along with different pressures. The limits of the sensing principle are fixed by heat transfer, i.e.:

- variation of the gas thermal conductivity of gas with pressure
- parasitic solid heat conduction for the sensing chip to the rest of the sensor core
- parasitic radiative heat transfer that becomes non negligible beyond a certain temperature

The modelling and simulation in COMSOL has shown the limits of the operating range dependence of the thermal conductivity with respect to pressure. After changing the pressure in the simulation, the steady state temperature was reached after a fairly long response time of 100 s compared to the 5 ms of the conventional Pirani gauges [10]. Indeed, when the thermal conductivity is too small at low pressure, the heat transfer process is very slow.

Modelling and simulation were used to design a new optimised chip. The equations were obtained using gas kinetic theory. A parameter sensitivity analysis was conducted to improve the vacuum sensing performance via dimensioning.

The surface to volume ratio, the gas gap and the emissivity of the interacting surfaces influence the heat transfer and, therefore, have been chosen based on their impact on heat transfer for further improvement for the pressure sensing performance.

Further extensions of the sensor's operating range were achieved with heat transfer enhancement techniques, more precisely with optimisation of the dimensions of the sensing chip. The radiative heat transfer has been addressed by modifying the chip surface emissivity as well as the emissivity values of the surrounding surfaces. After working on extracting the maximum of 'useful signal' from the gas, effort

was invested on amplifying this useful signal at the chip level. In order to reduce the thermal losses due to solid conduction, the chip was suspended via wires inside a microchannel. The current size of the chip is a major challenge to the current bonding technologies especially soldering. The electrical contacting of the chip is still a risky and delicate task.

The chip which is the sensing unit needed to be connected to all other units. The heating unit is responsible for locally heating the chip: a gold thin film layer acts as a joule resistance bottom of the chip powered by means of induction coupling between two coils, a transmitting coil outside a vacuum chamber and a receiving coil inside a vacuum chamber, both being as compact as possible. The gold layer at the chip bottom represented a manufacturing challenge since it required processing both sides of the chip, the SAW transducer at the top and the joule resistance at the bottom.

The interrogation unit is made of a transmitting and a receiving antenna. The transmitting antenna is located outside the vacuum chamber connected to a Vector Network Analyzer. The receiver antenna is inside the sensor core and connected to the sensing chip. The receiver antenna needed to be as small as possible to fit inside the compact sensor core. The operating frequency of the SAW is 2.45 GHz inside the Industrial Scientific Medical frequency band. This range is indeed free for use and easy to couple with commercial electronics. However, using a small receiving antenna with a small surface captures only a small portion of the electromagnetic waves radiated by the transmitting antenna which makes the energy transmission rather poor. To address this issue, the transmitter and receiver antennae were separated by a very small distance of a few mm. The measured antenna gain was lower than indicated in the technical sheet which reduced the coupling distance from 2 cm at the maximum to 5 mm only. The Rx coil and Rx antenna inside the sensor core were placed together with their coupling electronics on a Printed Circuit Board (PCB) of 15 mm by 11 mm by 2 mm. A PCB was assembled on a 15 mm by 11 mm by 3 mm Flame Resistant 4 board and a coupling distance of 7 mm was achieved.

The packaging had to ensure the enclosure of this PCB, the protection of the chip and the contact between the chip and the gas. The chip was therefore placed inside a microchannel crossing the sensor core enabling gas circulation. The chip was connected to the heating and interrogation unit via four wires suspending it at the same time. The electrical contacting of the chip with the rest of the PCB was challenging with respect to the available technologies. This work confronted the limits of miniaturisation and semiconductor processes namely wirebonding, soldering and chip suspending. The whole packaging of the sensor has a compact cubic form made of a material compatible with vacuum. The Polytetrafluoroethylene (PTFE) polymer was chosen for its cost and to avoid outgassing. It is also particularly suitable for drilling small radii holes for wires. The target interrogation distance of 2 cm was not reached.

The analysis of the state of the art prior to the research work presented here highlights several technical issues and challenges:

- Vacuum sensors still have very restricted sensing ranges, hence the necessity for several transducers combined to sense high vacuum to atmospheric pressure.
- The sensors have bulky wiring, housing and a rather high power consumption.

- Wireless interrogation and heating for pressure and vacuum sensing is still not reliable enough.
- No thermal analysis of SAW sensors in vacuum using gas kinetic theory is available.

This research work suggests several solutions to these preliminary issues, which are :

- A compact sensing system with extended range and sensitivity compared to existing devices was developed.
- Miniaturised wireless technologies were implemented. Small conditioning electronics for wireless transmission were validated.
- Limits of some semiconductor processes were pushed:
 - Processing the chip on two sides, top and bottom
 - soldering of small surfaces
 - wirebonding with suspended wires
- A smaller chip was designed.
- RFID was introduced on the sensor as well.
- A system integration in a tiny space compatible with two distinct waves propagations was achieved.
- After varying several dimensional parameters of the sensor chip, simulation showed that pressures between 10^{-4} Pa and 10^5 Pa can be sensed via the gas thermal conductivity variation.

The investigation of different heating methods, different interrogation methods, different chip materials and different packaging materials lead to interesting conclusions in order to improve vacuum sensor performances:

- use of a piezoelectric substrate with the highest Temperature Coefficient of Frequency increases the sensitivity
- implementation of a wireless transmission method compatible with vacuum chambers made of stainless steel removes the bulky wiring. This can be achieved by using a glass window or even using the metallic material as an intermediate antenna
- energy range necessary for the sensor operation is compatible with the possible coupling distance in a vacuum environment.

This thesis corresponds in a certain extent to a new product development addressing industrial and research issues pushing the limits of available semiconductor technologies (e-beam lithography, wirebonding, soldering). In vision of market introduction, further industrial aspects such as the trademark Vacube and certification processes were addressed.

Recommendations for future work

It has been demonstrated in the present study that a compact wireless vacuum micro sensor with wide measurement range is feasible. The device can now be optimised and further developed.

The sensor was developed in a way to be compatible with state of the art technologies including SAW, RFID, Bluetooth or even WiFi. Considering the latest technologies, the sensor was designed to be integrated to the current vacuum sensor market landscape.

The electrical contacting designed based upon soldering and wirebonding was only partly achieved due to the necessity to process the chip on both sides. In this case only front end processing at the wafer level can be successful considering the size of the chip as opposed to the back end process applied.

The experiments show that such a compact sensor can be integrated inside a vacuum environment. Better alternatives were later found to improve the prototype performances among which the use of a higher quality polymer.

One of the further research topics is the numerical and experimental investigation of the sustainable suspension of the chip inside the microchannel via bonding wires in terms of wire material, thickness and bonding technology used. In deed, the material, thickness, the position and the technology used for the wires influences the long term stability of the wires and therefore of the whole sensor. The optimisation of these parameters depends on the desired mechanical stability all along a reasonable cost and processing time. Simulation should be used to find the optimal position, material and thickness of the wires to ensure a successful manufacturing process. Besides, the overall heat transfer analysis could still be improved. More experimental data should be collected to evaluate the gas thermal conductivity, the accommodation coefficient and the temperature coefficient of frequency so as to improve the accuracy of the simulation.

A comprehensive numerical study with the chip, the PCB and the packaging together should be performed to obtain better heat transfer analysis. The method to evaluate the Temperature Coefficient of Frequency (TCF) of the substrate material needs to be further examined in order to know if piezoelectric materials with higher sensitivity to temperature are available although the current sensitivity to temperature of the current crystals is not the limiting factor of the sensor performance.

Further Rx antennae should be investigated in order to increase the energy transfer while maintaining a reduced size. A higher energy transfer could reduce the response time by heating faster and increase the sampling rate by delivering more sensing data. One solution mentioned in the literature is using the metallic vacuum pipes as intermediate antennas. However, the limited space available for the Rx antenna is a major constraint.

The implementation of wireless vacuum compact sensors in research and industrial vacuum installations would enable a more thorough and comprehensive pressure monitoring leading to better vacuum process quality for many domains of application especially the semiconductor industry.

Finally, the consideration of extending the compact wireless vacuum micro sensor to further sensors such as temperature, flow velocity could open up new opportunities in research and in industry as well.

Bibliography

- [1] H. Baltes, O. Brand, J. G. Korvink, R. Lenggenhager, and O. Paul, "Imems - integrated micro electro mechanical systems by vlsi and micromachining," in *ESSDERC '94: 24th European Solid State Device Research Conference*, Sep. 1994, pp. 273–280.
- [2] A. Pohl, "A review of wireless saw sensors," *IEEE Transactions on Ultrasonics, Ferroelectrics, and Frequency Control*, vol. 47, no. 2, pp. 317–332, March 2000.
- [3] A. Schütze, N. Helwig, and T. Schneider, "Sensors 4.0—smart sensors and measurement technology enable industry 4.0," *Journal of Sensors and Sensor systems*, vol. 7, no. 1, pp. 359–371, 2018.
- [4] N. Khalil, M. R. Abid, D. Benhaddou, and M. Gerndt, "Wireless sensors networks for internet of things," in *2014 IEEE ninth international conference on Intelligent sensors, sensor networks and information processing (ISSNIP)*. IEEE, 2014, pp. 1–6.
- [5] S. Dushman, *Scientific Foundations of Vacuum Technique*. New York, USA: Chapman & Hall, 1962.
- [6] I. L. Chuang and Y. Yamamoto, "Simple quantum computer," *Phys. Rev. A*, vol. 52, pp. 3489–3496, Nov 1995.
- [7] S. Stoukatch, L. Francis, F. Dupont, and M. Kraft, "Low-cost microfluidic device micromachining and sequential integration with saw sensor intended for biomedical applications," *Sensors and Actuators A: Physical*, vol. 319, p. 112526, 2021.
- [8] F. L. Duan, Z. Xie, Z. Ji, J. Li, Z. Liu, B. Zou, and H. Weng, "Wireless passive temperature measurement for aero-and astro-system by using surface acoustic wave sensors," in *AIAA Scitech 2021 Forum*, 2021, p. 1502.
- [9] A. H. Rasolomboahanginatovo, Y. Sanogo, F. Domingue, and A. O. Dahmane, "Custom pxie-567x-based saw rfid interrogation signal generator," *IEEE Sensors Journal*, vol. 16, no. 24, pp. 8798–8806, Dec 2016.
- [10] F. Völklein, M. Grau, A. Meier, G. Hemer, L. Breuer, and P. Woias, "Optimized MEMS Pirani sensor with increased pressure measurement sensitivity in the fine and high vacuum regime," *Journal of Vacuum Science Technology A*, vol. 31, no. 6, p. 061604, 09 2013.

- [11] P. Nicolay and M. Lenzhofer, "A wireless and passive low-pressure sensor," *Sensors*, vol. 14, no. 2, pp. 3065–3076, 2014.
- [12] R. Figliola and D. Beasley, *Theory and Design for Mechanical Measurements*. Wiley, 2020.
- [13] C. Lipson and N. Sheth, *Statistical Design and Analysis of Engineering Experiments*. McGraw-Hill, 1973.
- [14] P. Ripka and A. Tipek, *Modern sensors handbook*. Wiley Online Library, 2007.
- [15] C. M. Close, D. K. Frederick, and J. C. Newell, *Modeling and analysis of dynamic systems*. John Wiley & Sons, 2001.
- [16] J. Devkota, P. Ohodnicki, and D. Greve, "Saw sensors for chemical vapors and gases," *Sensors (Switzerland)*, vol. 17, 04 2017.
- [17] D. Morgan and E. Paige, "2 - acoustic waves in elastic solids," in *Surface Acoustic Wave Filters (Second edition)*, second edition ed., ser. Studies in Electrical and Electronic Engineering, D. Morgan and E. Paige, Eds. Oxford: Academic Press, 2007, pp. 38–67.
- [18] C. Steinem and A. Janshoff, *Piezoelectric sensors*. Springer Science & Business Media, 2007, vol. 5.
- [19] IEEE, "The authoritative dictionary of ieee standards terms, seventh edition," *IEEE Std 100-2000*, pp. 1–1362, 2000.
- [20] H. Baher, *Analog and digital signal processing*. John Wiley & Sons, 2001.
- [21] E. O. Doebelin, *System modeling and response: theoretical and experimental approaches*. John Wiley & Sons, 1980.
- [22] E. Smith, "Uncertainty analysis," *Encyclopedia of environmetrics*, vol. 4, pp. 2283–2297, 2002.
- [23] J.-P. Viricelle and C. Pijolat, "Introduction to eurosensors 2017. paris, 3–6 september 2017," 2017.
- [24] S. Kandlikar, S. Garimella, D. Li, S. Colin, and M. R. King, *Heat transfer and fluid flow in minichannels and microchannels*. Elsevier, 2005.
- [25] S. Toto, P. Nicolay, G.-L. Morini, M. Rapp, J. Korvink, and J. Brandner, "Design and simulation of a wireless saw–pirani sensor with extended range and sensitivity," *Sensors*, vol. 19, p. 2421, 05 2019.
- [26] F. Sharipov, "Heat transfer in the knudsen layer," *Physical Review E*, vol. 69, no. 6, p. 061201, 2004.

- [27] R. Puers, S. Reyntjens, and D. D. Bruyker, "The nanopirani—an extremely miniaturized pressure sensor fabricated by focused ion beam rapid prototyping," *Sensors and Actuators A: Physical*, vol. 97-98, pp. 208 – 214, 2002, selected papers from Eurosenors XV.
- [28] M. Grau, F. Völklein, A. Meier, C. Kunz, J. Heidler, and P. Woias, "Method for measuring thermal accommodation coefficients of gases on thin film surfaces using a mems sensor structure," *Journal of Vacuum Science & Technology A*, vol. 34, no. 4, p. 041601, 2016.
- [29] K. Jousten and S. Naef, "On the stability of capacitance-diaphragm gauges with ceramic membranes," *Journal of Vacuum Science & Technology A*, vol. 29, no. 1, p. 011011, 2011.
- [30] A. L. Hughes, "A simple knudsen gauge," *Review of Scientific Instruments*, vol. 8, no. 11, pp. 409–412, 1937.
- [31] W. Jitschin and M. Ruschitzka, "Metrological properties of the thermal conductivity gauge," *Vacuum*, vol. 44, no. 5-7, pp. 607–609, 1993.
- [32] K. Jousten, F. Boineau, N. Bundaleski, C. Illgen, J. Setina, O. M. Teodoro, M. Vicar, and M. Wüest, "A review on hot cathode ionisation gauges with focus on a suitable design for measurement accuracy and stability," *Vacuum*, vol. 179, p. 109545, 2020.
- [33] K. Jousten, "On the gas species dependence of pirani vacuum gauges," *Journal of Vacuum Science & Technology A: Vacuum, Surfaces, and Films*, vol. 26, no. 3, pp. 352–359, 2008.
- [34] X. Wang, C. Liu, Z. Zhang, S. Liu, and X. Luo, "A micro-machined pirani gauge for vacuum measurement of ultra-small sized vacuum packaging," *Sensors and Actuators A: Physical*, vol. 161, no. 1, pp. 108 – 113, 2010.
- [35] F. Zhang, Z. Tang, J. Yu, and R.-C. Jin, "A micro-pirani vacuum gauge based on micro-hotplate technology," *Sensors and Actuators A: Physical*, vol. 126, pp. 300–305, 02 2006.
- [36] T. Brun, D. Mercier, A. Koumela, C. Marcoux, and L. Duraffourg, "Silicon nanowire based pirani sensor for vacuum measurements," *Applied Physics Letters*, vol. 101, no. 18, p. 183506, 2012.
- [37] K. Khosraviani and A. Leung, "The nanogap pirani - a pressure sensor with superior linearity in atmospheric pressure range," *2008 IEEE 21st International Conference on Micro Electro Mechanical Systems*, pp. 900–903, 2008.
- [38] W. Jitschin and S. Ludwig, "Dynamical behaviour of the pirani sensor," *Vacuum*, vol. 75, no. 2, pp. 169–176, 2004.
- [39] P. K. Weng and J. Shie, "Micropirani vacuum gauge," *Review of Scientific Instruments*, vol. 65, no. 2, pp. 492–499, 1994.

- [40] F. Voelklein and A. Meier, "Microstructured vacuum gauges and their future perspectives," *Vacuum*, vol. 82, pp. 420–430, 12 2007.
- [41] (2022) MS Windows NT kernel description. [Accessed October 23rd, 2022]. [Online]. Available: <http://web.mit.edu/viz/EM/visualizations/coursenotes/modules/guide11.pdf>
- [42] Y. Lu and W. Ki, *CMOS Integrated Circuit Design for Wireless Power Transfer*, ser. Analog Circuits and Signal Processing. Springer Singapore, 2017.
- [43] S. Stoecklin, A. Yousaf, T. Volk, and L. Reindl, "Efficient wireless powering of biomedical sensor systems for multichannel brain implants," *IEEE Transactions on Instrumentation and Measurement*, vol. 65, no. 4, pp. 754–764, April 2016.
- [44] A. P. Sample, D. T. Meyer, and J. R. Smith, "Analysis, experimental results, and range adaptation of magnetically coupled resonators for wireless power transfer," *IEEE Transactions on Industrial Electronics*, vol. 58, no. 2, pp. 544–554, Feb 2011.
- [45] H. K. Kang, Y. D. Chung, and S. W. Yim, "Conceptual design of contactless power transfer into hts receiver coil using normal conducting resonance antenna," *Cryogenics*, vol. 63, pp. 209 – 214, 2014.
- [46] V. T. Kilic, E. Unal, E. Gonendik, N. Yilmaz, and H. V. Demir, "Strongly coupled outer squircle–inner circular coil architecture for enhanced induction over large areas," *IEEE Transactions on Industrial Electronics*, vol. 63, no. 12, pp. 7478–7487, Dec 2016.
- [47] F. Aki, T. Loi, H. Saito, N. Yoshimura, and K. Mitobe, "Study of wireless temperature measurement induction heating system using magnetic properties of au-coated ferromagnetic implant with low curie temperature," *Electronics and Communications in Japan*, vol. 101, no. 6, pp. 58–66, 2018.
- [48] S.-k. Baek, J. Min, and J.-H. Park, "Wireless induction heating in a microfluidic device for cell lysis," *Lab Chip*, vol. 10, pp. 909–917, 2010.
- [49] Byoung-Ok Jun, Jong Gu Kang, Ji-Woong Choi, and Jae Eun Jang, "The study of wireless thin film transistor with micro magnetic induction coupling antenna structure," in *14th IEEE International Conference on Nanotechnology*, Aug 2014, pp. 794–798.
- [50] E. F. Stehlin, D. McCormick, S. C. Malpas, B. P. Pontré, P. A. Heppner, and D. M. Budgett, "Mri interactions of a fully implantable pressure monitoring device," *Journal of Magnetic Resonance Imaging*, vol. 42, no. 5, pp. 1441–1449, 2015.
- [51] Z. Qi, Y. Zhuang, X. Li, W. Liu, Y. Du, and B. Wang, "Full passive uhf rfid tag with an ultra-low power, small area, high resolution temperature sensor suitable for environment monitoring," *Microelectronics Journal*, vol. 45, no. 1, pp. 126 – 131, 2014.

- [52] W. R. Heinzelman, A. Chandrakasan, and H. Balakrishnan, "Energy-efficient communication protocol for wireless microsensor networks," in *Proceedings of the 33rd Annual Hawaii International Conference on System Sciences*, Jan 2000, pp. 10 pp. vol.2–.
- [53] K. Länge, B. E. Rapp, and M. Rapp, "Surface acoustic wave biosensors: a review," *Analytical and bioanalytical chemistry*, vol. 391, no. 5, pp. 1509–1519, 2008.
- [54] C. Fu, Y. Ke, M. Li, J. Luo, H. Li, G. Liang, and P. Fan, "Design and implementation of 2.45 ghz passive saw temperature sensors with bpsk coded rfid configuration," *Sensors*, vol. 17, no. 8, 2017.
- [55] S. Rokhlin, L. Kornblit, and G. Gorodetsky, "Surface acoustic wave pressure transducers and accelerometers," *Progress in Aerospace Sciences*, vol. 21, pp. 1 – 31, 1984.
- [56] J. Rodríguez-Madrid, G. Iriarte, O. Williams, and F. Calle, "High precision pressure sensors based on saw devices in the ghz range," *Sensors and Actuators A: Physical*, vol. 189, pp. 364 – 369, 2013.
- [57] L. Rana, R. Gupta, M. Tomar, and V. Gupta, "Zno/st-quartz saw resonator: An efficient no2 gas sensor," *Sensors and Actuators B: Chemical*, vol. 252, pp. 840 – 845, 2017.
- [58] Q. Jiang, X. Yang, h. g. Zhou, and J. Yang, "Analysis of surface acoustic wave pressure sensor," *Sensors and Actuators A: Physical*, vol. 118, pp. 1–5, 01 2005.
- [59] A. Müller, G. Konstantinidis, I. Giangu, G. C. Adam, A. Stefanescu, A. Stavriniadis, G. Stavriniadis, A. Kostopoulos, G. Boldeiu, and A. Dinescu, "Gan membrane supported saw pressure sensors with embedded temperature sensing capability," *IEEE Sensors Journal*, vol. 17, no. 22, pp. 7383–7393, Nov 2017.
- [60] G. Borrero, J. Bravo, S. Mora, S. Velásquez, and F. Segura-Quijano, "Design and fabrication of saw pressure, temperature and impedance sensors using novel multiphysics simulation models," *Sensors and Actuators A: Physical*, vol. 203, pp. 204 – 214, 2013.
- [61] V. Kutiš, G. Gálik, V. Královič, I. Rýger, E. Mojto, and T. Lalinský, "Modelling and simulation of saw sensor using fem," *Procedia Engineering*, vol. 48, pp. 332 – 337, 2012, modelling of Mechanical and Mechatronics Systems.
- [62] P. Maurya and N. Mandal, "Design analysis of wireless pressure measurement by integrating surface acoustic wave sensor with bourdon tube," *IEEE Sensors Journal*, vol. 18, no. 21, pp. 8996–9004, Nov 2018.
- [63] A. Talbi, F. Sarry, L. Le Brizoual, O. Elmazria, and P. Alnot, "Sezawa mode saw pressure sensors based on zno/si structure," *IEEE Transactions on Ultrasonics, Ferroelectrics, and Frequency Control*, vol. 51, no. 11, pp. 1421–1426, Nov 2004.

- [64] P. Nicolay, “Les capteurs à ondes élastiques de surface. applications pour la mesure des basses pressions et des hautes températures,” Ph.D. dissertation, Université Henri Poincaré, Nancy, 2007.
- [65] P. Nicolay, O. Elmazria, F. Sarry, L. Bouvot, N. Marche, and H. Kambara, “Innovative surface acoustic wave sensor for accurate measurement of subatmospheric pressure,” *Applied Physics Letters*, vol. 92, no. 14, p. 141909, 2008.
- [66] D. Mercier, G. Bordel, P. Brunet-Manquat, S. Verrun, O. Elmazria, F. Sarry, B. Belgacem, and J. Bounoua, “Characterization of a saw-pirani vacuum sensor for two different operating modes,” *Sensors and Actuators A: Physical*, vol. 188, pp. 41–47, 2012, selected papers from The 16th International Conference on Solid-State Sensors, Actuators and Microsystems.
- [67] K. J. Singh, O. Elmazria, F. Sarry, P. Nicolay, K. Ghoumid, B. Belgacem, D. Mercier, and J. Bounoua, “Enhanced sensitivity of saw-based pirani vacuum pressure sensor,” *IEEE Sensors Journal*, vol. 11, no. 6, pp. 1458–1464, 2011.
- [68] Z. Gao, Z. Chen, X. Huang, R. Tong, and M. Wang, “Design and implementation of saw reader receiving circuit,” in *2013 Symposium on Piezoelectricity, Acoustic Waves, and Device Applications*, Oct 2013, pp. 1–4.
- [69] F. Lurz, T. Ostertag, B. Scheiner, R. Weigel, and A. Koelpin, “Reader architectures for wireless surface acoustic wave sensors,” *Sensors*, vol. 18, no. 6, p. 1734, 2018.
- [70] Y. Pan, N. Mu, B. Liu, B. Cao, W. Wang, and L. Yang, “A novel surface acoustic wave sensor array based on wireless communication network,” *Sensors*, vol. 18, no. 9, 2018.
- [71] K. A. Cook-Chennault, N. Thambi, and A. M. Sastry, “Powering MEMS portable devices—a review of non-regenerative and regenerative power supply systems with special emphasis on piezoelectric energy harvesting systems,” *Smart Materials and Structures*, vol. 17, no. 4, p. 043001, jun 2008.
- [72] M. J. Madou, *Fundamentals of microfabrication: the science of miniaturization*. CRC press, 2002.
- [73] M. Altissimo, “E-beam lithography for micro-/nanofabrication,” *Biomicrofluidics*, vol. 4, no. 2, p. 026503, 2010.
- [74] U. of Michigan. (2020) Electron beam lithography. [Accessed October 2nd, 2022]. [Online]. Available: https://Inf-wiki.eecs.umich.edu/wiki/Electron_beam_lithography
- [75] J. Korvink, O. Gruschke, and V. Badilita, “Introduction to microsystem technologies 2,” University Lecture at the Karlsruhe Institute of Technology, 2019.

- [76] A. C. Fischer, J. G. Korvink, N. Roxhed, G. Stemme, U. Wallrabe, and F. Niklaus, "Unconventional applications of wire bonding create opportunities for microsystem integration," *Journal of Micromechanics and Microengineering*, vol. 23, no. 8, p. 083001, jun 2013.
- [77] K. Poole and M. Michaelis, "Hialvac and teflon outgassing under ultra-high vacuum conditions," *Vacuum*, vol. 30, no. 10, pp. 415 – 417, 1980.
- [78] A. P. Miiller, "Measurement performance of high-accuracy low-pressure transducers," *Metrologia*, vol. 36, no. 6, pp. 617–621, dec 1999.
- [79] J. Ruellan, "Design, fabrication and characterization of a silicon nanowire based thermal conductivity detector," Theses, Université Grenoble Alpes, May 2015.
- [80] M. Grau, F. Völklein, A. Meier, C. Kunz, I. Kaufmann, and P. Woias, "Optimized mems pirani sensor with increased pressure measurement sensitivity in the fine and rough vacuum regimes," *Journal of Vacuum Science & Technology A*, vol. 33, no. 2, p. 021601, 2015.
- [81] C.-K. Leong, Y. Aoyagi, and D. Chung, "Carbon black pastes as coatings for improving thermal gap-filling materials," *Carbon*, vol. 44, no. 3, pp. 435–440, 2006.
- [82] S. Toto, G.-L. Morini, and K. Haas-Santo, "Thermal behaviour of a saw transducer for pressure measurements." MIGRATE Workshop - June 29 - 30, 2017. Bulgarian Academy of Sciences.
- [83] R. Van Eck, M. Klep, and J. Schijndel, "Surface to surface radiation benchmarks," in *COMSOL conference, 12-14 October 2016, Munich, Germany*, 10 2016.
- [84] L. B. Thomas and R. E. Brown, "The accommodation coefficients of gases on platinum as a function of pressure," *The Journal of Chemical Physics*, vol. 18, no. 10, pp. 1367–1372, 1950.
- [85] D. Royer and E. Dieulesaint, *Ondes élastiques dans les solides: Génération, interaction acousto-optique, applications*, ser. Enseignement de la physique. Masson, 1999.
- [86] A. Guha, H. Li, Z. Sun, C. Ma, D. Werschmoeller, and X. Li, "Wireless acquisition of temperature data from embedded thin film sensors in cutting insert," *Journal of Manufacturing Processes*, vol. 14, no. 3, pp. 360 – 365, 2012.
- [87] P. Nicolay, O. Elmazria, and X. Perois, "A miniaturized saw-pirani sensor," in *2012 IEEE International Ultrasonics Symposium*, 04 2012, pp. 1541–1544.
- [88] H. Reichl, "Packaging and interconnection of sensors," *Sensors and Actuators A: Physical*, vol. 25, no. 1, pp. 63 – 71, 1990, proceedings of Eurosensors IV held jointly with Sensoren Technologie und Anwendung.

- [89] D. Sameoto, S.-W. Lee, and M. Parameswaran, "Electrical interconnection through optimized wirebonding onto SU-8 structures and actuators," *Journal of Micromechanics and Microengineering*, vol. 18, no. 7, p. 075023, jun 2008.
- [90] J.-N. Aoh and C.-L. Chuang, "Development of a thermosonic wire-bonding process for gold wire bonding to copper pads using argon shielding," *Journal of Electronic Materials*, vol. 33, no. 4, pp. 300–311, 2004.
- [91] P. F. Bordui, D. Jundt, E. M. Standifer, R. G. Norwood, R. L. Sawin, and J. D. Galipeau, "Chemically reduced lithium niobate single crystals: Processing, properties and improved surface acoustic wave device fabrication and performance," *Journal of Applied Physics*, vol. 85, pp. 3766–3769, 04 1999.
- [92] M. Berg, "Methods for antenna frequency control and user effect compensation in mobile terminals," Ph.D. dissertation, University of Oulu, Faculty of Technology, Department of Communications Engineering; Centre for Wireless Communications; Infotech Oulu, P.O. Box 4500, FI-90014 University of Oulu, Finland, 2011.
- [93] S. Toto, P. Nicolay, G. Morini, Rapp, J. Korvink, and J. Brandner, "Design and simulation of a wireless saw–pirani sensor with extended range and sensitivity," *Sensors*, vol. 19, p. 2421, 05 2019.
- [94] N. S. Jeong and F. Carobolante, "Wireless charging of a metal-body device," *IEEE Transactions on Microwave Theory and Techniques*, vol. 65, no. 4, pp. 1077–1086, April 2017.
- [95] P. L. M. Heydemann, C. R. Tilford, and R. W. Hyland, "Ultrasonic manometers for low and medium vacua under development at the national bureau of standards," *Journal of Vacuum Science and Technology*, vol. 14, no. 1, pp. 597–605, 1977.
- [96] H. Chaloupka, N. Klein, M. Peiniger, H. Piel, A. Pischke, and G. Splitt, "Miniaturized high-temperature superconductor microstrip patch antenna," *IEEE Transactions on Microwave Theory and Techniques*, vol. 39, no. 9, pp. 1513–1521, Sep. 1991.
- [97] O. J. Wenzel and C. K. Bak, "The micro pirani™: A solid state vacuum gauge with wide range," *Vakuum in Forschung und Praxis*, vol. 10, 1998.

8 Acknowledgements

This PhD thesis defense shall be the conclusion of many years of scientific and technical, coordination, administrative and negotiation work. Beyond the outcome of the thesis, this journey taught me a lot about the essence of science, engineering and life in general. A journey that I tried to cross with as much conscience, ethics and respect to people as I could give.

I would like to express my sincere gratitude to my supervisor Prof. Juergen Brandner for giving me the opportunity to conduct my thesis in his group. Working under your supervision taught me a lot, on the scientific side but also on the personal side. Your support, guidance and warnings are invaluable, and I am thoroughly gratified by all the knowledge and experienced that I acquired thanks to you.

I would like to communicate my devoted tribute to Prof. Korvink for the administrative and technical support and for greeting my colleagues and me in his institute.

I am very obliged and thankful to PD Dr. Ulrich Gengenbach for examining my thesis. Your insightful comments were dependable tools to make this thesis work proceed.

This Ph.D thesis was pursued within the Marie Curie ITN MIGRATE with the funding grant agreement 643095. MIGRATE (Research and training network on MIniaturized Gas flow foR Applications with enhanced Thermal Effects) is a multi-partner Innovative Training Network (ITN- European Training Network), assessing research and applications for thermal aspects for gas microflows. This is why I would also like to thank the whole MIGRATE network and the European Commission for this unique opportunity to develop a research career with a challenging project. I also want to thank the coordination of the project and the constant administrative support provided by Martin Knapp and Verena Tomczyk. Then, I would like to thank my second supervisor Prof. Gian Luca Morini for his support and patience with me during my stay in Bologna and throughout all my thesis for all my initiatives and activities.

I will not forget to thank Dr. Martin Wuest who greeted me for a secondment at INFICON supported me with all the administrative aspects and made sure I had everything I needed for my research at INFICON Liechtenstein. Dr. Wuest continued supporting me in the hard times or writing this thesis, pushing me forward and providing me with invaluable feedback all the time.

I won't forget to express the gratitude to Dr. Pascal Nicolay for his technical support throughout all the thesis.

I would like to warmly thank Dr. Michael Rapp for his very insightful suggestions that inspired me for the development of a new sensor.

I would like to thank the whole KIT IMT staff for its technical support but in particular Achim Voigt who provided me with invaluable support and suggestions that enabled my work.

I wish to warmly thank Dr. Mazin Jouda, Dr. Omar Nassar and Dr. Hossein Davoodi for their technical support during the design and manufacturing of my sensor.

I want to thank Ms. Suparna Sundarayyan for her hard work and support for my thesis through her own Master thesis.

I thank my fellow ESRs labmates who became my friends and supported me and entertained me throughout the whole Ph.D period especially Natasa Djordjevic, Danish Rehman, Daniel Mariuta, Nicolas Le Touz and Guillermo Lopez Quesada.

I gained a lot of knowledge from the work with all the colleagues that I had the chance to collaborate with in the Karlsruhe Institute of Technology, the University of Bologna and the company INFICON in Liechtenstein.

This thesis was also the occasion to join several engineering classes at the KIT: introduction to mechatronics, virtual engineering, introduction to microsystems and fluid mechanics. Those classes enabled me to gain knowledge and insights in several topics that proved helpful for the finalisation of the thesis.

In the time slot I had, I tried to make the most of the opportunities I had in terms equipments and infrastructure and competences that I had access to. An effort of adaptation was necessary to integrate 4 different institutions in three different countries, namely KIT IMVT, UNIBO, KIT IMT and INFICON.

After taking a full-time job as a development engineer for self-sustainment purposes, I strived to address all the challenges and issues in order to obtain my Ph.D on October first, 2022.

In the end, I am grateful to my family and friends who remembered me in their prayers for the ultimate success. They gave me enough moral support, encouragement and motivation to accomplish this goal.

Karlsruhe, im Monat JJJJ

M.Sc. M.Sc. CSCA Sofia Toto

List of Figures

2.1	Components of a general measurement system. From [12].	10
2.2	Wheatstone bridge circuit configuration for a sensor.	16
2.3	Common elements of instrument error from [12].a) Hysteresis error b) Linearity error c) Sensitivity error d) Zero shift (null) error e) Repeatability error.	20
2.4	Development steps of a miniaturised sensor. From [23].	23
2.5	Main characteristic length scales at molecular level. From [24].	24
2.6	Gas flow regimes for usual microsystems. From [24].	27
2.7	Knudsen number vs pressure vs dimension of the channel. From [25].	27
2.8	Thermal conductivity of nitrogen versus pressure for the device presented in [10].	30
2.9	Structure of Inficon ceramic diaphragm gauge. From [29].	32
2.10	Structure of a piezoresistor based pressure sensor. From [29].	33
2.11	Liquid manometer principle retrieved from www.engineeringclicks.com on 10/10/2021.	34
2.12	Principle of the thermal conductivity gauge. From [31].	36
2.13	Gas dependence of the Pirani heat transfer gauge. From [33].	37
2.14	Schematic cross section of MEMS Pirani sensor presented in [10].	40
2.15	Schematic drawing of a typical Pirani sensor with a thin heated wire mounted on a cylindrical housing. From [38].	41
2.16	Wheatstone bridge containing the MEMS Pirani sensor. From [10].	42
2.17	Pirani sensor behaviour modelling.	43
2.18	Magnetic field lines of one coil alone. Retrieved from [41]	44
2.19	Magnetic field lines of two coupled coils. Retrieved from [41]	46
2.20	Ideal transformer: (a) circuit; and (b) circuit model. From [42].	47
2.21	Ideal coupled coils (a) in the time domain with a resistive load and (b) in the s-domain with a load impedance $Z_L(s)$. From [42].	47
2.22	(a) Transformer model of ideal coupled coils (b) equivalent circuits on each side. From [42].	48
2.23	Displacement of a rectangular grid during propagation of bulk acoustic wave. a) Longitudinal wave. b) Transverse wave. From [17].	56
2.24	Displacement of a rectangular grid during propagation of a Rayleigh wave. From [17].	56
2.25	Structure of an interdigital transducer. From [53].	59
2.26	Delay line IDT structure. From [54].	60
2.27	Resonator IDT structure. From [55].	61
2.28	SAW IDT with signal processing circuit from [9].	65
2.29	Schematic of the electron beam lithography process. Picture retrieved from [74].	68
2.30	Schematic of the sputtering process.	68
2.31	Schematic of ball-bonding process. From [76]	69
2.32	Schematic of PCB cross-section. From [75].	70
3.1	Thermal response of a cylindrical Pirani wire computed from [38].	74

3.2	Thermal conductivity of the gas versus pressure for different temperatures from [36].	75
3.3	Thermal conductivity of the gas versus pressure for different gas gaps from [36].	76
3.4	Ratio of gas conductance to total conductance computed from [10].	77
3.5	Ratio of the gaseous heat transfer over the total heat transfer in a Pirani sensor in high vacuum computed from [10].	78
3.6	Gaseous thermal conductivity and total thermal conductivity versus sensor heated area. Computed from [35]	79
3.7	Gaseous conductivity for different heater areas computed from [35]	80
3.8	Model used for the parameter sensitivity analysis. From [82].	81
3.9	Thermal response of the infinite periodic sensor at 10^{-4} Pa for substrate emissivities of 0.01, 0.1, 0.2, 0.3, 0.4 and 0.75.	82
3.10	Thermal response at different pressures for an emissivity of 0.4.	83
3.11	Variation of the SAW substrate thickness.	84
3.12	Thermal response obtained for different lengths of the gas column.	85
3.13	Variation of the microchannel surface emissivity.	87
3.14	Variation of width of the substrate.	88
3.15	Variation of the pitch of the metallic electrodes.	89
3.16	Variation of the width of the metallic electrodes.	90
3.17	Variation of the coating of the substrate.	91
3.18	Variation of the height of the electrodes.	92
3.19	Thermal response when varying the power supply.	93
3.20	Simulated geometry.	94
3.21	Simulated geometry.	94
3.22	Microchannel filled with nitrogen.	95
3.23	Simulated geometry. A 1 cm^3 PMMA cube is crossed at its center by a $600\text{ }\mu\text{m}$ diameter cylindrical microchannel. The 1 mm by $400\text{ }\mu\text{m}$ by $600\text{ }\mu\text{m}$ chip is suspended inside the microchannel. The x and y axes units are identical.	96
3.24	Boundary heat source at the bottom side of the chip.	96
3.25	Diffuse surface for radiative heat transfer.	97
3.26	Heat capacity of nitrogen.	99
3.27	Mesh used.	102
3.28	Temperature of the chip vs time at 10^{-4} Pa. The steady state temperature is reached after 38 s.	104
3.29	Steady state temperature of the chip in K vs thermal conductivity at different pressures. The thermal conductivity of the gas depends on pressure, which means that the final temperature of the chip also depends on pressure and is used to measure it.	105
3.30	Thermal response of the simulated sensor at several pressures.	106
3.31	Temperature distribution after 200 s of heating.	106
3.32	Location of the study point.	107
3.33	Temperature distribution after 100 s at the sensor axis.	107
3.34	Chip surface temperature at 10^{-4} Pa.	108
3.35	Chip surface temperature at atmospheric pressure.	108
3.36	Radiosity at high vacuum.	109
3.37	Radiosity of the chip and microchannel at atmospheric pressure.	109

3.38	Calculated calibration curve of the sensor. The curve shows the pressure induced frequency shift for an initial pressure of 10^5 Pa and an initial frequency of 2.45 GHz. The characteristic S-shape profile of the thermal conductivity vs pressure can also be observed for the frequency shift but on the opposite direction since the temperature coefficient of frequency is negative.	110
3.39	MOSFET circuit simulated.	114
3.40	Output current across the 5Ω resistor.	115
4.1	Schematic explosive design of the SAW-Pirani sensor system designed containing: the sensing chip, the heating unit, the interrogation unit and the packaging	117
4.2	Block diagrams of (a) near field and (b) far field wireless power transfer system. From [43].	120
4.3	Relationship between coupling distance and coil diameter. From [42].	121
4.4	MOSFET Circuit Layout designed with the software Sprint Layout.	123
4.5	Schematic of the signal transmission between SAW chip and the respective antennae.	123
4.6	Johanson antenna dimensions extracted from its technical sheet.	126
4.7	WE antenna dimensions extracted from its technical sheet.	126
4.8	Thickness versus power for a constant supplied current of 300 mA.	129
4.9	Layer structure of the designed chip.	129
4.10	Structure of the designed chip. The Lithium Niobate substrate has a gold resistive layer sputtered and 2 wires for electrical connection at its bottom. On top of the substrate the IDT structure made of the main IDT and 3 reflectors is etched via e-beam lithography. Bonding pads on the top and bottom of the main IDT are electroplated for the electrical connection.	131
4.11	Structure of the wireless vacuum sensor. The design shows a $1 \times 1 \times 1 \text{ cm}^3$ Polymethylmethacrylate (PMMA) cube crossed at its center by a microchannel corresponding to the packaging variant 1. The sensing SAW–Pirani chip (variants 1,2 or 3) is inserted inside the microchannel. The heating coil and the interrogation antenna are buried inside the core of the sensor.	132
4.12	Possible cross sections for the microchannel crossing the sensor: quadratic with holding cavities, circular and quadratic and size-matching.	133
4.13	Possible cross sections for the microchannel crossing the sensor: quadratic with holding cavities, circular and quadratic and size-matching.	133
4.14	Packaging variant 2 with chip variant 3, antenna variant 2, PCB variant B combined.	134
4.15	Two PCB layouts designed with Sprint Layout.	135
5.1	Manufactured PCB prior to soldering. On the left side, the top surface of the PCB is depicted, on the right side the bottom surface of the PCB is depicted. Two different alternatives for two different antennas were prepared. The alternative A was prepared for the antenna P/N 2450AT18B100 from the company Johanson Technology and the alternative B was prepared for the antenna WE-MCA 7488940245 from Wuerth Elektronik. The image on the left side shows the top layer with the pads for the antenna and the coil. The image on the right side shows the soldering pads for the SAW chip. On the top layer, the receiver coil and the receiver antenna were connected and at the bottom layer, the SAW chip was connected to the receiver antenna.	138

5.2	PCB with soldered components. On the left side the bottom part of the PCB containing the SAW chip, on the right side the top part of the PCB containing the heating unit Rx part and interrogation unit Rx part.	139
5.3	Packaged SS2452BB2 SAW chip from SAW Components.	140
5.4	SAW chip with IDT resonator structure prior to manufacturing.	140
5.5	Layer structure of the chip. On the bottom a 100 nm gold layer. On top of it, a 20 nm Chromium layer. On top of it, the Lithium Niobate substrate. On top of it, the Aluminum IDT electrodes.	141
5.6	PCB for the MOSFET.	142
5.7	Complete heating unit. On the left side the Tx part and on the right side the Rx part.(1) Oscilloscope (2) Arbitrary Waveform Generator (3) Power source (4) MOSFET circuit (5) Tx and Rx coils (6) Tx coil (7) Rx coil.	142
5.8	Transmitting antenna connected to the Mini VNA Tiny.	143
5.9	Sensor PTFE packaging. The left piece represents the top part of the channel containing the 4 holes at its middle. The middle part corresponds to the bottom part of the channel with the 2 lateral channels for the glue. The right part corresponds to the top cover of the sensor covering the PCB.	144
5.10	Manufacturing of the heating resistive layer and electrical contacting of the chip. Soldering a 100 μm diameter aluminum wire on the gold layer at the bottom of the chip. The chip is located at the center and placed on a metallic film for protection purposes.	144
5.11	Sputtering of the gold layer at the bottom of the chip.	145
5.12	Wirebonding 25 μm gold wire on aluminum pad(c).	145
5.13	PCB containing the heating unit and interrogation unit of the sensor.	146
5.14	Coils with different sizes and inductances.	154
5.15	Complete heating and interrogation unit setup.	155
5.16	Transmitting patch antennae tested.	156
5.17	SAW peak obtained with different PMMA window thicknesses.	158
5.18	SAW peak obtained with different Quartz window thicknesses.	159
5.19	Prototype characterisation with different materials in between outside vacuum.	160
5.20	Current across the 1 Ω resistance according to the coupling distance.	161
5.21	Identification of the SAW signal.	163
5.22	SAW peak frequency versus temperature measured.	164
5.23	Testing the heating and interrogation unit together. The transmitter coil can be seen on the top, the transmitting antenna in the middle and the VNA on the bottom. In the left part, the receiver unit with the receiver coil, the receiver antenna and the SAW chip can be seen. The clamps visible were occasionally used to check the current values.	165
5.24	Schematic of the vacuum test rig showing its components.	168
5.25	Top view of the test rig showing the window. The Tx coil and the Tx antenna are placed on top of the window: (a) SMA cable going to the Network Analyzer. (b) Sensor PCB. (c) Transmitting coil. (d) Cable inside vacuum connecting the receiver coil and the heating resistor. (e) PMMA window.	169
5.26	Complete test rig: (a) Voltage source. (b) Arbitrary Waveform Generator. (c) Vacuum pump. (d) Valve to protect the turbo pump. (e) Pressure sensor. (f) Vector Network Analyzer. (g) Window setup shown in Figure 5.25.	170

5.27	Frequency sweep between 2.3 GHz and 2.5 GHz obtained from the software interface of the mini VNA Tiny. 2 SAW peaks can be distinguished. The sharpest peak corresponding to the first resonance of the SAW chip is always between 2.4 GHz and 2.5 GHz as indicated in the data sheet of the chip The blue curve represents the S11 amplitude in dB and the red curve represents the S11 phase in degrees	173
5.28	SAW peak frequency vs pressure.	174
5.29	Knudsen number of the flow simulated.	177
5.30	Sensitivity of the SAW chip resonance frequency vs pressure in Hz/Pa. A logarithmic scale for the pressure axis was used for the sake of clarity.	178
5.31	S_{11} gain at the SAW chip resonance frequency vs pressure in dB.	179
5.32	S_{11} phase at the SAW chip resonance frequency vs pressure in degree.	180
5.33	Equilibrium temperature of the chip versus pressure.	181
6.1	New chip design.	186
6.2	New packaging design.	186
9.1	Mean free path versus pressure	213
9.2	Transition pressure corresponding to a Knudsen number of 10 using the hard sphere model [24]	213
9.3	Gaseous conductivity for different heater areas computed from [35]	214
9.4	Output voltage versus pressure from [97]	214
9.5	Conductivity versus pressure	215
9.6	Role of the miniaturization	215
9.7	Ratio of the gaseous heat transfer over the total heat transfer in the Pirani sensor presented in [10] in rough vacuum	215

List of Tables

2.1	Physical phenomena used by active sensors.	12
2.2	Sensitive electric properties in passive sensors.	13
2.3	Sensing principles and variables presented	13
2.4	Manufacturer's specifications : Typical Pressure Transducer. From [12].	22
2.5	Vacuum levels according to the ISO 21360 Norm	30
2.6	Detection principles and pressure ranges of MEMS Pirani gauges	45
2.7	Linear coefficient for physical effects on SAW substrate materials.	59
2.8	Temperature coefficient of frequency of several piezoelectric materials	61
3.1	Computed thermal conductivity of nitrogen.	81
3.2	Substrate emissivities tested.	82
3.3	Thermal conductivity at pressures between 10^{-4} Pa and 1 Pa for several gas column lengths.	86
3.4	Dimensions of the geometry simulated in Comsol.	95
3.5	Boundary conditions assigned to the model.	96
3.6	Material properties of Lithium Niobate.	97
3.7	Material properties of nitrogen.	98
3.8	Material properties PMMA.	98
3.9	Thermal conductivity values.	100
3.10	Radiative heat transfer boundary conditions.	101
3.11	Mesh statistics.	101
3.12	Size.	102
3.13	Mesh properties.	103
3.14	Computation information.	103
3.15	Simulation results.	105
3.16	Frequency shift at selected ranges. The frequency shift per decade is in the kHz range or higher and can easily be measured using a Vector Network Analyzer.	111
3.17	Knudsen number of the flow and type of flow according to the pressure value.	112
4.1	Chip variants used in the thesis.	118
4.2	Interrogation antennas used in the thesis.	118
4.3	Sensor packaging used in the thesis.	119
4.4	PCBs manufactured in the thesis.	119
4.5	Comparison between Wuerth Elektronik and Johanson antenna.	127
4.6	Comparison between Wuerth Elektronik and Johanson antenna gains.	127
4.7	Piezoelectric materials properties.	130
5.1	Components of the MOSFET circuit.	141
5.2	Current across the receiver coil based on position and type of resonance.	155

5.3	Current across the receiver coil based on position and type of resonance.	162
5.4	Computed sensitivity of the resonance frequency to pressure.	176
5.5	Sensitivity of the prototype.	182

9 Appendices

9.1 Pirani curves obtained with Matlab

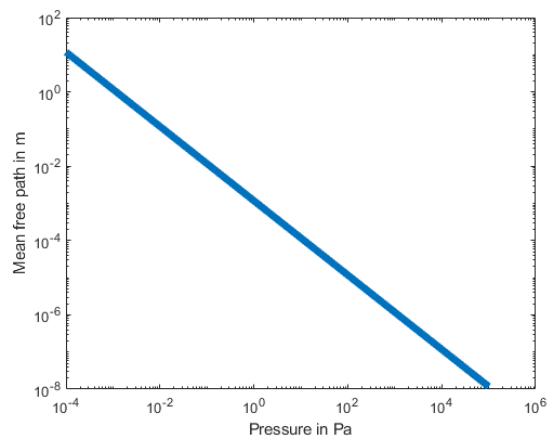


Figure 9.1 – Mean free path versus pressure

The mean free path represents the distance crossed by a molecule before colliding with another one or with the walls which creates heat transfer. It is a figure of merit for Pirani sensing. The mean free path versus pressure for Nitrogen molecules was plotted using the model described in [10] Volklein. It varies between 10 m approx at 10^{-4} Pa and 10 nm at atmospheric pressure.

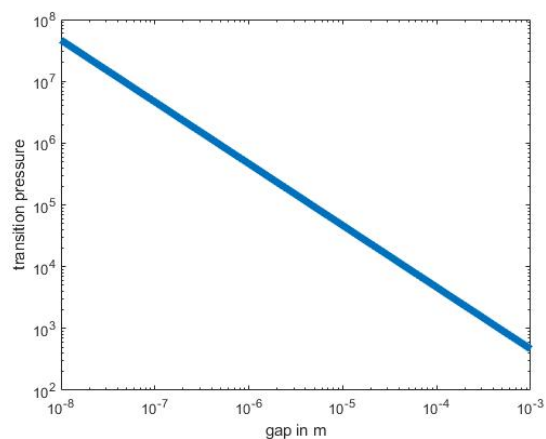


Figure 9.2 – Transition pressure corresponding to a Knudsen number of 10 using the hard sphere model [24]

The transition pressure corresponds to the transition between the transition flow and the free molecular flow. The transition pressure depends on the gas and the geometry of the device. A device with a gas gap of 10 nm has a transition pressure of 60 MPa and a gap of 1 mm corresponds to a transition pressure of 800 Pa approximately.

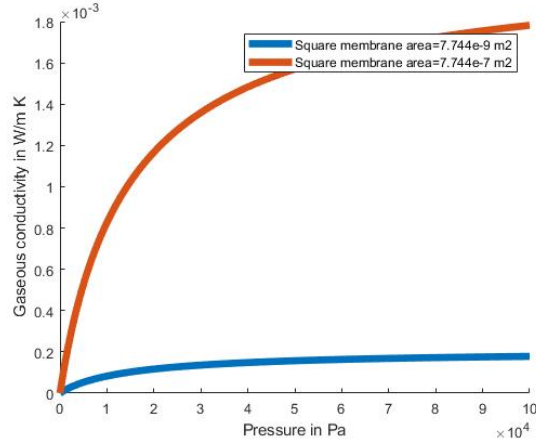


Figure 9.3 – Gaseous conductivity for different heater areas computed from [35]

In Pirani sensing, the heated area impacts the surface to volume ratio, the general power consumption and the heat balance. A smaller area reduces parasitic heat transfer and increases the signal to noise ratio, which shows the relevance of miniaturization for Pirani sensors.

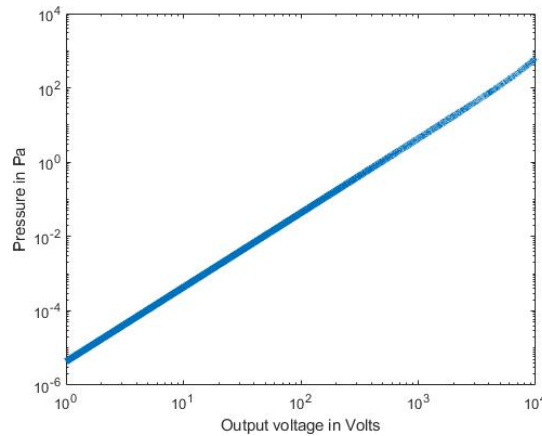


Figure 9.4 – Output voltage versus pressure from [97]

The final signal for a Pirani sensor is a voltage. In the plotted model, the voltage varies over several decades of pressure through the sensing range.

For Pirani sensing, the measurement signal comes from the pressure dependent thermal conductivity of the gas.

Variation of the heater surface area influences the value of the parasitic heat transfer and therefore the signal to noise ratio for Pirani sensing.

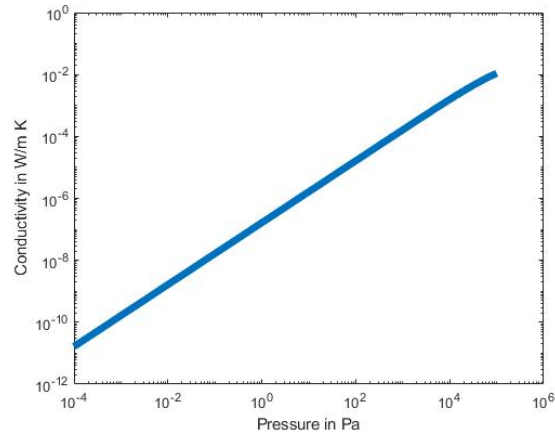


Figure 9.5 – Conductivity versus pressure

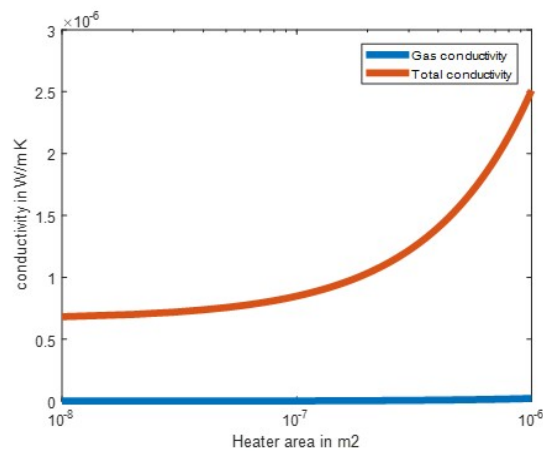


Figure 9.6 – Role of the miniaturization

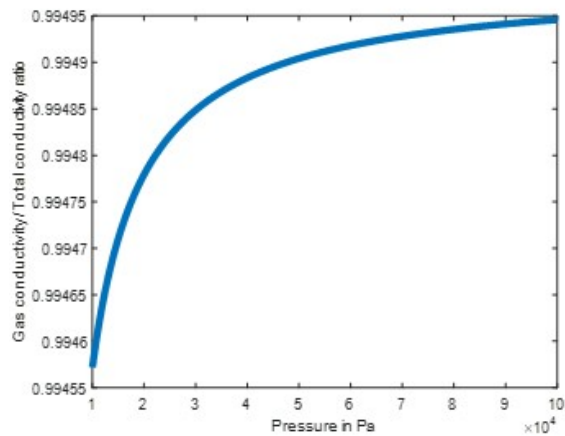


Figure 9.7 – Ratio of the gaseous heat transfer over the total heat transfer in the Pirani sensor presented in [10] in rough vacuum

For pressures higher than 10 000 Pa, the gaseous heat transfer represents more than 99% of the total heat transfer.